

IMMUNOTHERAPY FOR DESMOPLASTIC MELANOMA: NANO-MEDICINE
APPROACHES OF VACCINATION AND IMMUNE-MODULATION

Qi Liu

A dissertation submitted to the faculty at the University of North Carolina at Chapel Hill in
partial fulfillment of the requirements for the degree of Doctor of Philosophy in the Joint
Department of Biomedical Engineering.

Chapel Hill
2018

Approved by:

Leaf Huang

Rihe Liu

Zhen Gu

Kristy Ainslie

Philip Smith

David Zaharoff

© 2018
Qi Liu
ALL RIGHTS RESERVED

ABSTRACT

Qi Liu: Immunotherapy for desmoplastic melanoma: Nano-medicine approaches of vaccination and immune-modulation
(Under the direction of Leaf Huang)

Melanoma, the most lethal skin cancer, has an incremental incidence, few durable therapies, and a low survival rate of less than 10 % for late-stage patients in clinics. In desmoplastic melanoma, a rare histological variant of melanoma, the highly fibrotic morphology as well as the immune-suppressive tumor microenvironment led to distinct clinical behavior when compared with other melanoma subtypes, thus hindering treatment efficacy. To overcome these therapeutic hurdles, herein in this dissertation work I developed multiple innovative strategies based on targeted nano-delivery systems. These strategies include the effective delivery of therapeutic vaccination, immune-modulating chemo-drugs and active compounds, gene therapy, and a combination of chemo-immune initiated/guided treatment.

A total of five aims were sequentially designed, including 1) nano-vaccination. The tumor-specific antigen peptides were efficiently delivered to antigen-presenting cells along with immune-stimulating adjuvant. This therapeutic vaccine inhibited aggressive tumor growth. 2) nano-sunitinib. The FDA approved drug sunitinib was targeted delivered to the tumor with improved anti-tumor efficacy, furthermore, it largely remodeled immune suppressive microenvironment and facilitated vaccination efficacy. 3) nano-fraxinellone. The active compound fraxinellone was nano-delivered to the tumor microenvironment, inhibiting the transition of tumor associated fibroblasts and skewed TGF- β /IFN- γ balancing toward

pro-inflammatory settings. 4) nano-wnt5a trap. Key molecular wnt5a secreted by tumor cells in inducing dendritic cell tolerance and tumor fibrosis was locally trapped, thus significantly tuned immune recognition and surveillance of cancer progression. 5) nano-delivery of mitoxantrone and celastrol. Two drugs were screened out with highest anti-tumor and anti-fibrosis potentials and worked synergistically in inducing immunogenic tumor cell death and long-term memory immune responses.

Using animal models of desmoplastic melanoma, our nanomedicine designs significantly elicited an overall anti-tumor immunity with increased efficacy, safety profiles, and prolonged host survival, suggesting their high translatability to the clinic. This dissertation research work further sheds light on a deeper understanding of cancer type-specific microenvironment and immune modulators, as well as future mechanism studies in designing immunotherapy for desmoplastic melanoma.

ACKNOWLEDGEMENTS

I would like to thank Dr. Leaf Huang for serving as my mentor in my doctoral research, he has been taking over every ounce of burden on his shoulder to support my dissertation. As a passionate scientist and encouraging mentor, he always puts students at top priority. I adore him as role model for my future professional career. I also thank Shilling Huang, wife of Dr. Huang, for supporting me like own child. Thank you, dear Huang family, for your caring in my personal life, and my engagement in fellowship.

I thank Drs. Rihe Liu, Zhen Gu, Kristy Ainslie, Philip Smith, and David Zaharoff, for serving as my dissertation committee. Thank you for your valuable scientific advices which built up the strengths of my research. To Dr. Lei Miao, thank you for guiding me through rotation and teaching me from the start. To Dr. Limei Shen, for offering me tremendous input in scientific training, experimental designs and discussions. To Dr. Wantong Song, for your suggestions on scientific career development.

My dissertation is truly a team effort, especially the active collaboration with Dr. Hongda Zhu, Dr. Lin Hou, and Fengqian Chen, I thank you all for your important contribution and critical advice. The time and effort we spent together made up my best days and nights in Chapel hill.

I am also grateful to the past and current Huang lab members for your help:

Yun Liu, Dr. Xueqiong Zhang, Manisit Das, Dr. Andrew Satterlee, Dr. Yi Zhao, Dr. Matthew Haynes, Dr. Sai An, Sara Musetti, Mengying Hu, Dr. Yanzuo Chen and Dr. Nasha Qiu.

Personally, I have received tremendous support and encouragement from: Fengqian Chen, Limei Shen, Ning Cheng, Yanqi Ye, and Xueqiong Zhang. Thank you for accommodating me through ups and downs in daily routines.

Most importantly, I would love to thank my parents for their endless support and motivating me towards my goals. I am honored to be their child through this life journey.

Praise the Lord! For He can work through those who praise Him.

TABLE OF CONTENTS

LIST OF FIGURES.....	vii
LIST OF TABLES.....	x
LIST OF ABBREVIATIONS.....	xi
CHAPTER 1: INTRODUCTION.....	1
CHAPTER 2: NANO-VACCINATION.....	27
CHAPTER 3: NANO-SUNITINIB REMODELING OF TME FACILITATES VACCINATION.....	46
CHAPTER 4: NANO-FRAXINELLONE REMODELING OF TME FACILITATES VACCINATION.....	68
CHAPTER 5: NANO-MEDIATED WNT5A TRAPPING ENHANCES IMMUNOTHERAPY.....	96
CHAPTER 6: NANO-MEDIATED CHEMO-IMMUNO THERAPY ARRESTED TUMOR PROGRESSION AND INDUCED DORMANCY.....	123
CHAPTER 7: SUMMARY AND FUTURE PERSPECTIVES.....	154
REFERENCES.....	159

LIST OF FIGURES

Figure 1 - Targeted drug delivery to melanoma.....	2
Figure 2 - Characterization of the LCP NP-based BRAF peptide vaccine.....	30
Figure 3 - Antigen-specific immune response induced by the BRAF peptide vaccine.....	32
Figure 4 – Antitumor activity of the BRAF peptide vaccine in murine BRAF-mutant model.....	34
Figure 5 - Enhanced T-cell infiltration into tumor microenvironment-induced potent CTL killing.....	35
Figure 6 - Change of TME.....	37
Figure 7 - Safety profile of the BRAF peptide vaccination.....	38
Figure 8 - Characterization of SUN _b -NP and LCP-BRAF peptide vaccine.....	48
Figure 9 - Anticancer efficacy in advanced DM model.....	50
Figure 10 - Safety evaluations.....	51
Figure 11 - Pharmacokinetics and bio-distribution of SUN.....	52
Figure 12 - Structure changes in TME.....	55
Figure 13 - Change of tumor-infiltrating immune cells in TME.....	57
Figure 14 - RT-PCR elucidated inflammatory cytokines within the TME.....	58
Figure 15 - Oncogene expression levels.....	59
Figure 16 - Preparation and characterization of Frax NE <i>in vitro</i> and <i>in vivo</i>	71

Figure 17 - Tumor inhibition effects and TME changes <i>in vivo</i> after treatment with Frax.....	74
Figure 18 - Tumor inhibition effects and TME changes <i>in vivo</i> after treatment with Frax NE combined with vaccine.....	77
Figure 19 - Enhanced T-cell infiltration into TME-induced potent CTL killing.....	80
Figure 20 - Changes of tumor-infiltrating immune cells and cytokines in TME.....	83
Figure 21 - Safety evaluation of vaccine, Frax NE and Combo.....	86
Figure 22 - ICD induced by low dose DOX.....	98
Figure 23 - Wnt5a is a key molecule controlling the immunosuppressive and desmoplastic TME.....	100
Figure 24 - Local distribution and expression of Wnt5a trap.....	102
Figure 25 - Combination therapy significantly inhibited tumor progression.....	106
Figure 26 - Remodeling of TME.....	108
Figure 27 - Combination therapy demonstrated long-lasting overall immune response.....	110
Figure 28 - H&E morphology under different therapies.....	111
Figure 29 - Toxicity evaluation of therapies.....	112
Figure 30 - The design of chemo-immuno therapy.....	125
Figure 31 - The TME-responsive NP delivery platform.....	129
Figure 32 - The TME-responsive NP delivery platform.....	131

Figure 33 - Effective therapy significantly improved anti-tumor response and remodeled suppressive TME.....	135
Figure 34 - Effective therapy significantly enhanced cell apoptosis and cell cycle arrest.....	137
Figure 35 - Effective therapy remodeled immune profile within TME.....	138
Figure 36 - Second model of desmoplastic melanoma.....	139
Figure 37 - Enhancement of long-term immune surveillance, host survival, and memory immunity.....	140
Figure 38 - Long-term tumor dormancy and anti-metastasis efficacy of therapy.....	142
Figure 39 - Toxicity evaluation of therapies.....	144

LIST OF TABLES

Table 1. Characterization of SUN _{b-NP}	48
Table 2. <i>In vivo</i> pharmacokinetic parameters of ³ H-labeled SUN _{b-NP} and SUN solution in tumor-bearing C57BL/6 mice.....	53
Table 3. Antibody list.....	115
Table 4. Primer list for real-time PCR.....	121

LIST OF ABBREVIATIONS

α -SMA	α -smooth muscle actin
AEAA	Aminoethylanisamide
AKT	Serine/threonine-protein kinases
ALT	Alanine aminotransferase
APC	Antigen -presenting cell
AST	Aspartate aminotransferase
AUC	Area under the curve
BRAF	B-Raf Proto-Oncogene
Breg	Regulatory B cell
BSA	Bovine serum albumin
BUN	Blood urea nitrogen
CAR	Chimeric antigen receptor
CCL2	C-C motif chemokine 2
CEL	Celastrol
CFSE	Carboxyfluorescein succinimidyl ester
CMC	Carboxymethylcellulose
CTL	Cytotoxic T lymphocyte

CTLA-4	Cytotoxic T-lymphocyte antigen 4
CRT	Calreticulin
CUGBP-1	CUG-binding protein 1
CXCL12	C-X-C motif chemokine 12
CXCL13	C-X-C motif chemokine 13
DC	Dendritic cell
DFS	Disease free survival
DiI	1,1'-dioctadecyl-3,3,3',3'-tetramethylindocarbocyanine perchlorate
DL	Drug loading
DM	Desmoplastic melanoma
DMSO	Dimethyl sulfoxide
DOPA	Dioleoylphosphatidic acid
DOTAP	(±)-N,N,N-trimethyl-2,3-bis(z-octadec-9-ene-oyloxy)-1-propanaminium chloride
DOX	Doxrubicin
DSPE-PEG-2000	1,2-distearoyl-sn-glycero-3-phosphoethanolamine-N-[amino(polyethylene glycol)-2000]
DSPE-PEG-NHS	3-(N-succinimidylxyglutaryl)aminopropyl, polyethyleneglycol-

	carbamyl -distearoylphosphatidylethanolamine
ECM	Extracellular matrix
EE	Encapsulation efficiency
EMT	Epithelial-mesenchymal transition
EPR	Enhanced permeability and retention
FAK	Kinase integrin/focal adhesion kinase
FAP	Fibroblast Activation Protein
FGF-2	Fibroblast growth factor
FRAX	Fraxinellone
HCT	Hematocrits
HGB	Hemoglobin
HLA	Human leukocyte antigen
HMGB1	High mobility group box 1
ICD	Immunogenic cell death
IFN- α	Interferon alpha
IFN- γ	Interferon gamma
IGF-1	Insulin-like growth factors
IL-2	Interleukin-2

IL-4	Interleukin-4
IL-6	Interleukin-6
IL-10	Interleukin-10
LCP NP	Lipid-coated calcium phosphate nanoparticle
LDH	Lactate dehydrogenase
LN	Lymph node
LPD NP	Lipid-protamine-DNA nanoparticle
M1	M1 macrophage
M2	M2 macrophage
MDSC	Myeloid-derived suppressor cell
MEK	Mitogen-activated protein kinase
MIT	Mitoxantrone
NE	Nanoemulsion
NP	Nanoparticle
N-RAS	Neuroblastoma RAS viral oncogene homolog
ODN	Oligodeoxynucleotides
OS	Overall survival
PD-1	Programmed cell death 1

PD-L1	Programmed cell death-ligand 1
PFS	Progression-free survival
PI3K	Phosphatidylinositol-4,5-bisphosphate 3-kinase
PLT	Platelet
PTEN	Phosphatase and tensin homologue deleted on chromosome 10
RBC	Red blood cell
RGP	Radial growth phase
SUN	Sunitinib
SUN _b -NP	Sunitinib base-loaded NP
TAA	Tumor-associated antigen
TAF	Tumor-associated fibroblast
TAM	Tumor-associated macrophages
TEM	Transmission electron microscope
TGF- β	Transforming growth factor- β
Th1	Type 1 T helper
Th2	Type 2 T helper
THF	Tetrahydrofuran
TIL	Tumor-infiltrating lymphocyte

TME	Tumor microenvironment
Treg	Regulatory T cell
TUNEL	Terminal deoxynucleotidyltransferase-mediated nick end labeling
UV	Ultraviolet
VEGF	Vascular endothelial growth factor
VGP	Vertical growth phase
WBC	White blood cell
Wnt5a	Wnt family member 5A

CHAPTER 1

INTRODUCTION¹

1.1 Introduction and significance

Melanoma derived from melanocytes is the most aggressive type of skin cancer, it accounts for nearly 80 % of skin cancer deaths.¹ Despite recent improvements in prevention and early detection, approximately 20 % of melanoma patients still die from the disease. Melanoma incidence is not only correlated with age, but it is one of the most general causes of cancer and cancer deaths in people aged 20–35. Overall, melanoma is a strong example of how genetics and the environment cooperate to stimulate carcinogenesis.^{2,3} Conventional melanoma treatment, whether radiotherapy or chemotherapy, present a short therapeutic window and a high incidence of recurrence/metastasis.⁴ Major drawbacks of such therapies are that the tumor-specific immune response is insufficiently evoked and that the lack of specificity results in side effects to the whole-body immunity.⁵ Besides, the immune response of the tumor microenvironment (TME) has been poorly studied. The TME comprises not only tumor cells but also immune and interstitial cells. Thus, an effective therapy should be based upon the specific cancer type and a thorough understanding of its TME.⁶

Currently, there are five types of standard treatment for melanoma patients, including surgery, radiation therapy, chemotherapy, immunotherapy, and targeted therapy.⁷ In the study of

¹ This chapter previously appeared as an article in *Advanced Drug Delivery Reviews*. The original is as follows: Q Liu, M Das, Y Liu, L Huang. “Targeted drug delivery to melanoma.” *Advanced drug delivery reviews*. 2017 Sep 19.

new targeted therapies, B-Raf proto-oncogene (BRAF) and mitogen-activated protein kinase (MEK) specific inhibitors have emerged with distinct survival benefits. Despite ongoing advancement in the study of metastatic melanoma, emerging drug resistance and systemic toxicity limit efficacy. Overall, the success rate for the treatment of melanoma is relatively low.

Facing the challenges of off-target effects, serious toxic adverse effects, and short circulation time in conventional systemic drug administration, researchers have developed nanoparticle (NP) technologies as a means of overcoming these disadvantages. Over the past few years, significant advances in NP-based drug delivery has made it easier for researchers to develop effective treatments. Because NPs offer excellent barrier protection to avoid host immune system attack and enzymatic degradation, immune-modifiers can be administrated to downregulate oncogenes or restore tumor suppressor microenvironment for more effective cancer chemotherapy, thus combating drug resistance. NP-based strategies have presented effective delivery of therapeutically payload in treating melanoma (**Figure 1**).

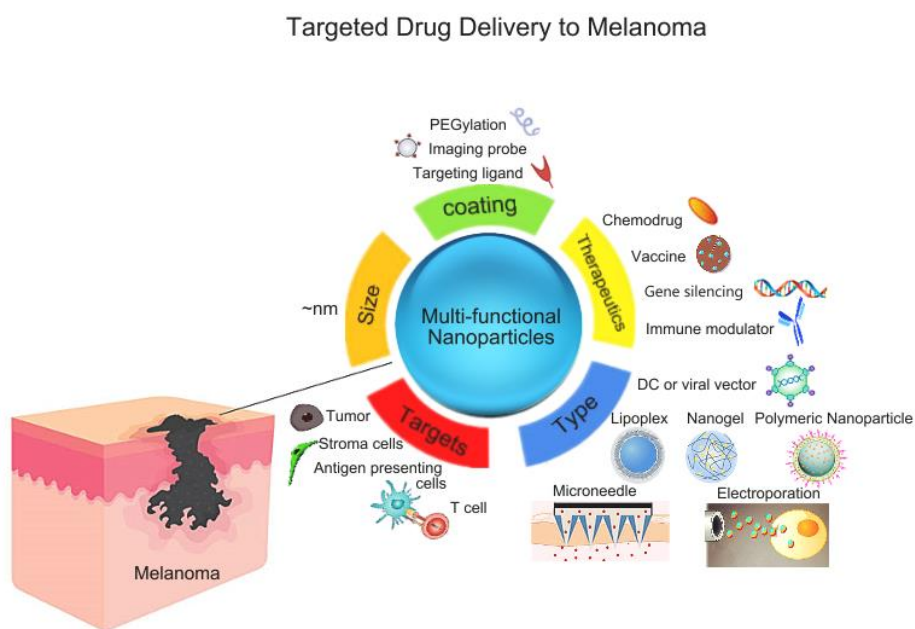


Figure 1. NP-based strategies for targeted drug delivery to melanoma

1.2 Biology of melanoma

Melanocytes are located at the bottom of the skin epidermal layer and are responsible for generating melanin, which is the pigment responsible for a suntan and protects the skin against damage from ultraviolet exposure. In general, people with pale skin color (e.g., Caucasians) have an increased risk of melanoma-genesis comparing to darker skin populations (e.g., Africans, East Asians, Hispanics). Similarly, people who have excessive sun exposure are at higher risk for tumorigenesis.

The development of melanoma is a multistep process with clinical and histological characteristics.⁸ Melanoma-genesis can be histologically divided into five stages. In stage one, acquired nevi form because of increased melanocyte proliferation. Nevi are benign skin lesions; however, most malignant melanomas are derived from nevi.⁹ In stage two, melanocytes grow into dysplastic nevi showing abnormal differentiation. In stage three, dysplastic nevi continue developing into the radial growth phase (RGP) primary tumor. RGP melanomas develop within the epidermis but do not have the ability to invade into the dermis. In stage four, RGP melanomas acquire invasive potential through genetic alterations and invade into the dermis. This is the so called vertical growth phase (VGP). At this phase, melanomas possess the potential of self-sufficient growth signals and the ability to invade, thus making treatment options more limited. In the fifth and last stage of melanoma development, the metastatic lesion is formed. In this stage, VGP melanomas continue to grow larger and invade surrounding tissues. Metastatic lesions form in distant organs the melanoma becomes metastatic.

During the past few decades, epidemiological studies have identified several melanoma risk factors. These factors include excessive ultraviolet (UV) light exposure, moles (nevi), family history of melanoma, and a weakened immune system.¹⁰

1.3 Oncogenic pathways

Melanoma cells develop multiple unique signaling pathways in regulating tumor proliferation, migration, cell differentiation, as well as apoptosis. Downregulated signaling pathways often lead to tumorigenesis for melanoma development. Signal pathways can be activated by external stimuli and function to convey a signaling cascade from the cell surface to intracellular downstream effectors or to be activated by constitutively activated internal oncogenes without external stimuli. Deregulated cell proliferation and apoptosis are two major common factors required for most of the human malignant tumor development that is mediated by oncogenic signaling pathways.

The neuroblastoma RAS viral oncogene homolog (N-RAS) oncogene is mutated at codon 61 in 20% of melanomas.⁹ Most mutations result in the constitutive activation of the N-RAS oncogene that then impairs guanosine triphosphate (GTP) hydrolysis.¹¹ Constitutively active N-RAS activates the BRAF/MEK/Extracellular Signal-regulated Kinase (ERK) (MAPK) and Phosphatidylinositol-4,5-bisphosphate 3-kinase (PI3K)/ serine/threonine-protein kinases (AKT) cascades that further facilitate the proliferation, evasion, and metastases of tumor cells.

A. MAPK and ERK1/2 pathways

The mitogen-activated protein kinase (MAPK) pathway is often referred to as the ERK1/2 signaling pathway for its growth factor receptor-mediated (e.g., epidermal growth factor receptor (EGFR)-mediated) activation initiated from the plasma membrane. Once activated, the MAPK pathway would facilitate a series of signaling cascades, including RAS/RAF/MEK/ERK. It begins with a growth receptor receiving stimuli and then activating RAS by converting inactive RAS-GDP to active RAS-GTP.¹² The active RAS-GTP recruits RAF and activates RAF by

phosphorylation specific to the cell membrane. Phosphorylated RAF then phosphorylates MEK1/2, which then activates ERK1/2 by phosphorylation. Activated ERK1/2 signaling pathway boosts cell proliferation by conveying signaling through protein phosphorylation to cytoplasmic and nuclear effectors. The phosphorylation results in fast cell proliferation by regulating Cyclin D1, p21, p27, and c-myc.¹³ The classic MAPK/ERK1/2 pathway needs extracellular stimuli to initiate activation of the signaling cascade. However, in melanoma and other human cancers, including thyroid and colorectal cancers, constitutively activated ERK1/2 signaling resulting from a BRAF (V600E) mutation could promote tumorigenesis.^{14, 15}

BRAF, also referred to as the proto-oncogene B-RAF or V-RAF murine sarcoma viral oncogene homolog B1, is a serine/threonine-protein kinase. B-RAF, A-RAF, and C-RAF (also known as RAF-1) constitute the RAF kinase family.¹⁶ Through a BRAF mutation, the MAP kinase pathway is activated in ~7 % of human carcinomas, with ~60 % of cutaneous melanomas having activating mutations.¹⁷ A BRAF mutation is very common in cutaneous melanoma; its incidence is very rare in acral, mucosal, conjunctival, and uveal melanomas.¹⁸ In 90 % of BRAF-mutant melanoma tumors, the BRAF mutation is a single-base missense from T to A; this would change valine to glutamic acid at codon 600 (V600E) in exon 15.¹⁹ Mutated BRAF (V600E) protein is highly activated comparing to wild-type, owing to a conformational transform in protein structure, where glutamate phosphorylation occurs at the thr598 and ser601 phosphorylation sites.²⁰

Although the BRAF (V600E)-initiated, constitutively-activated ERK1/2 pathway contributes to increased cell proliferation for tumor development, recent reports indicate hyper-activated ERK1/2 activity at a level that could lead to cell senescence for nevi formation without melanoma formation in transgenic mice. Previously, other groups have indicated that BRAF

(V600E) is critical to promoting melanocyte proliferation for the formation of benign nevi, but it is not the only key factor for melanoma development.²¹ Collectively, it is accepted that more than just a BRAF (V600E) mutation is required for melanoma development.

B. PI3K/AKT pathways

The PI3K/AKT pathway participates in fast cell proliferation, and drug resistance.²² The PI3K/AKT pathway is activated by extra-cellular stimulation of receptor tyrosine kinases. The activated AKT then trans-locates to the cytoplasm or nucleus to activate downstream effectors for different signaling cascades. During the process of activation, PI3K/AKT signaling can be inhibited by phosphatase and tensin homologue deleted on chromosome 10 (PTEN).²³

There are three AKT family members, AKT1, AKT2, and AKT3, known as important downstream effectors that relay the signal transduction cascade coming from PI3K. AKT3 plays major role in melanoma-genesis. Earlier immunohistochemical studies found that ~70 % of cutaneous melanomas have elevated AKT expression compared to normal melanocytes. Furthermore, previous studies have shown that, of the three AKT family members, major AKT3 activation facilitates tumor progression. Inhibition of AKT3 using siRNA leads to decreased melanoma development.^{24, 25}

1.4 Animal models in melanoma research

More advanced pre-clinical melanoma models have been developed that assemble the relevant clinical conditions. To gain a broader understanding of tumor biology, these *in vivo* models mirror true melanoma settings. The most widely used pre-clinical model are murine models, including but not limited to xenograft, syngeneic, and genetically engineered models.²⁶

A. Xenograft models

Xenograft models are built upon the inoculation of human melanoma cells into an immune-deficient mouse. Once subcutaneously implanted, melanoma cells proliferate and metastasize along lymphatic tissue and blood vessels, which strongly resemble the human condition.²⁷ Studies based on xenograft models mainly focus on tumor growth mechanisms, major tumorigenesis pathways, pharmaceutical therapy, bio-availability and toxicities.

Unfortunately, cultured melanoma cell lines are purified clones that differ from the original parent patient-derived cells. They may lose certain metastasis promoting markers while proliferating under the subcutaneous microenvironment. This results in irrelevant predictions of clinical outcome and explains many clinical trial failures.²⁸ Patient derived tumors can be xenografted directly into animal models, but the expenses of model establishment and maintenance are rather high, comparing to purified cell lines.

B. Syngeneic allograft

Syngeneic models are developed by inoculation of melanoma cells into the same species and genetic background.²⁹ These mice are immune-competent with a fully functional immune system. In the study of melanoma microenvironment, dendritic cells (DCs) presenting tumor released antigens, thus allow the natural interaction between melanocytes and immune cells, such as T cells and B cells.³⁰

Several types of cells have been applied to syngeneic transplantations. The most commonly utilized cell types are building upon C57BL/6J mice, which all induced by specific chemical reagents. This cell line, so called the B16 cell line, is characterized by a variety of behaviors including tumor growth, invasion, and metastasis. The two well-established sub-

clones, established by *in vivo* passaging are the B16F1 and B16F10 cell lines. B16F1 has the notable distinguishing feature of low metastatic potential and can therefore be used to study the growth of primary tumors. In contrast, B16F10 usually shows a higher metastatic ability to distant organs, with the highest probability of metastasis in the lungs.³¹ Due to its rapid growth and high turnaround rate, B16 models are perfect for animal *in vivo* studies. For instance, subcutaneous tumors usually reach therapeutic window within two to four weeks.³²

The B16 model has brought valuable insight into melanoma immunology studies, as well as immunotherapy strategies; however, when compared with human melanoma, the adhesion proteins and growth factors of mouse cell lines are quite different. Despite the B16 cells being able to produce a variety of sub-clones, they come from a unitary inbred mouse, thus unrepresentative of human conditions. Scientific interpretations based on such model can therefore be misleading.³³

C. Genetically engineered models (GEMs)

Genetic engineering models build upon transgenic mice with engineered gene expression specific to melanoma-genesis. We have gained a tremendous understanding of gene functions through studies of GEMs for effective targeting therapy. By combining with other neoplasm-inducing strategies such as UV-induction, melanoma development is more accurately assessed in a GEM. Compared with other pre-clinical models, GEMs are more precise in predicting drug efficiency.³⁴

RAS model. It has been found that RAS family proteins contain a high number of mutations in cutaneous melanoma.³⁵ Their specific mutations have been investigated in depth in murine models, in order to explain underlying mechanisms of melanoma-genesis.

PTEN/BRAF models. Researchers have found that 65 % of malignant melanoma cells carry somatic missense BRAF mutations. In most malignant melanoma cases, BRAF mutations and RAS mutations are mutually exclusive, whereas MAPK signal transduction is excessively activated.³⁶ The silencing of PTEN further induces excessive activation of AKT signal pathway, thus up-regulating BRAF gene expression to be activated.

RET model. This model is established upon the RET proto-oncogene, which encodes for glial cell-derived neurotrophic factor-specific receptor tyrosine kinase.³⁷ RET gene expression can cause the progressive growth of melanoma. As a result, benign melanoma tumors occur months later, followed by eventual malignant tumor growth and organ metastasis. During tumorigenesis, the MAPK signaling cascades are highly activated, where the expression of RET transgene is found to increase in a gradual manner.

Although GEMs models are highly applicable, we are still challenged with multiple limitations. Genetic modified murine strains accompanied with significant labor costs, and the expenditure is rather high. In addition, some genetic alterations have adverse effects on reproductive ability, thus dampen the effective genotyping for targeted therapy.

D. Physical or chemically induced models

Models induced by UV radiation could form highly assembled natural human melanoma-genesis. But the drawbacks of murine models are evitable when comparing to human conditions. For one, human skin and mouse skin melanoma cells reside in different locations. Human melanocytes are mainly located in the basal layer of the cuticle and the epidermal dermis junction; therefore, they are vulnerable to be invaded by UV radiation. However, in murine models melanocytes are in the deep dermis and are well protected, therefore there is less chance

of a natural occurrence of melanoma.³⁸ 7,12-Dimethylbenz[a]anthracene (DMBA) and 12-O-Tetradecanoylphorbol-13-acetate (TPA) can be utilized in situ to stimulate melanoma-genesis, but the tumor cells induced contain no melanin pigments, thus they are less representative of natural settings.³⁹

Research based on different murine models provide significant insights and valuable interpretations of melanoma development. By comparing respective advantages and disadvantages of each model, great progression has been achieved. The studies of various pre-clinical models are of great translational value in the diagnosis, treatment, and prevention of melanoma. Although currently incurable, an increasing understating of disease biology will offer more effective treatment options for patients with advanced melanoma.

1.5 Current treatment of melanoma

The first-line treatment options for melanoma patients are surgical removal and radiation therapy. Surgery can involve a wide local excision, lymphadenectomy, and sentinel lymph node (LN) removal. In many cases, surgical removal of melanoma can be combined with chemotherapy, radiation therapy, biologic therapy, and targeted therapy. Radiation therapy uses high-energy radiation to induce melanoma cell death. Depending on the site, radiation can be classified into two categories, external and internal.⁴⁰ An external source of radiation can be used to direct high-energy beams to the tumor with external therapy versus an internal therapeutic approach where radiation is targeted to internal metastatic melanoma using wire needles or catheters.⁴¹

Unfortunately, metastasis results in poor melanoma prognosis. Metastatic melanoma is aggressively resistant to chemotherapeutic regimes. Many studies on the molecular basis of melanoma survival and proliferation have identified apoptotic resistance of melanoma cells as the underlying cause of chemo-resistance.⁴² This presents a formidable challenge in devising treatment strategies for advanced melanoma, and until recently there was little advancement in standards of care. Dacarbazine has been the sole first-line treatment for melanoma since its FDA approval in 1976. It has demonstrated a response rate of 10–20 % in Phase I and Phase II clinical trials, but the benefit in overall survival (OS) has never been clearly established.⁴³ Interferon alpha (IFN- α), a type I interferon, is used for adjuvant immunotherapy in advanced melanoma; however, improvements in OS are debatable, and the clinical markers for the subset of patients sensitive to the adjuvant therapy have not been identified. High-dose Interleukin-2 (IL-2) was approved in 1998, but, again, the response rate is only about 10 %, and therapy involves grade 3 toxicities.⁴⁴

Advancement in understanding of cancer progression and survival has resulted in a resurgence of interest in developing newer therapeutic interventions in recent years.⁴⁵ Identification of driver oncogenic mutations in serine/threonine kinase BRAF, a critical functional component in the RAS-RAF-MEK-ERK-MAP kinase cascade, provided unique opportunities in the treatment of malignant melanoma. Vemurafenib and dabrafenib, two structurally unrelated inhibitors selectively targeting V600E, a missense mutation, that constitutes about 65 % of all malignant melanomas, resulted in improvement of disease free survival (DFS) and OS, leading to regulatory approval in 2011 and 2013.⁴⁶ However, this strategy can only address melanomas driven by the activating V600E mutation and suffers from resistance mechanisms driven by reactivation of the MAPK pathway, often paradoxically

induced by the inhibitors. Combined inhibition of BRAF and MEK can reduce disease progression risk by 25 % over BRAF inhibition alone and delay development of resistance, but it cannot overcome it altogether.⁴⁷

Immunotherapeutic strategies have been extensively investigated against melanoma in recent years. Tremendous excitement was generated as the “checkpoint inhibitors” demonstrated improvement in OS and DFS over conventional chemotherapy regimens. Ipilimumab, a monoclonal antibody targeting cytotoxic T-lymphocyte antigen 4 (CTLA-4), received FDA approval in 2011, followed by approval of Pembrolizumab and Nivolumab, antibodies against programmed cell death 1 (PD-1), in 2014.⁴⁸ However, new challenges rapidly emerged as a high proportion of patients demonstrated transitory or no responses against checkpoint inhibitors, while long-term survival and cure was further achieved in a small subset of patients. It is thus crucial to identify the right patient subset that may benefit from immunotherapy however no biomarker can currently predict clinical outcomes.⁴⁹

The CTLA-4 monoclonal antibody Ipilimumab and the BRAF kinase inhibitor vemurafenib changed the treatment landscape of metastatic melanoma. However, chemotherapy is still a relevant tool to clinicians because most patients do not respond to immunotherapy, and, further, not every patient carries the V600E mutation on BRAF. Even if a patient harbors the mutation and can be treated with the kinase inhibitor, drug resistance develops rapidly, and survival benefit is not significant over the long term.

1.5.1 Chemotherapy

As previously mentioned, Dacarbazine has been the standard of care for management of metastatic melanoma ever since its regulatory approval in 1976. The drug has a response rate of about 10–20 %; however, its OS benefit had never been validated in a randomized Phase III clinical trial. Temozolomide, an analog of dacarbazine, was not found to provide a significantly better response rate or OS when compared with dacarbazine in a European Phase III trial.⁵⁰ Apart from alkylating agents, other cytotoxic classes of drugs, like nitrosoureas, microtubule toxins, and taxanes, have been investigated for melanoma. These agents provided no significant OS benefit over dacarbazine. DNA-crosslinking agents like cisplatin also did not demonstrate a promising effect in melanoma. In one randomized Phase II trial, cisplatin was combined with WR-2721 (a chemoprotective agent for normal tissues against radiation therapy), alkylating agents, and platinum compounds. Cisplatin had a response rate of 16.3 % in single-arm treatment against a rate of 23.3 % in the combination arm. However, toxicity was not mitigated and rather was enhanced with the combination regimen, and no additional OS benefit was presented.

Immunological agents have been combined with chemotherapy, but the results have been less than satisfactory. IFN- α and IL-2 have been explored in combination with chemotherapeutic regimens in multiple clinical trials and Meta-analyses revealed that while the combination of immunological agents and cytotoxic drugs can significantly improve response rates, it provides no survival benefit. Furthermore, the toxicity in the combination regimens dampens the overall improvement in the response. Moreover, the combination of IFN- α with chemotherapy drugs was found to be associated with hematological toxicities.⁵¹

Angiogenesis has been established as one of the well-defined processes for tumor proliferation and survival.⁵² Vascular endothelial growth factor (VEGF) facilitates angiogenesis,

and chemotherapeutic resistance of metastatic melanoma is rendered, in part, by VEGF overproduction. Hence, combining chemotherapeutics with angiogenetic inhibitors, like monoclonal antibodies targeted against VEGF, is a clinically significant strategy. A combination regimen of paclitaxel, carboplatin, and bevacizumab, a monoclonal antibody targeting VEGF, in patients with Stage IV melanoma who have not qualified for surgery has been explored in a Phase II clinical trial.⁵³ The median progression-free survival (PFS) was about 6 months, while the median OS was about 12 months. A similar trial investigated the combination of temozolomide and bevacizumab against a combination regimen of nab-paclitaxel (Abraxane), carboplatin, and bevacizumab. Patients on the latter regime had a better PFS rate at 6 months (52.1 % vs. 32.8 %); however, that did not translate into higher OS (13.9 months vs. 12.3 months). There is at least one other trial that explored temozolomide and bevacizumab in chemotherapy-naïve patients and recorded a significantly higher OS in patients harboring the V600E BRAF mutation (12 months vs. 9.2 months). Researchers attempted to address chemotherapeutic resistance mediated by apoptotic resistance through a combination of chemotherapy with an antisense oligonucleotide against Bcl-2.⁵⁴ Oblimersen, a Bcl2 antisense oligonucleotide, was developed and investigated in combination with dacarbazine. No OS benefit was observed in the overall population, although the benefit was significant in patients with normal lactate dehydrogenase (LDH) levels. However, no significant benefit in a subpopulation of patients with low-normal LDH levels was determined in further studies.⁵⁵

1.5.2 Targeted therapy

The idea of targeted therapy against cancer is focused around the targets on which malignant cells must rely for progression, survival, and proliferation. Hyper-activated pathways

provide a therapeutic opportunity because progression of cancer cells can have a higher dependence on these pathways over normal cells. Kinases, phosphatases, and proteases are reasonable tools worthy of clinical investigation, because rationally designed drugs can bind selectively on active sites and potentially mediate a therapeutic effect.⁵⁶ However, NRAS and BRAF mutations are not simultaneously presented and implicated to drive pathogenesis in metastatic melanoma through the same pathway.

Ras farnesyl transferase inhibitors have been one of the earliest classes of drugs investigated in clinical trials; however, results have been generally disappointing.⁵⁷ Although tissue analyses showed potent target inhibition in advanced melanoma, no tumor response was demonstrated in a Phase II trial. Sorafenib, a broad-spectrum kinase inhibitor targeting both CRAF and BRAF, demonstrated a modest response of about 30 % when investigated in combination with carboplatin and paclitaxel; however, responses were disappointing as a monotherapy. The initial clinical success of vemurafenib and dabrafenib targeting BRAF (V600E), with 50 % response rates, was a breakthrough in the management of metastatic melanoma. However, initial excitement was rapidly replaced by disappointment as most patients suffered relapse, and molecular analyses revealed multiple pathways of acquired resistance, primarily by compensation from other pathways. Reactivation of MAPK and ERK has been demonstrated as a clinical marker of resistance development.⁵⁸ Trametinib, an MEK inhibitor, has been investigated in combination with BRAF inhibitors, and although PFS improves to 9–10 months, resistance development cannot be prevented in the long run. The mechanism underlying resistance is not clearly understood, although exome sequencing on a small number of patients revealed an activating mutation on MEK2. The potential of selective ERK inhibitors has been harnessed to address resistance against BRAF inhibition; however, this approach suffers from the

actuation of an ERK inhibition-mediated negative feed, leading to RAS and PI3K signaling.⁵⁹ Recently, the role of the TME in resistance-acquired, post-BRAF inhibition was suggested by Hirata et al. They demonstrated that BRAF inhibition triggers MAPK signaling in tumor-associated fibroblasts (TAFs), subsequently leading to kinase integrin/focal adhesion kinase (FAK) signaling and increasing tolerability of melanoma cells against BRAF inhibition. A BRAF and FAK inhibitor combination prevented ERK reactivation and improved tumor control, although a complete remission was not observed when investigated in preclinical models.⁶⁰

MEK and ERK reactivation, although common, is not the sole driver of resistance to a combination BRAF/MEK inhibitor, and receptor tyrosine kinase overexpression has been routinely observed to induce compensation by PI3K-AKT pathways.⁶¹ However, targeting the PI3K-AKT pathway is difficult because the mammalian target of rapamycin (mTOR) kinase inhibition induces reactivation of AKT signaling by feedback loops, and effective targeting becomes challenging.⁶²

About 15–20 % of melanomas harbor an NRAS mutation, and while there is an active interest in developing targeted therapies against BRAF mutation, successful therapies against NRAS mutant melanomas are an unmet medical need. NRAS mutant melanomas signal primarily through CRAF and not BRAF, and induction of MAPK signaling is triggered when treated with inhibitors targeting BRAF mutation.⁶³ The MAPK signaling cascade is still critical to NRAS mutant melanomas. Mono-therapy with MEK inhibitors like trametinib or selumetinib has been modest, and finding combinatorial additive therapies targeting downstream of NRAS is critical. Overall, targeted therapies have been clinically impactful for melanoma management, although they suffer from the drawback of resistance development after initial response or a lack of translation of target inhibition into disease control. The future of targeted therapies in

melanoma management rests on successful translation of the understanding of the biological mechanisms of resistance into clinically significant therapeutic combinations.

1.5.3 Immunotherapy

The clinical success of checkpoint inhibitors largely facilitates melanoma research, and there is considerable interest in understanding the immunology of melanoma and translating it to robust therapeutic strategies. The classic two-signal activation model was formulated out of basic research on understanding T-cell activation that involved the contribution of both antigens and secondary stimuli. The co-inhibitory receptors or the immune checkpoints like CTLA-4 and PD-1 promote downregulation by preventing T-cell activation.⁶⁴ Hence, negative regulatory mechanisms are a major hurdle in the T-cell response to tumors. The T cells may undergo functional inactivation and death in the TME, because PD-1 expressed on T cells engages with cancer cells (which would express programmed cell death-ligand 1, PD-L1).⁶⁵ Hypothesizing that the blockade could break tolerance and rescue the immune response, researchers developed monoclonal antibodies targeting the immune checkpoints.

A. Immune checkpoint inhibitors

Ipilimumab was the first successful checkpoint inhibitor in the clinics. It functions by binding to CTLA-4, thereby actuating down-regulation of the T-cell response. It received regulatory approval after demonstrating OS benefits in patients treated previously with chemotherapeutic regimens or IL-2. In one of the earliest trials, melanoma patients in Stage III or Stage IV who were not eligible for resection demonstrated a 10-month OS when treated with Ipilimumab in combination with gp100 peptide vaccine, against an OS of 6.4 months on vaccine

single-arm therapy. Interestingly, a recent meta-analysis revealed that about 20 % of patients with advanced melanoma may have long-term survival benefits, indicating the possibility of remission in a subset of patients. The next-generation antibodies targeting PD-1/PD-L1 entered clinical trials following Ipilimumab and pembrolizumab, a monoclonal antibody against PD-1, received accelerated approval in 2014. Pembrolizumab was compared against chemotherapy in patients non-responsive to Ipilimumab, and the 6-month response rate was approximately twice that of the chemotherapy arm. Nivolumab, another antibody targeting PD-1, was compared against the investigators' choice of chemotherapy and demonstrated an objective response in 31.7 % of the patients, as opposed to 10.6 % in its control arm. However, as with kinase inhibitors, the shortcomings of immune checkpoint inhibitors were quickly revealed because a large population of patients did not respond to therapy, while no bio-marker could be identified for patients who received long-term benefits.

With the success of mono-therapies, the exploration of CTLA-4 and PD-1 checkpoint inhibitors as a combination regimen was the next rational step. CTLA-4 and PD-1 are believed to have distinct regulatory roles, acting in different stages of T-cell activation. Targeting both checkpoints induced non-redundant changes in gene expressions and demonstrated a synergistic interaction.⁶⁶ The combination of Nivolumab and Ipilimumab has been demonstrated to provide a longer PFS benefit (11.5 months overall and 11.7 months in BRAF-mutant melanoma patients) in comparison to Nivolumab or Ipilimumab alone, which offered a PFS of 6.9 and 2.9 months, respectively. This was comparable to a dabrafenib and trametinib combination in melanoma patients with BRAF mutation (9.3–11.4 months). The trial further observed a similar PFS with Nivolumab or Nivolumab combined with Ipilimumab in patients positive for PD-L1. It will be worthwhile to look at long-term survival and investigate if PD-L1 expression can be exploited as

a clinical bio-marker to predict whether a patient is suitable for mono-therapy or combination therapy. Currently, other co-inhibitory receptors like Lymphocyte-activation gene 3 (LAG-3), mucin-domain containing-3 (TIM3), and T-cell immunoreceptor with Ig and ITIM domains (TIGIT) are being explored in clinical trials.⁶⁷

B. Therapeutic vaccines

A strong association between tumor-infiltrating cytotoxic T lymphocytes (CTL) and patient survival drove interest in the development of vaccine strategies to treat cancer. However, initial clinical trials did not offer any survival benefit, and in hindsight, this was primarily due to a lack of rational strategies.⁶⁸ Most therapeutic vaccines were aimed at induction of response against tumor-associated antigens (TAAs). Effective anti-tumor response, however, requires presentation of TAAs to T cells after distinct activation and maturation signals are received by antigen-presenting cells. Further, the activated T cells have to expand, travel to tumor sites, and infiltrate the immunosuppressive TME to be able to recognize and kill tumor cells. Some of the initial trials investigated free peptide antigens with poor pharmacokinetic profiles, administered without a delivery system or an immuno-stimulatory adjuvant, which contributed to failure and generated cynicism about the future of vaccines as an effective therapeutic strategy. As additional knowledge has been acquired about the immunology of cancer, the current focus has shifted to combining vaccines with other immunomodulatory agents. A melanoma peptide antigen vaccine (gp100) was investigated in combination with IL-2 and demonstrated a response rate of 16 % over 6 % and a median PFS of 17.8 months over 11.1 months. Metastatic melanoma patients were treated with DCs stimulated with an assortment of melanoma antigens, and the survival benefit in the immunized group was 13.6 months, over 7.3 months in the control group. However, as with most immunotherapies, only a subset of patients who were immunized

responded to the therapy, as demonstrated by a positive CTL response, extending to a longer survival benefit (21.9 months vs. 8.1 months). Recently, a tumor vaccine that secretes GM-CSF was in Phase III clinical trial. With the help of Ipilimumab, these patients bearing Stage III or Stage IV melanoma showed longer overall survival (17.5 months vs. 12.7 months).

Unfortunately, PFS was not clearly extended.

C. Emerging directions in immunotherapy

A few other active immunotherapy approaches involving T cells are currently generating interest in academic labs and clinics. Adoptive T-cell therapy is one of the most personalized and effective treatment methods available for management of metastatic melanoma, involving proliferation of tumor-infiltrating lymphocytes (TILs) *ex vivo* and transferring the TILs back to the patient augmented with other immuno-modulators like vaccines.⁶⁹ When combined with lympho-depletion, objective response rates can be dramatic and reach 49–72 % in metastatic melanoma patients, further providing durable survival benefits over the long term. However, one of the major hurdles that limit this otherwise effective treatment is the economic cost and skilled labor associated with this complex, personalized therapy. Chimeric antigen receptors (CARs), a class of engineered fusion proteins combining an antibody-derived antigen recognition domain and a signaling domain, can bypass immune escape exploited by malignant cells by their MHC-independent recognition of TAAs.⁷⁰ However, major clinical success of this modality is restricted to hematological cancers like multiple myeloma, and its impact on solid tumors is yet to be clinically validated.⁷¹ Currently, oncolytic virus is also FDA approved for melanoma treatment. An oncolytic virus is a virus that preferentially infects and kills cancer cells. As the infected cancer cells are destroyed by onco-lysis, they release new infectious virus particles or

virions to help destroy the remaining tumor while not harming normal tissue, as well as initiating innate and adaptive anti-tumor immunity.⁷²

BRAF inhibition and combination BRAF/MEK inhibition had been reported to be associated with higher CD8⁺ T-cell infiltration and PD-L1 expression.⁷³ Hence, a combination of MAPK signaling inhibitors with immune checkpoint inhibitors could be considered a critical therapeutic strategy. Treatment with BRAF inhibitors induces an increase in antigen expression and decrease of immunosuppressive factors.⁷⁴ The hypothesis is that the antigen-presenting cells could pick up antigen released from dying melanoma cells and cross-present them to T cells, therefore combination therapy with checkpoint inhibitors can potentially augment T-cell response. However, there are numerous limitations to this approach. For example, autoimmune toxicity is a primary concern. In fact, one of the early trials combining vemurafenib and Ipilimumab had to be terminated due to liver toxicity.⁷⁵ Efforts need to be focused to understand the immunological modulations followed by treatment with combinations of targeted therapies and immunotherapies and translate the knowledge into tailoring the appropriate dosage and schedule of therapeutics in subsequent clinical trials.

1.6 Demand of efficient delivery systems: Scope of nanomedicine

Nanomedicine involves the development and design of materials at the nanoscale and has been extensively investigated in the past few decades for development of efficient delivery systems for diagnostics and therapeutics in a multitude of diseases. Resistance to chemotherapeutics in melanoma has been attributed to high intra-tumoral pressure induced by stromal cells, poor perfusion, drug efflux, and intracellular entrapment, leading to inefficient

drug delivery. It is theoretically possible to design NP formulations capable of altering bio-distribution of therapeutic cargo and mediating better payload accumulation in a target of interest by active targeting.⁷⁶

There are many arenas in which NPs can potentially serve as robust delivery platforms. With increasing demand for combinatorial drug regimens, it is possible to harness the potential of NPs to precisely tailor the ratio of individual drugs and further mediate sequential release. Guo et al. demonstrated sensitization of melanoma cells to cisplatin therapy by co-delivery with rapamycin, an mTOR inhibitor that mediated microenvironment modulation and synergistically affected the efficacy of cisplatin.⁷⁷ Peptide antigens, when delivered systemically, suffer from suboptimal cytosolic delivery to DCs, and high-dose administration may induce significant toxicity. Xu et al. managed to co-encapsulate Trp2, a melanoma antigen with immune-stimulant CpG, on a lipid-calcium phosphate NP platform and induced a potent CTL response and superior tumor inhibition in a murine melanoma model. RNA interference is another key therapeutic application where NPs can serve as a potent delivery platform. Beloor et al. explored the potential of a polymer-based siRNA delivery platform to efficiently co-deliver a cocktail of siRNAs like Bcl-2, VEGF, and c-myc in a mouse xenograft tumor model and demonstrated robust tumor control. The Trp2 vaccine discussed earlier was less effective in a late-stage melanoma model.⁷⁸ In a follow-up study, a liposome-protamine-hyaluronic acid-based NP platform was exploited to deliver siRNA against transforming growth factor- β (TGF- β), because immunosuppressive cytokines like TGF- β were found to be elevated in a TME. Thus, the combination of an antigen-specific CTL response was harnessed to a rational modulation of an immune microenvironment using an NP-based delivery system.

Despite intensive pre-clinical development, success in the clinical setting has been disappointing so far due to rapid reticuloendothelial system (RES) clearance, difficulty related to scalability, and toxicity issues. The grand diversion between animal models and human diseases has further affected successful translations.⁷⁹ A considerable number of “multi-functional” NPs are currently under investigation in pre-clinical models and early clinical trials, although there is a long way to go before translation into a clinical modality.

1.7 Organization of this dissertation

In desmoplastic melanoma (DM), a rare histological variant of melanoma, the malignant tumor cells are surrounded by rich fibrous tissues, thus compromising the efficacy of therapeutic options. The interstitial cells, especially TAFs construct an extracellular matrix-rich structure and cytokine crosstalk, thus facilitating aggressive and highly metastatic tumor growth. Moreover, the fibrosis raises delivery barriers for effective therapies.

In the dissertation work, we grafted murine model of DM mimicking clinical settings. The BPD6 melanoma cell (BRAF^{V600E}, PTEN^{-/-}, syngeneic with C57BL/6) -inoculated mice sequentially bearing aggressively-grown and highly desmoplastic tumors. The oncogenic mutations in the BRAF gene (BRAF^{V600E} mutation is the major common one), which encodes a serine/threonine-protein kinase B-Raf, accounts for ~50 % of patient cases. When comparing to BRAF-wildtype, the DM tumors are often resistant to conventional chemotherapies. Hence, new treatments deemed necessary.

Recent advances in immunology and cancer biology, including a better understanding of signaling pathways in cancer progression, have promoted cancer immunotherapy as a new way

of halting growth and metastasis. Furthermore, developments in nanotechnology provide us with new approaches for targeted delivery of therapeutics to malignancy and improved efficacy. Thus, this dissertation is built upon DM as a disease model, to further investigate nano-approaches in immunotherapy.

Immunotherapy harnesses the patient's immune system to combat cancer. The typical strategy is to generate a large number of antigen-specific CTLs to battle against tumor cells by vaccination. Herein, we explored a new potent tumor-specific nano-vaccine in its preventive and therapeutic efficacy (**Chapter 2**). Furthermore, we explored targeted nano-delivery of TME-changing motifs, including FDA-approved anti-cancer chemo-drug Sunitinib (SUN) (**Chapter 3**) and active compounds Fraxinellone (Frax) (**Chapter 4**), in synergy with efficient vaccines. As a major component of suppressive TME, the TAFs are one of the major stroma cells that regulate tumor cell proliferation and metastasis and secrete extracellular macromolecules to stiffen the extracellular matrix (ECM). As two major dominators within the DM TME, tumor cells and TAFs further secrete key molecular controlling fibrosis and inducing DC tolerance, thus dampen effective antigen-presentation and the recruitment of effective CTLs. Therefore, mechanism study emphasis on interaction between TAFs and cells within TME are further investigated. Herein, gene-therapy "trapping" key molecule Wnt5a within TME (**Chapter 5**) and a design of combining chemo- with immune-therapy (**Chapter 6**) aiming at triggering effective immunogenetic tumor death and sustained immune surveillance are further developed.

1.8 Key novelties of research

- A. Deep understanding of TME and immune modulators in DM.
- B. Clinical translational designs of vaccination and TME-related therapeutic regimens.
- C. Nano-strategies applied in achieving high drug-loading efficiency, targeted local delivery and release of therapeutics, as well as low systemic toxicities of hosts for promising anti-tumor efficacy.
- D. Effective immune-surveillance in DM-bearing host and significant elongation of survival.

1.9 Contributions to the dissertation research

Dr. Leaf Huang mentored in the designs of all projects, the drafting and revision of all papers. All collaborators Dr. Hongda Zhu (chapter 3), Dr. Lin Hou (Chapter 4), Dr. Rihe Liu (Chapter 5), Fengqian Chen (chapter 6) participated in performing the experiments, analyzing the data, and drafting the manuscripts. All authors have discussed the results and commented on the published journals and submitted manuscripts.

1.10 Publications for different parts of this dissertation

Chapter 1: The majority of this chapter has been published in *Advanced Drug Delivery Reviews*. (Q Liu, M Das, Y Liu, L Huang. Targeted drug delivery to melanoma. *Advanced drug delivery reviews*. 2017 Sep 19.)

Chapter 2: The content has been published in *Cancer Immunology, Immunotherapy*. (Q Liu, H Zhu, Y Liu, S Musetti, L Huang. BRAF peptide vaccine facilitates therapy of murine BRAF-mutant melanoma. *Cancer Immunology, Immunotherapy* 2018 Feb;67(2):299-310)

Chapter 3: In preparation for publication in *Theranostics*.

Chapter 4: Accepted for publication in *Theranostics*, 2018. (L Hou*, Q Liu*, L Shen, Y Liu, X Zhang, F Chen, L Huang. Nano-delivery of fraxinellone remodels tumor microenvironment and facilitates therapeutic vaccination in desmoplastic melanoma)

Chapter 5: Published in *ACS Nano*. (Q Liu, H Zhu, K Tiruthani, L Shen, F Chen, K Gao, X Zhang, L Hou, D Wang, R Liu, L Huang. Nanoparticle-Mediated Trapping of Wnt Family Member 5A in Tumor Microenvironments Enhances Immunotherapy for B-Raf Proto-Oncogene-Mutant Melanoma. *ACS nano* 2018 Jan 31)

Chapter 6: Under review by *ACS Nano*, 2018.

CHAPTER 2

NANO-VACCINATION²

2.1 Introduction

Cancer immunotherapy primarily depends on tumor-associated antigens, which are overexpressed during malignant tumor cell development. The immune system is manipulated to recognize tumor-associated antigens and raise a specific immune response against the cancer cells. The typical strategy is to generate many antigen-specific T cells to battle the tumor by using cancer vaccines.⁸⁰ Notably, 50 % of human melanomas are driven by BRAF mutations, among which BRAF^{V600E} mutation is a majorly common one, characterized by aggressive growth and a highly immunosuppressive TME.⁸¹ These tumors are often resistant to immune vaccination therapy. Therefore, inducing a BRAF-mutation-specific and potent T-cell response to endogenous antigens remains challenging. The murine BRAF^{V600E} mutant peptide (mBRAF 594-602: FGLANEKSI) for the C57Bl/6 haplotype (H2D^b) was designed by modifying amino acids at the 5 and 9 positions to increase binding affinity using the Rammensee epitope prediction model.⁸² A previous report on type 1-polarized DCs pulsed with affinity-modified BRAF^{V600E} peptide showed antigen-specific CD8⁺ T-cell responses,⁸³ supporting mutated BRAF

² This chapter previously appeared as an article in *Cancer Immunology, Immunotherapy*. The original is as follows: Q Liu, H Zhu, Y Liu, S Musetti, L Huang. "BRAF peptide vaccine facilitates therapy of murine BRAF-mutant melanoma." *Cancer Immunology, Immunotherapy* 2018 Feb;67(2):299-310

as a potential immune system target. However, cell-based vaccination is both costly and less reproducible compared with an injectable chemical dosage of nano-formulation for targeted delivery of nano-formulation for targeted delivery to the draining LNs. In this study, we aimed to use a BRAF-mutant melanoma in a syngeneic mouse model to study tumor growth inhibition using a tumor-specific BRAF peptide vaccine delivered by DC-targeting NPs.

Our lab has established a nano-formulation called lipid-calcium-phosphate (LCP) NPs for delivering nucleic acids, peptides, and chemotherapeutic drugs.^{6, 84} The NP core, supported by lipid bilayers, may offer efficient encapsulation and delivery of acid and peptides. Injected NPs must overcome both kinetic and physical barriers after administration. This is especially true for peptides and nucleic acids. After the NP formulation is administered, it must protect the cargo molecules from enzymatic degradation by endogenous nucleases. It should also avoid aggregation, which can be accomplished by PEGylation. The BRAF peptide, along with CpG oligodeoxynucleotides (ODN) adjuvant, was formulated in LCP NPs with mannose modification and delivered to the DCs in the LNs. This approach was very effective in inducing an antigen-specific CTL response in the host and significantly inhibited primary BRAF-mutant melanoma growth. Variations in the extent to infiltrated suppressive leukocytes and T cells within the TME were also monitored after vaccination. The simple but sophisticated LCP NP design is an effective vaccine platform with great translational potential. The BRAF peptide vaccine, which has both MHC-I and HLA-restricted properties acts as a potent immunotherapy for BRAF-mutant melanoma.

2.2 Results and discussion

2.2.1 Affinity-modified BRAF peptide was readily packaged in LCP NPs

To achieve more efficient vaccination, we co-delivered NPs encapsulating both the tumor-specific antigen and an adjuvant to antigen-presenting cells (APCs). CpG ODN, a potent adjuvant, could be efficiently encapsulated in LCP NPs; this system was extensively characterized and optimized in our lab.⁸⁵ On the N-terminal of the BRAF peptide, phosphorylated serine residues were designed to facilitate CpG ODN encapsulation. CpG ODN was co-loaded in LCP NPs using a reverse oil-in-water micro-emulsion, amorphous calcium phosphate (CaP) precipitates were formed and then stabilized with DOPA. These particles cores were then coated with DOTAP/cholesterol and stabilized with DSPE-PEG and DSPE-PEG-mannose. The zeta potential, as determined by a Zetasizer, was approximately 15 mV, which was indicative of full PEGylation of the LCP NPs. Transmission electron microscope (TEM) images were taken to investigate the NP morphology and to confirm the size of the LCP NPs (**Figure 2 a-d**). The LCP NPs loaded with the modified BRAF^{V600E} peptide and CpG were spherical with a diameter of approximately 30 nm after uranium acetate staining. The encapsulation efficiency was about 60 % after optimization. Mannose modification achieved enhanced and prolonged accumulation of the NPs in the LNs, whereas the targeted delivery of NPs to draining LNs facilitated local DC activation (CD11c⁺CD86⁺), as well as local T-cell activation (CD8⁺CD69⁺), thus boosting immune efficiency (**Figure 2 e-f**).

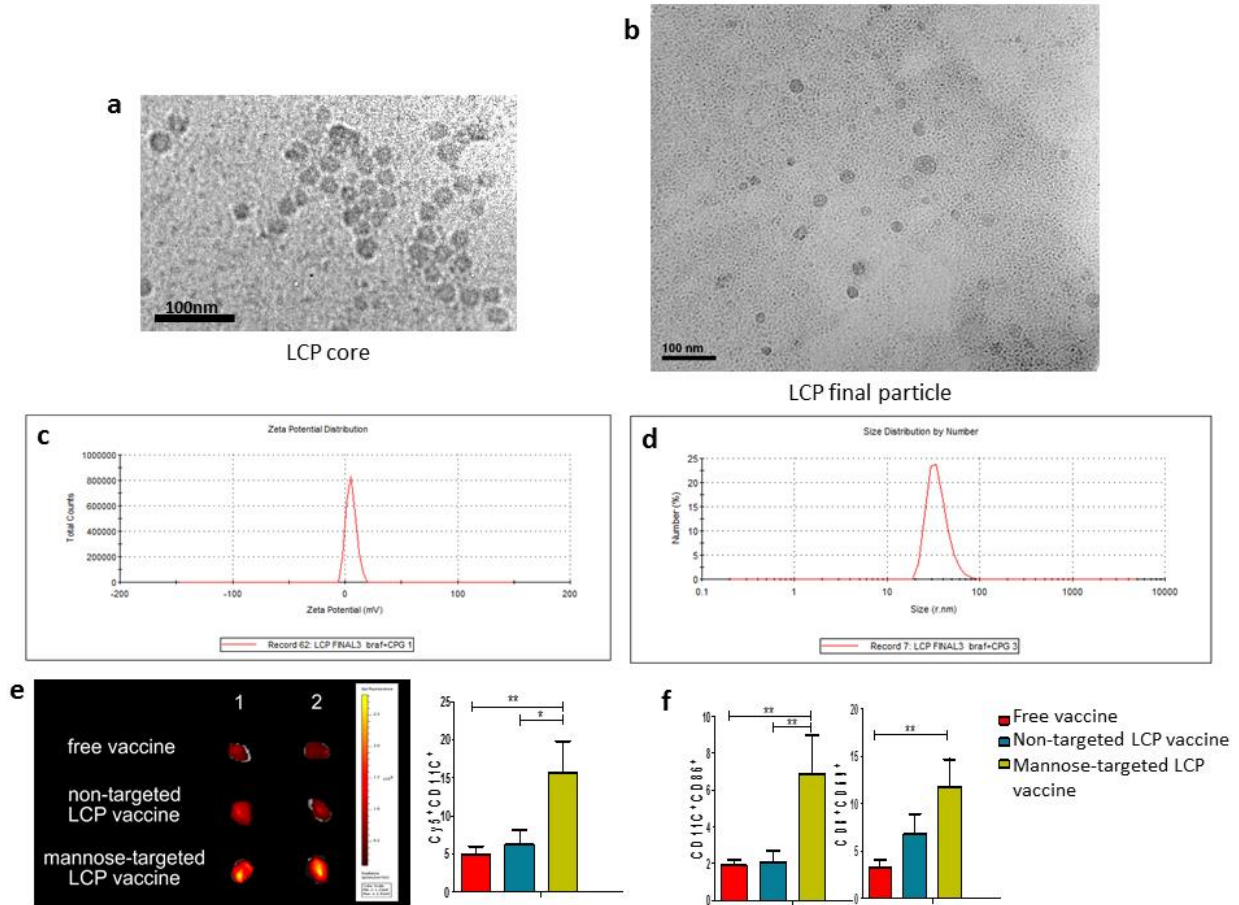


Figure 2. Characterization of the LCP NP-based BRAF peptide vaccine. LCP encapsulating the modified melanoma-specific antigen (BRAF^{V600E}) and adjuvant (CpG ODN) illustrated efficient antigen loading and DC activation. Panels (a) and (b) show TEM images of NP cores and final structure. Size distribution (c) and Zeta potential (d) show NP characteristics. Cy5-labeled NPs show enhanced accumulation in draining LNs and uptake in proximal DCs (e) after mannose-modified LCP encapsulation, which facilitated local DC activation and T-cell activation (f). n = 5, *: p < 0.05, **: p < 0.01.

2.2.2 BRAF peptide vaccine induced an antigen-specific immune response

We proceeded to evaluate therapeutic efficacy of vaccination in the murine BRAF-mutant melanoma syngeneic tumor model. CTLs can kill tumor cells, while interferon gamma (IFN- γ)-producing T cells secrete cytokines to modulate the TME. Therefore, an assay for antigen-specific CTL response measured the efficacy of vaccine formulation, moreover, measuring IFN- γ -producing T cells would predict systemic T-cell function upon antigen presentation.^{78, 86} LCP

NPs loaded with the modified tumor-specific BRAF-mutant peptide were subcutaneously inoculated in the flank of the mice. CTL and ELISPOT assays were performed 1 week later to examine the antigen-specific T-cell response.

As shown in **Figure 3a**, immunization with LCP-NPs encapsulating the modified BRAF-mutant peptide or CpG ODN alone boosted a modest (approximately 48 %) efficacy, whereas vaccination with empty particles or NP encapsulating BRAF^{WT} peptide (the wildtype (WT) group) showed no noticeable BRAF-mutant specific CTL results. Only the combined group with tumor specific peptide and adjuvant proved effective (approximately 80 % efficacy), indicating robust BRAF^{V600E}-specific responses.

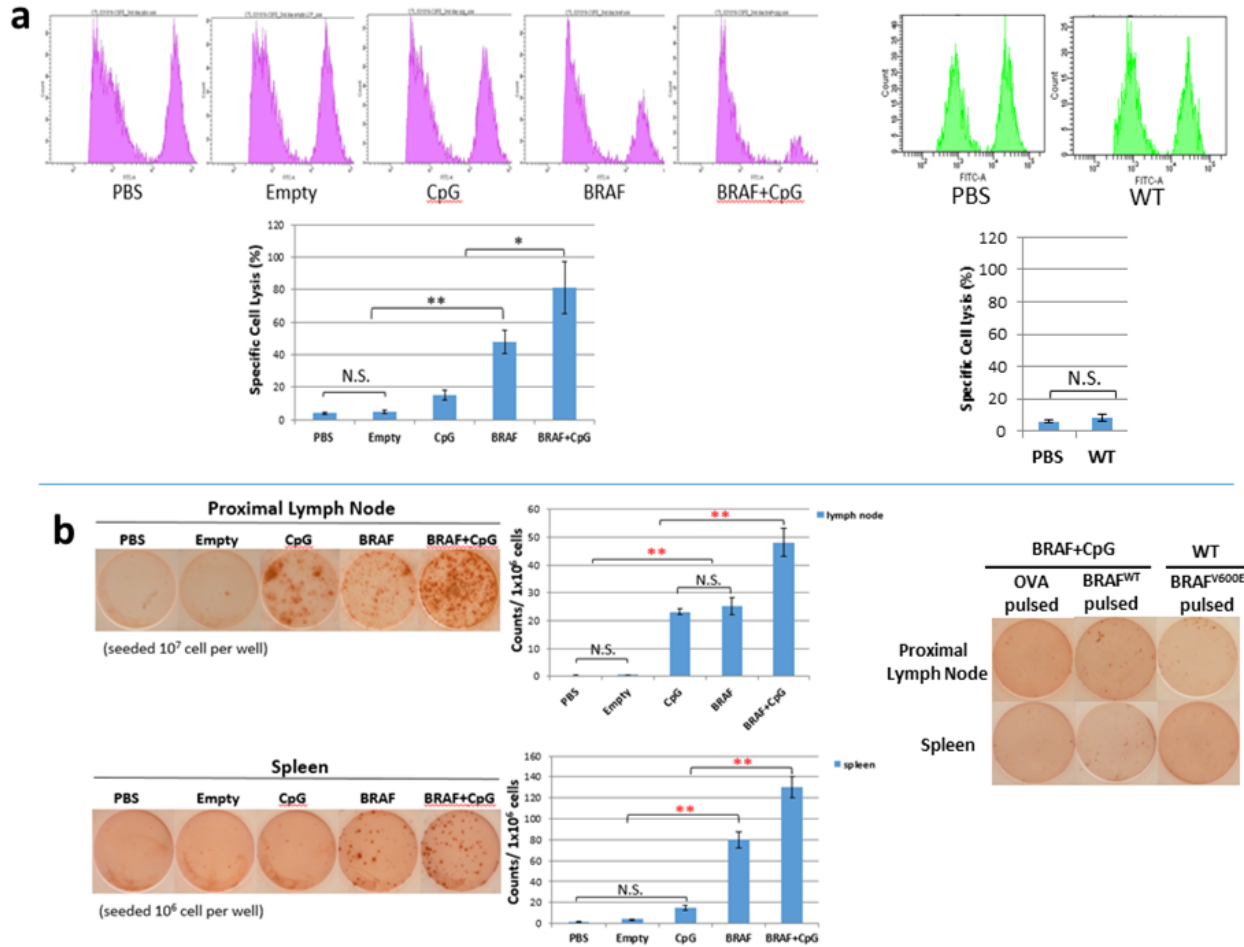


Figure 3. Antigen-specific immune response induced by the BRAF peptide vaccine. (a) *In vivo* CTL response after vaccination, $n = 5$. (b) IFN- γ production after vaccination was measured with ELISPOT assay system. One representative experiment from each group is shown. $n = 5$, N.S.: no significance, *: $p < 0.05$, **: $p < 0.01$.

Moreover, consistent with the CTL assay, we found no significant IFN- γ production of BRAF^{V600E}-pulsed cells in the spleens or LNs of naïve mice or empty NP-vaccinated mice, indicating none-detectable BRAF^{V600E}-specific CTL responses (**Figure 3b**). IFN- γ release is largely boosted only by tumor-specific peptide + adjuvant vaccination. OVA-pulsed or BRAF^{WT}-pulsed cells for any group in the spleen or LN also showed no significant IFN- γ production.

2.2.3 Enhanced T-cell infiltration into TME results in a superior antitumor vaccination effect

The therapeutic efficacy induced by the BRAF peptide vaccine was evaluated in a BRAF-mutant melanoma model. As **Figure 4** shows, this vaccine showed potent tumor growth inhibition compared with other groups. Empty LCP NPs and LCP NPs encapsulating CpG showed no significant therapeutic effect, whereas LCP NPs encapsulating the BRAF peptide showed modest efficacy, indicating the essential immune function of antigen presenting. Furthermore, the most effective anti-tumor action can only be achieved when using an adjuvant. Only the combined full vaccination significantly inhibited tumor growth ($p < 0.01$). Preventive vaccination further reduced melanoma risk. Giving two vaccination dosages (on day -14 and day -7 boosted), the rate of tumor progression was significantly decreased; the therapeutic group/control group (T/C) ratio was 22.3 %. Moreover, two out of ten mice achieved tumor-free survival, compared with the PBS control group, suggesting a potential preventive therapy for translational application.

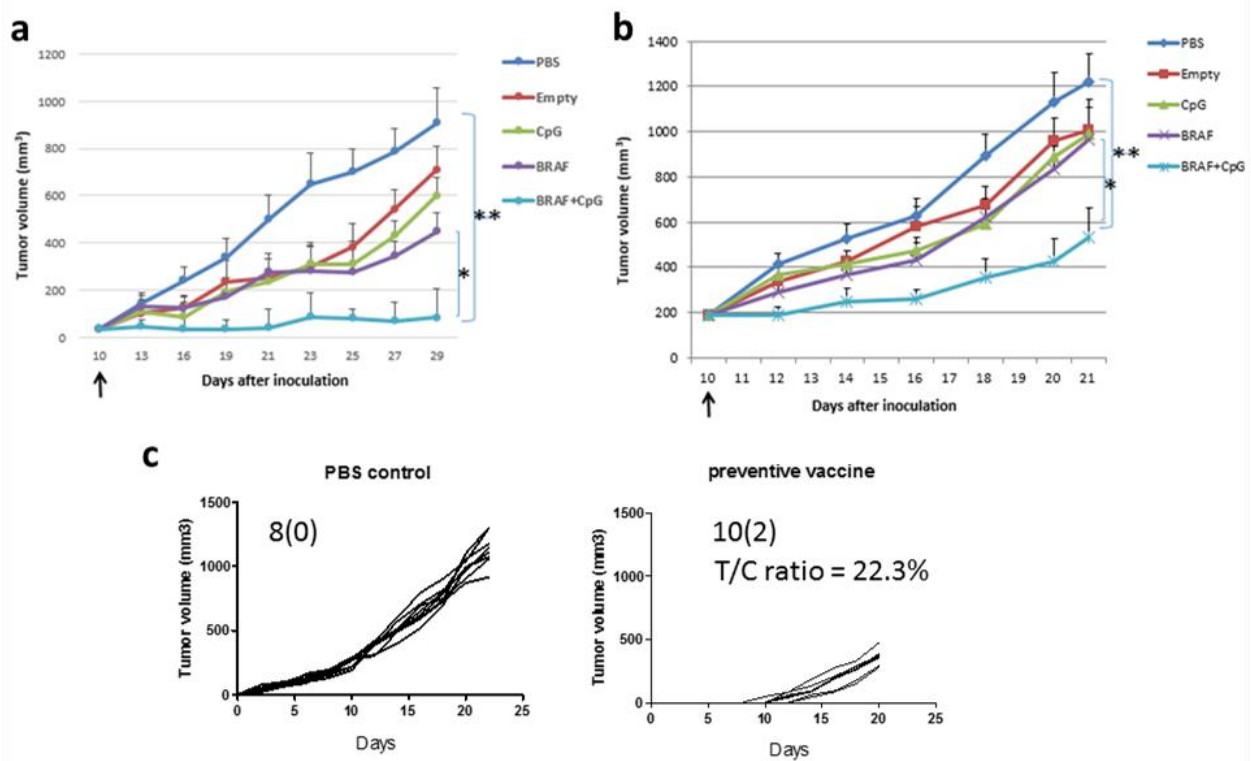


Figure 4. Antitumor activity of the BRAF peptide vaccine in murine BRAF-mutant model. Mice were subcutaneously inoculated with either 2×10^5 (a) or 1×10^6 (b) BPD6 cells on day 0. Vaccination with 5 % glucose (The PBS group), empty LCP (The Empty group), LCP-CpG (The CpG group), LCP-BRAF peptide (The BRAF group), or LCP-(BRAF+CpG) (The BRAF+CpG group) were given on day 10. Tumor growth was measured every 2–3 days. Five mice from each group were sacrificed on day 29, and tumors, whole blood, and organs were harvested for further study. $n = 5$, *: $p < 0.05$, **: $p < 0.01$. Preventive vaccination ($n = 10$) significantly reduced tumor growth compared with PBS control ($n = 8$), with T/C ratio of 22.3 %. Two animals in the vaccinated group did not grow tumors (c).

The vaccine's enhanced antitumor effect was accompanied by an increase in CD8⁺ T-cell population in the tumors, as determined by both flow cytometry analysis and immunofluorescence staining (**Figure 5**). Tumor tissue slices from mice treated with the BRAF peptide vaccine showed extensive T-cell infiltration into the tumor region (**Figure 5a**). The tumors were further collected and dispersed into single cells. CD8⁺ T-cell (CD8⁺CD45⁺) and T-cell activation (CD8⁺CD62L⁻) were analyzed with flow cytometry. The results confirm that the CD8⁺ T-cells significantly increased in number upon activation (**Figure 5b**). These data suggest the possibility that tumor-antigen-presenting APSs would significantly enhance CD8⁺ T-cell

activation and proliferation. The antigen-specific CD8⁺ T-cell killing induced potent cell death within the TME, as indicated by terminal deoxynucleotidyltransferase-mediated nick end labeling (TUNEL) assay (**Figure 5c**).

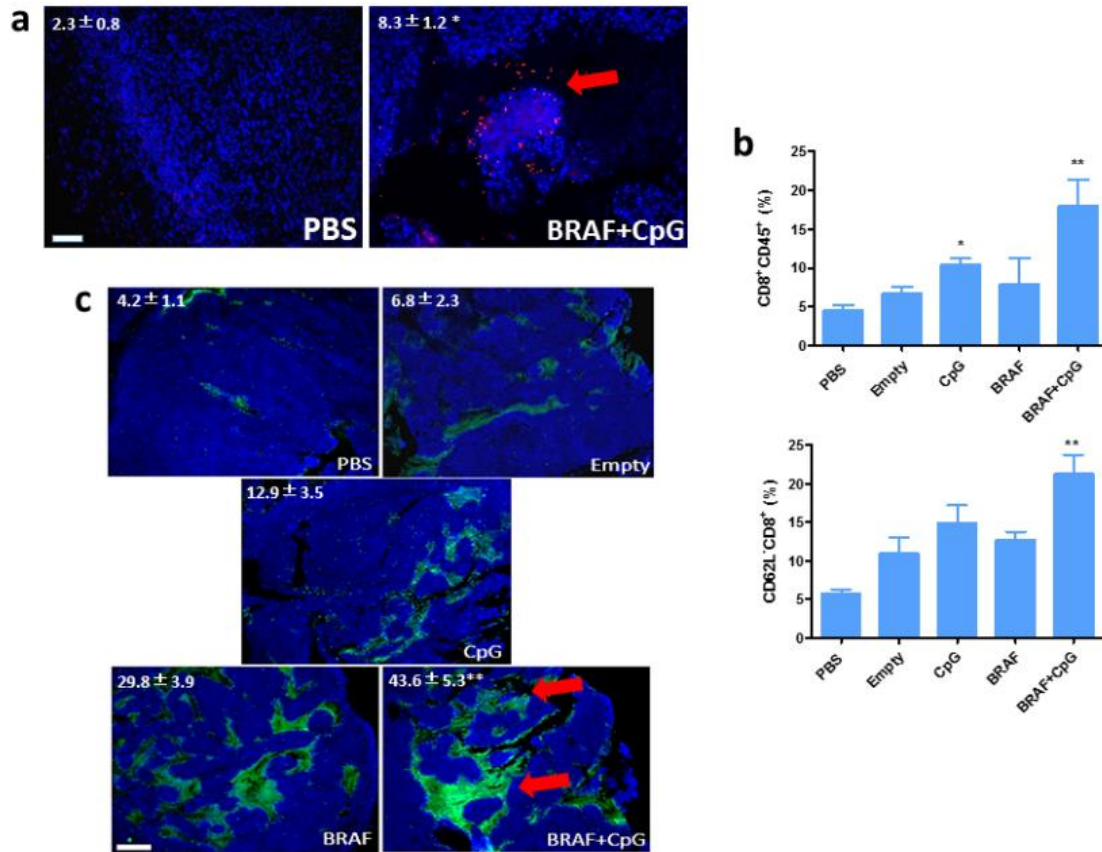


Figure 5. Enhanced T-cell infiltration into TME-induced potent CTL killing. (a) Tissue sections from murine BRAF-mutant model with different treatments were stained for CD8⁺ (red) and DAPI (blue), then analyzed by immunofluorescence microscopy. Scale bars indicate 200 μ m. Arrow indicated infiltrating CTLs. (b) The percentage of CD8⁺ T-cell (CD8⁺CD45⁺) and its activation (CD8⁺CD62L⁺) within tumor regions were quantified by flow cytometry. (c) TUNEL assay indicating apoptotic cell death. Scale bars indicate 300 μ m. Arrows indicate apoptotic regions. Numbers in the panel indicate average values of three samples per group, quantified by Image J. *: $p < 0.05$, **: $p < 0.01$.

2.2.4 Changes of tumor-infiltrating immune cells and collagen within the TME

To further elucidate the effect of BRAF peptide vaccination in improving T-cell infiltration, the changes of the related immunosuppressive subsets such as regulatory T cells (Tregs) and myeloid-derived suppressor cells (MDSCs) were evaluated, which contribute to a complicated interplay network with CD8⁺ T-cell antitumor activity within the collagen-rich BRAF-mutant murine model.⁸⁷ The accumulation of these immunosuppressive cells was measured by flow cytometry. As shown in **Figure 6a-b**, the percentages of Tregs and MDSCs in the BRAF peptide vaccine group were much lower than in other groups. Macrophages are another important component of the suppressive tumor immune microenvironment. As shown in **Figure 6c**, vaccination could efficiently stimulate macrophages to an advantageous tumor-suppressive M1 macrophage (M1) state. Vaccination significantly increased cytokine production of IFN- γ and Interleukin-4 (IL-4) and decreased anti-inflammatory C-C motif chemokine 2 (CCL2) and Interleukin-6 (IL6) production (**Figure 6e**). The BRAF control group alone is insufficient to build up Type 1 T helper (Th1) type immunity. Interestingly, it correlated with increased Tregs and MDSCs. Tumor profiling of cytotoxic T-cell (CD8⁺CD45⁺), T-cell activation (CD8⁺CD62L⁻), MDSCs (CD11b⁺Gr1⁺), Tregs (CD4⁺Foxp3⁺), and the M1 (F4/80⁺Ly6C⁺) to M2 macrophage (M2) (F4/80⁺CD206⁺) ratio indicated a strong correlation between high levels of MDSCs and Tregs present in TME with loss of T-cell function (activation). Furthermore, a significant decrease in collagen after vaccination indicated a change of the TME morphology that favored further CTL infiltration (**Figure 6f**). Although we found no significant increase in infiltrating CD4⁺ T cells after vaccination (**Figure 6d**), there was an overall significant remodeling of the suppressive TME in favor of immunotherapy.

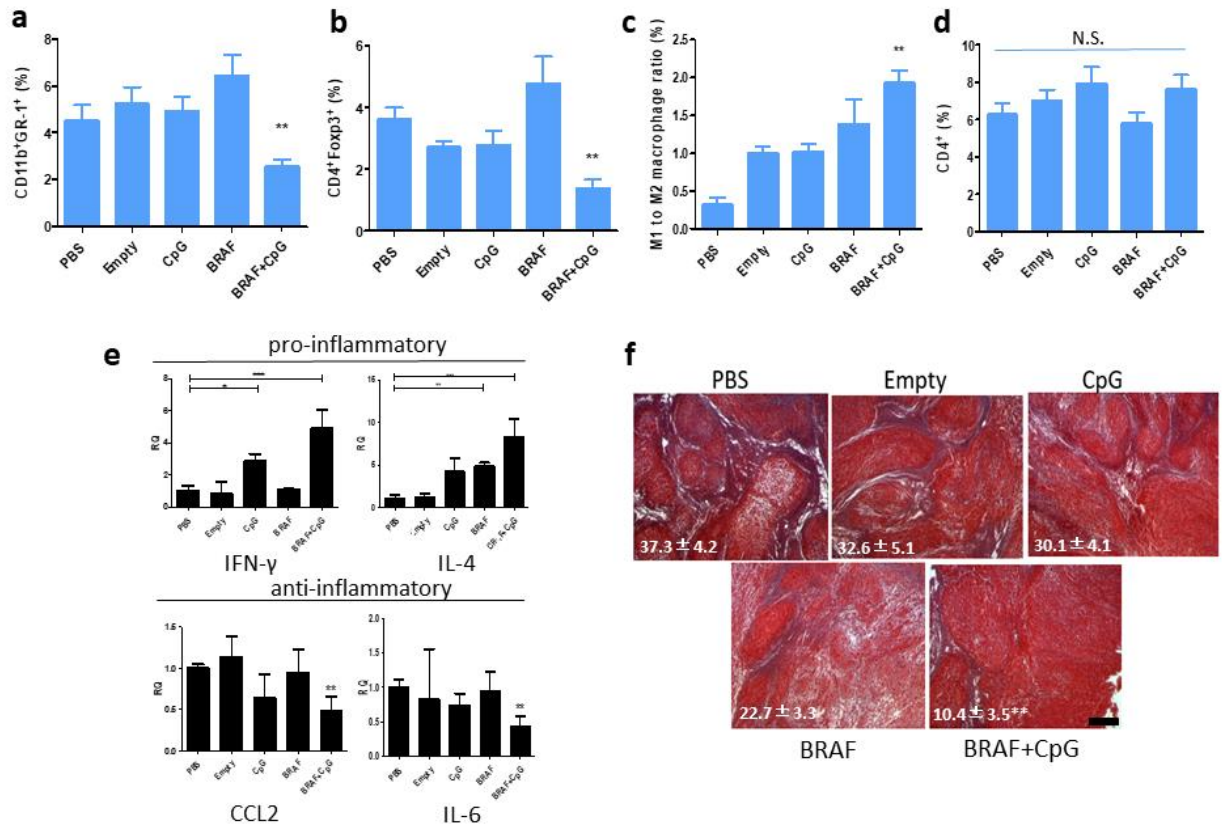


Figure 6. Change of TME. The percentage of MDSCs (a), Treg cells (b), M1-to-M2 ratio (c) and CD4⁺ T cells (d) within tumor regions were quantified by flow cytometry. Rt-PCR elucidated inflammatory cytokine profile within TME (e). Masson's trichrome staining (f) indicating change in collagen after different treatments. Numbers in the panel indicate average values of three samples per group, quantified by Image J. n = 5. *: p < 0.05, **: p < 0.01. Scale bars indicate 300 μ m.

2.2.5 Toxicity evaluation

There was no significant loss in mice body weights, which might indicate none detectable treatment toxicity. No significantly noticeable morphological changes occurred in major organs (**Figure 7**). Additionally, serum biochemical value analysis demonstrated normal liver (aspartate aminotransferase (AST), alanine aminotransferase (ALT)) and kidney (creatinine, blood urea nitrogen (BUN)) function. Whole blood cell counts remained constant within normal ranges for all the groups, suggesting that no systemic anemia or inflammation occurred after treatments.

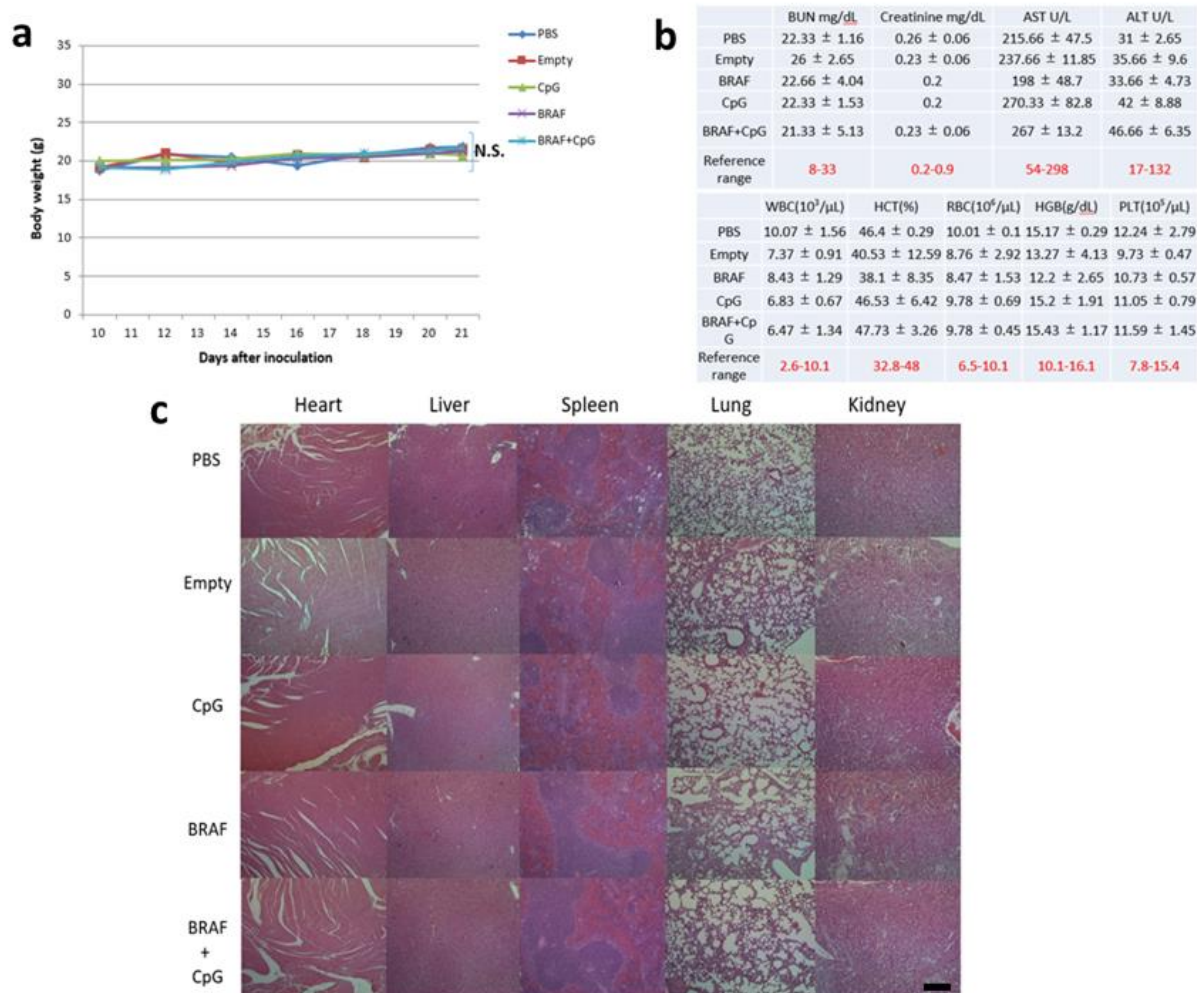


Figure 7. Safety profile of the BRAF peptide vaccination. (a) Body weights of mice in each group. (b) Whole blood and serum toxicity evaluation. (c) H&E morphology evaluation. The BPD6-bearing mice were divided into five groups with different treatments. Body weights were evaluated every 2-3 days. Mice were euthanized at the endpoint with blood and major organs collected for blood serum, and H&E tests. Scale bars indicate 300 μ m. n = 5. N.S.: $p > 0.05$.

2.3 Conclusion

Management of advanced melanoma is still a major challenge, and the development of a better understanding of melanoma biology is essential to design new therapeutic strategies and address present challenges associated with existing therapies. In the present work, vaccination using NP-delivery effectively treated aggressive growth of BRAF-mutant melanoma. In summary of current strategy: on one side, by predicting peptide-MHC class I binding using

artificial neural networks (the NetMHC 4.0 developed by Technical University of Denmark),^{88, 89} we identified the murine BRAF^{V600E} peptide FGLANEKSI as a strong binder with binding affinity of 104.92 nM and 0.07% rank (strong binders are defined as having %rank<0.5, and weak binders with %rank<2). On the other side, *In vivo* studies demonstrated that a single vaccination can induce a strong antigen-specific CTL response and potent tumor growth inhibition for approximately 2 weeks. Again, our LCP NPs provided enhanced vaccination efficacy. LCP, as a Ca²⁺ reservoir, could effectively modify the intracellular calcium dynamics that drive DC maturation for antigen presentation in a timely manner.⁹⁰ This advantage allowed the DCs to orchestrate cytokine production and antigen presentation to induce a potent immune response.

CD8⁺ T-cell-mediated immunity was one crucial mechanism for enhanced antitumor immunity.⁹¹ BRAF peptide vaccination induced a local enhancement of tumor-specific T-cell infiltration, thus facilitating immune response activation, resulting in a long-term sustained effect. After vaccination, cytotoxic T cells increasingly infiltrated TME derived inflammatory cytokines such as IFN- γ and IL-4 and therefore amplified macrophage polarization. The inflammatory TME facilitated further Ly6C⁺ monocyte differentiation into M1-like functional phenotypes (F4/80⁺Ly6C⁺). These M1 state macrophages were recruited predominantly to the site of cancer. These key effector cells in the TME boosted local tumor antigen uptake and provided protection against tumor cells. Vaccination, when given at an early stage of tumor progression (tumor volume approximately 50 mm³ or smaller), would effectively skew immune reactions towards Th1 type. Our data showed a significant decrease in anti-inflammatory cytokines such as CCL2 and IL6. The Th1 type TME promoted effective CTL infiltration rather than activation of Tregs. These cytokine mediators regulated the expansion, migration, and

activation of immune suppressive cells in a combinatorial manner. The attraction of CCL2 to MDSCs is well documented.⁹² Increased IL6 signaling also promotes MDSCs proliferation once infiltrated. These vaccine data suggested a potential immunotherapy by blocking IL6 or CCL2 within TME at an early stage of melanoma progression. Although there was no significant increase in TME infiltrating CD4+ T cells after vaccination, one approach to improve efficacy is to co-load BRAF class II peptides into the same NP delivery system, thereby enhancing the T helper cell memory response. Overall, the modified TME would further enable syngeneic mono-antibody or chemotherapeutic nano-therapy, providing a promising strategy of combining immune therapy with chemotherapy. Thus, targeting TME-changing motifs along with efficient vaccination is a viable future research direction. One proposed project is to apply BRAF peptide vaccination on genetically engineered BRAF-mutant murine model, and plan to test this on a humanized murine model.

Dysplastic nevi, also known as unusual-looking benign (noncancerous) moles, are common among Caucasians.⁹³ These atypical moles greatly increase the risk of developing melanoma, even if there is no family history of melanoma.⁹⁴ The BRAF peptide vaccine, which can be designed as human leukocyte antigen (HLA)-restricted, may thus be developed as a preventive vaccination for use alongside regular exams. Theoretically, NP platforms can be exploited for combinatorial therapy by designing multimodal particles to further clinical translation.⁹⁵

2.4 Materials and Methods

2.4.1 Materials

Dioleoylphosphatidic acid (DOPA), (\pm)-N,N,N-trimethyl-2,3-bis(z-octadec-9-ene-oyloxy)-1-propanaminium chloride (DOTAP), 1,2-distearoyl-sn-glycero-3-phosphoethanolamine-N-[amino(polyethylene glycol)-2000 (DSPE-PEG-2000) and 3-(N-succinimidylxyglutaryl)aminopropyl, polyethyleneglycol-carbamyl distearoylphosphatidylethanolamine (DSPE-PEG-NHS) were purchased from Avanti Polar Lipids (Alabaster, AL). H-2Db restricted peptides original BRAF^{V600E} (FGLANEKSI), BRAF^{WT} (FGLANVKSI), modified BRAF^{V600E} peptide (pSpSSFGLANEKSI), and control peptide OVA (SIINFEKL) were purchased from Peptide 2.0 (Chantilly, VA). PEG-DSPE-Mannose was synthesized from DSPE-PEG-NHS and 4-Amino phenyl-mannopyranoside. CpG ODN 1826 (5'-TCCATGACGTTCTGACGTT-3') and Cy5-labeled ODN (5'-CAAGGGACTGGAAGGCTGGG-3') were purchased from Sigma Aldrich (St. Louis, MO).

2.4.2 Cell Lines

Murine BRAF-mutant melanoma cell line BPD6 (BRAF^{V600E}, PTEN^{-/-}, syngeneic with C57BL/6) was obtained from Brent Hanks (Duke Cancer Institute, Durham, NC) and cultivated in RPMI-1640 Medium (Invitrogen, Carlsbad, CA) supplemented with 10 % FBS (Invitrogen) and 1 % Penicillin/Streptomycin (Invitrogen) at 37 °C and 5 % CO₂.

2.4.3 Preparation and Characterization of Vaccine Formulation

The LCP NP was synthesized in a water-in-oil reverse micro-emulsion.⁹⁶ Ca phase was formed by mixing 600 μ L of 2.5 M CaCl₂ with or without peptide and/or CpG ODN in a 20 mL Cyclohexane/Igepal CO-520 (71:29, V: V) solution (oil phase). The oil phase was formed by mixing 600 μ L of 12.5 mM Na₂HPO₄ (pH = 9.0). We stirred both phases for 5 min then added 400 μ L of 20 mM DOPA for 25 min. We then added 40 mL of ethanol and collected cores by

centrifugation. Ethanol washes were followed before collection of the cores. Final LCP NPs were formed by mixing 1 mL CaP cores, 100 μ L of 20 mM DOTAP, 100 mL cholesterol, 10 mL DSPE-PEG-2000, and 10 μ L DSPE-PEG-mannose. After removal of chloroform under reduced pressure, final particles were dispersed in 100 μ L of 5 % glucose. Transmission electron microscopy (JEOL 100CX II TEM, JEOL, Japan) was used for particle characterization. Particle size and zeta potential were measured with a Malvern Zetasizer Nano ZS in water (Malvern, United Kingdom). DC accumulation of DSPE-PEG-mannose modified LCP NPs in the draining LNs was investigated by using LCP NPs containing a Cy5-labeled oligonucleotide and flow cytometry analysis of NP uptake in CD11c⁺ DCs.

2.4.4 Tumor Growth Inhibition

Female C57BL/6 mice (6–8 weeks old) were purchased from Charles River Laboratories (Wilmington, MA). All animal studies were approved by the IACUC Committee at the University of North Carolina at Chapel Hill (UNC). On day 0, mice were inoculated subcutaneously with 1×10^6 BPD6 cells on their lower flank. Once the tumor volume reached approximately 50 mm³ ($0.5 \times \text{length} \times \text{width} \times \text{height}$), mice were then randomized into five groups (n = 5-7) as follows: Untreated group (PBS group), Empty LCP NP (Empty group), CpG LCP NPs (CpG group), BRAF LCP NPs (BRAF group), and BRAF + CpG LCP NPs (BRAF + CpG group). Vaccination with LCP NPs was performed on day 10. We monitored tumor size (using digital calipers) and animal weight every 2–3 days. Mice were sacrificed before tumors reached 20 mm in one dimension. At the endpoint, tumors, major organs, and blood samples were harvested and tested. We evaluated antitumor efficacy by comparing relative tumor volume (RTV) value and T/C ratio. $RTV = V_t/V_0$, V_t and V_0 represent the tumor volume measured at

each timepoint interval and Day 0. $T/C (\%) = RTV \text{ of therapeutic group} / RTV \text{ of control group} \times 100 \%$. $T/C \leq 42 \%$, active, $T/C \leq 10 \%$, highly active.

2.4.5 *In Vivo* CTL Assay

In vivo CTL was conducted per a previously published protocol.⁷⁸ Mice were vaccinated with different formulations on the lower flank. Seven days later, the mice were intravenously injected with a mix of 5×10^6 splenocytes, half of which were pulsed by BRAF^{V600E} peptide (10 μ M) while the other half were pulsed by OVA peptide (10 μ M). The BRAF^{V600E} pulsed cells were labeled with 4 μ M carboxyfluorescein succinimidyl ester (CFSE) and OVA pulsed cells with 0.4 μ M CFSE. These two population were referred to as CFSE_{high} (BRAF^{V600E} pulsed cells) and CFSE_{low} (OVA pulsed cells). After 18 h, splenocytes were collected and analyzed by flow cytometry. CFSE_{high} and CFSE_{low}, as well as *in vivo* BRAF^{V600E} specific lysis was calculated.⁹⁷ The experiments were conducted in triplicate. Specific lysis was calculated as follows.

$$\% \text{ specific lysis} = (OVA * x - BRAF) / (OVA * x) \times 100 \%,$$

where $x = BRAF/OVA$ from naive mice.

2.4.6 ELISPOT Assay for IFN- γ Production

Mice were vaccinated with different formulations of treatment. Seven days later, spleen and draining LNs were collected into single cells and seeded on the capture antibody-coated 96-well plate. IFN- γ production was measured with BDTM ELISPOT assay system (BD Pharmingen, San Diego, CA) per the manufacturer's instructions.⁸⁶

2.4.7 Flow Cytometry Assay

Immune cell populations were analyzed by flow cytometry. Briefly, Tumor tissues or LNs were collected using collagenase A at 37 °C for 40-50 min. Single cells were harvested in PBS and stained with fluorescein-conjugated antibodies. Penetration buffer (BD, Franklin Lakes, NJ) was added for any intracellular cytokine staining.

2.4.8 Immunofluorescence Staining

Staining was performed following tissue deparaffinization, antigen retrieval, permeabilization, and bovine serum albumin (BSA) blocking. Primary and secondary antibodies conjugated with fluorophores (BD, Franklin Lakes, NJ) were incubated overnight at 4 °C. Cell nuclei were counterstained with DAPI (Vector Laboratories Inc., Burlingame, CA). Images were collected using fluorescence microscopy (Nikon, Tokyo, Japan) and analyzed using Image J software. Three randomly fields were selected.

2.4.9 TUNEL Assay

Assay performed following DeadEnd Fluorometric TUNEL System (Promega, Madison, WI) instructions⁹⁸ and imaged using fluorescence microscopy. Fluorescently stained FITC (green) positives were defined as TUNEL-positive nuclei. Three fields were randomly selected and quantified.

2.4.10 H&E Morphology Evaluation and Blood Chemistry Analysis

At the endpoint of the tumor inhibition study, mice with different treatments were all subjected to toxicity assays. Both whole blood and serum were collected. We collected and compared whole blood cellular components and tested for indicators of renal and liver function

such as creatinine, BUN, serum AST and ALT. Organs were collected and send out for H&E staining by UNC histology facility.

2.4.11 Statistical Analysis

We used Prism 5.0 Software to conduct one-way ANOVA and a two tailed Student's t-test and compared the data with those for the PBS control group. P-values less than 0.05 were considered significantly different.

CHAPTER 3

NANO-SUNITINIB REMODELING OF TME FACILITATES VACCINATION

3.1 Introduction

Melanoma vaccines could induce a tumor-specific immune response to inhibit micro-metastasis in its early stages when the suppressive effects of an advanced tumor are not yet an obstacle. In the previous work, a LCP NP as a nano-based carrier to efficiently deliver a tumor-specific antigen, the BRAF^{V600E} peptide, and CpG ODN (a Toll-like receptor 9 agonist) adjuvant elicited a robust antigen-specific cytotoxic T-cell response and potent tumor growth inhibition against the established DM (BRAF-mutant) model in its early stages.⁹⁹ However, it remained difficult to control tumor growth effectively once the tumor progressed to a later stage, likely due to presence of the immune-suppressive TME. The tumor immune-suppressive microenvironment limits effector T-cell activity, which is a major hurdle for an effective vaccine therapy, thus contributing to tumor progression.⁸⁰ SUN malate is an oral broad-spectrum tyrosine kinase inhibitor. SUN has antiangiogenic and tumor apoptosis properties, which also shows immunomodulatory features.¹⁰⁰ It has become an attractive drug to explore for treating melanoma.^{101, 102} In our previous work, the aminoethylanisamide (AEAA)-modified polymeric NPs were utilized as the drug delivery system for loading in-dissolvable drug such as SUN base (SUN_b-NP) or rapamycin, enhanced the antigen-specific immune response and exhibited effectively anticancer activity in BRAF-wildtype melanoma model.¹⁰³ Compared with wildtype

BRAF, i.e., the murine B16F10 model, BRAF-mutant melanoma is characterized by more aggressive growth and by the existence of a highly immune-suppressive desmoplastic TME. In clinical trials, such patients with BRAF-mutant melanoma were largely incapable of achieving long-lasting remissions from novel immunotherapies, for example, with the cytokine IL 2 therapy. The major reason why this type of tumor has relatively low response to immunotherapy might be limited by T-cell transportation and loss of tumor antigen presentation due to immune-suppressive TME.^{17, 99} There are still much challenges in TME remodeling in the advanced BRAF-mutant melanoma. Herein, we hypothesized that SUN_b-NP may work synergistically with our NP vaccine for therapy of advanced DM. The combination therapy may remodel the immune-suppressive microenvironment, achieve enhanced antigen-specific CTL response and increase antitumor effect on late-stage tumor. Data were collected and under peer-review in *Molecular therapy*. (H Zhu*, Q Liu*, L Miao, S Musetti, L Huang. Remodeling Immune Suppressive Microenvironment of Desmoplastic Melanoma to Facilitate Vaccine Immunotherapy)

3.2 Results and discussion

3.2.1 Characterization of SUN_b-NP and LCP-BRAF peptide vaccine

Polymeric micelles provide an advantageous platform to deliver hydrophobic drugs to tumor.¹⁰⁴ Here, SUN base was encapsulated into targeted AEAA-modified poly-lactidglycolic-acid poly (ethylene glycol) (PLGA-PEG-AEAA) micelles per the previously described protocol,¹⁰³ drug loading (DL) and encapsulation efficiency (EE) of SUN_b-NP was $11.6 \pm 0.4 \%$ and $73.5 \pm 2.4 \%$, respectively. SUN_b-NP was spherical with uniform size distribution (**Figure 8**

A and C) and showed smaller size than the blank polymer micelles (NP) (85.7 ± 2.3 nm & 116.4 ± 3.3 nm, respectively) owing to hydrophobic interactions between SUN and the hydrophobic cores of polymeric micelles (**Table 1**). The smaller size of SUN_b-NP could enhance vessel permeability through the enhanced permeability and retention (EPR) effect and avoid rapid RES elimination.¹⁰⁵ **Figure 8D** showed that SUN_b-NP had excellent stability *in vitro*. The cytotoxicity of SUN_b-NP slightly enhanced compared to SUN solution since the micellar nanoparticles increased cellular uptake above that of the free drug (**Figure 8E**).

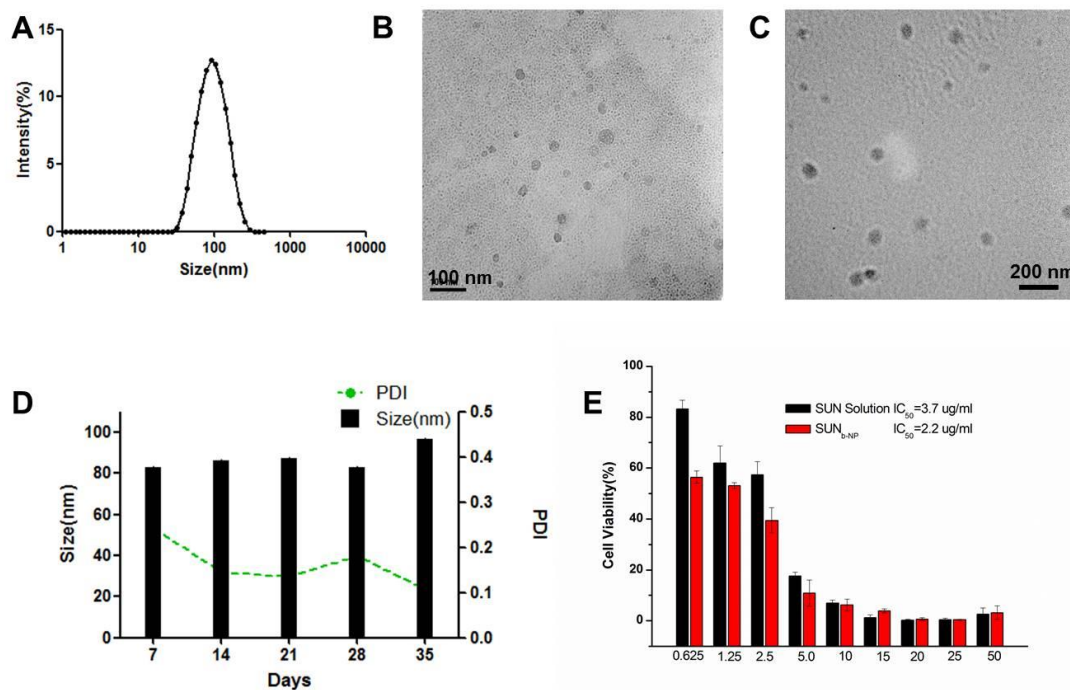


Figure 8. Characterization of SUN_b-NP and LCP-BRAF peptide vaccine. (A) Size distribution of SUN_b-NP. (B) TEM images of LCP NP-based BRAF peptide vaccine. (C) TEM images of SUN_b-NP after negative staining. (D) *In vitro* stability of SUN_b-NP at 4 °C. (E) Cytotoxicity of SUN solution and SUN_b-NP against BPD6 cells after 48 h. The error bars in the graphs represent standard derivations (n=5).

Table 1. Characterization of SUN_b-NP (n=3)

	Blank NP	SUN _b -NP
Size (nm)	116.4±3.3	85.7±2.3
Zeta (mV)	-17.0±0.3	7.0±0.2

The LCP NP was established for the delivery of nucleic acids and peptides.¹⁰⁶ It is particularly suitable for delivery of a peptide antigen together with a nucleic acid adjuvant to the DCs, because the NP vaccine can effectively modify the intracellular calcium dynamics and drive the maturation of dendritic cells for antigen presentation in a timely manner.^{107, 108} The BRAF peptide and CpG oligonucleotide adjuvant were encapsulated into LCP NPs using the method previously described. TEM analysis showed the NPs were spherical and had a diameter of around 30 nm after negative staining with uranium acetate (**Figure 8B**). Encapsulation efficiency was about 60 % for both the BRAF^{V600E} peptide and CpG.

3.2.2 *In vivo* anti-tumor efficacy

A mannose-modified LCP NP encapsulated the BRAF peptide vaccine could induce a favorable antigen specific CTL response and anti-tumor efficacy in early stage of murine DM model (less than 200 mm³ in tumor volume), but it exhibited only a partial antitumor effect in advanced stage.⁹⁹ In this study, the therapeutic efficacy induced by SUN_b-NP combination with the BRAF peptide vaccine was evaluated with advanced stage of DM model (300 ~ 400 mm³ in tumor volume). In the tumor growth curve shown in **Figure 9**, vaccine monotherapy exhibited only a partial antitumor effect. Interestingly, SUN_b-NP group showed improved tumor growth inhibition efficacy than the vaccine group ($p < 0.01$, SUN_b-NP vs vaccine, $n=5-8$), and combo group achieved the highest anti-tumor efficacy among all groups. The result indicated the tumor-specific immune function elicited by the vaccine could be boosted by SUN_b-NP. Furthermore, an overall survival analysis showed that the median survival for the combo group was 41 days, as opposed to 27, 28 and 33 days for PBS, vaccine and SUN_b-NP groups, respectively (**Figure 9B**), and achieved long-lasting overall response and superior therapeutic effect ($p < 0.001$, $n=10-18$). The inhibition ratios based on the tumor weight (**Figure 9C**) were consistent with tumor volume

measurement. The TUNEL apoptosis assay in **Figure 9D** and **E** also indicated that SUN_b-NP could significantly enhance the tumor-specific immune response and induce higher cellular apoptosis.

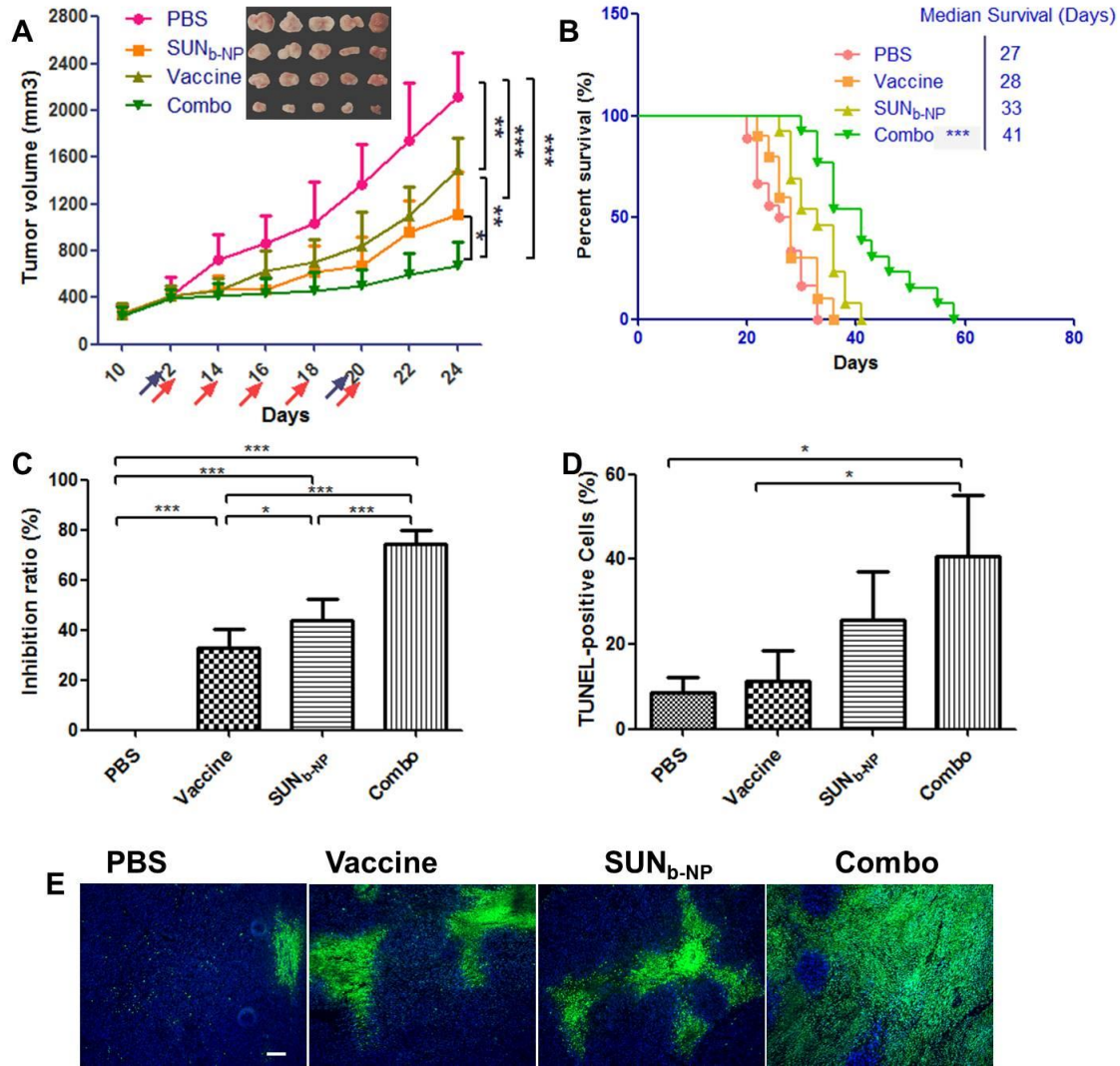


Figure 9. Anticancer efficacy in advanced DM model. Mice were subcutaneously inoculated on day 0 with 1×10^6 BPD6 cells. Vaccination with LCP-BRAF peptide vaccine was *s.c.* injected at a dose of 200 $\mu\text{g/kg}$ on day 12 and 20; SUN_b-NP was administered *i.v.* from day 12 and injected every other day at a dose of 20 mg/kg with 5 total administrations, respectively. Body weight and tumor size were detected every two days. Blood samples, major organs and tumor tissue were harvested on day 24. (A) Tumor volumes of mice via function of time. The arrows indicate the time of drug administration (blue for vaccine and red for SUN_b-NP, $n=5-8$). (B) Survival of mice in different treatment groups ($n=10-18$). (C) Tumor inhibition ratio. (E) TUNEL-positive cells in tumor sections stained using commercial apoptosis detection kit (green). DAPI (blue) stained the cell nuclei, and the white scale bar represents 100 μm . Three selected randomly images were quantified by Image J (in D). * $p < 0.05$, ** $p < 0.01$, *** $p < 0.001$.

No significant loss in body weight (**Figure 10A**) demonstrated minor toxicity of treatments. No significantly noticeable morphological changes in the major organs (**Figure 10D**) and normal ranges in serum biochemistry (**Figure 10 B and C**) suggested no systemic toxicity occurred after treatments.

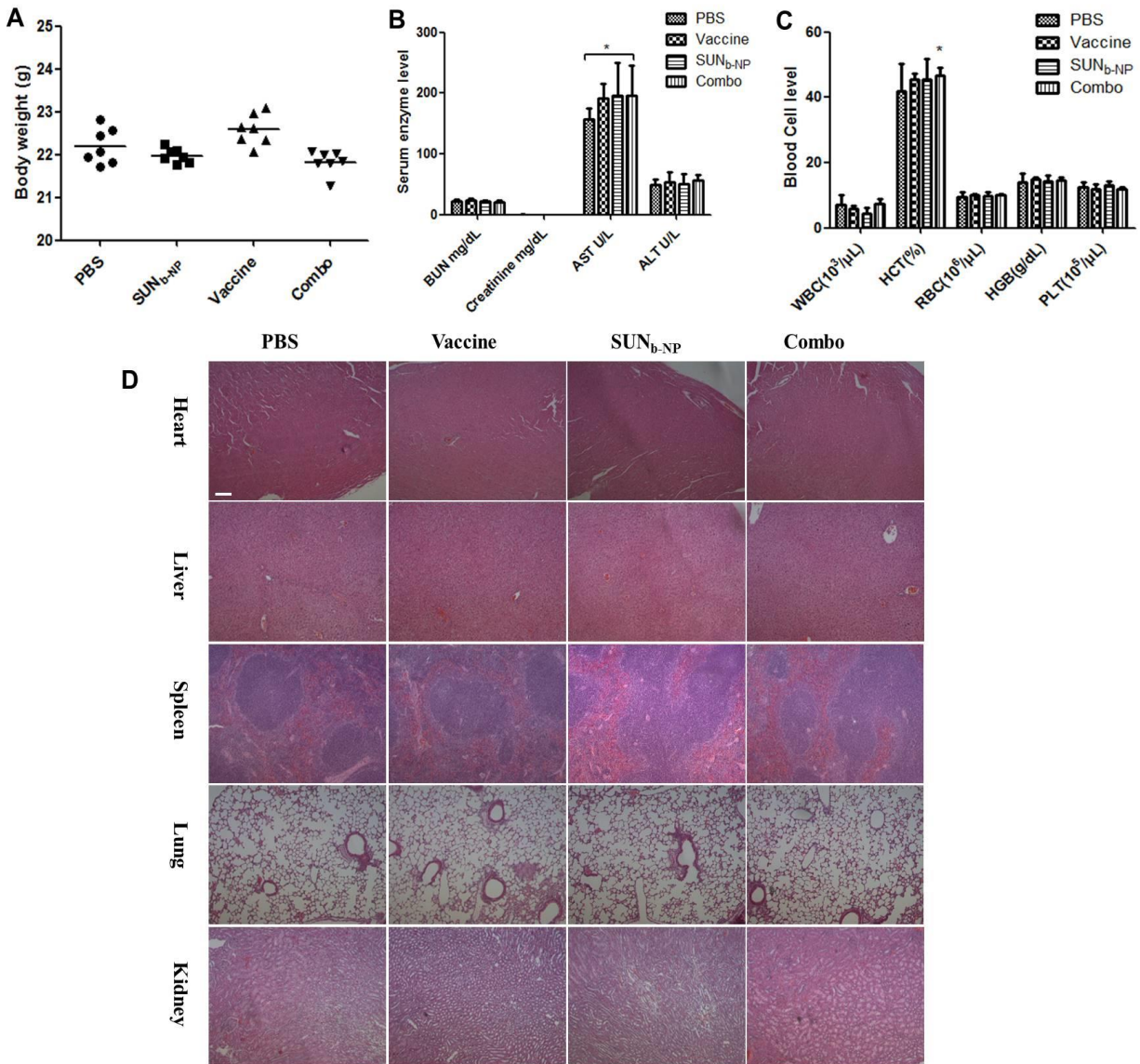


Figure 10. Safety evaluations. (A) Body weight change of BPD6 tumor-bearing C57BL/6 mice after treatments. (B) Liver, kidney function assays and (C) whole blood cell analysis after treatment. (D) H&E-stained heart, liver, spleen, lung, and kidney sections from BPD6 tumor-bearing C57BL/6 mice after treatment. The white scale bar represents 100 μm. Results were expressed as the mean ± S.D. (n = 4-5).

3.2.3 Pharmacokinetics and bio-distribution of SUN_b-NP

As shown in **Figure 11** and **Table 2**, the area under curve (AUC) value of ³H-labeled SUN_b-NP after *i.v.* administration was 2.2 times higher than that of SUN solution. As **Figure 11B** shown, SUN accumulation in tumors of SUN_b-NP group was ~3 fold higher than SUN solution at 2 and 4 h after treatment. Bio-distribution study clearly showed a dominant accumulation of ³H-labeled SUN polymer micelles in the tumor (as of targeted delivery) and liver (as of major systemic clearance route) after *i.v.* administration (**Figure 11C**). The results of pharmacokinetics and bio-distribution studies indicated that AEAA-modified polymer micelles could selectively deliver SUN to the tumor and achieve higher bioavailability.

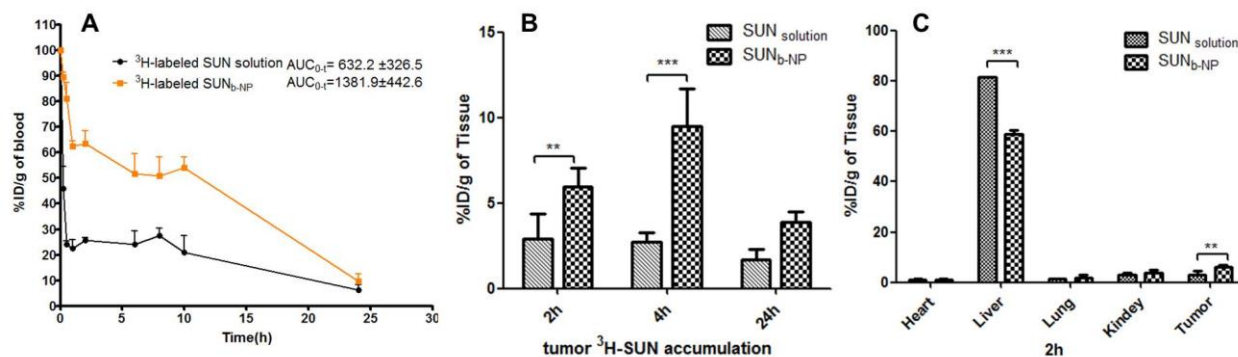


Figure 11. Pharmacokinetics and bio-distribution of SUN. (A) *In vivo* pharmacokinetics of ³H-labeled SUN_b-NP and SUN solution in BPD6 tumor-bearing C57BL/6 mice after treatment. (B) Tumor accumulation of ³H-labeled SUN_b-NP and SUN solution at t = 2, 4 and 24 h after treatment. (C) Organs (heart, liver, lung, kidney, spleen) and tumor accumulation of ³H-labeled SUN_b-NP and SUN solution at post-injection 2 h. The dose of ³H-labeled SUN was 50 μ Ci/kg. ** $p < 0.01$, *** $p < 0.001$. n=3.

Table 2. *In vivo* pharmacokinetic parameters of ³H-labeled SUN_b-NP and SUN solution in tumor-bearing C57BL/6 mice (n = 5)

	³ H SUN solution	³ H SUN _b -NP
K (h ⁻¹)	0.10±0.03	0.01±0.01
AUC _{0-t} (mg.h/mL)	632.2±326.5	1381.9±442.6
AUC _{0-∞} ((mg.h/mL)	688.1±367.3	1698.3±406.2
T _{1/2} (h)	7.5±0.8	5.3±0.6

3.2.4 TME remodeling by SUN_b-NP

Structural changes in the TME. Here, the change of the vessel distribution and morphology in tumor was measured using CD31 (a blood vessel marker) immunofluorescence staining. As shown in **Figure 12** (1st row), vessels were abundantly distributed in the tumor of PBS and vaccine group (red). High interstitial fluid pressure within the TME leaded to thin and elongated vessel structure (indicated by arrows), which greatly impeded the transport of drug from vessels. Interestingly, the vessels in the combination therapy treatment group showed a round morphology (indicated by arrowhead), as well as significantly decreased vessel density (**Figure 12B**). We have also tested the NP penetration into the tumor by using DiI-loaded PLGA NPs (**Figure 12A**, 4th row). The PBS and vaccine group exhibited weak fluorescence due to poor tumor permeability, but SUN_b-NP alone and combined treatment with vaccine elicited stronger and more widespread red fluorescence. The 1,1'-dioctadecyl-3,3,3',3'-tetramethylindocarbocyanine perchlorate (DiI) fluorescence intensity increased markedly in the combination therapy group ($p < 0.05$ compared with vaccine or SUN_b-NP group, **Figure 12E**), which indicated the combo group displayed the highest permeability in the tumor. Tumor-associated collagen and elastin in tumor tissues was characterized with the expression of α -smooth muscle actin (α -SMA, a TAF marker).¹⁰⁹ Representative immunostaining showed that

both the expression of α -SMA content and fibroblast population were decreased in SUN_b-NP group and combined treatment group (**Figure 12A**, 2nd row and **C**). SUN_b-NP combined with the vaccine almost removed the fibroblast population in cancerous tissue, indicating SUN significantly modulated TME modification through depleting TAFs. The over-expressed collagen in tumors could impede the function of antitumor immune cells and enhance tumor cell migration.¹¹⁰ The morphology and content of collagen were observed using Masson's trichrome staining. BPD6 melanoma contained a collagen-rich stromal structure compared with BRAF-wildtype melanoma B16F10. There was a significant decrease in collagen content after BRAF vaccination treatment in early tumor stages. Here, the fibrous structures using collagen staining (in blue) significantly decreased and almost disappeared in the SUN_b-NP treated group and combined treatment group (**Figure 12A**, 3rd row and **D**). Overall, these data indicated that SUN_b-NP combined with BRAF vaccination elicited the most significant changes of the TME morphology in such way that should favor further CTL infiltration.

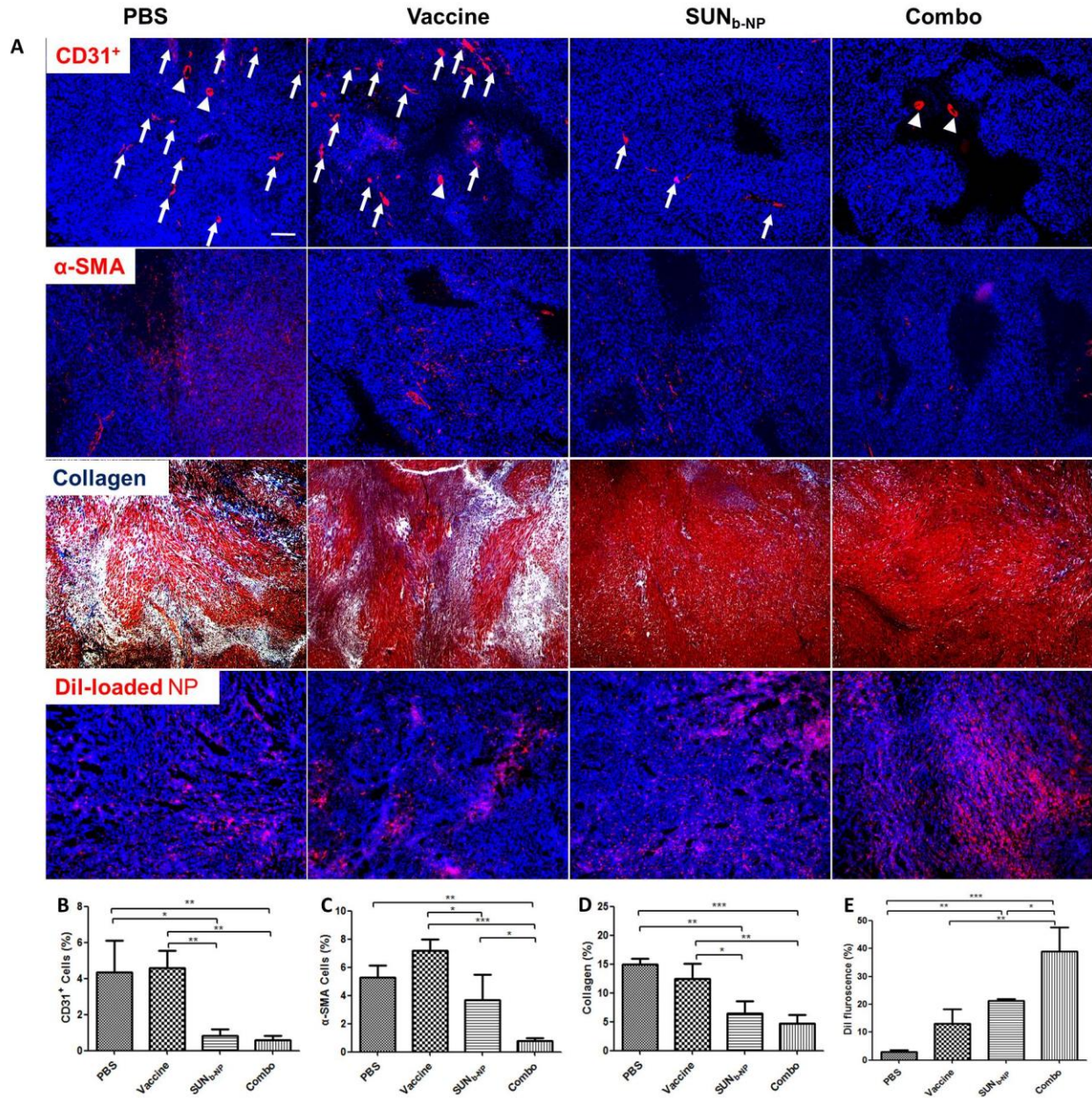


Figure 12. Structure changes in TME. (A) CD31⁺ antibody (red) visualized tumor vasculature (1st row, arrows and arrowheads indicated the elongated vessels or round vessels, respectively); α -SMA antibody (red) characterized TAFs in tumors (2nd row); Collagen fibers was stained with Masson's trichrome (blue, 3rd row); Tumor permeability of Dil-loaded NP (red, 4th row). DAPI (blue) stained the cell nuclei, and the white scale bar represents 200 μ m. To quantify the data in the images, three selected randomly images were analyzed using Image J (B, C, D and E, respectively). * $p < 0.05$, ** $p < 0.01$, *** $p < 0.001$.

Change of immune cells within the TME. Structural changes in the TME also favor the infiltration of immune cells into the tumor.⁹¹ The enhanced antitumor effect in three treatment groups was accompanied by an increase in CD8+ T-cell population in the collagen-rich BPD6 model, as measured by immunofluorescence staining and flow cytometry (**Figure 13A and B**). Vaccination increased CD8+ T-cells, but also led to an increase in immunosuppressive cells (MDSCs and Tregs), which could impair the T-cell activation and result in poor anti-tumor efficacy. As shown, the percentages of Tregs and MDSCs¹¹¹ in BRAF vaccine monotherapy group was higher than other groups, which was an important factor for the partial anti-tumor efficacy of vaccine alone treatment. However, the percentages of Tregs and MDSCs were significantly lower in the SUN_b-NP group and combination therapy than the vaccine monotherapy group ($p < 0.001$), indicating the superior ability of SUN to remodel the suppressive TME in favor of immunotherapy.

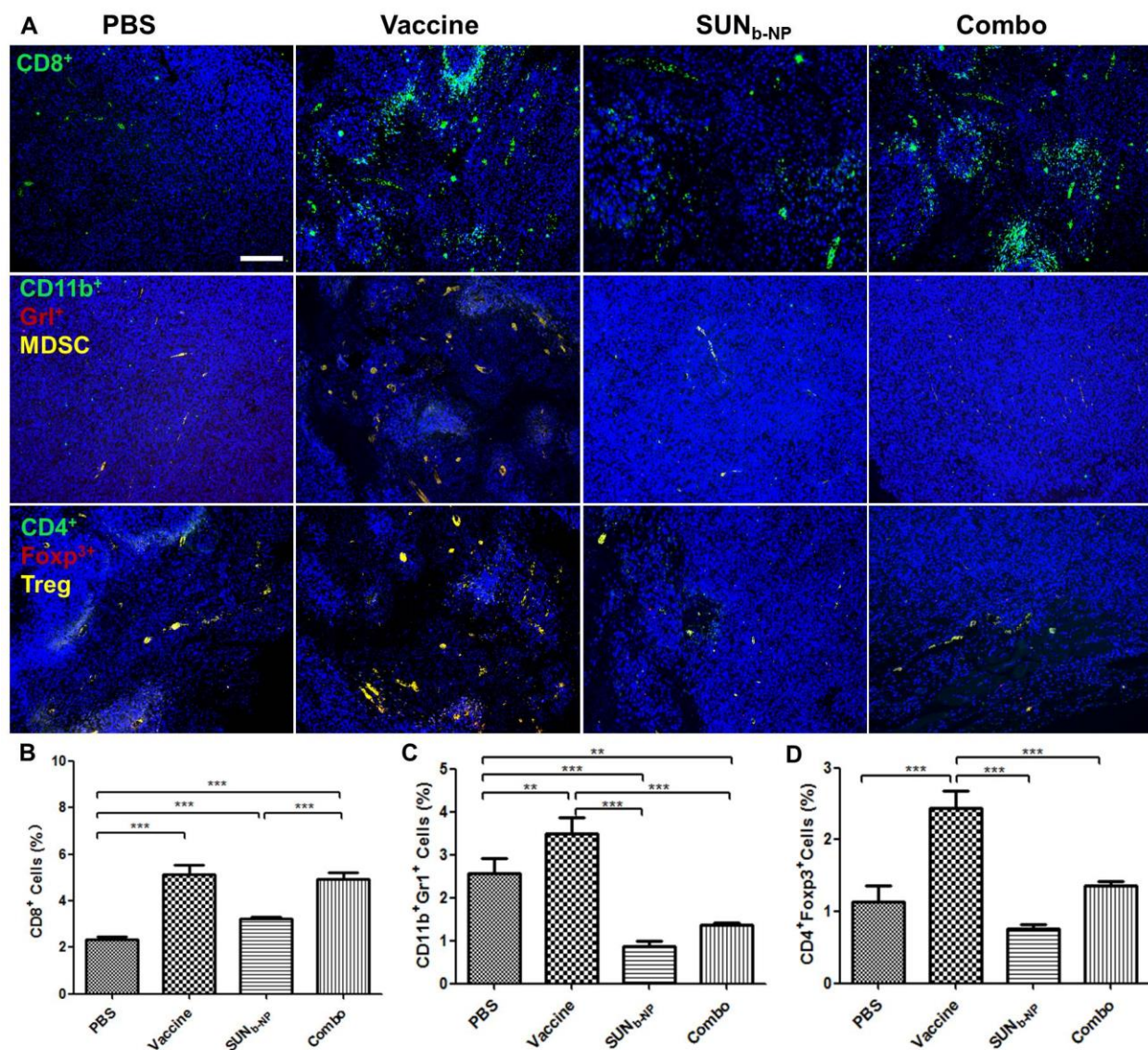


Figure 13. Change of tumor-infiltrating immune cells in TME. (A) CD8⁺ T cells, MDSCs and Tregs cells using immunofluorescence staining, scale bar represents 100 μ m. (B, C, D) The percentage of CD8⁺ T-cell, MDSCs and Tregs cells within tumor regions were analyzed using flow cytometry. * $p < 0.05$, ** $p < 0.01$, *** $p < 0.001$, $n = 3$.

Cytokine expression in the TME. As shown in **Figure 14**, the cytokine expression after treatment with BRAF vaccine alone resulted in both escalated Th1 and Th2 cytokine expression. The high level of Interleukin-10 (IL10), IL6 and TGF- β were responsible for the poor anti-tumor efficacy of vaccine alone treatment group at the advanced stage of tumor growth.¹¹² However,

combination therapy group significantly increased cytokine production of IFN- γ and IL-2, and decreased Type 2 T helper (Th2) cytokine expression, which would facilitate tumor antigen presentation and enhance cytotoxic T-cell-mediated tumor-specific killing, halting tumor progression.¹¹³

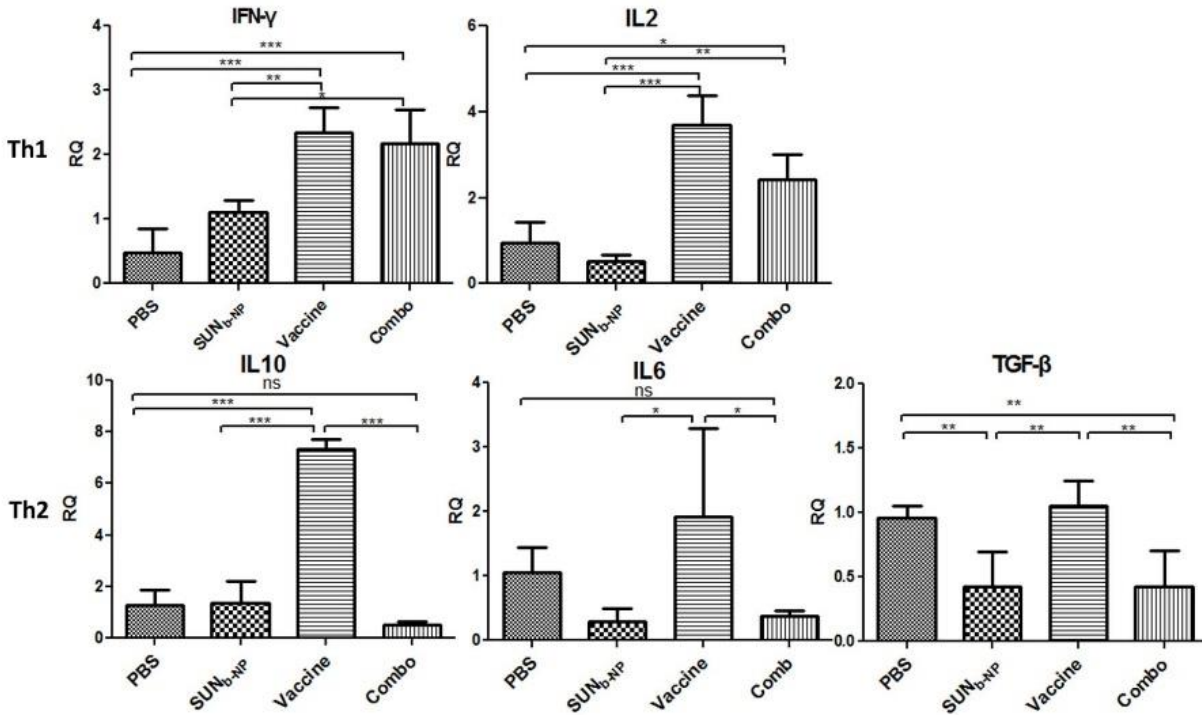


Figure 14. RT-PCR elucidated inflammatory cytokines within the TME. * $p < 0.05$, ** $p < 0.01$, *** $p < 0.001$, $n = 5$.

3.2.5 Signaling pathway determination

To explore the underlying mechanism of SUN_b-NP on remodeling the TME, expression levels of several signaling molecules such as Stat3, AKT and PD-L1 were examined using western blot analysis. In **Figure 15A** and **B**, the p-Stat3 levels were not reduced in the vaccine monotherapy, whereas BRAF vaccine together with SUN_b-NP efficiently decreased the p-Stat3 level in the tumor. SUN_b-NP alone showed only a modest reduction. A similar decreased pattern

in p-AKT expression was detected in the combination therapy. Reduction of p-Stat3 and p-AKT should associate with reduced tumor growth.¹⁰¹ As shown, tumor PD-L1 expression level in mice treated with BRAF vaccine alone and SUN_b-NP, respectively, exhibited a significant inhibition, though the combination therapy did not enhance the downregulation. The results indicated that down-regulated check point PD-L1 could enhance antigen-specific CTL killing of the tumor cells.

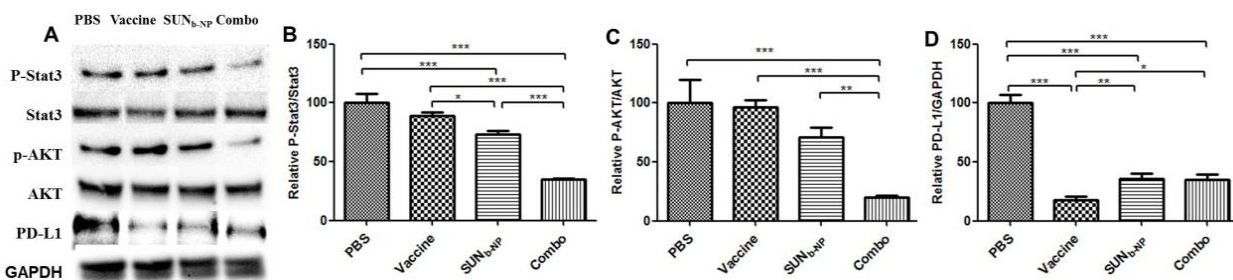


Figure 15. Oncogene expression levels. The level of p-Stat3, p-AKT and PD-L1 in tumor were examined by western blotting. (A) Relative band intensity was quantified by Image J (B, C, D). * $p < 0.05$, ** $p < 0.01$, *** $p < 0.001$, $n = 3$.

3.3 Conclusion

Our previous work proved that SUN encapsulated into targeted PLGA-PEG-AEAA micelles could specifically remodel the immune suppression in BRAF-wildtype melanoma model (B16F10) and enhance the antigen-specific immune response. Compared with B16F10 model, the BRAF-mutant melanoma had richer the dense collagen matrix, which induced high interstitial fluid pressure and obstructed the therapeutic efficacy of drugs. Immune-suppressive TME often exists in advanced malignancy grades, which support immunologic escape, drug resistance, tumor recurrence and metastasis. Considering the many formidable barriers, we provided a possible approach to synergistically combine SUN_b-NP with vaccine therapy for the advanced DM.

Why the combination treatment group could boost tumor-specific immune response and achieve the improved antitumor efficacy compared to vaccine monotherapy group? As shown in this study, SUN_b-NP could normalize vasculature in tumor and significantly reduce the collagen and tumor-associated fibroblasts through depleting TAFs. High interstitial fluid pressure within the TME often leads to thin and elongated micro-vessel structure, which greatly impede the transport of drug from vessels. The normalized vasculature in the tumor should enhance the delivery of drug and the infiltration of lymphocytes into the tumor. In addition, the over-expressed collagen in tumors can inhibit the function of antitumor immune cells and enhance tumor cells migration. Structural changes in the TME also favored the infiltration of immune cells into the tumor. CD8⁺ T-cell mediated immunity is one crucial mechanism for enhanced antitumor immunity. To further elucidate SUN_b-NP and vaccination in improving CD8⁺ T-cell infiltration, we also evaluated the changes of the related immunosuppressive cell subsets such as Tregs and MDSCs, which contributed to a complicated interplay network with CD8⁺ T-cell antitumor activity within the collagen-rich DM model. The vaccination increased CD8⁺ T cells and induced a local enhancement of tumor-specific T-cell infiltration. It also led to an increase in immunosuppressive cells (MDSCs and Tregs), which could impair the T-cell activation and result in poor anti-tumor efficacy. SUN_b-NP combination therapy treatment could reduce the MDSCs, Tregs and improve CD8⁺ T-cell infiltration, indicating the superior ability of SUN to remodel the suppressive TME in favor of immunotherapy.

Immune-suppressive cells in tumor express cytokines to shape the TME. Th1 cytokines including IFN- γ , IL2 and Th2 cytokines such as IL6, IL10 and TGF- β present to elicit or inhibit anti-tumor immunity respectively. Thus, cytokine profiles of Th1 increase or Th2 loss reflect the pharmacological action of effective treatments on the suppressive cells during tumor growth. Our

data showed that combination therapy group significantly increased cytokine production of IFN- γ and IL-2 and decreased Th2 cytokines expression, which would facilitate tumor antigen presentation and promote effective CTL infiltration, halting tumor progression.

Expression levels of several signaling molecules such as Stat3, AKT and PD-L1 could explore the underlying mechanism of SUN_b-NP on remodeling the TME from immune-suppressive to immune-responsive. Phosphorylated Stat3 and AKT represent the activated form of these proteins, which would further play an important role in tumor cell apoptosis and tumor immune evasion. Reduction of phosphorylated Stat3 activity could enhance the antitumor effects due to expression of activated p-Stat3 reduce tumor cell death, which was consistent with our tumor growth inhibition result. Meanwhile, Stat3 is involved in the accumulation of tumor-associated MDSC and Tregs, which plays an important role at the suppressing immune responses. Our results demonstrated that the decreased p-Stat3 expression by SUN could reduce MDSC and Tregs. IL-6 mediating signaling could also activate Stat3, supported by the decreased level of IL-6 in the tumor tissue among SUN_b-NP and combo group in our study. A similar decreased pattern in p-AKT expression was detected in the combination therapy. The inhibitory cytokines secreted by tumor cells for instance TGF- β , IL-10 and the inhibitory molecules such as PD-L1 expressed by TAFs could induce T-cell suppression. The results indicated that SUN_b-NP and the combination therapy down-regulated the inhibitory cytokines and enhanced antigen-specific CTL killing of the tumor cells.

In conclusion, SUN_b-NP combined with the vaccine can remodel immune suppressive microenvironment in the advanced DM to facilitate vaccine immunotherapy without detectable side effects. If BPD6 and B16F10 models represent typical BRAF mutation and wild-type

melanoma, respectively, our current and previous study strongly demonstrate the clinical potential of SUN_b-NP for all melanomas, especially when combined with a tumor vaccine.

3.4 Materials and Methods

3.4.1 Reagents

DOPA, DOTAP, and DSPE-PEG2000 were purchased from Avanti Polar Lipids (Alabaster, AL). PEG-DSPE-mannose was synthesized using DSPE-PEG-NHS (Avanti Polar Lipids, Alabaster, AL) and 4-amino phenyl-mannopyranoside (Sigma-Aldrich, St. Louis, MO). Cholesterol was obtained from Sigma-Aldrich (St. Louis, MO). H2D^b restricted peptides including the original BRAF^{V600E} (FGLANEKSI), BRAF^{WT} (FGLANVKSI), modified BRAF^{V600E} peptide, the ‘BRAF’ (pSpSSFGLANEKSI), and control peptide OVA (SIINFEKL) were obtained from Peptide 2.0 (Chantilly, VA). CpG ODN 1826 (5'-TCCATGACGTTTCCTGACGTT-3') was purchased from Sigma Aldrich (St. Louis, MO). SUN base and SUN malate were purchased from Selleckchem (Houston, TX) and Sigma-Aldrich (St. Louis, MO) respectively. ³H-Labeled SUN TFA salt (20 Ci/mmol) was obtained from ViTrax (Placentia, CA). Acid-terminated poly (lactic/glycolic acid, 50:50) (PLGA) was purchased from DURECT (Pelham, AL). PLGA-PEG and PLGA-PEG-MBA were synthesized using PLGA, mPEG3500-NH₂.HCl, tBOC-PEG3500-NH₂.HCl (JenKem Technology, Allen, TX) and aminoethylanisamide (Sigma-Aldrich, St. Louis, MO) as previously described and ¹H NMR confirmed the structure.

3.4.2 Animals and cell lines

Female C57BL/6 mice (6–8 week) were purchased from Charles River Laboratories (Wilmington, MA). All animal studies were carried out under the protocols which were approved by the IACUC committees at the University of North Carolina at Chapel Hill. Murine BRAF-mutant melanoma cell line BPD6 (BRAF^{V600E}, PTEN^{-/-}, syngeneic with C57BL/6) was obtained from Dr. Brent Hanks (Duke Cancer Institute) and cultured in RPMI-1640 Medium (Invitrogen, Carlsbad, CA) containing 10 % (v/v) fetal bovine serum (Invitrogen, Carlsbad, CA) and 1 % Penicillin/Streptomycin at 5 % CO₂ and 37 °C.

3.4.3 Preparation and characterization of the formulations

The BRAF peptide encapsulated LCP NP vaccine was formulated by reverse micro-emulsion technique as previously described.⁹⁶ SUN base was loaded into polymeric micelles nanoparticle using the solvent displacement method.⁷⁷ Five mg SUN base and 30 mg PLGA-PEG/ PLGA-PEG-AEAA /PLGA polymers (weight ratio 7:2:1) were added in 600 µL tetrahydrofuran (THF). Under stirring, the mixed solution was dropwise added into 5 mL water. Removing of THF using reduced pressure, the SUN_b-NP was further purified by centrifuging (6,000 g × 15 min) to remove un-encapsulated drug. SUN_b-NP containing ³H-labeled SUN base were prepared using the method described above, with the dose of ³H-labeled SUN fixed at 5 µCi/mL. TEM (JEOL 100CX II TEM, JEOL, Japan) and Malvern Zetasizer Nano ZS (Malvern, Worcestershire, United Kingdom) were used to characterize micelles nanoparticles. UV spectrophotometer (BeckmanCoulter, Atlanta, GA) was measured for drug loading. DL and EE of SUN_b-NP were calculated according to the previously formulas. The particle size and drug content were monitored for stability evaluation during storage at 4 °C.

3.4.4 *In vitro* cytotoxicity studies

The cytotoxicity of SUN_b-NP and SUN malate (SUN solution) against the BPD6 cells were evaluated using MTT assay *in vitro*. The SUN solution (10 mg of SUN malate in 1 mL DMSO) and SUN_b-NP were diluted to the designed series concentration of SUN (from 0.625 to 50 µg/mL) with culture medium. The BPD6 cells were seeded in 96-well plates at 5×10^3 cells/well and added into series concentration of SUN_b-NP or SUN solution. The cell viability was performed using MTT assay after incubation for 48 h. IC₅₀ value of SUN_b-NP or SUN solution was calculated using GraphPad Prism software.

3.4.5 *In vivo* anticancer efficacy

Murine DM model was built by inoculating subcutaneously with 1×10^6 BPD6 cells on the right flank of mice. Once tumor volume grew to 300~400 mm³ (length \times width \times width $\times 0.5$), mice were divided into 4 groups randomly as follows (n=5-8 per group): (1) Untreated control group (PBS); (2) LCP-BRAF peptide vaccine at 200 µg BRAF peptide /kg (vaccine); (3) SUN_b-NP at 20 mg SUN base/kg (SUN_b-NP); (4) LCP-BRAF peptide vaccine at 200 µg BRAF peptide /kg plus SUN_b-NP at 20 mg SUN base/kg (Combo). For the vaccination group and combo group, vaccination with LCP NPs was *s.c.* injected on day 12 and 20. SUN_b-NP was administered *i.v.* from day 12 and injected every other day with 5 total administrations. Body weight and tumor size were detected every two days. Blood samples, major organs and tumor tissue were obtained and tested for toxicity evaluation on day 24. Survival of murine BRAF-mutant melanoma model in different treatment groups (n=10~18 per group) was executed under same treatment as in tumor inhibition study.

3.4.6 *In vivo* pharmacokinetics and bio-distribution

Pharmacokinetics and bio-distribution studies of SUN_b-NP were evaluated using ³H-labeled SUN polymer micelles on DM model. A dose of 20 mg/kg SUN_b-NP or SUN solution containing ³H-labeled SUN TFA salt at 50 µCi/kg was *i.v.* injected, when tumor volume grew to ~ 300 mm³. After injection 15 min, 30 min, and 1, 3, 4, 8, 20, and 24 h, blood samples were gathered from caudal vein. Under same treatments, major organs and tumor tissue were collected when the mice were sacrificed 2, 4, and 24 h post-*i.v.* injection. Briefly, the samples (100 mg tissues or 20 mg blood) were digested by NCS[®] II Tissue Solubilizer (Amersham Biosciences Corp. NJ-) at 60 °C overnight, then added 200 µL of H₂O₂ (30 % in water) and vortexed to remove potential pigmented quenching agents. The sample was added to 4 mL scintillation cocktail (Thermo Fisher Scientific Inc., MA) and analyzed with a liquid scintillation counter (Beckman coulter LS6500). The pharmacokinetics and bio-distribution were evaluated using percentage of the injected dose in blood samples or tissue (% ID/g). All tests were performed 3 times.

3.4.7 Tumor permeability

For the imaging of micelle nanoparticle distribution and tumor permeability, DiI as probe was loaded in polymer micelles according as described in section of formulation preparation. DiI-loaded NP was administered *i.v.* with a single dose of 0.5 mg/kg on the tumor-bearing mice which were under same treatment as in tumor inhibition study. The tumor tissues were collected 24 h post-injection. To visualize micelle nanoparticle penetration, the tumor was lyophilized and sectioned. Images were collected by fluorescence microscopy (Nikon, Tokyo, Japan) and analyzed using Image J software. Three randomly fields were selected.

3.4.8 TME remodeling

Parameters including TME markers (CD31, α -SMA, collagen and immune cell) were used to illuminate TME remodeling process. Vessels were stained with CD31 using tumor frozen sections. First antibody was added and incubated overnight at 4 °C, following incubation with fluorophore-conjugated secondary antibody (BD, Franklin Lakes, NJ) for 1 h at room temperature. Tumor-associated fibroblasts (TAF) and collagen were characterized by α -SMA and Masson Trichrome kit respectively. The change of immune cell subsets such as antitumor cytotoxic T cell (CD8+ molecular markers), Tregs and MDSCs in TME were visualized using immunofluorescence staining. Staining was performed with paraffin section following tissue deparaffinization, antigen retrieval, permeabilization, and BSA blocking. T cells, Tregs and MDSCs were defined using FITC-conjugated rat-anti-mouse CD8a, FITC-conjugated rat-anti-mouse CD4 and PE-conjugated rat-anti-mouse Foxp3, FITC-conjugated rat-anti-mouse CD11b and PE-conjugated rat-anti-mouse Gr1 respectively. Collagen was visualized according to Masson Trichrome kit's instructions. Apoptotic tumor cells were characterized using the TUNEL assay kit (Promega, Madison, WI) and performed following TUNEL System instruction. Nuclei were double stained with DAPI (Vector Laboratories Inc, Burlingame, CA). Images were observed by fluorescence microscopy and analyzed using Image J software. Three randomly fields were selected.

3.4.9 Flow cytometry analysis

Immune cell populations in tumor tissue were analyzed using flow cytometry. Fresh tumor tissues from *in vivo* anticancer efficacy experiment were collected with 1 mg/mL collagenase A (Invitrogen) and 200 μ g/mL DNAase I (Invitrogen) at 37 °C for 40-50 min to generate single cells suspension. Single cells in PBS were stained with fluorescein-conjugated antibodies,

intracellular cytokine staining need to add penetration buffer (BD, Franklin Lakes, NJ). Flow cytometry was performed 3 times for each group. The results were analyzed by CellQuest software (BD Biosciences, San Jose, CA).

3.4.10 Western blot analysis

The expression level of several signaling proteins in tumor tissue was evaluated using western blot. Tumors lysates were prepared and analyzed, then equal amounts protein of treatment group was separated by 10 % SDS-PAGE electrophoresis and transferred to polyvinylidene difluoride membranes (Bio-Rad) for immunoblotting as document described method.¹¹⁴ Primary antibodies against p-AKT, AKT, p-Stat3, Stat3 and PD-L1 (1:500-1,000 dilution, Cell Signaling, Beverly, MA) were directed, GAPDH (Cell Signaling, Beverly, MA) was detected as loading control. After washing, the membrane was incubated with horseradish peroxidase conjugated secondary antibody (1: 1,000 dilutions, Cell Signaling, Beverly, MA) and developed using the Pierce ECL Western Blotting Substrate (Thermo, Rockford, IL). The expression level of each protein was quantified with ImageJ software, and performed in triplicate in each group.

3.4.11 Statistical analysis

A two-tailed Student's t-test and one-way ANOVA were utilized to analyze in GraphPad Prism 5.0 Software (San Diego, CA). Data were shown as mean \pm S.D., Values were indicated significantly difference when * $p < 0.05$; ** $p < 0.01$ and *** $p < 0.001$.

CHAPTER 4

NANO-FRAXINELLONE REMODELING OF TME FACILITATES VACCINATION

4.1 Introduction

The stroma of the DM includes TAFs, T cells, B cells and immunosuppressive cells. TAFs are one of the most prominent stromal cell types. It has been reported that TAFs are the receivers as well as the inducers of tumorigenic activation signals. Emerging evidence suggests that TAFs can modulate the immunosuppression of TME through diverse mechanisms, thereby supporting tumor progression.^{115, 116} For example, TAFs can suppress CTL-driven antitumor immunity and mediate immune suppression by modulating myeloid cells, such as tumor associated macrophages (TAMs), MDSCs, and tolerogenic DCs. TAFs can also mediate epithelial-mesenchymal transition (EMT) of carcinoma cells, thereby contributing to the progression of cancer. Additionally, some growth factors secreted by TAFs like TGF- β play an important role in promoting the carcinogenic process.¹¹⁷ As a result, a bi-directional activation between cancer cells and TAFs has been identified as the leading cause to form the malignant phenotype of cancer.¹¹⁵ Taken together, TAFs are the potential target for treatment of desmoplastic melanoma and targeting TAFs will render both malignant and stromal compartments more responsive to immunotherapies. Encouragingly, our previous investigation on modifying TAFs through delivery of apoptosis-reducing ligand has proved effective to treat desmoplastic cancers.^{108, 118}

In recent years, we have studied natural products which target TAFs, especially on the interaction loop between TAFs and cancer cells. The focus of this work is on TGF- β , one of the key mediators for fibroblast activation and tissue fibrosis.¹¹⁹ Frax, a compound isolated from the root bark of *Dictamnus dasycarpus*, is reported to resolve liver fibrosis by reducing CUG-binding protein 1 (CUGBP1) expression and consequently regulating TGF- β and IFN- γ signaling.¹²⁰ Other studies have examined Frax for its actions such as anti-inflammatory, neuroprotective, antinociceptive, and vasorelaxation activities.^{121, 122, 123} However, the effect of Frax on TAFs in TME has not been studied. Therefore, as a part of our research on TAFs modification, we investigated the anti-fibrotic properties of Frax in TME. To enhance the targeting ability, AEAA was added on the surface of formulation.¹²⁴

As accumulating investigations have proved the importance of TME modulation in alleviating the offensive behavior of melanoma,^{125, 126} we hypothesize that targeted delivery of Frax to the tumor site will lead to deactivation of TAFs and reduce tumor load. Nevertheless, remodeling TME alone might affect tumor growth partially. To further improve anti-cancer activity, vaccination in DM is proposed to be combined herein. In this study, a synergistic therapy combined Frax and tumor-specific peptide vaccine was hypothesized to regulate the TME and negate its suppressive surroundings, thus increasing the anti-tumor immune response, inhibiting tumor growth and prolonging the survival duration.

4.2 Results and discussion

4.2.1 Preparation and characterization of Frax NE

Frax is so hydrophobic that it is very difficult to be loaded into traditional drug delivery systems. It is well-known that nanoemulsion (NE) is a colloidal particulate system, which is manufactured to improve drug solubilization and enhance therapeutic efficacy. As a result, Frax was formulated in the NE.^{127, 128} In NEs, the combination of surfactants with oils offers a superior advantage over co-solvent system or other nanocarriers in terms of drug-loading capacity for hydrophobic compounds. To avoid the toxicity of traditional small molecular surfactants, we used the biocompatible lecithin from soybean as the emulsifier herein. To achieve tumor targeting ability, AEAA was used as the targeting group on the NE, as our previous studies have confirmed that AEAA is the sigma receptor ligand, which is overexpressed on cancer cells and TAFs.^{124, 129} Moreover, the preparation procedure of Frax NE was much simpler than that of other nano-systems, and thus endowing it with translational potential.

Frax NE was prepared by the method of ultrasonic emulsification, which is very efficient in constructing this formulation. The Frax NE concentrated solution appears opalescence with a yellow color, and the average particle size was 148.1 ± 1.3 nm. The morphology of NE by TEM analysis was shown in **Figure 16**, revealing spherical shape and uniform droplet. The concentration of Frax in the NE was 2 mg/mL, the encapsulation efficiency was about 90 % and Frax NE was found to be stable for about 20 days of storage at room temperature. There was no significant difference in diameter size, appearance and dilution ability, which indicated that Frax NE was chemically and physically stable.

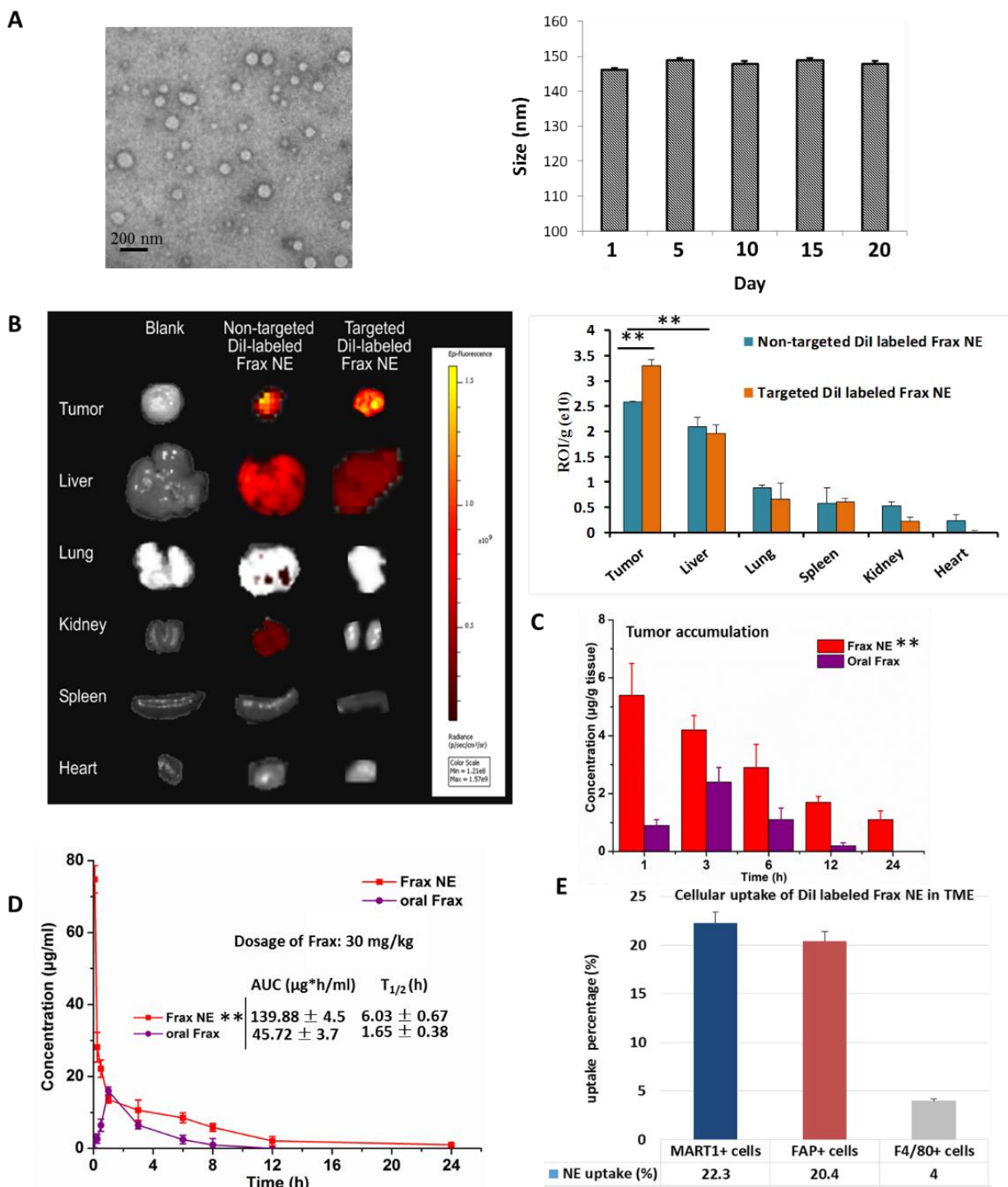


Figure 16. Preparation and characterization of Frax NE *in vitro* and *in vivo*. (A) TEM image and *in vitro* stability of Frax NE. (B) IVIS image and quantitative analysis of DiI-labeled Frax NE with or without targeting ligand in BPD6 tumor bearing mice. (C) Quantitative analysis for tumor accumulation of Frax *in vivo* using LC/MS. (D) PK analysis of Frax NE *in vivo* using LC/MS. (E) Cellular uptake of DiI-labeled Frax NE in TME, measured by flow cytometry. (n = 3, * P < 0.05, ** P < 0.01, *** P < 0.001)

To investigate the accumulation of NE in tumors, the biodistribution of DiI-loaded NE with or without AEAA modification was recorded using IVIS imaging (**Figure 16B**). 24 h post-injection, the higher fluorescence signal in tumors was observed even without targeting ligand. This enhanced distribution of DiI-labeled NE at tumor site was attributed to the EPR effect. By contrast, AEAA-modified DiI-loaded NE demonstrated higher tumor targeting ability, and semi-quantitative biodistribution analysis in major organs was also performed. The ratio for fluorescence intensity to tissue weights of AEAA-modified NE was significantly increased at tumor region and decreased at other organs as compared to that of non-targeted NE.

Furthermore, the plasma concentration-time and tissue distribution profiles of Frax were characterized after intravenous administration of Frax NE (30 mg/kg) and oral administration of Frax suspension, respectively. As shown in **Figure 16C and D**, data fitting results displayed that the pharmacokinetics behavior of Frax NE fitted a two-compartment model, the value of total AUC was $139.88 \pm 4.5 \mu\text{g}\cdot\text{h/mL}$, and $t_{1/2}$ was $6.03 \pm 0.67 \text{ h}$. This suggested that Frax NE can circulate for a longer time in the blood than Frax oral suspension. Notably, the Frax accumulated in the tumor was dramatically greater than that of the oral control. The MRT ($0 \rightarrow \infty$) values of Frax for Frax NE was 2.9-fold compared with the control, which indicated that the injected NE were targeted to and stayed in the tumor tissue for an extended time.

After confirming the targeting ability of Frax NE, especially with the AEAA-modification, the DiI-loaded NE accumulation in various cell populations within the tumor was further performed by flow cytometry. Based on the results (**Figure 16E**), we found that approximately 22.3 % of NE in the TME was taken up by the tumor cells (MART1 positive) and 20.4 % was absorbed by TAFs (FAP positive) 24 h post-injection. In most cases, the uptake of nanoparticles

results from the binding with cell surface, and thus more AEAA-modified NE entered cells with overexpressed sigma receptor regardless of size compared to non-targeted NE, as expected.

4.2.2 Evaluation of therapeutic efficacy and changes in TME after Frax NE treatment

The antitumor efficacy of Frax was investigated after we have confirmed the tumor-targeting ability of Frax NE. Therapy began when tumor sizes reached 200 mm³ to form the stromal-vessel structure. The tumor volume curve (**Figure 17**) demonstrated that Frax treatments can significantly inhibit tumor growth compared with PBS group. In addition, Frax NE exhibited higher antitumor effect, even though the dosage of Frax oral suspension was 4 times higher than Frax NE. Moreover, the inhibition ratios of these two Frax formulations were calculated based on the tumor weight at the endpoint (**Figure 17B**). IRs for Frax NE and Frax oral were $35.3 \pm 2.5\%$ and $51.0 \pm 3.5\%$, respectively, which agreed with the results of tumor inhibition measurements.

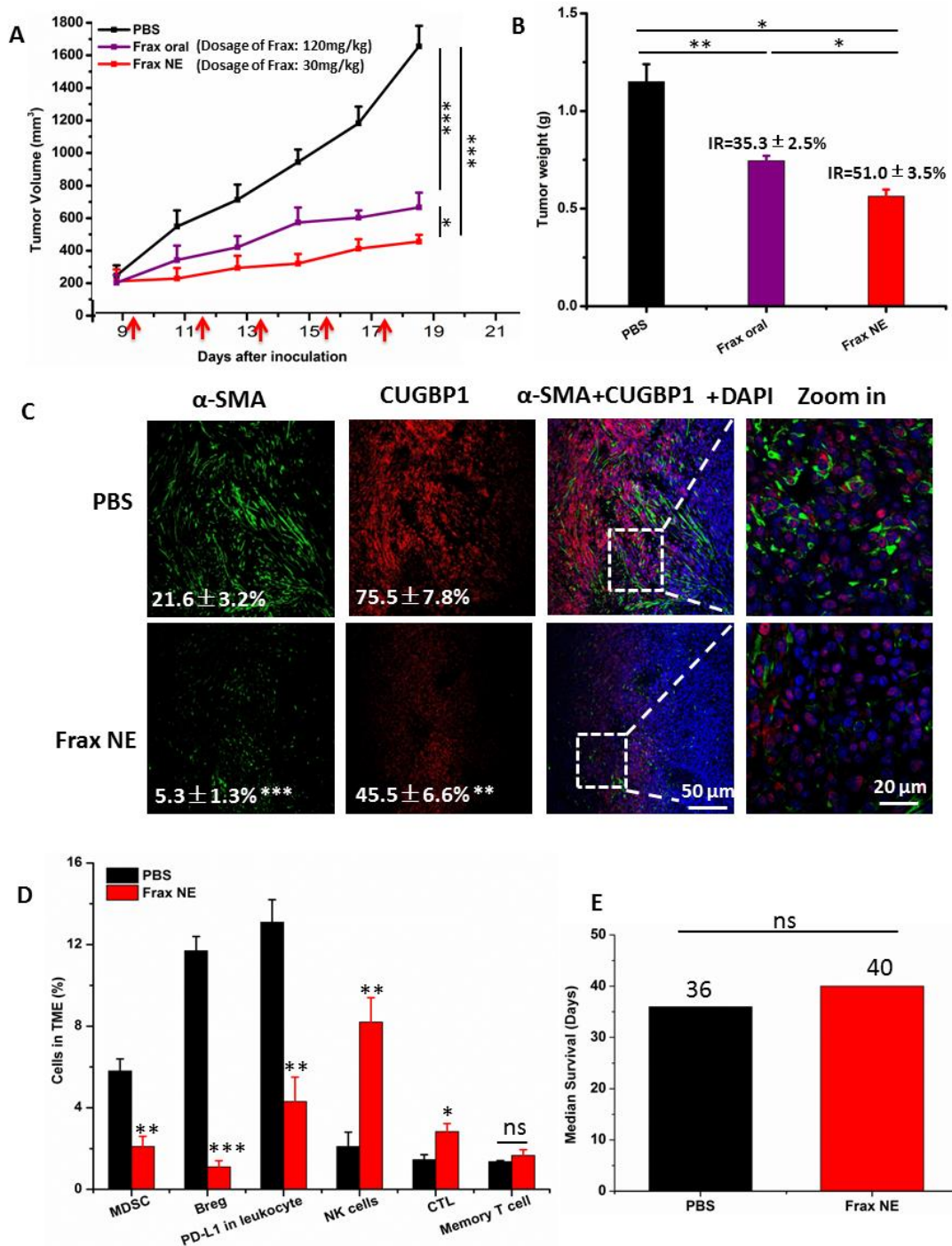


Figure 17. Tumor inhibition effects and TME changes in vivo after treatment with Frax. (A) Tumor volume change as a function of time. The dosage of Frax by oral administration is 4 times higher than that of Frax NE by intravenous injection. Frax was administrated *p.o.* or *i.v.* every other day for 5 times (small arrows under the axis represent the day of dosing). (B) Tumor weight at the end of the experiment (day 23). Inhibition ratio (IR) is calculated. (C) Confocal analysis for α -SMA and CUGBP1 from tumor tissue sections. (D) Comparison of different immune cells in TME between BPD6 tumor bearing mice with and without treatment using flow cytometric analysis. (E) The survival data from treatment and without treatment groups. Numbers shown in white indicate the average % of each cell type in the tumor. The statistical analyses were calculated by comparison with the control group if not specifically mentioned. Data show mean \pm S.D.. (n = 5-8, * P < 0.05, ** P < 0.01, *** P < 0.001)

Because Frax was reported to treat liver fibrosis,¹²⁰ we initially examined the changes of TAFs as well as the CUGBP1 levels in tumor tissue samples. CUGBP1, standing for CUG-binding protein 1, was reported to be involved in posttranscriptional regulatory networks, TGF- β /IFN- γ balancing, fibro-genesis and tumorigenesis.¹³⁰ It is also the target of Frax. As can be seen in **Figure 17C**, α -SMA positive TAFs were significantly reduced in Frax NE group compared with untreated PBS group, and the morphology of TAFs also changed from compact ribbons to small dots. Noteworthy, the CUGBP1 expression was decreased with downregulating fibrosis.

We have showed Frax NE could suppress tumor growth and formation of TAFs, but the reason for these effects needed to be further studied. Firstly, we confirmed that empty NE without Frax had no influence on tumor growth by using MTT and tumor volume observation (data not shown). Therefore, we looked for the alterations of immune cell populations in the TME. In tumor-bearing hosts, the immune suppressive cells such as MDSC as well as regulatory B cells (Bregs), and PD-L1 play crucial roles in immune suppression, and converse of their function is important for immunotherapeutic treatment.¹³¹ As seen in **Figure 17D**, the percentage of MDSC (CD11b⁺Gr1⁺), Bregs (CD1d⁺CD19⁺) and PD-L1 in leukocytes in the Frax NE group were much lower than the PBS group, measured by flow cytometry of whole tumor tissue. On the contrary, CTLs and natural-killer (NK) cells increased significantly, which suggested that the change of the TME morphology might facilitate T cell infiltration and innate immune response. There was no significant difference for memory T cells between PBS group and Frax NE group. Although we have found Frax NE could inhibit tumor growth, possibly due to the remodeling of TAFs and TME as aforementioned, the survival duration was not prolonged, and tumors grew back after drug withdrawal (**Figure 17E**).

4.2.3 Frax NE improves the antitumor effect and reprograms TAFs when combined with BRAF peptide vaccine in stroma-rich melanoma

To improve the antitumor efficacy of Frax NE and increase the survival rate, combination therapy was taken into consideration. As Frax NE could remodel TAFs and reduce intra-tumor suppressive cells in the TME, we hypothesized that combination therapy with a vaccine that induces antigen-specific CTL response would be successful, especially in advanced BRAF-mutant melanoma. Our group has developed a BRAF peptide vaccine previously,⁹⁹ and it could be introduced into combo group herein.

Compared with PBS group, all treatment groups showed reduced tumor growth rates (**Figure 18A**). As expected, the combo group exhibited the best anti-cancer effects, suggesting the advantages of combination therapy. Meanwhile, in an overall survival analysis after the final day of treatment, median survival was also elevated in combo group (**Figure 18B**), conveying not only a potent therapeutic effect but also a long-lasting overall response.¹⁰⁶

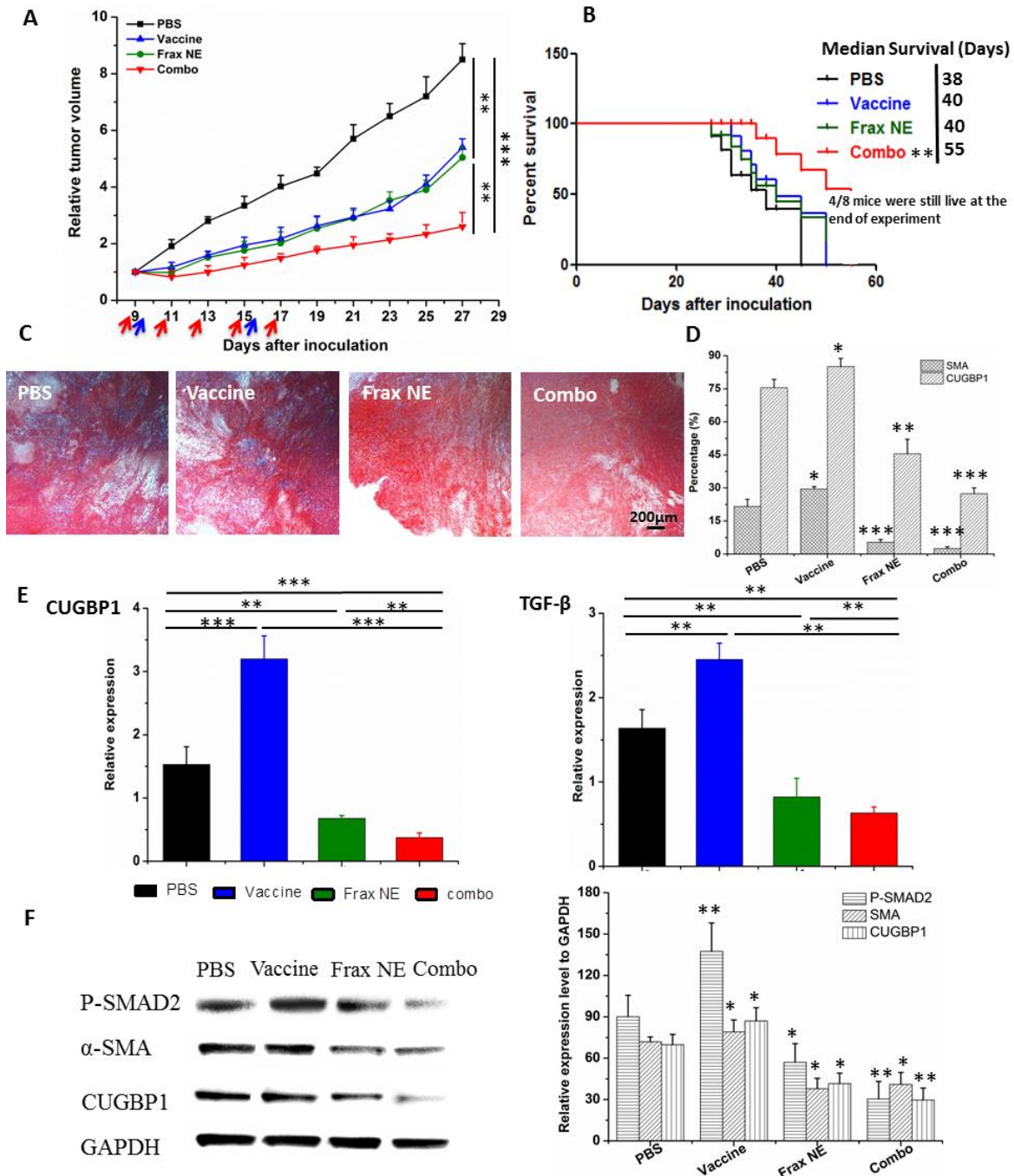


Figure 18. Tumor inhibition effects and TME changes *in vivo* after treatment with Frax NE combined with vaccine. (A) Tumor inhibition curve of BPD6 tumor bearing mice using different formulation treatment (PBS, Vaccine, Frax NE and Combo). Frax (red arrow) was administrated *i.v.* every other day for 5 times at the dose of 30 mg/kg. For the vaccine alone and combo therapy groups, vaccination (blue arrow) was administrated on day 9 and boosted on day 15 subcutaneously. (B) The survival proportions of the treated groups. (C) Masson's trichrome stain for collagen. (D) Quantitative analysis of α -SMA and CUGBP1 to evaluate the effects of different treatments on the inhibition fibroblast by confocal microscopy. (E) Changes of cytokines in TME using quantitative RT-PCR. (F) Western blot analysis of BPD6 tumor protein levels after different treatments. The statistical analyses were calculated by comparison with the control group if not specifically mentioned. All data show mean \pm S.D.. (n = 8-10, * P < 0.05, ** P < 0.01, *** P < 0.001)

To investigate the mechanism of anti-tumor effects, we firstly used Masson's Trichrome staining to study the morphology and collagen content of tumors after treatment. In **Figure 18C**, collagen deposition and fibrosis were observed abundantly in tumor sections of untreated group. By contrast, Frax NE and Combo treatment significantly ameliorated the pathological changes. Simultaneously, percentage of α -SMA and CUGBP1 was quantitatively analyzed by Image J under confocal imaging (**Figure 18D**), which displayed the similar trends as aforementioned. However, α -SMA in vaccine only and PBS group were alike, while CUGBP1 in whole tumor increased partially. Moreover, the relative mRNA expression of CUGBP1 was a further evidence of our staining analyses (**Figure 18E**, left panel).

We wondered about underlying relationship between treatment and TAFs after confirming that Frax might have an influence on changes of TAFs. As it is commonly accepted that the majority of TAFs are transdifferentiated from resident fibroblasts in response to TGF- β ,^{132, 133} the TGF- β expression and downstream portions of TGF- β signaling pathway, involving P-SMAD2 and α -SMA were examined. Data demonstrated that treatment with Frax alone or combined with vaccine resulted in reduced TGF- β expression, but it was also noteworthy that vaccination significantly increased the expression of TGF- β in the TME on a RNA level (**Figure 18E**, right panel), which would inhibit the development of anti-tumor immunity.¹³⁴

Western blotting (**Figure 18F**) revealed that P-SMAD2 level dramatically reduced in tumors in Frax NE and Combo groups, but vaccine monotherapy increased this protein partially compared to PBS treated group. Decreased α -SMA and CUGBP1 expression after treatment agreed with the results previously.

4.2.4 Apoptosis of neighboring tumor cells caused by combination therapy of Frax NE and BRAF peptide vaccine inducing antigen-specific immune response

To study the potential effects from the histological cross-sections, tumor cell apoptosis was quantified via a TUNEL assay (**Figure 19A**). All the three treatment groups displayed a greater number of apoptotic cells, than PBS group, and the combo group exhibited the highest level of cell apoptosis ($46.6 \pm 2.7 \%$). These findings correlated with the tumor inhibition data as above, which was possibly due to the immune cells killing induced potent cell death within the TME.

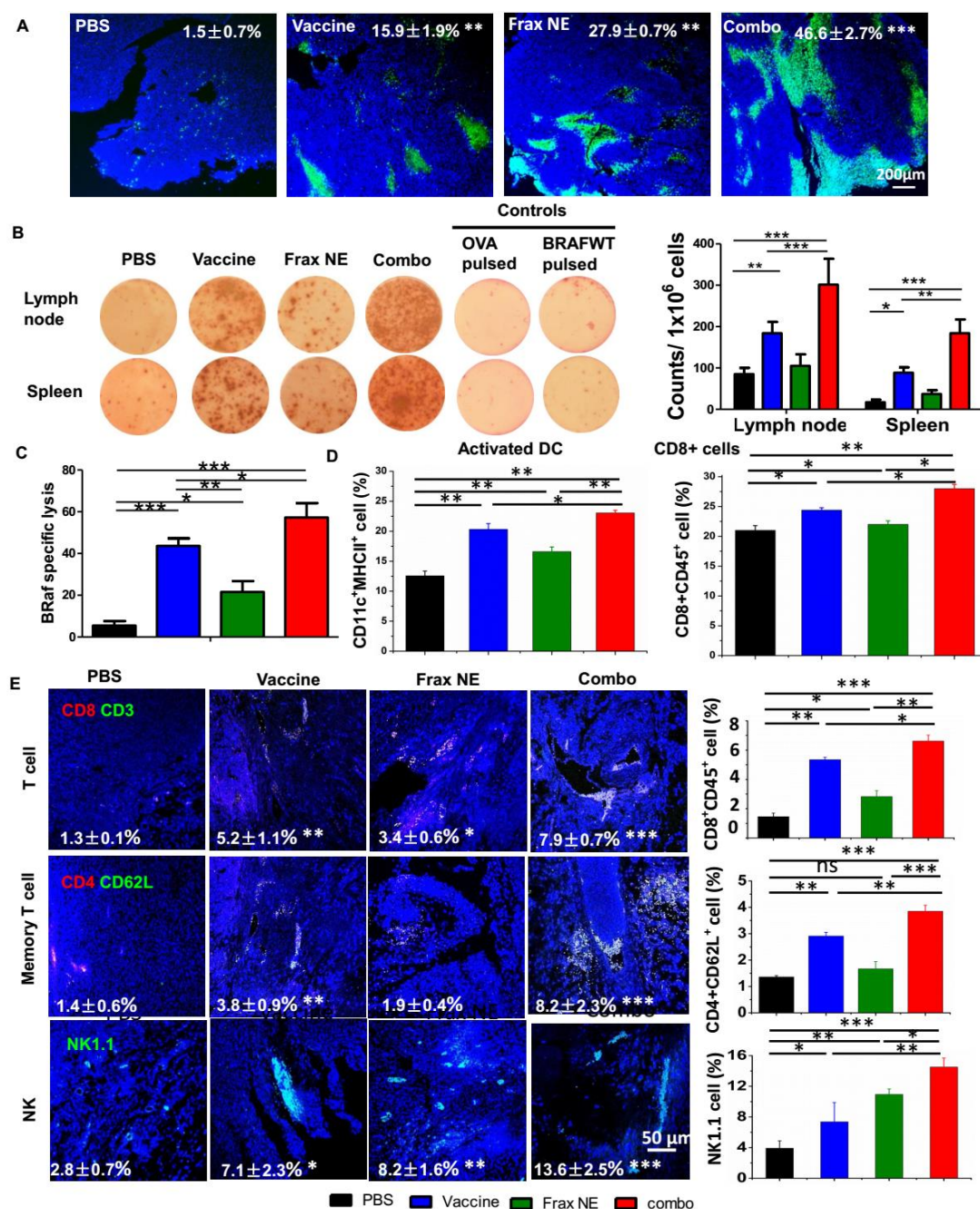


Figure 19. Enhanced T-cell infiltration into TME-induced potent CTL killing. (A) TUNEL staining of tumor sections after different treatment. (B) IFN- γ production after treatment was measured with ELISPOT assay system. (C) *In vivo* CTL response after treatment with either Frax NE, vaccine or combo was measured through CFSE high/low staining of splenocytes collected from naïve mice which were pulsed with BRAFV600E peptide (CFSE_{high} cells) or with OVA control peptide (CFSE_{low} cells), respectively. An equal mixture of both pulsed cells was injected into the vaccinated mice via tail vein. 18 h after injection, mice were euthanized and splenocytes were collected, washed and analyzed via flow cytometry. (D) Changes of immune cells quantified by flow cytometric analysis in lymph node. (E) Confocal and flow cytometric analysis of immune cells infiltration in TME. Numbers shown in white indicate the average % of each cell type in the tumor. The statistical analyses were calculated by comparison with the control group if not specifically mentioned. All data show mean \pm S.D.. (n = 6, * P < 0.05, ** P < 0.01, *** P < 0.001)

To further determine whether the antitumor potency was caused by a robust immune response, antigen-specific CTL response and IFN- γ production ELISPOT assay were performed. ELISPOT assay results in **Figure 19B** confirmed the eliciting IFN- γ release capacity of vaccine as our published paper.⁹⁹ Moreover, Frax NE also boosted modest efficacy, and combo group exhibited the most sufficient stimulation to secrete IFN- γ . For the CTL assay (**Figure 19C**), mice immunized with BRAF peptide showed partial (approximately 43.6 %) efficacy, whereas mice receiving combination therapy proved the most effective (about 57.2 %), indicating that combination therapy can induce a potent in vivo CTL response compared to monotherapy.

It is well known that as an essential component of vaccination, DCs are required to home to secondary lymphoid organs to prime T cell responses.^{135, 136} We detected the DCs and T cell population by flow cytometric analysis (**Figure 19D**), and data revealed that three treatment groups all promoted DC activation, with an increase of 0.5 - 1-fold compared with PBS group. Among these, combo group possessed the greatest capacity to facilitate DC activation and induced the highest level of CD8⁺ T cells within LNs. Memory T cells and activated NKs, which might play a critical role in the initiation of T-cell responses by contributing to DC maturation, demonstrated the similar trend as above, within LNs (data not shown). These results confirmed that manipulating the DCs could induce T-cell activation and proliferation.¹³⁷

Along with the increase of active DCs and T cells in LNs, immune boosting cells such as CD8⁺ T cells, memory T cells and NK cells were found to be increased in tumors, which was determined by both immunofluorescence staining and flow cytometry (**Figure 19E**). As can be seen from the tumor slices, small amounts of T cells were observed in the tumor region, but they were in the border of tumor tissue. In comparison, both vaccine and Frax NE group showed boosted T cells penetration in the TME, but the most extensive T-cell infiltration was found in

the combo group. Interestingly, memory T cells in the tumor region were not altered much in the Frax NE, while the markedly enhancement was found in the other two groups, especially in the combo group. Significantly, NKs that participated in the early immune response against the tumor and contributed to the adaptive immune response were elevated 3-8 folds after treatment, and combo group had nearly 14 % of NKs within TME. In agreement with the staining results, flow cytometry analysis confirmed our observation. It was found that IFN- γ within whole tumor also increased on the mRNA level and in leukocytes cell level (data not shown).

4.2.5 Remodeling TME and enhanced immune cell infiltration result in the superior antitumor effect of combination therapy

Collectively, we have seen Frax NE combined with BRAF peptide vaccine has triggered the best immunotherapeutic efficacy, including improved tumor inhibition, T-cell penetration, NKs activation and IFN- γ secretion. Together with results that collagen deposition and TAFs decreased remarkably in TME, antitumor effects were probably due to remodeling of the immunosuppressive TME. Therefore, immunosuppressive cells within the TME such as MDSCs, Bregs and TAMs, which were the dominating myeloid infiltrates, were examined by immunostaining of tumor sections and flow cytometry.

As shown in **Figure 20A**, the percentage of MDSCs in Frax NE and combo group were much lower than the control group, whereas more MDSCs were found in vaccine-only group (measured by immunostaining and flow cytometry). Meanwhile, the ratio of TAMs exhibiting M1 signatures (tumor-suppressing) to M2 signatures (tumor-promoting) significantly increased, which was modulated by TAFs in the TME. In addition, PD-L1 immune checkpoint on leukocytes accordingly decreased (measured by flow cytometry, data not shown).

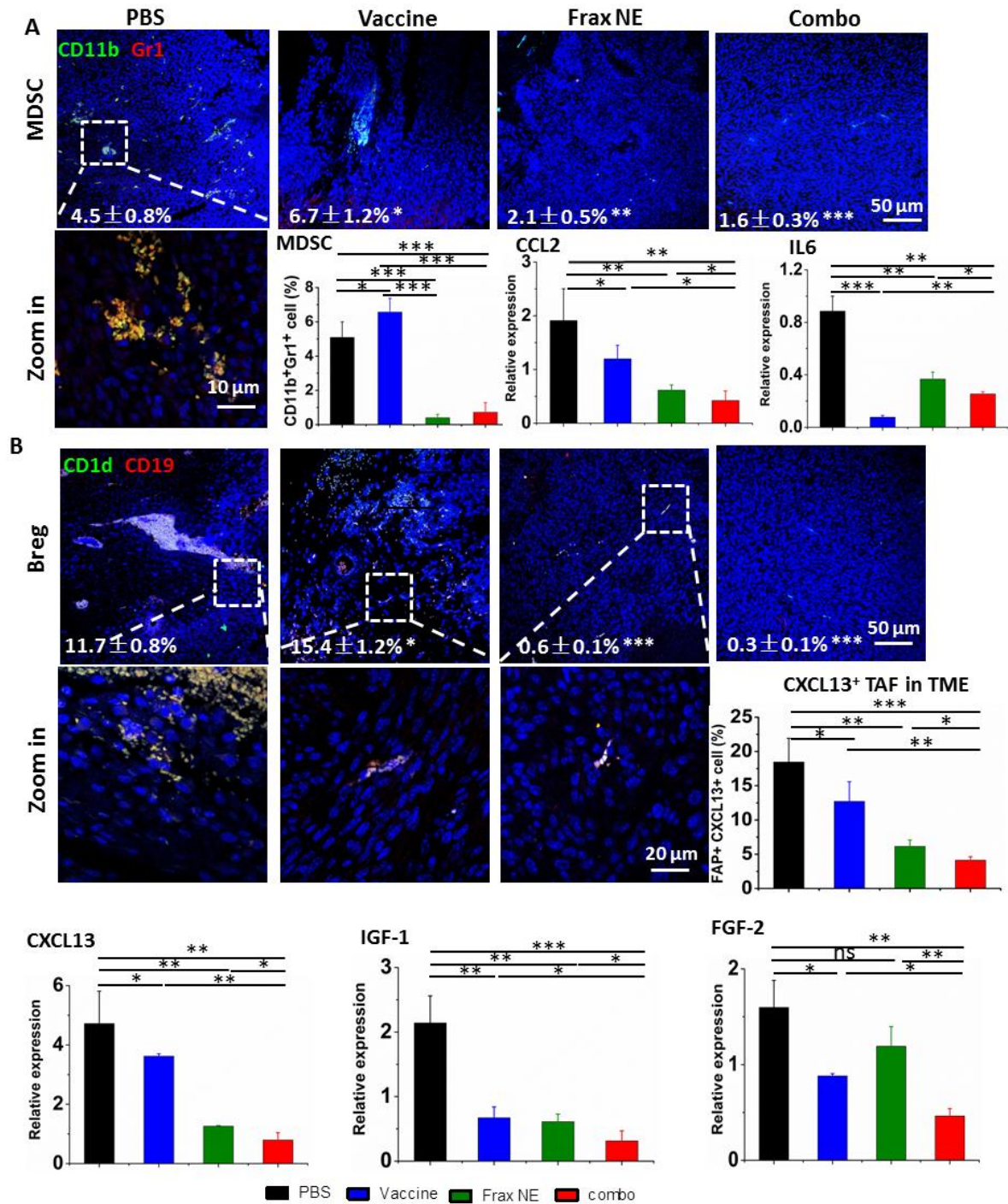


Figure 20. Changes of tumor-infiltrating immune cells and cytokines in TME. C57BL/6 mice were inoculated with 1×10^6 BPD6 cells on day 0. Vaccine was injected on day 9 and 15; Frax NE were *i.v.* administered on days 9, 11, 13, 15 and 17 at a dose of 30 mg/kg alone or combined with vaccine, respectively. Mice were sacrificed on day 23 and tumors were harvested for immunostaining evaluation, flow cytometry and quantitative RT-PCR assay to detect the MDSC (A) and Bregs (B). CCL2 and IL6 mediate MDSC recruitment. CXCL13, IGF-1 and FGF-2 facilitate B cells within TME to differentiate into Bregs. Numbers showing in white indicate the average % of each cell type in the tumor. The statistical analyses were calculated by comparison with the control group if not specifically mentioned. All data show mean \pm S.D.. (n = 6, * P < 0.05, ** P < 0.01, *** P < 0.001).

According to the reports that IL-6 and CCL2 produced by TAFs mediated MDSC recruitment and differentiation of macrophages into pro-tumor M2 phenotype,^{138, 139} the mRNA expression of IL6 and CCL2 was checked by quantitative RT-PCR (**Figure 20A**). Treatment resulted in reduction of these two Th2 cytokines which are critical for immunosuppression, thus inhibiting tumor progression. Although IL6 in Frax NE and combo group exhibited a little higher expression than vaccine, it still did not change the overall tendency compared to PBS group. It was worth mentioning that IFN- γ , the Th1 cytokine which was more effective in eliciting anti-tumor immunity, was also dramatically elevated on mRNA level, especially in combo group (RT-PCR, data not shown).

Interestingly, we noticed that a large amount of Bregs appeared in TME. Bregs, originated from normal B cells, were attracted by tumor cells and converted into Bregs by highly expressed TGF- β within TME. Bregs can induce the generation of MDSCs and promote tumor cells to form a suppressive milieu.¹⁴⁰ However, Frax NE and combo treatment significantly downregulated the Bregs, indicating that Frax NE could remodel the immunosuppressive TME in favor of therapy (**Figure 20B**). As C-X-C motif chemokine 13 (CXCL13), which is predominantly secreted by TAFs and cancer cells, played a vital role in attracting B cells into microenvironment,¹⁴¹ we detected this chemokine through flow cytometry and RT-PCR analysis. As expected, CXCL13 level within TME was much lower in Frax NE and combo group, compared with PBS group, and after vaccine treatment, it was also partially reduced.

Furthermore, Insulin-like Growth Factors (IGF-1, produced by tumor stroma-derived cells) and Fibroblast Growth Factor (FGF-2, produced by tumor cells) expression, two important growth factors involved in tumor associated B cells in crosstalk with tumor cells,¹¹⁷ were both suppressed compared with PBS group. As reported, FGF-2 plays a key part in conversing normal

B to tumor-associated B cells and could induce B cells to generate inflammatory factors and cytokines, most notably IGF-1. On the other hand, IGF-1 can form heterogeneous tumor subpopulations possessing cancer stem cell-like properties. Therefore, Frax might have an important part in disturbance of this interaction.

Meanwhile, C-X-C motif chemokine 12 (CXCL12), also known as stromal-derived factor 1 (SDF-1), is a key chemokine inhibiting T-cell infiltration.¹⁴² Inhibiting of CXCL12/CXCR4 axis has become a promising TME-modulating strategy that improves the checkpoint inhibitor efficacy.¹⁰⁶ We found CXCL12 significantly decreased on mRNA transcriptional level (RT-PCR, data not shown), thus further facilitating effective immune killing of cancer cells.

4.2.6 Safety evaluation for the different treatments

Safety evaluation is an important aspect for development of immunotherapy. The body weight of the above regimens did not cause loss throughout the tumor inhibition experiment (**Figure 21A**). Administration of all formulations showed no significant changes in ALT, AST, creatinine, or BUN levels, suggesting that there was no severe damage to renal and hepatic functions. Further analysis of blood cell levels demonstrated no signs of change compared with control healthy mice (data not shown). Moreover, the H&E staining results also indicated no morphological differences in major organs after treatment (**Figure 21B**).

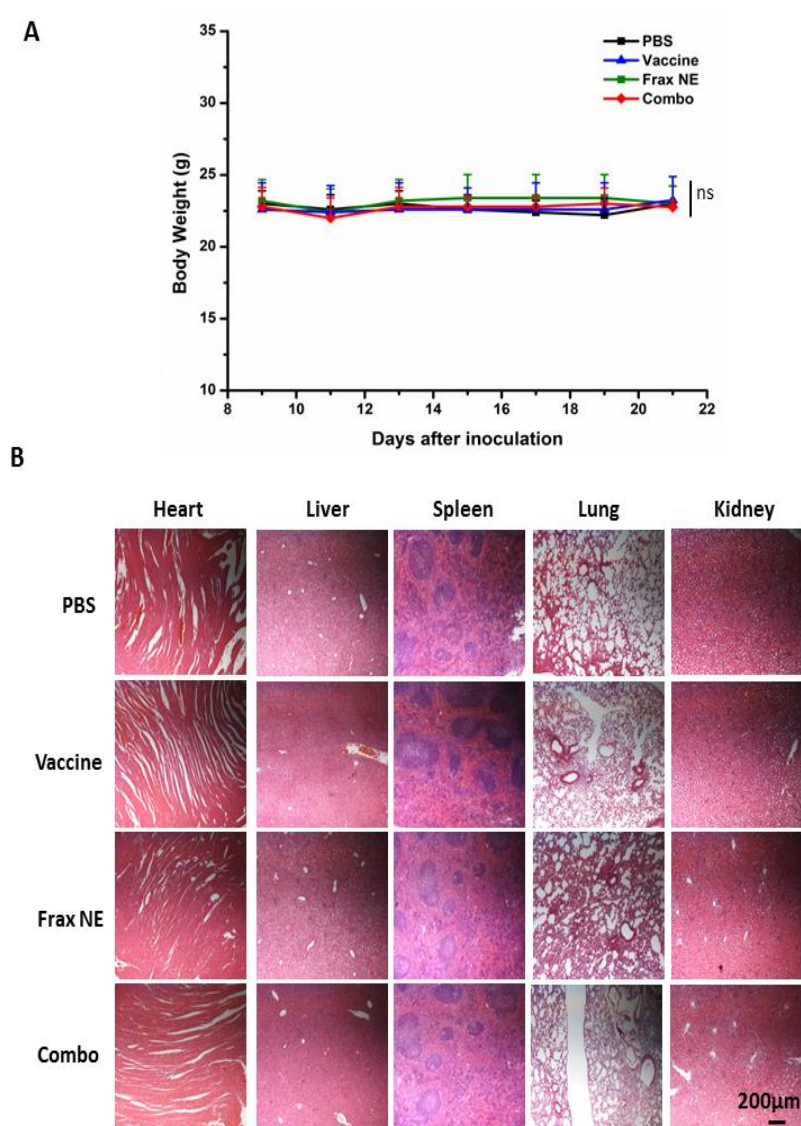


Figure 21. Safety evaluation of vaccine, Frax NE and Combo. (A) Body weight change. (B) H&E morphology evaluation of major organs after treatment. ns: $P > 0.05$.

4.3 Conclusion

TAFs are believed to be essential for synthesis and deposition of the ECM by producing various collagens as well as fibronectin and can act like a mutagen that increases the tumorigenic ability of cancer cells.¹⁴³ In addition, TAFs are a rich origin of different secreted factors such as cytokines, chemokines (e.g., IL6, CXCL12, CXCL13), and growth factors including TGF- β ,

FGF as well as VEGF, which mediate the communication between the cancer cells and TAFs.¹¹⁵ Nowadays, it has been generally accepted that TGF- β can transform normal fibroblasts into TAFs and regulate pivotal biological functions in cancers, rendering TGF- β more attractive in the field of cancer immunotherapy.^{144, 145} Taken together, a natural product Frax, which was recently reported to treat liver fibrosis by inhibiting TGF- β signaling and triggering IFN- γ signaling,¹²⁰ was considered in our investigation to remodel TME by targeting TAFs.

Notably, Frax NE herein indeed demonstrated antitumor efficacy in DM model, which is extremely formidable to cure. Unfortunately, there are only a few reports about pharmacology of Frax, most of which are focused on the anti-bacterial, anti-inflammatory and neuroprotective properties.^{121, 123, 146} We noticed that as a component of *Dictamnus dasycarpus* root bark, the anticancer activity was mentioned nebulously in some introduction of projects, books or Chinese patents. But the molecular mechanism of Frax in cancer has not been characterized. As aforementioned, Wu etc. reported that Frax could reduce the mRNA and protein expression of α -SMA by inhibiting CUGBP1, which balancing the TGF- β /IFN- γ signaling pathways, for the therapy of liver fibrosis. Accumulating evidences have indicated that TGF- β /SMAD signaling is the most crucial pathway in the pathogenesis of fibrosis. Moreover, several studies showed that paracrine secretion of TGF- β can activate stromal fibroblast and produce immune-suppressive effects to modulate the TME for the benefit of melanoma growth. Therefore, we questioned whether Frax inhibited tumor growth by such mechanism. We found that protein expression of α -SMA and CUGBP1 in NIH-3T3 cell line (which were activated with 10 ng/mL TGF- β mimicking TAFs in vitro¹⁴⁷) were both downregulated by Frax NE in a dose-dependent manner. But Frax NE only had a slight influence on BPD6 tumor cells even with a high dosage, which indicated that our formulation primarily focused on TAFs, not tumor cells (data not shown).

Furthermore, Frax NE also reduced mRNA expression of TGF- β and its downstream protein SMAD2 phosphorylation in BPD6 tumor bearing mice after treatment, accompanied by decreased protein expression of α -SMA and CUGBP1. It was accordant with the process of well-established TGF- β /SMADs signaling pathway. Briefly, TGF- β 1 binds with its receptor II (T β RII) and activates the TGF- β receptor type II-kinase, resulting in phosphorylation of SMAD2 and SMAD3, which then associate with the SMAD4 to form a heteromeric complex to regulate transcription of target gene, relating to fibrosis.¹⁴⁸ These findings suggested that Frax NE might play a crucial role of inhibiting TGF- β signaling to suppress TAFs in the TME, possibly regarding downregulation of CUGBP1. Recently, some studies revealed that CUGBP1 is overexpressed in cancer tissue and accompanying with its binding target transcripts, they will function to control cellular growth as well as homeostasis. So, we hypothesize that disruptions by Frax in this network might also interfere the development of tumor, and the in-depth mechanism is explored in our ongoing research.

Meanwhile, our results displayed that Frax NE triggered IFN- γ production and downregulated IL6 as well as TNF- α expression. IFN- γ , an immunomodulatory cytokine secreted by immune cells such as CD4⁺ Th1 cells, CD8⁺ T cells and NKs, can act on TAFs and change their promoting effects on tumor growth by inhibiting activation and proliferation of fibroblasts.¹⁴⁹ On the contrary, IL6 and TNF- α are pro-inflammatory cytokines that can induce generation of free radicals and damage DNA, potentially leading to tumor initiation and enhancement of tumor invasive properties.¹⁵⁰ Changes of these cytokines also provide us the elucidation for the antitumor efficacy of Frax NE. It is worth mentioning that Kim et al. and Wu et al. both confirmed the anti-inflammatory effect (inhibit the release of IL6 and TNF- α) of Frax

associating with NF- κ B signaling pathway, which regulates the transcription of most inflammatory factors.^{121, 123}

Many treatments for cancer, especially aiming at TAFs, continue to evolve, including TGF- β inhibitors (antisense oligonucleotides, monoclonal antibodies and small molecules) and IFN- γ .^{151, 152} Anti-TGF- β therapy aims to not only tumor cells but also the TME, thus generating systemic effects on tumorigenesis. However, long-time use of these medications can cause severe side effects (vascular problems and multi-organ inflammatory disease) and its clinical failure is mainly due to the poor pharmacokinetics and low specificity. We found that Frax NE improved its pharmacokinetics profile and did not produce any adverse reactions at the tested dosage levels in mice, although administered for a long time. Therefore, our fibroblast-targeting Frax NE could be able to interrupt the interaction between TAFs and the tumor, thus resulting in the modulation TME, and if combined with vaccine, the suppression of tumor growth, and prolongation of host survival would be enhanced.

In summary, we successfully developed Frax NE, a TAFs-targeted formulation of anti-fibrosis TCM, which could interfere the crosstalk between TAFs and tumor cells, changed cytokine profiles as well as stromal structures, and dramatically decreased MDSCs and Bregs in the TME, thereby remodeling the immunosuppressive microenvironment. After combination with vaccine, the enhanced synergistic antitumor efficacy was achieved through abrogating tumor-associated immune suppression and promoting immune cells infiltration, such as CTLs, NK cells and memory T cells. Hence, our investigations provided an immunotherapeutic strategy for the treatment of advanced DM.

4.4 Materials and Methods

4.4.1 Materials

Frax was purchased from Shanghai Tauto Biotech Co. Ltd (Shanghai, China). Lecithin from soybean was purchased from Santa Cruz Biotechnology, Inc (Dallas, Texas). DOPA, DOTAP, DSPE-PEG-2000, and DSPE-PEG-NHS were purchased from Avanti Polar Lipids (Alabaster, AL). Pluronic F68 was provided by BASF (Florham Park, NJ). DSPE-PEG-aminoethyl anisamide (DSPE-PEG-AEAA) was synthesized based on the previous reported methods.¹⁵³ Briefly, 4-methoxybenzoyl chloride and 2-bromoethylamine hydrobromide were mixed at room temperature for 6 h. Then, DSPE-PEG-NH₂ was added into above solvent and stirred in oil bath for 24 h. Finally, the reactant was washed and lyophilized for further use.

4.4.2 Cell lines and animals

Murine BRAF-mutant melanoma cell line BPD6 (BRAF^{V600E}PTEN^{-/-}, syngeneic with C57BL/6) was provided by Brent Hanks (Duke Cancer Institute, Durham, NC) and cultivated in DMEM Medium (Invitrogen, Carlsbad, CA) containing 1% Penicillin/Streptomycin (Invitrogen) and 10 % bovine calf serum at 37 °C with 5 % CO₂. Female C57BL/6 mice (6–8 weeks old) were ordered from Charles River Laboratories (Wilmington, MA). All animal handling procedures were approved by the University of North Carolina at Chapel Hill's Institutional Animal Care and Use Committee.

4.4.3 Preparation and characterization of Frax loaded AEAA-modified NE (Frax NE)

Frax NE was prepared by ultrasonic emulsification method. In brief, Frax was firstly dissolved in dimethyl sulfoxide (DMSO) (no more than 1% in total formulation) and mixed with lecithin from soybean and sesame oil. Subsequently, Pluronic F68 solution (100 mg/mL)

containing targeting ligand DSPE-PEG-AEAA was added into the drug mixture as above drop by drop under stirring. After stirring for 5 min at room temperature, the resultant mixture was ultrasonicated on ice bath for 5 min to produce NE. The particle size and morphological examination of Frax NE was determined by a Malvern ZetaSizer Nano series (Westborough, MA) and a JEOL 100CX II TEM (JEOL, Japan), respectively. The encapsulation efficiency of AEAA-modified NE is measured using HPLC (Shimadzu LC-20AT, Kyoto, Japan). In vitro stability was evaluated by determining the diameter size by DLS (Malvern, United Kingdom) at room temperature.

To investigate the targeting ability of this NE, DiI-labeled NE with or without AEAA were prepared by the same method as above without addition of Frax but with 0.5 % DiI added. After intravenous injection of DiI-labeled NE for 24 h, mice were euthanized, and tumors as well as major organs (heart, liver, spleen, lung and kidney) were collected. The bio-distribution was visualized and quantitatively measured with IVIS[®] Kinetics Optical System (Perkin Elmer, CA). The excitation wavelength was set at 520 nm, while the emission wavelength was 570 nm.

Additionally, intra-tumoral cellular uptake by cells of interest (tumor cells and TAFs) was evaluated by flow cytometry. Briefly, tumor tissues were dissociated with 1 mg/mL collagenase (Invitrogen), and 200 µg/mL DNAase (Invitrogen) in DMED/2 % FBS for 40 min to generate a single-cell suspension. Tumor cells were stained with PE-conjugated MART1 antibody (Melan-A antibody, sc-20032 PE, Santa Cruz Biotechnology), and TAFs were stained with FAP antibody (anti-Fibroblast activation protein antibody, abT28244, Abcam). The cells were then subjected to flow cytometric analysis, and the ratios of DiI-loaded NE distributed in different cell populations were calculated.

Furthermore, LC/MS instrument (Shimadzu LCMS-2020, Kyoto, Japan) was also utilized to quantitatively analyze the accumulation of Frax NE in tumor site at predetermined times (1, 3, 8, 12, 24 h) and study the pharmacokinetics profile. Separation of analytes was carried out on Thermo Scientific C18 column (100 mm × 4.6 mm, 2.6 μm) (Thermo Fisher Scientific, Waltham, MA USA), the flow rate was set to 0.2 mL/min, and column temperature was 35 °C.

4.4.4 Tumor growth inhibition

The stroma-rich desmoplastic melanoma model was established as previously reported. Mice were inoculated subcutaneously with 1×10^6 BPD6 cells on their lower flank. When the tumor volume reached about 200-300 mm³, mice were separated into the following groups (n = 6): Untreated group (PBS), Frax oral suspension group (Frax oral, 120 mg/kg), and Frax NE group (Frax NE, 30 mg/kg). As the control, Frax oral was prepared by suspending Frax directly in a 0.5 % of carboxymethylcellulose (CMC) solution with grinding. Frax was administrated *p.o.* or *i.v.* every other day for 5 times, and the tumor volumes were monitored by caliper every 2 days and calculated as $(a \times b^2)/2$, where “a” represents the larger diameter and “b” represents the smaller one. At the endpoint of tumor inhibition study, we sacrificed the mice, and tumors were harvested and weighed. The inhibition ratio (IR) was defined as $IR (\%) = ((W_c - W_t)/W_c) \times 100$, where W_c and W_t are the average tumor weights for the control group and each treatment group, respectively.

To evaluate the combination therapy with BRAF peptide vaccine, BPD6 tumor bearing mice (tumor volume reached about 200-300 mm³) were randomly divided into four groups (n = 8 - 10): Untreated group (PBS), Frax NE group (Frax NE, 30 mg/kg), BRAF peptide vaccine group (Vaccine, (BRAF peptide + CpG) 100 μg/mice) and Frax NE combined with BRAF peptide

vaccine group (Combo). BRAF peptide vaccine was prepared as described previously. For the single vaccine and combo therapy groups, vaccination was administrated on day 9 and boosted on day 15 subcutaneously. Intravenous injections of Frax NE were also given every 2 days for a total of 5 doses. Tumor volume was measured as above, and mice were sacrificed before tumor volume reached 2000 mm³ under animal safety protocol.

Long-term survival was also monitored on BPD6 bearing mice with different treatments (n = 8, in each treatment group). Kaplan-Meier curves and Median Survival were quantified and calculated using GraphPad.

4.4.5 Immunofluorescence staining and Masson trichrome staining

Tissue section staining was executed following the procedure of deparaffinization, antigen retrieval, permeabilization, and 1 % BSA blocking. Primary antibodies with or without fluorophores conjugation were incubated at 4 C° overnight. The samples used non-conjugated primary antibodies was treated with secondary antibodies for 1 h at room temperature on the next day. Nuclei were counterstained with DAPI (Vector Laboratories Inc., Burlingame, CA). Images were acquired using fluorescence microscopy (Nikon, Tokyo, Japan) and five fields were selected at random for quantitative analysis by Image J software.

The Masson Trichrome assay was performed to detect collagen among tumor tissue. Tumor slides were stained using a Masson Trichrome Kit by the UNC Tissue Procurement Core.

4.4.6 Flow cytometry analysis

Immune cell populations in tumor and LNs were detected by flow cytometry. In brief, tumors were treated with collagenase A and DNAase for 40 min at 37 C°. Then, single cells in

treated tumors and LNs were collected in FACs buffer. For intracellular staining, the cells were treated with penetration buffer (BD, Franklin Lakes, NJ) as the manufacture's instruction suggested. Different kinds of immune lymphocytes were stained with different kinds of fluorescein-conjugated antibodies.

4.4.7 Western blot analysis

Western blot was performed on proteins extracted from the tumor tissues after treatment or cells in the lysis buffer. The extracted proteins were separated by 4 – 12 % sodium dodecyl sulfate polyacrylamide gel electrophoresis (SDS-PAGE electrophoresis) (Invitrogen) and transferred onto polyvinylidene difluoride (PVDF) membranes (Bio-Rad, Hercules, California). The membranes were incubated with the indicated antibodies at 4 C° overnight. Primary antibodies were directed against P-SMAD2 (Cell signaling, 3108S), α -SMA (Abcam, ab124964), CUGBP1 (Abcam, ab129115) and GAPDH (Santa Cruz Biotechnology, sc-25778). Membranes were then incubated with a horseradish peroxidase coupled secondary antibody, and signals were observed using the Pierce ECL Western Blotting Substrate (Thermo, Rockford, IL). The relative expression level of protein was quantified with Image J software.

4.4.8 Quantitative real-time PCR assay

Whole RNA was obtained from tumor tissues using an RNeasy kit (Qiagen, Valencia, CA), and cDNA was reverse-transcribed using the SuperScript First-Strand Synthesis System for RT-PCR (Invitrogen, Grand Island, NY). 100 ng of cDNA was amplified with Taqman Universal Probes Supermix System (Bio-rad, Hercules, CA) and mouse-specific primers. Primers for mouse TGF- β , CUGBP1, CCL2, IL6, CXCL13, IGF-1, FGF-2 and CXCL12 were purchased from ThermoFisher Scientific (Waltham, MA USA). The GAPDH RNA expression was used as

inner control. Reactions were conducted using a 7500 Real-Time PCR System, and the data were analyzed with the 7500 Software.

4.4.9 TUNEL assay

Slides were deparaffinized and stained using a TUNEL assay kit (Pierce, Madison, WI) according to the manufacturer's instruction. Cell nuclei that were stained with FITC (green) were defined as TUNEL-positive nuclei. The images were acquired using fluorescence microscopy (Nikon, Tokyo, Japan) and quantitatively analyzed on Image J.

4.4.10 Safety evaluation

Body weights of mice were measured every other day starting from the treatment. At the endpoint, the mice were sacrificed, blood was collected, and plasma was obtained by centrifugation at 4000 rpm for 5 min. BUN, creatinine, AST and ALT levels were detected as indicators of renal and hepatic function. Whole blood was also gathered for the measurement of myelosuppression by counting the Red blood cells (RBC), white blood cell (WBC), platelets (PLT), hemoglobin (HGB) and hematocrits (HCT). Major organs, such as heart, liver, spleen, lung and kidney were fixed and used for H&E staining by UNC histology facility to evaluate the organ-specific toxicity.

4.4.11 Statistical analysis

Results were expressed as mean \pm S.D., and statistically evaluated by Student's test or one-way analysis of variance (ANOVA). P values smaller than 0.05 were significant.

CHAPTER 5

NANO-MEDIATED WNT5A TRAPPING ENHANCES IMMUNOTHERAPY³

5.1 Introduction

Despite considerable advancement in the study of cancer biology and drug discovery, it is still a major undertaking to cure most advanced melanoma patients. Even with conventional anticancer chemotherapy, the first line response rate remains low.^{6, 154} Based on clinical evidence of chemotherapy, the definition of immunogenic cell death (ICD) was derived, revealing how tumor-specific immune responses shape the therapeutic outcome.¹⁵⁵ ICD refers to the apoptosis of tumor cell that does release tumor associated antigens, and sequentially stimulate a specific immune response against such antigens. The ICD, in turn, will improve the immunogenic potential as a form of DC vaccines. Therapeutic vaccination can be clinically successful as a monotherapy; however, in DM the immunosuppressive TME placed a major hurdle for treatment efficacy.^{83, 99} Herein, ICD-mediated vaccination should be combined with a co-treatment that overcomes immune evasion to achieve desired therapeutic efficacy.

It has been reported that in advanced melanoma patients, expression of the soluble Wnt family member 5A (Wnt5a) ligand induces a paracrine signaling pathway that drives local DC

³ This chapter previously appeared as an article in *ACS Nano*. The original is as follows: Q Liu, H Zhu, K Tiruthani, L Shen, F Chen, K Gao, X Zhang, L Hou, D Wang, R Liu, L Huang. "Nanoparticle-Mediated Trapping of Wnt Family Member 5A in Tumor Microenvironments Enhances Immunotherapy for B-Raf Proto-Oncogene-Mutant Melanoma." *ACS nano* 2018 Jan 31.

tolerization and fibrotic TME.¹⁵⁶ Interestingly, melanoma-derived Wnt5a promotes tumor growth and metastasis, which correlates with the inhibition of antitumor adaptive T-cell responses. We hypothesize that compared with wild-type tumor, BRAF-mutant melanoma correlates with increased Wnt5a release. Furthermore, Wnt5a represents a critical mediator of tumor immune evasion and immunotherapy resistance, and the inhibition of this soluble mediator will augment the efficacy of vaccination.

In this work, we designed and generated a fusion protein that specifically and potently binds to and disrupts the biological functions of Wnt5a. For local TME ‘trapping’, plasmid containing the Wnt5a trap cDNA was formulated and specifically delivered to the DM murine model in a syngeneic host by using a cationic nanocarrier, the lipid-protamine-DNA (LPD) NPs. We found that the administration of the trap along with immunogenic cell death-mediated vaccination generated robust innate and adaptive immune responses, resulting in significant tumor regression in the murine model. Moreover, this combination therapy delayed tumor metastasis and improved long-term survival, providing a strong rationale for pursuing this strategy in clinical studies.

5.2 Results and discussion

5.2.1 ICD induced by low dose DOX

For effective cytotoxic T cell killing, we introduced low dose DOX to induce immunogenic cell death within the tumor, thus aiding in activating immune microenvironment. DOX is a small molecule drug that has been used as a first line chemotherapy for the treatment of melanoma. It has been reported that low dose of Dox induced ICD in various cancer cell lines

including wild-type melanoma (B16F10).¹⁵⁷ To determine the best dosing strategy of DOX-induced ICD, MTT assay was performed (**Figure 22A**). Followed by calreticulin (CRT) exposure and high mobility group box 1 (HMGB1) release as standard markers for drug-induced (0.2 mM DOX) tumor cell immunogenicity, ICD was detected on BPD6 cell line *in vitro* (**Figure 22B**).

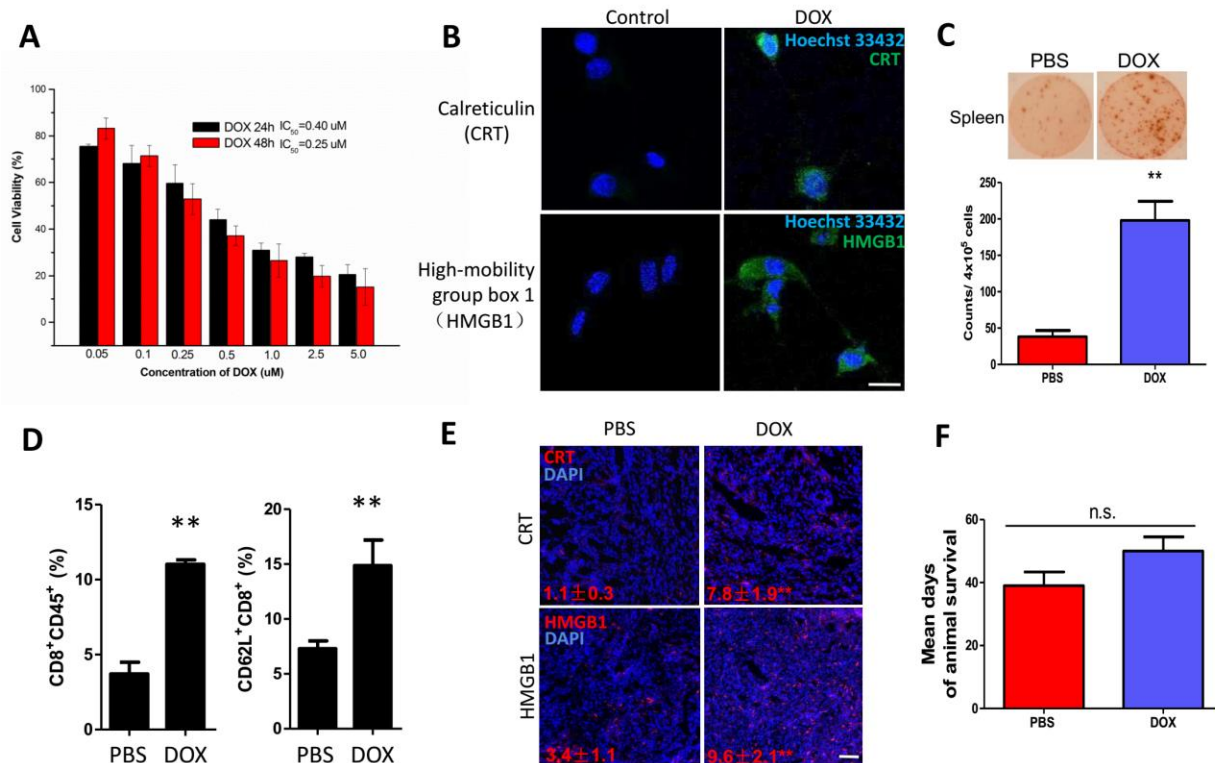


Figure 22. ICD induced by low dose DOX. (A) MTT result on BPD6 cell line *in vitro*, n = 5. (B) Fluorescence imaging detecting ICD markers: CRT and HMGB1 on BPD6 cells treated with low dose of DOX. Cell nuclei were stained with Hoechst 33432. Scale bar indicates 10 μm. (C) ELISpot test depicting IFN-γ secreted by re-stimulated splenocytes of mice treated with or without low dose DOX, n = 3. (D) Flow cytometry analysis shows ICD induced increase in: intra-tumoral inflammatory cells (CD8⁺CD45⁺) and activation of CD8⁺ T cell within TME, n = 3. (E) HMGB1 and CRT immunofluorescence staining in tumors slide sections, treated with or without low dose of DOX, n = 3. Scale bar indicates 300 μm. (F) Mean days of mouse survival in PBS and low dose DOX treated groups, n = 8-10. Data present mean ± SE. n.s.: p > 0.05, **: p < 0.01.

Low dose DOX efficiently induced IFN-γ production under antigen re-stimulation *in vitro*, analyzed by ELISpot assay, indicating strong systemic immune response against the tumor-

specific antigen mimicking *in vivo* settings (**Figure 22C**). Thus, low dose DOX (0.544 mg/kg) was given *i.p.* to mice, at an early point of desmoplastic tumor growth, as to induce ICD and the release of tumor antigens for effective DC presentation and cytotoxic T cell recruitment. After DOX treatment, we found induced intra-tumoral inflammatory cells and activated CD8⁺ T cell greatly increased within whole tumor (**Figure 22D**). DOX therapy significantly increased HMGB1 and CRT *in vivo*, as stained in tumor sections (**Figure 22E**), which further confirmed ICD production *in vivo*, and demonstrated an effective way of boosting systemic immunity. Although the DOX treatment showed modest tumor growth inhibition, we found no significant prolongation of host survival, necessitating further investigation into remodeling the immunosuppressive TME.

5.2.2 Wnt5a is a key molecule controlling the immunosuppressive desmoplastic TME

Wnt5a is a member of the Wnt family that plays pivotal roles in activating several noncanonical Wnt signaling pathways. In normal tissues, such pathways mainly regulate major developmental processes, including stem cell self-renewal, proliferation, differentiation, and polarity.¹⁵⁸ It has been reported that homozygous Wnt5a-ko-mice died postnatally, associated with significant lower dermal lymphatics and multiple defects including skeletal and internal organs.¹⁵⁹ Wnt5a-deficient mice resulted in reduction of Wnt/ β -catenin signaling, which would impair osteoblast differentiation and enhance adipocyte differentiation.^{156, 160} Moreover, the abnormal activation or inhibition of Wnt5a signaling has been demonstrated in controlling tumor progression, more specifically, in an immunosuppressive manner.¹⁵⁶ In melanoma, previous studies have demonstrated that Wnt5a promotes differentiation of monocytes into tolerogenic DCs, thus hindering antigen presentation and effective T-cell mediated killing. Furthermore, tolerogenic DCs mediate Treg cell differentiation in the presence of TGF- β . More recently,

Wnt/TGF- β signaling pathway has been further investigated, in the present of upregulating Yes-Associated Protein 1 (YAP)/transcriptional coactivator with PDZ-binding motif (TAZ) signaling, thus directly linked to physiological morphology of fibrosis (**Figure 23A**).

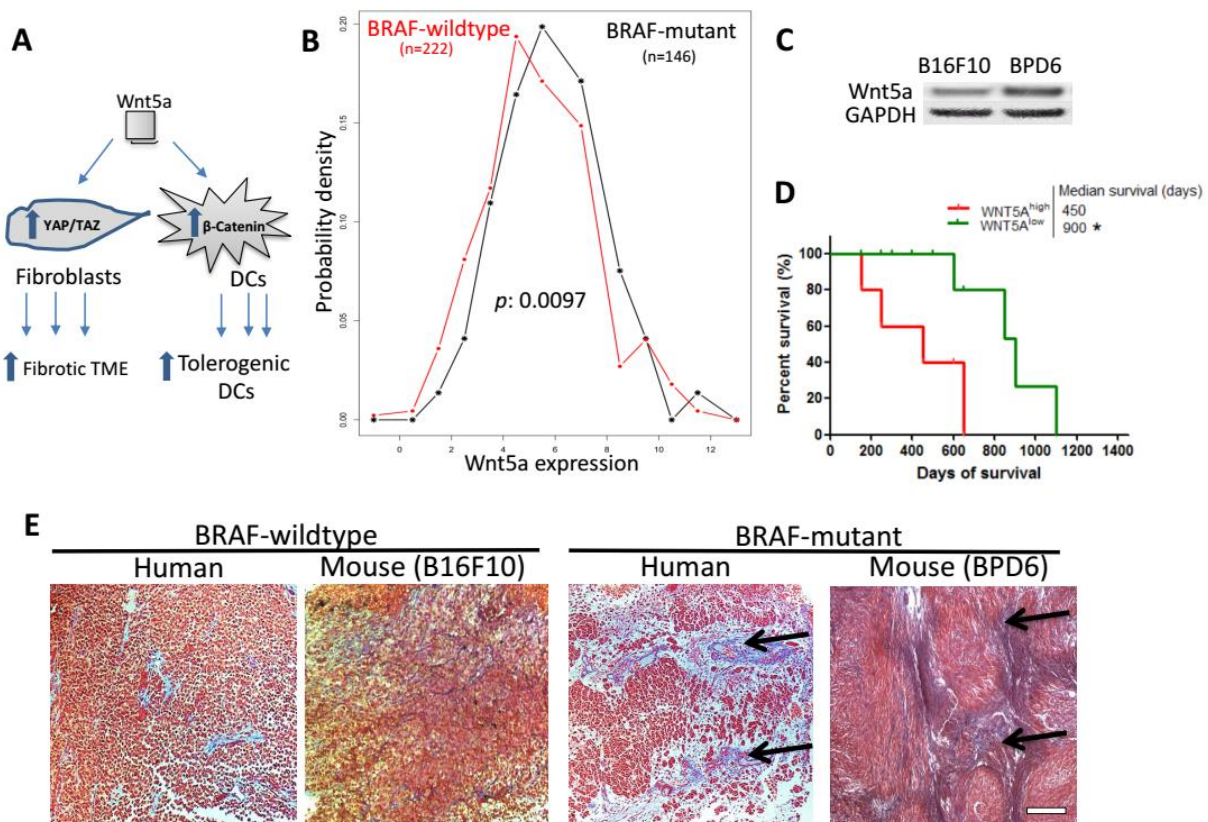


Figure 23. Wnt5a is a key molecule controlling the immunosuppressive desmoplastic TME. (A) Figure legend depicting Wnt5a functions on both DCs and Fibroblasts within TME. Wnt5a is highly expressed among BRAF-mutant melanoma, compared to BRAF-wild-type, in both clinical (panel B, TCGA database, $n = 368$) and murine samples (panel C, Western blot, $n = 3$). (D) High level of Wnt5a correlates with poorer patient overall survival. $n = 29$. (E) Masson's trichrome staining illustrating BRAF-mutant melanoma with desmoplastic collagen-rich TME (black arrows), compared to wild-type in both human and mouse specimens. Scale bar indicates 300 μ m. $n = 3$. *: $p < 0.05$, **: $p < 0.01$.

We first confirmed that high expression level of Wnt5a was present in melanoma tissue of both patients and murine models (**Figure 23B** and **C**), with significantly difference ($p = 0.0097$ from TCGA analysis) between BRAF-mutant and wild-type tumors. Western blot analysis further confirmed this difference in murine melanoma cell lines, *i.e.* B16F10 (BRAF-wild type):

BPD6 (BRAF-mutant). In melanoma patients, excessive Wnt/ β -catenin level has been associated with poorer response to immune checkpoint therapies.¹⁶¹ Our analysis based on the TCGA database further confirmed a strong correlation ($p = 0.005$) between higher Wnt5a expression with shorter patient overall survival (**Figure 23D**).

In this work, we used the BPD6 model that highly resembles aggressive clinical melanoma for therapeutic studies.¹⁶² Compared to the wildtype, BRAF-mutant melanoma demonstrated a desmoplastic collagen-rich TME in both murine and human specimens (**Figure 23E**). Since Wnt5a plays an important role in mediating immunosuppressive desmoplastic morphology, we hypothesized that effective local and transient inhibition of Wnt5a would remodel the suppressive TME and facilitate immunotherapy without systemic disruption of the multifaceted roles of Wnt5a in normal organ functions.

5.2.3 Local distribution and transient expression of Wnt5a trap

To efficiently compete with endogenous Wnt5a receptors and ‘trap’ Wnt5a locally within TME, we developed a trimeric trap that binds to mouse Wnt5a with a K_d in the range of medium nano-molars (**Figure 24B**). Wnt proteins are secreted glycoproteins that bind to the N-terminal extracellular cysteine-rich domain (CRD) of the Frizzled (FZD) receptor family. Quantitative measurement of the interactions between different isoforms of Wnt ligand and FZD receptor is challenging due to the lipid modification of Wnt that makes expression, purification and crystallization of active Wnt ligands difficult. The problem is further complicated by the significant promiscuity where a certain FZD receptor binds to multiple Wnt ligands.

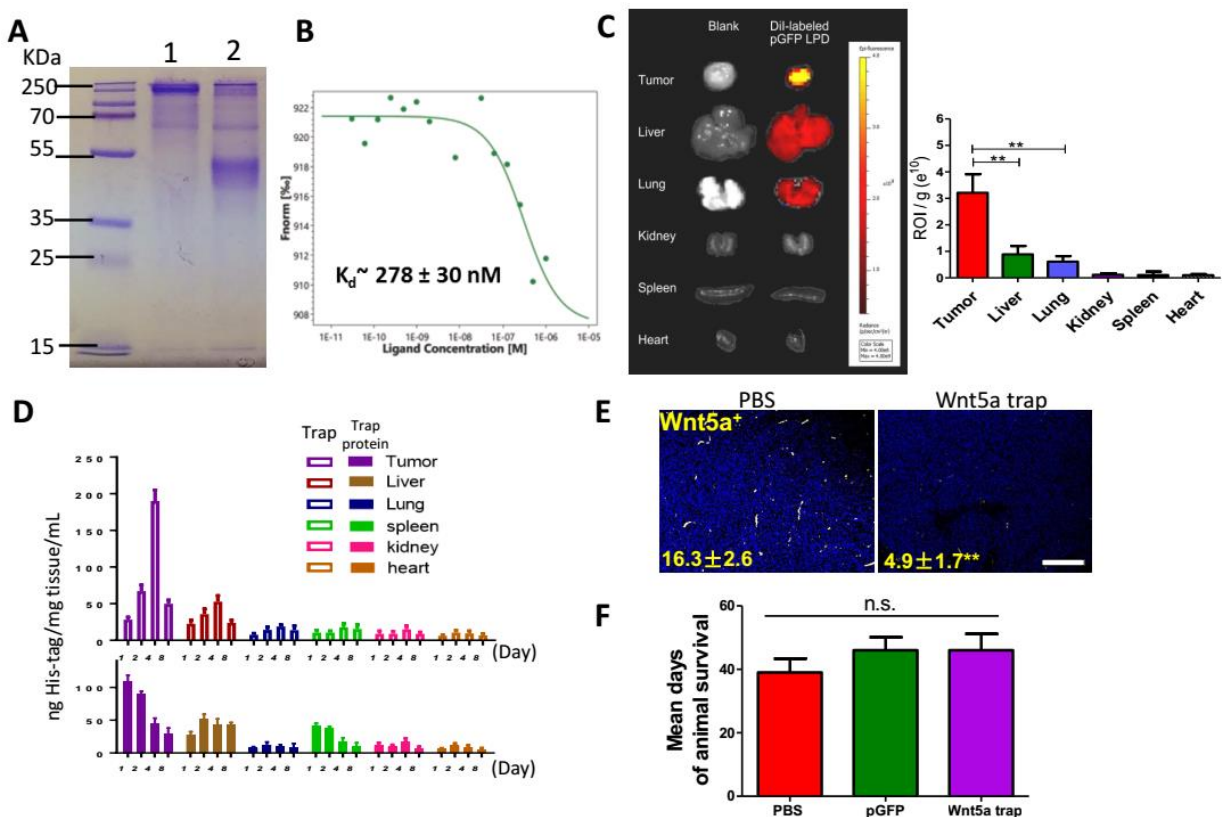


Figure 24. Local distribution and expression of Wnt5a trap. (A and B) Development and characterization of Wnt5a Trap protein. (A) SDS-PAGE of the Wnt5a trap in the presence (lane 2) and absence (lane 1) of reducing agent DTT. (B) The binding affinity between Wnt5a and FZD7-based trap measured by MST. (C) Bio-distribution of DiI-loaded LPD NPs among tumor and organs. $n = 3$. (D) Expressions of His-tagged Wnt5a trap in different organs were quantified by ELISA and compared with the injection of free trap protein. $n = 5$. (E) Fluorescent imaging depicting effective local Wnt5a trapping in tumor slide sections. Numbers indicate Wnt5a expression (yellow). Scale bar indicates 300 μ m. (F) Mean days of mouse survival. $n = 8-10$. Data present mean \pm SE. n.s.: $p > 0.05$, **: $p < 0.01$.

We chose the CRD of FZD7 to develop a Wnt5a trap for the following considerations. First, FZD7 is one of the highest expressing FZD receptors in DCs, and tolerogenic DCs are the major immune cells we want to target in the work. Second, in the process of tumor progression, FZD7 is found most commonly upregulated among the whole FZD family. This finding is confirmed in various types of cancer, include colorectal cancer, triple negative breast cancer, etc. Third, FZD7 plays a vital role in the interaction between cancer stem cell and tumorigenesis. Therefore, an affinity molecule based on the CRD of FZD7 has the potential to serve as a decoy

to trap Wnt5a while at the same time competitively reduce the numerous biological functions of this highly expressing FZD receptor. Since the oligomeric status of Wnt ligands Wnt5a was implicated in the literature, we designed a trimeric Wnt5a trap with multi-valency and avidity feature by genetically fusing the CRD of FZD7 with a robust trimerization domain from cartilage matrix protein (CMP-1) that is very abundant in mouse and human cartilage.¹⁰⁶ The strong hydrophobic and ionic interactions among this trimerization domain result in a parallel, disulfide-linked, and rod-shaped trimeric structure with high stability. Since the trimeric trap is formed through self-assembly of three identical monomers, it only requires a relatively small gene to encode the monomeric trap, making the gene to be delivered much shorter and easier to encapsulate.

To construct such an original Wnt5a trap, the optimized coding sequence for the monomeric trap was cloned into the expression vector pcDNA3.1, driven by a CMV promoter. To facilitate trap secretion after expression, a strong signaling peptide from human serum albumin preproprotein was incorporated at the N-terminus, whereas an FLAG/His (6×) tag was also brought in at the C-terminus, thus to facilitate protein purification and in vivo expression analysis. The recombinant Wnt5a trap was expressed in and purified from 293 T cells. The theoretic MW of the monomeric trap should be around 26 kDa but significant glycosylation is expected, as shown in **Figure 24A** with higher MW. We characterized the binding strength and specificity of the FZD7 CRD and Wnt5a. As shown in **Figure 24B**, the resulting FZD7-based trap should bind to Wnt5a with a K_d in the range of medium nano-molars.

The LPD NP formulation, which preferentially delivers macromolecules including plasmid DNA for tumor immunotherapy, has been well established in the Huang lab.¹⁰⁸ To prepare LPD, plasmid DNA encoding for Wnt5a trap protein was condensed with cationic protamine to form a

slightly anionic complex core. The core was further coated with the preformulated cationic liposomes (DOTAP, Cholesterol and DSPE-PEG), and modified with tumor targeting ligand DSPE-PEG-AEAA. The size (~100 nm), the spherical shape, as well as homogenous distribution of LPD NPs were confirmed by TEM images consistent with DLS size distribution (data not shown). Through IVIS imaging, DiI-loaded NPs were found mainly distributed in the tumor 24 h after *i.v.* injection into mice (**Figure 24C**). Although liver may take up NPs, it was significantly lower than tumor ($p < 0.01$). Within the liver, NPs of size ~100 nm mainly internalized by Kupffer cells under phagocytosis, but PEGylated NPs are taken up less efficiently than more charged NPs.¹⁶³ Kupffer cells are non-parenchymal cells within the liver that are very difficult to transfect, even with Lipofectin® (superior to other lipids for transfection), the transfection efficiency remains low.¹⁶⁴ The Wnt5a trap expression within other major organs was minor and transient. This is presumably due to the efficient targeting effect of AEAA against sigma receptor 1 that is highly expressed on the surface of melanoma cells.

By introducing His-tag into the C-terminus of plasmid map, the expression of the Wnt5a trap against Wnt5a was assessed through ELISA, and further compared with the injection of purified trap protein (**Figure 24D**). His-tag ELISA showed the expression of trap was transient within one week. Consistent with IVIS imaging, tumor is the major trap producing organ with the help of AEAA targeted local NP delivery. Compared to direct injection of trap protein, the half-life of plasmid delivery was significantly prolonged. As illustrated in **Figure 24D**, free protein trap was cleared rapidly, with significantly lower concentration among all organs at each timepoint being monitored. Within the tumor, the AUC value for trap expression using NP delivery of plasmid DNA was 2.3-fold higher than that of the free protein trap. Presumably, the trap binding with Wnt5a prevents the Wnt5a binding with anti-Wnt5a antibody, thus the local

concentration of Wnt5a measured in the tumor was significantly reduced (**Figure 24E**), indicating that the locally expressed and secreted Wnt5a trap neutralized Wnt5a in situ. Nevertheless, we found no significant elongation in the host survival, compared to the PBS control (**Figure 24F**), suggesting that remodeling of TME by trapping Wnt5a alone was insufficient for effective tumor therapy.

5.2.4 Combination of DOX-induced ICD and Wnt5a trapping significantly inhibited tumor progression

Effective tumor immunotherapy is often achieved by combination with the stimulation of the immune system, *i.e.* with a vaccine, or by remodeling the TME. As demonstrated above, neither ICD induced by low dose DOX (a form of vaccine) nor Wnt5a trap (a TME modulator) could produce significant host survival prolongation in this aggressive melanoma model. Therefore, we explored whether a combination of both therapies could bring in a synergistic therapeutic effect.

Indeed, with the help of low dose DOX, the local Wnt5a trapping strategy greatly inhibited tumor growth (**Figure 25A**). Significantly, the median survival of the mice treated with ICD/trap combo therapy was prolonged from approximately 45 days to 65 days (**Figure 25B**). To address the action mechanism, we performed treatment by pre-depletion of CD4⁺ or CD8⁺ T cells. As shown in **Figure 25C**, the therapeutic effect was partially abolished by the pre-treatment with either anti-CD8 or anti-CD4 antibody, whereas it was not affected when an isotype matched IgG control was used in the pre-treatment. TUNEL assay demonstrated a large increase of apoptotic cells within TME, indicating local tumor cell death (**Figure 25D**). There was also a significant ($p < 0.01$) decrease in collagen content (by Masson Trichrome staining) of the tumor with the

combination therapy (**Figure 25E**). In either case, DOX treatment alone or Wnt5a trap alone had brought only a partial effect.

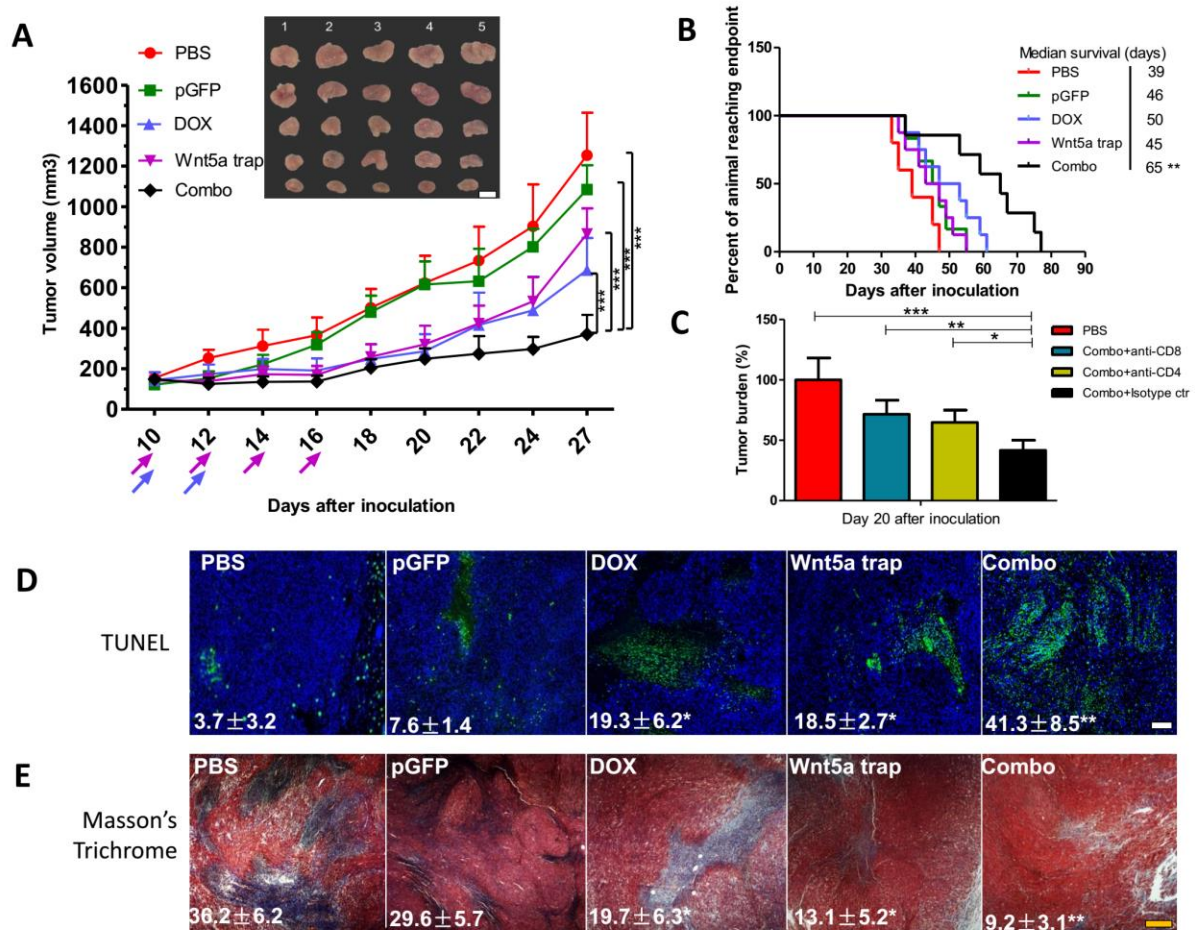


Figure 25. Combination therapy significantly inhibited tumor progression. (A) Tumor inhibition of combination therapy, compared with untreated or monotherapy groups. $n = 8$. (B) Long term survival monitored over two months. $n = 8-10$. (C) Tumor bearing mice were pretreated with 3 daily injections of anti-CD8 and/or anti-CD4 antibody (300 μ g/mice) to deplete the CD8⁺ and/or CD4⁺ T cells in vivo. Isotype IgG was used as control. The efficacy of combination therapy with or without different T cell depletion was compared by monitoring tumor burden after treatment cycles. $n = 5$. (D) TUNEL assay depicting apoptotic region within tumor slide sections. $n = 3$. (E) Masson's trichrome staining depicting collagen distribution within TME. $n = 3$. Scale bars indicate 300 μ m. *: $p < 0.05$, **: $p < 0.01$, ***: $p < 0.001$.

5.2.5 Treatment-induced remodeling of the TME

To investigate whether the immunosuppressive microenvironment of the tumor was indeed remodeled after the combination therapy, we analyzed the immune cells in the tumor by flow

cytometry. As illustrated in **Figure 26A**, the efficient tumor inhibition could be attributed to the remodeling of the immunosuppression of TME,¹⁶⁵ including significant increased CD103⁺ DCs (required for antigen transportation, T cell priming, as well as induction of intact anti-tumor immunity¹⁶⁶), increased DC maturation (CD8⁺CD11c⁺), enhanced effector T cells infiltration (CD45⁺CD8⁺) and activation (CD8⁺CD62L^{low}), and the reduction in the suppressive immune cells such as MDSCs, M2 macrophages and PD-L1⁺ cells (CD274⁺). Meanwhile, immune cytokines such as IL-12 α , TNF- α and IFN- γ were dramatically increased at detected transcriptional level (**Figure 26C**), indicating a Th-2 to Th-1 phenotype switch to an immunostimulatory TME. The switch would greatly facilitate tumor antigen presentation (with a specific increase in IL-12 α) and result in an intensified cytotoxic T cell mediated tumor-specific killing, as demonstrated by extensive IFN- γ production in ELISpot assay (**Figure 26B**). IFN- γ is produced mainly by CTLs mediating adaptive immune responses. The ELISpot assay used in our study detected and enumerated antigen-reactive T cells that secrete IFN- γ in vitro upon re-stimulation by tumor-specific antigen, mimicking systemic immune response *in vivo*.

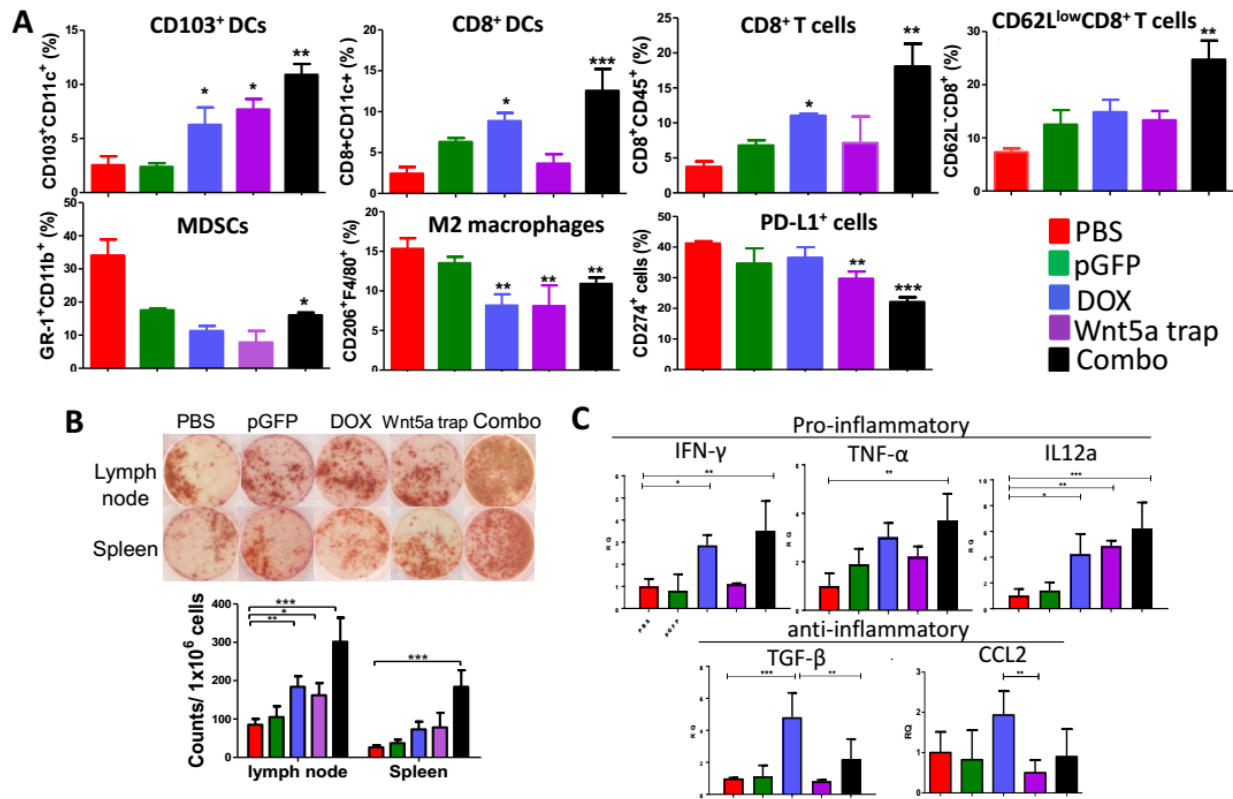


Figure 26. Remodeling of TME. (A) Flow cytometry analysis of immune functioning cells within TME. $n = 3$. (B) ELISpot assay depicting IFN- γ production under different treatments. $n = 3$. (C) RT-PCR analysis of both pro-inflammatory and anti-inflammatory cytokines within TME. $n = 6$. *: $p < 0.05$, **: $p < 0.01$, ***: $p < 0.001$.

5.2.6 Combination therapy demonstrated long-lasting suppressed tumor metastasis

Over two months of survival study, we kept monitoring tumor metastasis in major organs. Consistent with the clinical observation, we found that liver and lung were the major metastatic sites in the untreated murine model.¹⁶⁷ The observed long-term efficacy could be due to many factors. For one, innate immunity alone would be sufficient, particularly natural killer (NK) cells, has been reported to prevent metastasis in nude mice which are immune deficient. Secondly, the significant tumor inhibition would restrict cancer cell spreading, possibly via suppressing the EMT by down-regulating pro-metastatic markers, such as CCL7/CCR3 or CCL21/CCR7 cross-talks.^{168, 169}

Nevertheless, at late stage of tumor inhibition, the recruitment of both CD8⁺ and CD4⁺ T lymphocytes for an efficient systemic immune response would help in tumor restriction and reducing metastasis. CD8 T cells are critical in direct anti-tumoral activities. In our study, effective DC activation (CD11c⁺MHCII⁺) was observed, CD8⁺ T cells and CD69⁺CD8⁺ T cells were also found increased within LNs (**Figure 27C**), as well as within TME (**Figure 27A**, CD8⁺ and CD62L^{low}CD8⁺ T cells). Memory CD8 T cells (CD8⁺CD44⁺) were also found significantly increased within TME (**Figure 27D**). For CD4 T cells, we found a significant increase in memory CD4 T cells (CD4⁺CD62L⁺) within TME (**Figure 27A**) and LNs (**B**). Furthermore, CD4⁺ T cells were sorted (at the endpoint of tumor inhibition study) from spleens of mice subjected to either Combo therapy or PBS as control. Among which, antigen-specific CD4 cells undergo in vitro proliferation when re-stimulated with tumor cell lysate containing tumor antigens (**Figure 27E**). The division of these antigen-reactive cells (Q1 population) was significantly increased, indicating a generation of memory CD4 immunity in vitro mimicking *in vivo* settings.

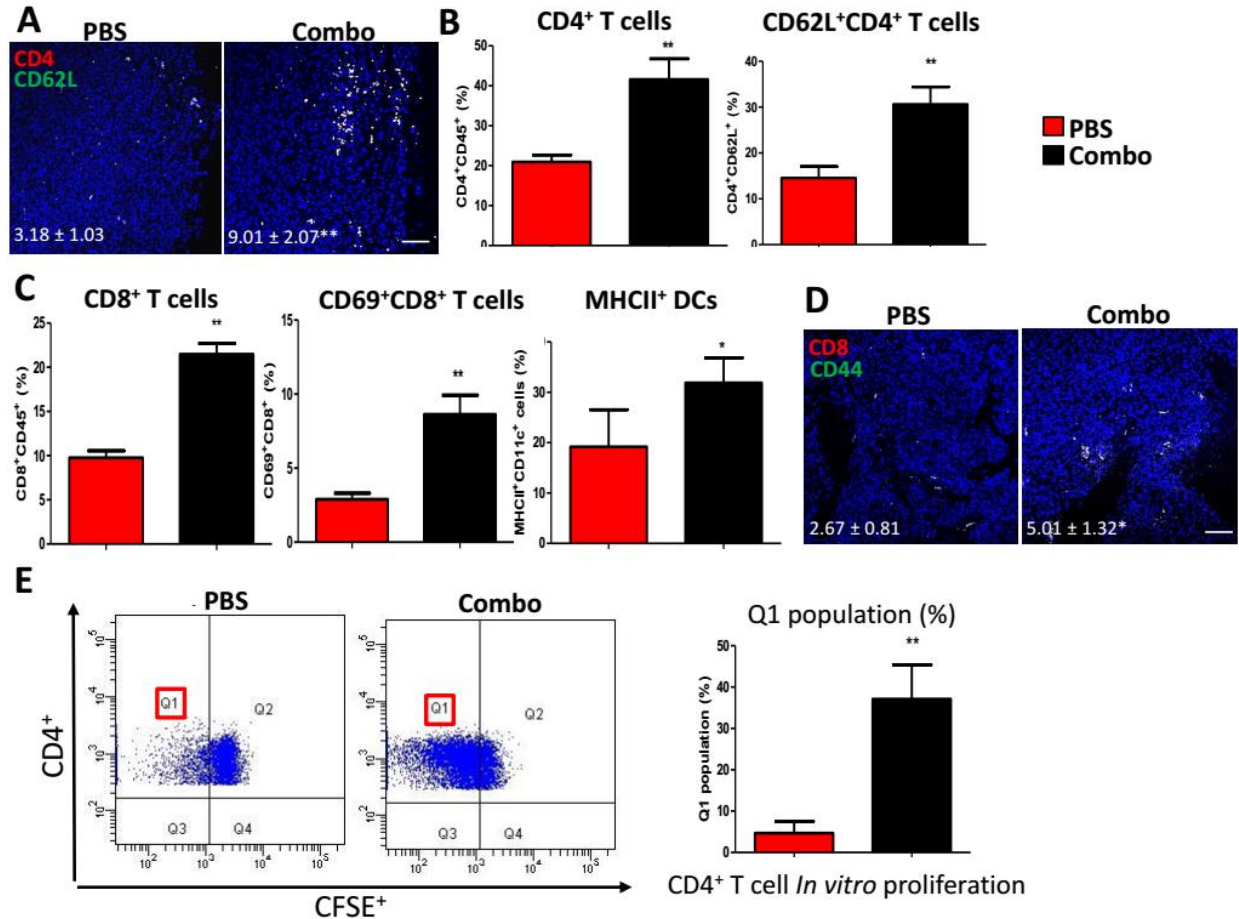


Figure 27. Combination therapy demonstrated long-lasting overall immune response. (A) Immunofluorescent staining for memory CD4 T cells within TME. n = 3. Scale bar indicates 100 μ m. (B) and (C) Flow cytometry analysis of T cells and DCs functions within draining LNs. n = 3. (D) Immunofluorescent staining for memory CD8 T cells within TME. n = 3. Scale bar indicates 100 μ m. (E) In vitro CD4⁺ T cell proliferation assay depicting division of antigen-reactive cells (Q1) between groups. n = 3. *: p < 0.05, **: p < 0.01.

5.2.7 Safety evaluation of the combination therapy

We evaluated the safety and side toxicity of the therapies by performing extensive toxicological pathology analysis. It has been reported that Wnt5a plays an important role in the liver. Wnt5a, also participates in hepatic stellate cell activation through Wnt/Ca²⁺ pathway and may serve as a therapeutic target in the treatment of liver fibrosis.¹⁷⁰ Thus, the homeostasis of Wnt5a is directly associated with proper liver functions and worth further investigation. Minor

and transient Wnt5a trapping might be beneficial. Throughout the trapping therapeutic window and tumor inhibition study, we found no significant morphological damage was caused in the liver, neither in other major organs, including kidney, lung, spleen, and lung. Compared with non-tumored control group, mice under different treatment of therapies demonstrated none noticeable systematic toxicities (**Figure 28**). No significant body weight changes were found in any of the treatment groups (**Figure 29A**). The serum biochemical parameter analysis and the whole blood cell counts remained within the normal ranges for all the groups, suggesting no systemic anemia or inflammation occurred after treatments, nor major liver disfunctions noticed (**Figure 29B**).

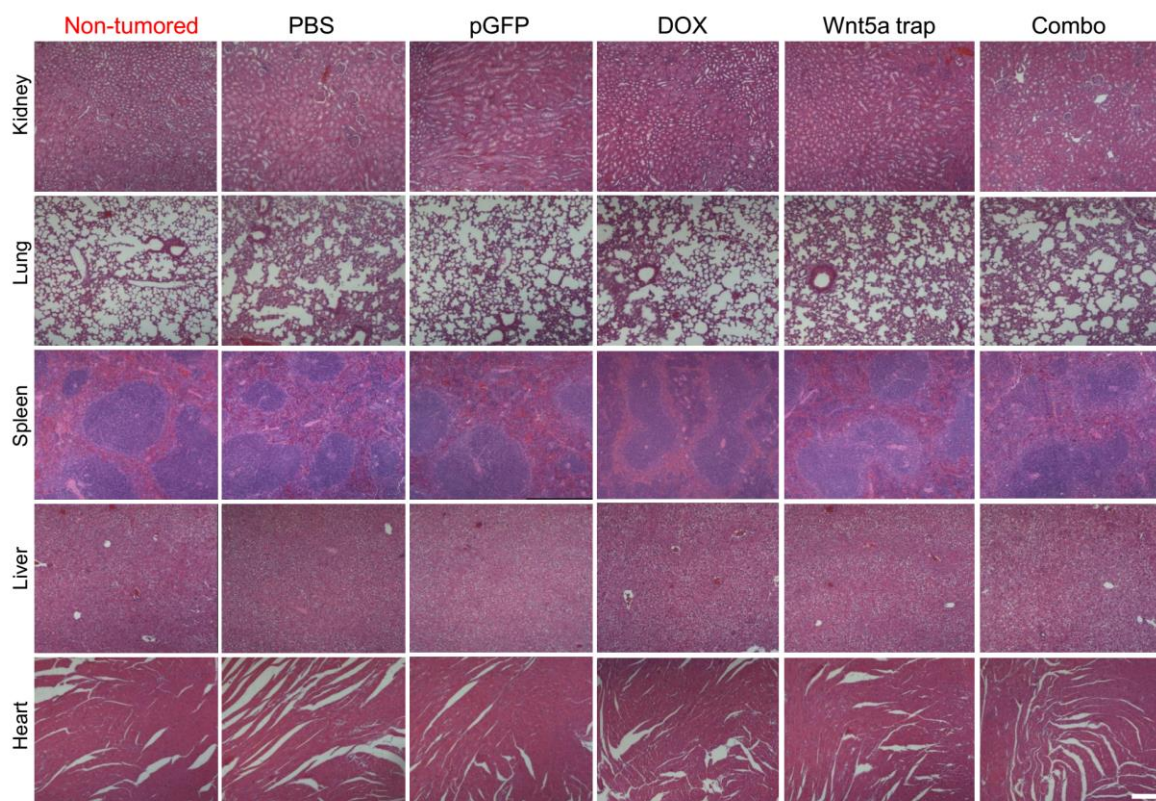


Figure 28. H&E morphology under different therapies. At the endpoint of tumor inhibition study, mice were humanely euthanized, major organs were collected, sectioned, and stained for H&E analysis. Non-tumored mice were also examined as control. Scale bar indicates 300 μm .

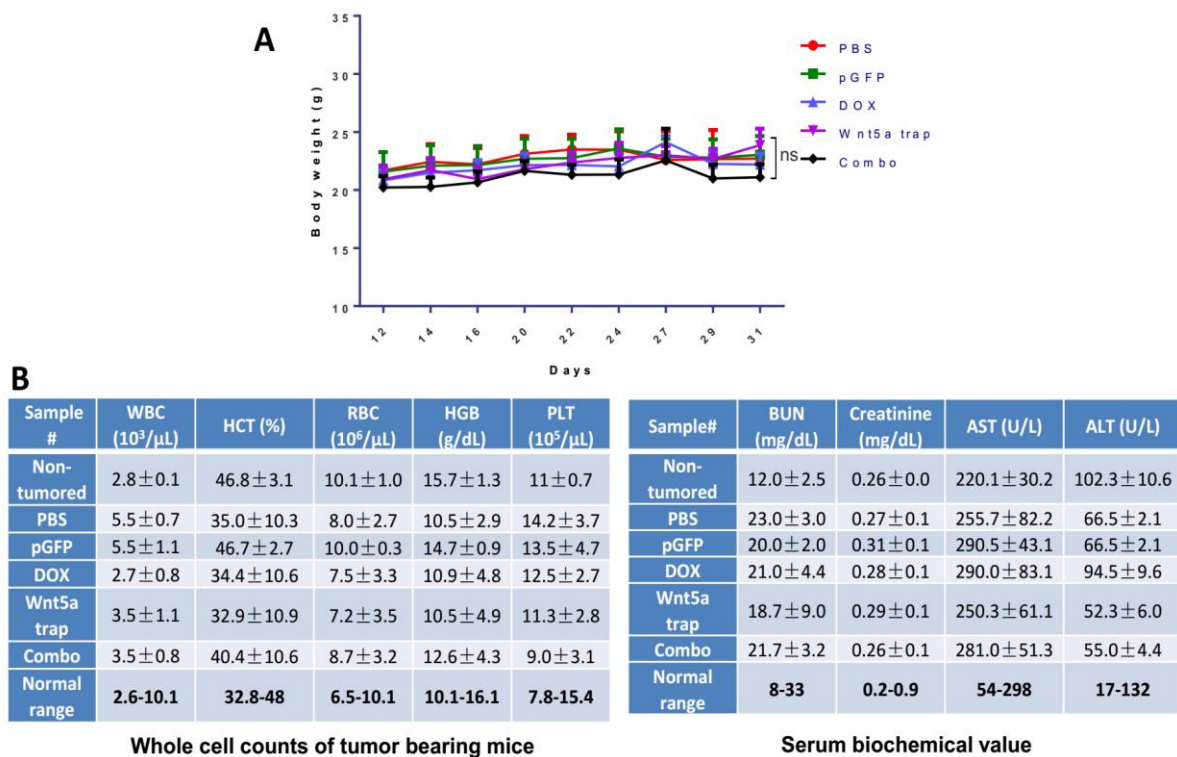


Figure 29. Toxicity evaluation of therapies. (A) Mice body weight changes under tumor inhibition study. (B) Whole cell counts and serum biochemical marker analysis of tumor bearing mice. Fresh whole blood and serum were collected at endpoint of study. Non-tumored mice were also examined as control. $n = 5$. n.s.: $p > 0.05$.

5.3 Conclusion

Among human melanoma, the activation of tumor cell intrinsic Wnt/ β -catenin pathway mediates the deficiency in T cell priming tumor-associated antigens in vivo, followed by resistant to anti-PD-L1 and anti-CTLA4 blockage therapy. Owing to its diverse functions, Wnt5a signaling in immunosuppression and cancer progression is varied and complex with mechanism still elusive, and whether it plays a role in cancer promotion or suppression depends on specific cancer types. The persistent activation of Wnt5a and its downstream signaling pathways in BRAF-mutant type is particularly mortal. So far, systemically applied monoclonal antibodies (mAbs) against Wnt5a are not yet available for patients. Moreover, without specific targeting, a

disruption in the functioning of Wnt5a molecule among normal tissues may lead to imbalance in immunologic tolerance and result in severe inflammatory diseases.¹⁷¹ In our established Wnt5a^{high} DM mouse models, the advantage of our approach is to locally normalize, rather than systemically deplete, the expression of Wnt5a within TME under a transient therapeutic window. Compared to systemic large-size (~150 kDa) mAb therapies which have been reported with subsequent multiple autoimmune diseases,¹⁷² the local and transient expression of a small-size (~26 kDa) Wnt5a ‘trap’ by tumor-specific NP delivery offers great advantages in both therapeutic efficacy and safety. Basically, what we have established is a “Wnt5a KD” tumor model in a transient way. The Wnt5a trap used in this work is based on the CRD of FZD7. Since FZD7 is also implicated in the interaction with other Wnt ligands, it is possible that levels of Wnt ligands other than Wnt5a (*i.e.* Wnt3a) were also reduced in TME.¹⁷³

Conclusively, the local and transient Wnt5a trapping efficiently remodels the fibrotic immunosuppressive TME, recovers DC functions, and facilitates T cell infiltration, providing a promising platform for the treatment of DM. This is especially true when combined with a commonly accepted chemotherapy that can further stimulate immune responses, or other forms of tumor-specific vaccination. Currently, we are further investigating into formulation scale-up, prolonged safety evaluation, as well as any potential side effects associated with change in dosing strategy.

5.4 Materials and methods

5.4.1 Materials

DSPE-PEG-2000, DOPA and DOTAP were purchased from Avanti Polar Lipids (Alabaster, AL). The DSPE-PEG-AEAA was synthesized according to previous publication of our lab. DOX, cholesterol and protamine were purchased from Sigma-Aldrich (St. Louis, MO). DiI was purchased from ThermoFisher Scientific (Waltham, MA).

5.4.2 Cell lines and animals

Murine BRAF-mutant melanoma cell lines BPD6 was kindly provided by Brent Hanks (Duke Cancer Institute) and cultivated in RPMI-1640 Medium added with 10 % FBS and 1 % Penicillin/Streptomycin (Invitrogen, Carlsbad, CA) at 37 °C and 5% CO₂. Six-week-old female C57BL/6 mice were purchased from Charles River Laboratories. All animal regulations and procedures were accepted by Institutional Animal Care and Use Committee, University of North Carolina at Chapel Hill.

5.4.3 Antibodies

InVivoMAb anti-mouse CD8 α of clone 53-6.7 and anti-mouse CD4 of clone GK1.5 were purchased from BioXcell (West Lebanon, NH). Primary antibodies, fluorescent conjugated primary and secondary antibodies used for immunostainings (IF), western blots (WB), and flow cytometry (flow cytr) were listed in **Table 3**.

Table 3. Antibody list

Antibodies	Company	Catalog	Application
Anti-CD8 (PE-conjugated)	BD	553032	flow cyt, IF
Anti-CD4 (FITC-conjugated)	BD	561828	flow cyt, IF
Anti-CD11b (FITC-conjugated)	BD	553310	flow cyt
Anti-Gr1 (Ly-6G and Ly-6C) (PE-conjugated)	BD Pharmingen™	553128	flow cyt
Anti-CD45 (FITC-conjugated)	BD Pharmingen™	553080	flow cyt
Anti-CD62L (FITC-conjugated)	BD Pharmingen™	553150	flow cyt, IF
Anti-CD44 (FITC-conjugated)	BD Pharmingen™	553133	IF
Anti-CD103 (PE-conjugated)	Biolegend	121406	flow cyt
Hoechst 33342	ThermoFisher	H1399	IF
ProLong™ Diamond Antifade Mountant with DAPI	ThermoFisher	P36971	IF
Anti-CD206 (FITC-conjugated)	Biolegend	141704	flow cyt
Anti-F4/80 (FITC-conjugated)	BD Pharmingen™	565410	flow cyt
Anti-CD274 (PE-conjugated)	BD Pharmingen™	558091	flow cyt
Anti-CD11c (FITC-conjugated)	BD Pharmingen™	557400	flow cyt
Anti-CD69 (FITC-conjugated)	BD Pharmingen™	553236	flow cyt
Anti-MHCII (PE-conjugated)	BD Pharmingen™	553570	flow cyt
Anti-Wnt5a	Abcam	Ab72583	WB, IF
Anti-CRT	Abcam	Ab2907	IF
Anti-HMGB1	Abcam	Ab18256	IF
GAPDH	Santa Cruz	I3015	WB

5.4.4 Wnt5a expression in TCGA human patients and survival analysis

The TCGA SKCM (Skin Cutaneous Melanoma)) cohort data was downloaded from the Broad Institute Genome Data Analysis Centers (GDAC) by using its fbget tool to directly access the GDAC FireBrowse API interface. All the samples are either “TP” or “TM” type. For Wnt5a expression analysis, we noticed a significant difference in Wnt5a expression levels between

“TP” and “TM” types. The results shown are based on all “TM” type samples, as the majority of the samples are “TM”. The same trend was observed for the “TP” samples. The p-value was calculated with a t-test. For the survival analysis, we chose to use the “TP” samples, since these patients were diagnosed at earlier stages than the “TM” patient and their survival data is thus relatively more accurate. The survival time was calculated as days to death for deceased patients, and the days to last follow-up for alive patients. Data were represented as scatterplot of Wnt5a mRNA expression level vs days of survival for human primary solid SKCM tumor samples. Kaplan-Meier curves and Median Survival were quantified and calculated using Prism 5.0 Software. P-value less than 0.05 was considered significantly difference. *: $p < 0.05$, **: $p < 0.01$, ***: $p < 0.001$.

5.4.5 Construction of Wnt5a trap gene

To construct the Wnt5a trap plasmid (pWnt5a trap), the codon-optimized coding sequences of the N-terminal extracellular cysteine-rich domain (CRD) of mouse FZD7 (residues 33-180) and the C-terminal trimerization domain of cartilage matrix protein (residues 458-500) were used for assembling the trap gene. A flexible hinge region with optimized length was introduced between the Wnt5a-binding CRD and the trimerization domain. The final sequence for the monomeric Wnt5a trap codes for a secretion signaling peptide, Wnt5a-binding FZD7 CRD, hinge peptide, trimerization domain, FLAG tag, and His (6×) tag, respectively. The complete cDNA was cloned into pcDNA3.1 between Nhe I and Xho I sites and the accuracy was confirmed by DNA sequencing.

5.4.6 Expression and purification of recombinant trap protein

293T cells were cultured until 70-80 % confluence. To transfect the cells, 24 µg pTrap (or pcDNA3.1 negative control) and 40 µL lipofectamine were added to each 10-cm plate. The serum concentration was reduced after transfection. The 293T cells were monitored each day to ascertain their survival. Ten mL supernatant was harvested after 24, 48, and 72 h, and kept at 4 °C for further purification. The supernatants were concentrated with 10 kDa MWCO spin filters to 200 µL and subjected to His-Mag-Ni-Sepharose beads to purify His (6×)-tagged trap protein. The purified proteins were analyzed on 10 % SDS-PAGE gel.

5.4.7 Binding kinetics

The binding affinities of FZD-CDR-based proteins to Wnt5a were accessed with Microscale Thermophoresis (MST). In brief, Wnt5a-binding protein was first fluorescently labeled by using RED-tris-NTA dye. Ten µL of the labeled protein was then supplied to 10 µL of serially 2-fold diluted mouse Wnt5a using a PBST buffer (PBS with 0.05 % Tween 20). The resulting samples were subsequently loaded into capillaries, and the thermophoresis of each sample was measured using Auto Red laser power and medium MST power on Monolith NT.115 (NanoTemper Technologie, Munich, Germany).

5.4.8 Preparation and Characterization of LPD

LPD NPs were synthesized according to published procedures from Huang lab.¹¹⁸ Briefly, DOTAP and cholesterol (1:1, mol/mol) liposomes were prepared by a hydration-extrusion method. LPD cores were self-assembled as adding 100 µL of 20 µg protamine in DI water to 100 µL of 50 µg Wnt5a trap plasmid. After incubation for 10 min at room temperature, 60 µL of the liposomes were added. We then introduced 10 µL DSPE-PEG and 10 µL DSPE-PEG-AEAA at

60 °C for 15 min. Finally, 20 μ L 20 % glucose solution was added to adjust the osmotic pressure. NP size and NP surface charge were measured by a Malvern ZetaSizer Nano series (Westborough, MA). Followed by negatively staining, NPs were imaged with a JEOL 100 CX II TEM (JEOL, Japan).

5.4.9 Tumor growth inhibition, metastasis suppression and survival analysis

On day 0, mice were inoculated subcutaneously with 1×10^6 BPD6 cells on lower flank area. Once tumor volume reached $\sim 200 \text{ mm}^3$ ($0.5 \times \text{length} \times \text{width} \times \text{height}$), mice were then randomized into 5 groups ($n = 5\sim 8$) as follows: Untreated group (the PBS group), Control plasmid trap (the pGFP group), Low dose DOX (the DOX group), Wnt5a trap (the Wnt5a trap group), and Combination of low dose DOX with Wnt5a trap (the Combo group). DOX group was *i.p.* treated (0.544 mg/kg) on day 10 and 12. Control or Wnt5a trap was *i.v.* treated (50 μ g plasmid/mouse) on day 10, 12, 14 and 16. Tumor size (digital caliper) and animal weight were monitored every 2–3 days. Mice were sacrificed before tumors reached 20 mm in one dimension. At the endpoint, tumors, major organs and blood samples were harvested and tested. Long-term survival was also monitored for over two months. Kaplan-Meier curves and Median Survival were quantified and calculated using Image J. At the endpoint of survival monitor, metastasis study was performed as major organs were harvested, fixed and processed with H&E staining for pathology observation.

5.4.10 Bio-distribution of LPD NPs

DiI-labeled LPD NPs were synthesized with liposomes containing approximately 0.05 % of hydrophobic dye DiI. Mice were intravenously injected with DiI-labeled LPD NPs and sacrificed after 24 h. Tumor and major organs were collected accordingly and subject to IVIS[®]

Kinetics Optical System (Perkin Elmer, CA) (excitation/emission = 520/560 nm) for imaging and quantifications.

5.4.11 Expression of Wnt5a trap

Mice bearing BPD6 allografts were intravenously injected with LPD NPs containing 50 µg plasmid. Mice were humanely sacrificed at 1, 2, 4, 8 days post final dosage. Tumor and major organs were harvested, and total protein were purified and quantified with BCA Protein Assay Kit (Pierce, Rockford, IL). Expression of Wnt5a trap was quantified with ELISA (Cell Biolabs, INC., n = 5) using anti-His antibody against the His-Tag engineered at the C-terminus of Wnt5a. Trap protein was also directly intravenously injected into mice and compared with the plasmid counterpart.

Tumor bearing mice treated with pGFP were sacrificed two days after final dose. Liver, lung, and tumor were further sectioned by a cryostat (H/I Hacker Instruments & Industries, Winnsboro, SC) to quantify the distribution of LPD NPs within these tissues. Accumulation and distribution of NPs among these tissues were quantified to compare (n = 3).

5.4.12 Flow cytometry assay

Immune cell populations were analyzed by flow cytometry. Briefly, Tumor tissues or LNs were collected by collagenase A at 37 °C for 40-50 min. Single cells were harvested in PBS and stained with fluorescein-conjugated antibodies. Penetration buffer (BD, Franklin Lakes, NJ) were added for any intracellular cytokine staining.

5.4.13 In vitro CD4⁺ T cell purification and proliferation

At the endpoint of tumor inhibition study, the CD4 positive T cells were sorted from whole spleen of mice among PBS or Combo groups. Sorted cells were stained with 5 μ M CFSE, pulsed with DOX-treated cell lysate and cultured with RBC-depleted splenocytes as well as 25 U/mL IL-2 + 5 μ g/mL soluble CD28 in vitro (0.5×10^5 cells/well in 96-well plate, with 200 μ L compete culture medium) for 3-4 days. All cells before/after culture were subject to flow cytometry for quantification of CD4⁺CFSE⁺ cell population. The percentage of CD4⁺ cell proliferation (Q1 population) was quantified by CFSE staining via flow cytometry, and the divisions of antigen-reactive cells were statistically compared between groups, quantified by Flowjo software.

5.4.14 Immunofluorescence staining

Staining was performed on paraffin-embedded sections from tumor tissues. Briefly, all tissues for paraffin-embedding were resected, rinsed in PBS, and placed in 4 % PFA for over 48 h at 4 °C. Immunofluorescence staining was performed by deparaffinization, antigen retrieval, permeabilization, and blocking in 1 % BSA. All antibodies conjugated with fluorophores were incubated overnight at 4 °C, followed by nuclei counterstained with Prolong® Diamond Antifade Mountant with DAPI (ThermoFisher Scientific). Stained slides were imaged with Zeiss 880 Confocal microscopy (Germany). Three randomly microscopic fields were selected and quantified by Image J software.

5.4.15 ICD determination

ICD dosing was determined by in vitro CRT exposure and HMGB1 release. Briefly, BPD6 cells treated with low dose of DOX were harvested, PBS washed and fixed in 0.25 % PFA.

Primary and secondary antibodies were diluted in blocking buffer and added to collected samples for 30 min each. Cells were then mounted, and nuclei were stained with Hoechst 33432 (ThermoFisher Scientific), followed by Confocal imaging. For intracellular staining of HMGB1, cells were permeabilized with 0.1 % Triton X-100 for 10min before blocking.

5.4.16 Quantitative real-time PCR (RT-PCR) assay

Total RNA was extracted from the tumor tissues following protocol of RNeasy[®] Microarray Tissue Mini Kit (Qiagen, Hilden, Germany). We then reverse-transcribed cDNA with iScript cDNA Synthesis Kit and amplify cDNA with iScript Reverse Transcription Supermix for RT-PCR (Bio-Rad, Hercules, CA). RT-PCR primers, all mouse specific, are listed in **Table 4**. RT-PCR reactions were performed with 7500 Real-Time PCR System and subject to analysis with 7500 Software, compared to and normalized by GAPDH endogenous control.

Table 4. Primer list for real-time PCR

Antibodies	Applied Biosystems/Ref
Mouse IFN- γ	Mm01168134_m1
Mouse IL12 α	Mm00434169_m1
Mouse TNF- α	Mm00443260_g1
Mouse TGF- β	Mm01178820_m1
Mouse CCL2	Mm00441242_m1
Mouse GAPDH	Mm99999915_g1

5.4.17 TUNEL assay

Assay performed following DeadEnd Fluorometric TUNEL System (Promega, Madison, WI) instruction and imaged with fluorescence microscopy. Fragmented DNAs of apoptotic cells were fluorescently stained with FITC and defined as TUNEL-positive nuclei. Slides were mounted, and nuclei were stained with Prolong[®] Diamond Antifade Mountant with DAPI (ThermoFisher Scientific), followed by imaging under Confocal microscopy. Three fields were randomly selected and quantified.

5.4.18 H&E staining and blood toxicity analysis

At the endpoint day of tumor inhibition study, tumor bearing mice under different treatments were humanely sacrificed, whole blood, serum, and major organs were harvested. Organs were collected for H&E staining by UNC histology facility. Indicators of renal and liver function such as creatinine, BUN, serum AST and ALT were tested based on blood and serum.

5.4.19 Patient tumor samples

H&E sections from paraffin-embedded biopsies of BRAF-mutant melanoma patients were obtained from Department of pathology, Xinhua Hospital, China according to an approved patient sample management protocol. Informed consent was obtained from patient before evaluation.

5.4.20 Statistical analysis

One-way ANOVA and a two tailed Student's t-test were performed in Prism 5.0 Software. Data were compared with PBS control group. P-value less than 0.05 was considered significantly difference.

CHAPTER 6

NANO-MEDIATED CHEMO-IMMUNO THERAPY ARRESTED TUMOR PROGRESSION AND INDUCED DORMANCY

6.1 Introduction

In DM, the interstitial cells especially TAFs construct an extracellular matrix-rich structure and cytokine crosstalk, thus facilitating aggressive and highly metastatic tumor growth. Moreover, the fibrosis raises delivery barriers for effective therapies.^{108, 174} In this work, we confirmed tumor cells and TAFs as major dominators within TME. Such domination resulted in the recruitment of immune cells - especially MDSCs, Tregs and TAMs - that collectively form the suppressive immune microenvironment.¹⁶⁵ Consequentially, the highly immunosuppressive TME supports “tumor immunoediting”, thus inducing the tumor progression and further the drug resistance.¹⁷⁵

The field of onco-immunology recently validates that conventional cancer therapies may achieve a sustained patients outcome by arising innate and adaptive immunity against tumor.^{176, 177} For such purpose, specialized chemo-drugs which empowering ICD and immune-stimulatory side effects have been employed.¹⁷⁸ Such “Chemo-immuno therapy” offers new therapeutic options for conventional drugs. The common mechanism of inducing ICD by reported chemo-drugs (mitoxantrone (MIT), DOX, oxaliplatin, bortezomib) involves the induction of endoplasmic reticulum (ER) stress,¹⁷⁹ but their potency requires enhancement. Thus, in addition to target depletion of the dominators (tumor cell and TAFs) within the TME and more

importantly, to effectively trigger ICD in DM, we screened drugs that could work synergistically. Our hypothesis was that the synergy will significantly reduce the effective drug dose if the drugs could be delivered together at an optimal dose ratio. We further hypothesized that improved ICD could induce long lasting anti-tumor immunity which would elicit prolonged progression free survival of the host. To achieve the highest anti-cancer efficacy, we used a nanoparticle (NP) delivery system that specifically targets and triggers drug-release to deliver sufficient drugs with high concentration and with the synergistically optimal combination ratio at the tumor site. This chemo-immuno therapy strategy holds promise to prime robust innate and adaptive immune responses, arrest cancer progression and induce tumor dormancy. Data were collected and under peer-review in *ACS Nano*. (Q Liu, F Chen, L Hou, L Shen, X Zhang, D Wang, L Huang. Nanocarrier-Mediated Chemo-Immuno Therapy Arrested Cancer Progression and Induced Tumor Dormancy in Desmoplastic Melanoma)

6.2 Results and discussion

6.2.1 The design of chemo-immuno therapy

DM presents a highly fibrotic TME in comparison to non-desmoplastic subtypes. **Figure 30A** depicts a typical collagen-rich morphology (predominantly produced by TAFs) in DM, compared with relatively non-desmoplastic ones, in both human patients and preclinical mouse models. Importantly, the metastatic rate of clinical primary melanoma significantly increased from 44.56 % (non-desmoplastic) to 50.45 % (desmoplastic subtypes). Among which, lung and distant lymph nodes (LNs) are the major identified loci (analyzed from The Cancer Genome Atlas (TCGA), data not shown).

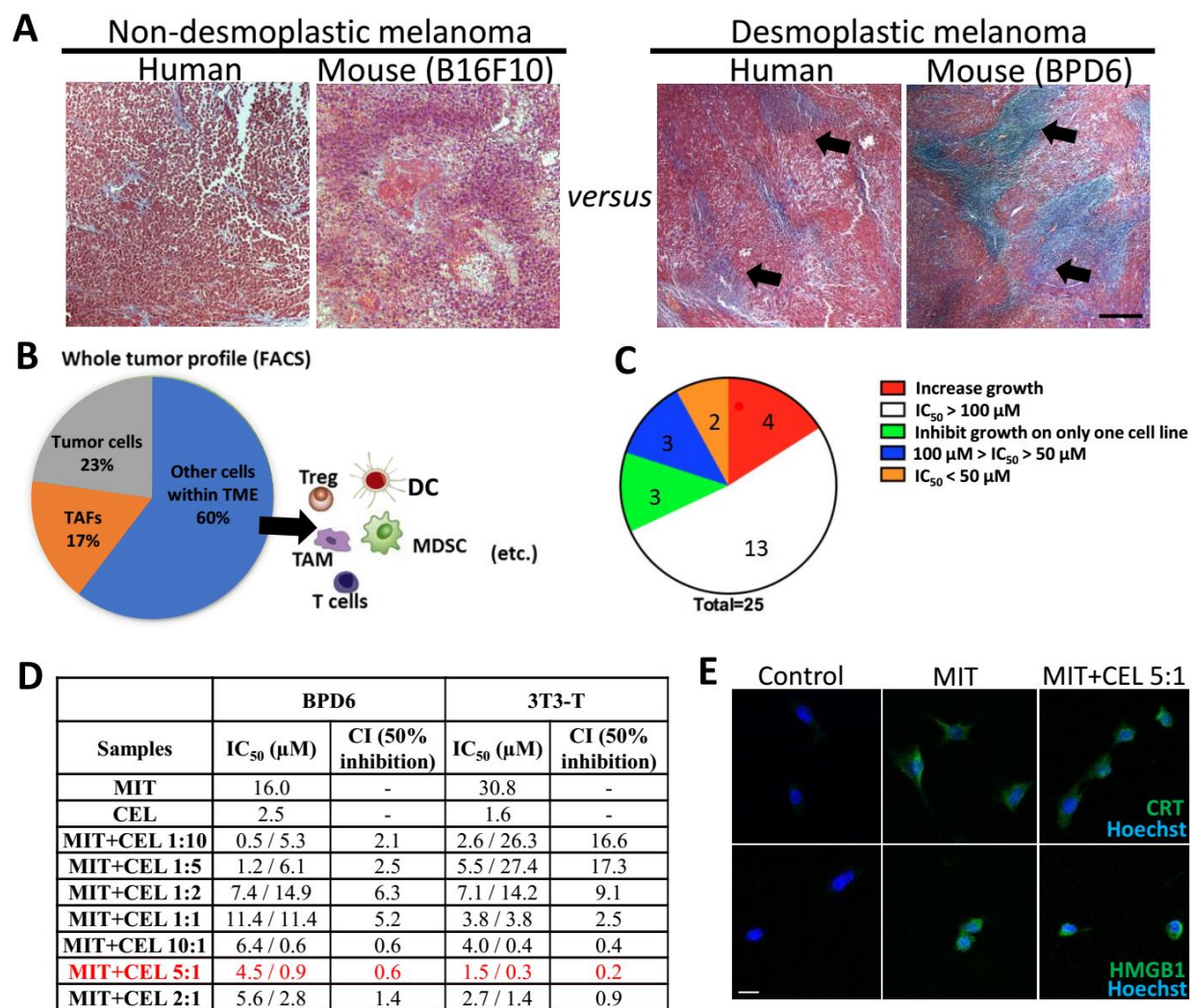


Figure 30. The design of chemo-immuno therapy. (A) Masson's trichrome staining illustrating desmoplastic melanoma with collagen-rich TME (blue-stained collagen, black arrows highlighted), compared with relatively non-desmoplastic samples from patients and mouse tumor specimens. Scale bar indicates 300 μm . (B) Flow cytometry analysis showing major cell populations within TME. (Tumor cells: MART1+; TAFs: FAP+). (C) A total of 25 candidate drugs were screened using MTT assay. MIT and CEL were selected among lowest IC_{50} . $n = 5$. (D) Cytotoxicity and combination index of MIT, CEL, and optimized ratios of MIT+CEL on both BPD6 cells (desmoplastic melanoma cells) and 3T3-T cells (TGF- β activated fibroblast, mimicking TAFs in vivo). 24 h incubation. $n = 5-8$. (E) ICD induced by MIT and MIT+CEL (combination ratio of 5:1) on tumor cells. Fluorescence imaging detecting ICD markers: CRT and HMGB1. Cell nuclei were stained with Hoechst 33432. Scale bar indicates 10 μm . $n = 3$.

In study of desmoplastic TME, we performed a whole tumor profiling assay (**Figure 30B**, using flow cytometry) on murine tumor model, where the presence of ~23 % tumor cells and ~17 % TAFs were found. To target depletion of these two dominators of tumor mass, as well as

inducing tumor ICD, we designed a cancer-specific “chemo-immuno therapy”. A total of 25 candidate drugs were screened with MTT assay in vitro. Among these were 4 well-reported ICD-inducing chemo-drugs and 21 active compounds from traditional Chinese medicine (TCM) extracts (for full list, see Materials section). As illustrated in **Figure 30C**, MIT and celastrol (CEL) were among the most effective ($IC_{50} < 50 \mu M$) in both the desmoplastic melanoma cell line (BPD6) and a model TAF cell line (TGF- β activated NIH 3T3 cells, referred to as 3T3-T).

MIT, clinically used in treating malignant melanoma,^{180, 181} can trigger ICD in various cancer types.¹⁵⁵ CEL, a pentacyclic triterpene extracted from *Tripterygium wilfordii* (Thunder God Vine), which is reportedly an immune-stimulatory, anti-inflammatory and anti-cancer agent,¹⁸² has further elicited potent anti-tumor and anti-fibrosis potential in the murine DM model (**Figure 30D**). Such active compounds from TCM has been reported to increase efficacy of chemo-drugs as well as to decrease toxicity.^{129, 183} Thus, we explored the possible synergy between these two drugs.

As shown in **Figure 30D**, various combinations of these two drugs were tested for their half maximal inhibitory concentration (IC_{50}) and the combination index (CI). In both tumor and TAF cell lines, significantly lower IC_{50} of MIT was achieved after combining MIT with CEL, indicating that CEL increased the sensitivity of cells to MIT. For example, IC_{50} of MIT in BPD6 cells decreased from 16.0 to 4.5 μM and from 30.8 to 1.5 μM in 3T3-T cells, respectively, when tested in a drug ratio of 5:1 (marked in red). IC_{50} values for CEL were similarly decreased in both cell lines. We have also examined the synergistic effect¹⁸⁴ among 7 combination ratios of MIT to CEL (1:10, 1:5, 1:2, 1:1, 10:1, 5:1, and 2:1). Among these, 5:1 and 10:1 showed strong synergy. The strongest CIs were 0.2 in TAF cell line and 0.6 in tumor cell line. Thus, CEL enables enhanced cytotoxicity of MIT in a best combination ratio of 5:1 (MIT: CEL=5:1,

referred to as MIT+CEL 5:1). Such high therapeutic efficacy achieved at low-doses would allow reduction of side-effects and satisfies the prerequisite of ICD-inducing chemo-drugs which should be used in a low-dose range.

The application of CEL in anticancer therapy has elucidated its role in calcium-mediated activation of ER stress.¹⁸⁵ When calcium is released from ER and mitochondria, un/mis-folded proteins accumulate within the ER. The impaired activities of chaperones (e.g., HSP90) and disabled processing of proteins further promote proteasome function, thus initiating cell apoptosis and paraptosis. Thus, CEL has demonstrated its great potential in facilitating ICD. Upon stress and apoptosis, CRT translocated from ER lumen to the surface of cancer cells, with increased release of HMGB1.¹⁸⁶ With CRT exposure and HMGB1 release as standard markers for drug-induced tumor cell immunogenicity,¹⁵⁷ we confirmed that both MIT itself and MIT+CEL 5:1 effectively induced ICD in tumor cell line (**Figure 30E**), indicating the potential for synergistic chemo-immuno therapy. It would be beneficial to track the trafficking of each drug in tumor cell intracellular organelle distribution, thus to further elucidate the mechanism underlying ICD.

6.2.2 The TME-responsive NP delivery platform

Despite the advantages and great promise of combination drugs, obstacles aligned between the ideal optimal synergistic ratio and the ratio at the tumor sites. Conventional drugs distributed all over the body, with only minor portion insufficiently delivered to the tumor. Thus, we applied a TME-responsive NP platform in purpose to enhance precisely-targeted and fast-released delivery of drugs, and subsequently induce ICD onsite.

To construct such NP delivery platform as aforementioned, the APS (AEAA-Polymer-Disulfide bond) NPs were synthesized by Michael addition polymerization (**Figure 31A**), based on the synthesis scheme of disulfide linkages in (β -amino ester) copolymers that was previously reported.¹⁸⁷ In addition, we synthesized and added AEAA ligand to the copolymers for targeting purpose. AEAA is a high-affinity ($K_d = 9$ nM) ligand for sigma receptors which are over-expressed on both melanoma and TAFs.¹²⁴ The signal peaks in **Figure 31A** (¹H NMR spectrum) represent functional groups such as PEG-AEAA and tertiary amine, indicating a successful synthesis of the APS copolymer. The analysis of characteristic peaks is described in Materials section.

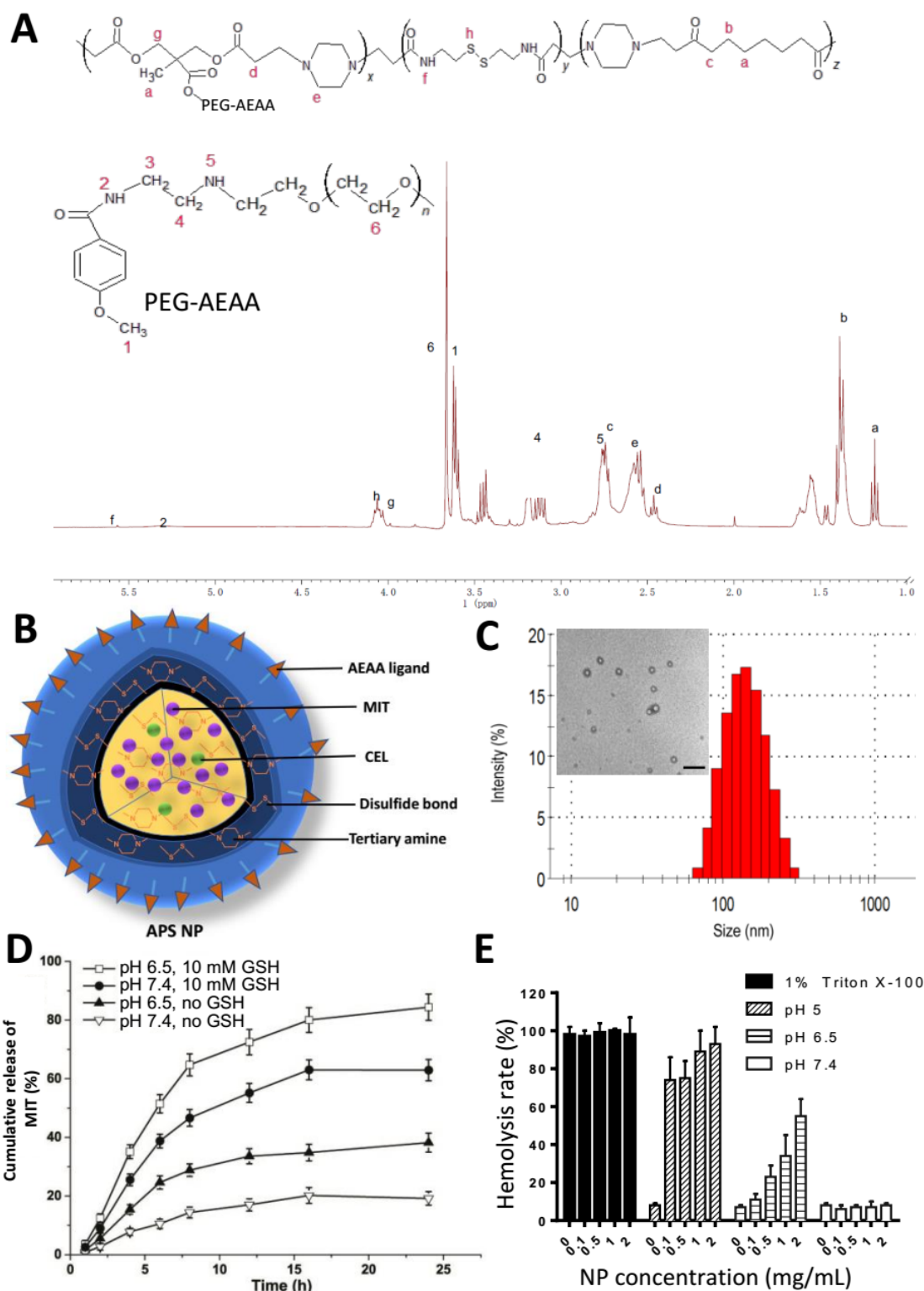


Figure 31. The TME-responsive NP delivery platform. (A) Synthesis scheme of the NP and ^1H -NMR spectrum interpretation result. (B) Graphical structure and composition of APS NP. (C) NP DLS size and TEM image. Scale bar indicates 500 nm. (D) The in vitro MIT release from NPs in changing pH and GSH conditions. $n = 4$. (E) NP hemolysis assay. $n = 4$.

Based on the optimized combination ratio as described above, MIT and CEL were co-loaded (5:1, molar ratio) into APS NPs with a solvent evaporation procedure. Its illustrative feature (**Figure 31B**), TEM morphology image and NP size distribution (**Figure 31C**) are shown. Essential characterization of drug-loaded NP and NP itself, including nanoparticle particle size, zeta potential, polydispersity index (PDI), drug loading efficacy (DLE) and drug encapsulation efficiency (DEE) are listed in **Figure 32A**. Importantly, the zeta potential reversed from a negative charge (pH 7.4) to positive (pH 6.5) due to tertiary amines protonated in the copolymer. In blood (pH ~7.4), the negative charge of APS NPs can be leveraged to reduce rapid NP clearance in the circulation without interacting with blood components which are mostly also negatively-charged. Due to acidic microenvironment (pH ~6.5) in solid tumors, APS NPs triggered a charge-reversal process thus attracting their combination with negatively-charged cell membrane. In turn, this charge-reversal effect enables NPs to be internalized at the TME and minimizes their distribution among normal tissues.^{188, 189} These features offer excellent possibility for inducing local ICD at the tumor site.

A

Samples	Size (nm)	PDI	Zeta potential (mV)		EE (%)	LE (%)
			pH 7.4	pH 6.5		
Blank NP	97±5	0.01±0.03	-15.3±2.4	27.2±3.4	-	-
MIT+CEL NP	112±6	0.12±0.03	-17.6±3.1	29.8±4.2	89.2±2.1 (MIT) 78.3±4.5 (CEL)	8.1±1.9 (MIT) 7.0±2.3 (CEL)

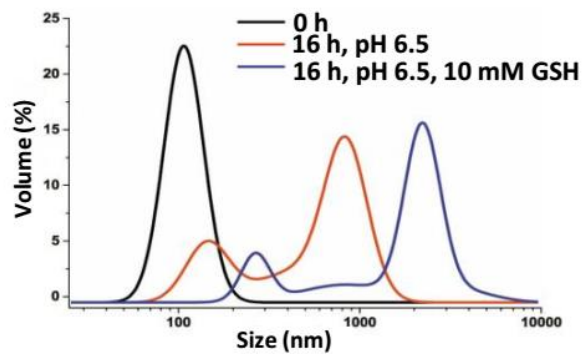
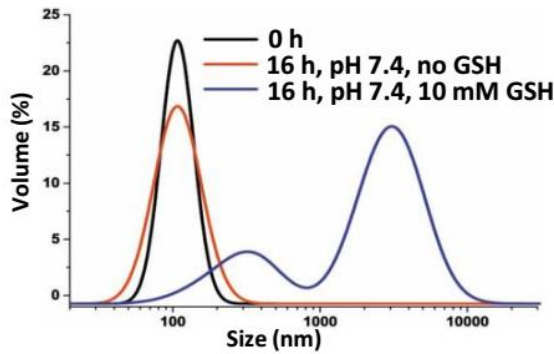
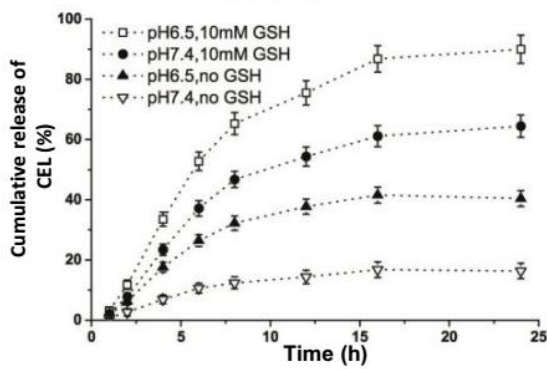
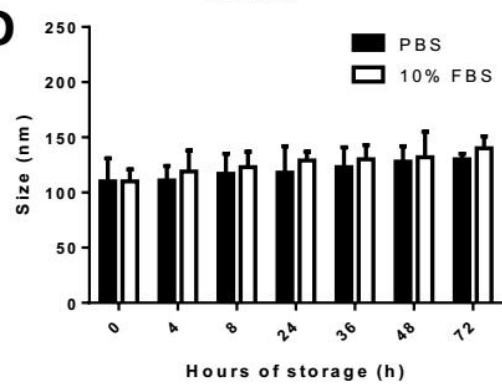
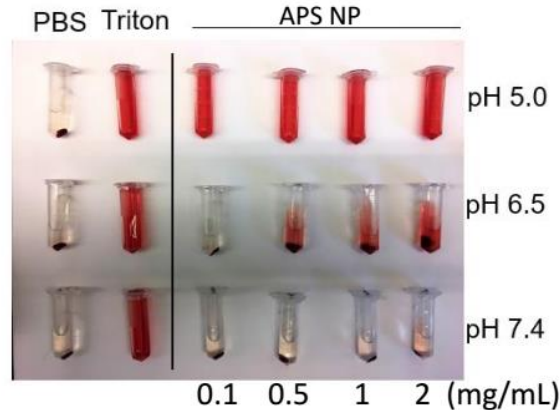
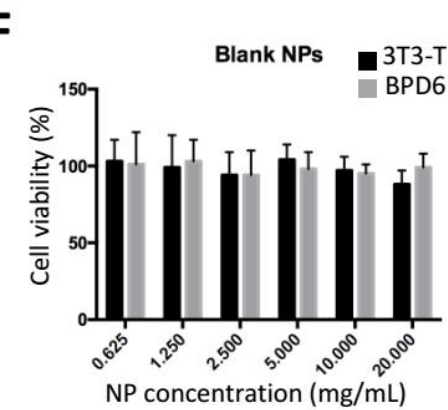
B**C****D****E****F**

Figure 32. The TME-responsive NP delivery platform. (A) Characterization of blank and drug-loaded NPs. (B) NP DLS in changing pH and GSH conditions. $n = 4$. (C) The *in vitro* CEL release from NPs in changing pH and GSH conditions. $n = 4$. (D) Stability of drug-loaded NP in PBS and 10% fetal bovine serum (FBS), respectively, 72 h, $n = 4$. (E) The representative image of hemolysis assay. (F) Cytotoxicity of blank NPs (of different concentration) on 3T3-T and BPD6 cell lines (24 h incubation), $n = 4$.

An effective drug delivery system allows rapid drug release inside the cancer cell. To achieve optimal drug ratio promptly, as well as improve anti-cancer efficacy, TME-specific glutathione (GSH) property has been employed. The concentration of GSH in the cytosol of cancer cells (~2-10 mM) was remarkably higher than that of extracellular matrix and blood (~2-20 μ M).^{104, 190} Furthermore, GSH level in cancer cells are over 4-fold higher than normal cells.¹⁹¹ To confirm such TME-responsive property, the synthesized NPs were tested in changing pH and GSH conditions. As shown in **Figure 32B**, the particle size dramatically increased in the presence of 10 mM GSH compared with no GSH condition, possibly due to disulfide-bond breakage in a reductive manner.¹⁹² A pH change from 7.4 to 6.5 further facilitated NP response to GSH. Thus, these NPs were unstable in either acidic or reductive conditions. Both are favorable properties for anti-cancer drug delivery.¹⁹³

As a result, MIT (**Figure 31D**) and CEL (**Figure 32C**) were being triggered to release from NPs. In the condition of pH 7.4, MIT and CEL loaded NPs released less than 20 % in 24 h. However, at pH 6.5 (simulating the acidic tumor extracellular microenvironment), the drug release slightly increased to ~40 % due to ionization of tertiary amines. The slightly acidic environment led to NP leakage but did not collapse the NPs. Moreover, in the addition of 10 mM GSH (which simulated the reductive environment inside the cancer cells), the release increased to ~60 % due to the rupture of disulfide linkage, indicating that the core of NPs had collapsed. A combination effect was observed in pH 6.5 and 10 mM GSH condition, where more than 80 % of drugs were released. Such high releasing property would help achieve the optimal ratio for drug-induced ICD at the tumor site.

To mimic the blood physiological conditions, APS NPs were added to 10 % fetal bovine serum (FBS) or PBS in vitro for 72 h, and no significant change in size was found, suggesting

their stability (**Figure 32D**). To further evaluate the biocompatibility, a hemolysis assay was employed investigating the interaction between NPs and red blood cells (RBCs). As shown in **Figures 31E** and **23E**, 1 % Triton was used as a positive control which had roughly a 100 % hemolysis rate. At pH 7.4, four concentrations of NPs (0.1, 0.5, 1, and 2 mg/mL) were observed with less than 10 % hemolysis. However, the hemolysis rate increased at pH 6.5 and 5.0; especially in maximum conditions (1 or 2 mg/mL of NP at pH 5.0), the hemolysis rate was close to 100 %, indicating strong interactions between NPs and RBCs. Importantly, blank NP itself showed no significant cytotoxicity in either tumor cells or TAFs (**Figure 32F**). To conclude, the NP deliver platform responded in accordance to TME-mimicking factors and showed a high biocompatibility profile.

6.2.3 Nanocarrier-mediated chemo-immuno therapy significantly improved anti-tumor response and remodeled suppressive TME

To achieve sufficient efficacy, we first examined the delivery of MIT and CEL in TME-responsive NP among DM tumor-bearing mice. Through IVIS imaging, Cy5-loaded NPs mainly distributed in the tumor 24 h after *i.v.* injection (**Figure 33A**), compared with other major organs. Although liver took up NPs, it was significantly lower than the tumors on the per gram weight basis ($p < 0.01$) (**Figure 33B**). With the help of sigma receptor-targeting, we found that most of the NPs were taken up by tumor cells and TAFs within the TME (measured by flow cytometry, data not shown). Furthermore, pharmacokinetic profiles of MIT and CEL were characterized after *i.v.* administration of drug-loaded NPs and free drug suspension, respectively. As shown in **Figure 33C**, the injected NPs offered targeted delivery of MIT and CEL to and stayed in the tumor for a significantly increased amount compared with injected free drugs (measured by LC/MS). Within the tumor, the area-under-curve values of nano-delivered drugs

were significantly higher than those of the free drugs (2.9-fold increase in MIT and 3.8-fold increase in CEL). Importantly, the amounts of drugs in the tumor resembled the designed optimal ratio in vitro at least in the early time points (at 4 h, ratio was 6.1:1; 8 h was 5.0:1; 12 h was 4.0:1, 24 h was 3.1:1). In comparison, the free drugs failed to retain such ratio (7.1:1; 13.9:1; 9.9:1; 8.9:1, respective to 4 measured time points). This result indicated the benefit of using a controlled-release nanocarrier system.

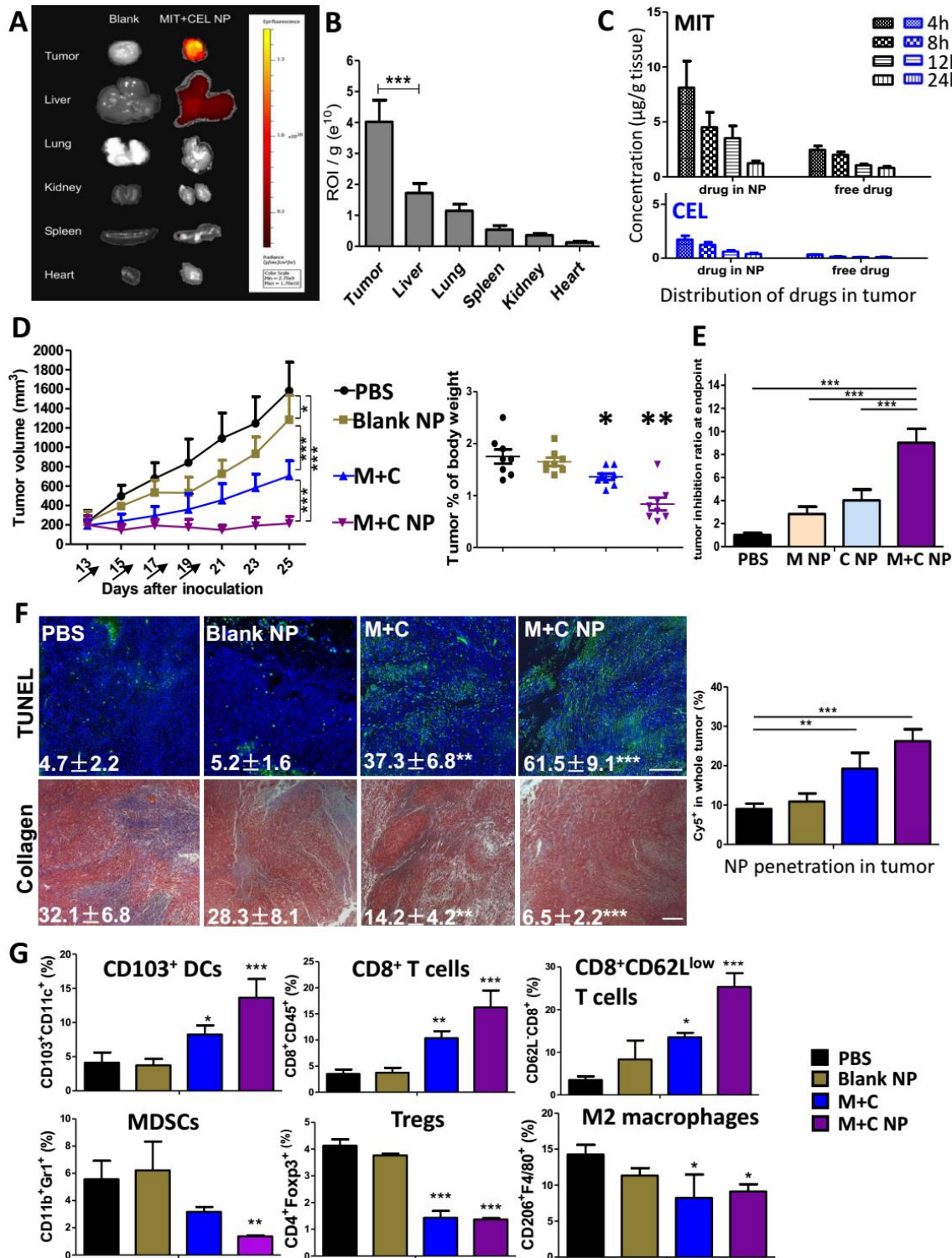


Figure 33. Effective therapy significantly improved anti-tumor response and remodeled suppressive TME. (A) NP distribution in tumor-bearing mouse. Mice were intravenous injected with Cy5 (3 μg/kg)-loaded NPs and measured by IVIS imaging 24 h post-injection. n = 3; (B) Region-of-interest intensity of fluorescence signals among tumor and organs. n = 3; (C) Pharmacodistribution of MIT and CEL within tumor measured by LC/MS, n = 5; (D) Tumor inhibition study and tumor weight comparison. Arrows indicate days of drug injection. Dosage: for M+C group: ~2 mg/kg of CEL per dose; for M+C NP group: ~160 μg/kg of CEL per dose. Tumors were surgical removed

from host at endpoint of study, weighted and compared between groups. n = 10-12; (E) Relative tumor inhibition ratio between M+C NP, M NP+N NP group, and single drug NP groups at day 23 after tumor inoculation. n = 5; (F) Cell apoptosis measured by TUNEL staining and collagen morphology changes measured by Masson's trichrome staining (left panel), scale bar indicates 300 μ m. n = 3. Right panel indicates Cy5-loaded NP penetration within TME after different treatments, measured by fluorescence imaging of tumor frozen sections. n = 5. (G) Flow cytometry analysis of immune functioning cells within TME. n = 3. *: $p < 0.05$, **: $p < 0.01$, ***: $p < 0.001$.

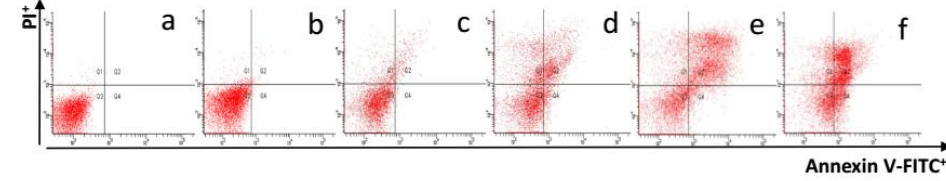
Through NP encapsulation and delivery, the cytotoxicity of drugs was ~6-fold enhanced in comparison to free drugs in combination (measured by IC_{50} , data not shown). Furthermore, on animal model bearing DM tumors (**Figure 33D**), the mice treated with MIT and CEL loaded NPs (denoted as the M+C NP group) presented a significant tumor-killing effect, with only ~1/13 dosage compared to free drugs administrated in combination (the M+C group). As shown in Figure 3D, the delivery of low-dose drugs largely inhibited tumor growth. Moreover, tumor mass was significantly restrained with lower tumor weight. Such therapeutic strategy also achieved best anti-cancer effect in comparison to single drug-loaded NP groups (**Figure 33E**).

DMs are well-known for their immunoediting ability and resistance to immunotherapy. The significant tumor inhibition by delivered drug combination, also referred to as “the elimination phase” of cancer immunoediting, is mainly resulted from the following factors:

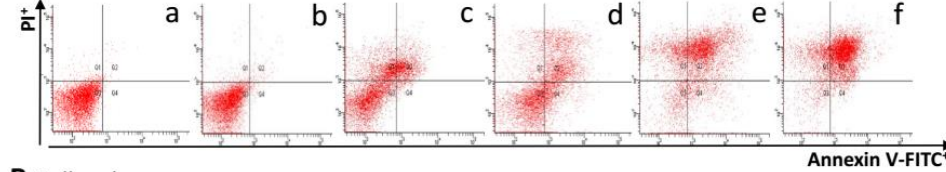
1) Effective apoptosis induced by MIT and CEL (shown in vivo by TUNEL assay in Figure 3F, and in vitro by quantitative cell apoptotic assay and cell cycle analysis in **Figure 34**). In the cell apoptosis assay, M+C NP caused a dramatic increase in the total apoptosis rate (> 60 %) in both tumor cells and TAFs (**Figure 34A and C**). Enhanced apoptosis could be the result of the G1 phase shift to the G2/M phase in the cell cycle. As shown in **Figure 34B and D**, M+C NP group also had a higher percentage of G2/M phase cells, suggesting a synergistically blockage of cell mitosis compared with all controls. These data indicated an increased level of cell apoptosis, possibly due to ICD.

A Apoptosis assay

For BPD6:

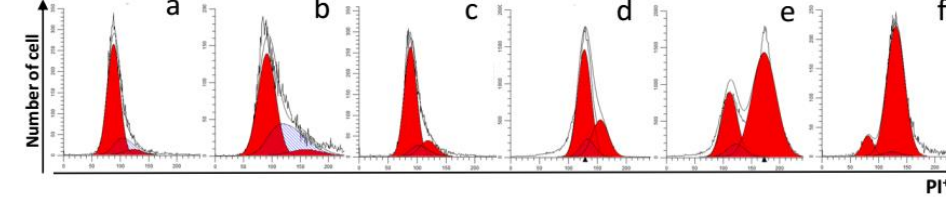


For 3T3-T:



B Cell cycle assay

For BPD6:



For 3T3-T:

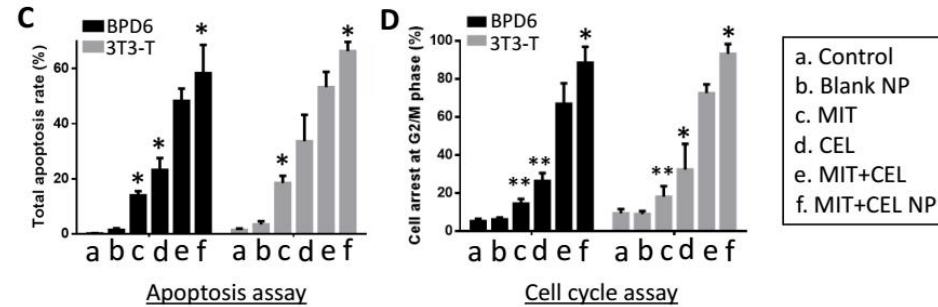
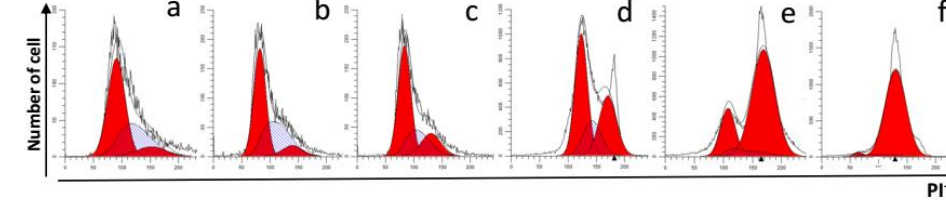


Figure 34. Effective therapy significantly enhanced cell apoptosis and cell cycle arrest. (A) Quantitative cell apoptotic assay among BPD6 cells and 3T3-T cells under different treatments for 48 h, measured by flow cytometry. $n = 3$. For each panel, top left (Q1) presents necrotic cells; top right (Q2) presents late apoptotic cells; bottom left (Q3) presents live cells; bottom right (Q4) presents early apoptotic cells. (B) Cell cycle analysis measured by flow cytometry, 48h, $n = 3$. (C) Histogram of total apoptosis rate. Total apoptosis rate=Q2+Q4. All data compared with MIT+CEL group. (D) Histogram of cell arrest at G2/M phase. All data compared with MIT+CEL group. *: $p < 0.05$, **: $p < 0.01$, ***: $p < 0.001$.

2) Change of TME morphology that facilitated further delivery of therapeutics. As shown in **Figure 33F**, collagen deposition and fibrosis were abundant in tumor sections of the untreated

group. By contrast, the in vivo tumor model depicted significantly decreased collagen density and increased NP penetration under the treatment of M+C NP (**Figure 33F**, right panel).

Collagens were predominantly produced by TAFs, which were the target of both MIT and CEL.

3) The immune-stimulatory effects that counteracted immune-suppression induced by TME dominators. As shown in **Figure 33G** and **Figure 35**, the effective elimination of tumor cells and TAFs dampened the secretion of immune-suppressive TGF- β , IL6, CCL2 and IL-10 network. Thus, suppressive immune cell (MDSC, Treg, and TAM) were significantly reduced. Antigen presenting cells within TME, mostly dendritic cells (DCs) were normally inhibited in antigen-recognition functions and were tolerogenic to immune-stimulators under immune-suppressive environment.¹⁹⁴ After treatment, DC functions were largely recovered with CD103⁺ DC significantly increased, suggesting that the local effective ICD would help release tumor-associated antigens and facilitated DC maturation with cross-priming ability to CD8⁺ CTLs. As a result, IFN- γ increasingly released to stimulate tumor-specific immunity and inhibit the tumor growth. It is known that perforin and granzymes released by CTLs enable non-apoptotic pathways of cell death, thus offering an effective treatment of cancer by modulating the immune system.^{195, 196}

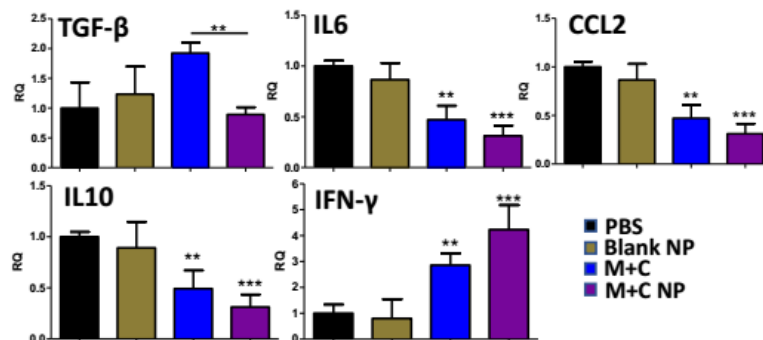


Figure 35. Effective therapy remodeled immune profile within TME. RT-PCR analysis of both pro-inflammatory and anti-inflammatory cytokines changes within TME. n = 6-8. *: p < 0.05, **: p < 0.01, ***: p < 0.001.

To examine the observed therapeutic efficacy in other models of desmoplastic melanoma, we established a second DM model using D4M cells (BRAF^{V600E}, syngeneic with C57BL/6 mice). As shown in **Figure 36**, like the BPD6 tumor model, these tumors also presented a desmoplastic morphology. Following same treatment protocols, the M+C NP group mitigated the desmoplastic structure compared with the PBS group, resulting in superior tumor growth inhibition as compared with all other controls.

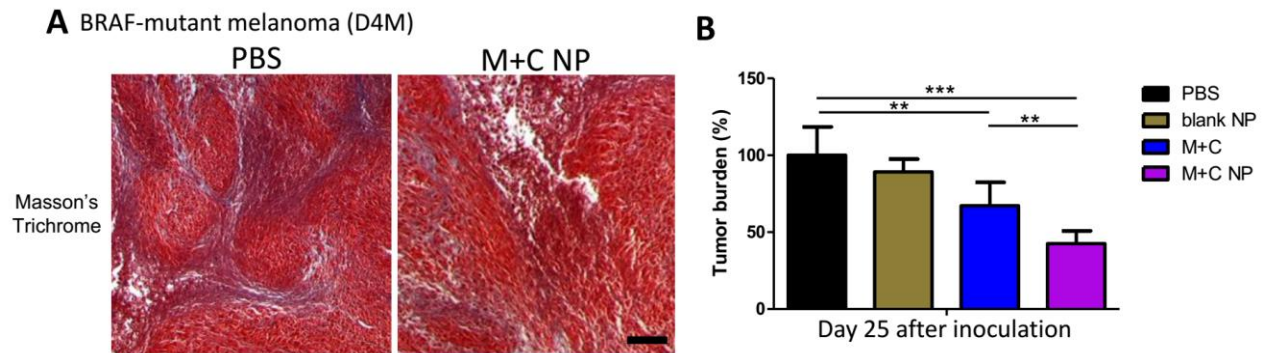


Figure 36. Second model of desmoplastic melanoma. (A) Masson's trichrome staining depicting collagen morphology change in TME. Scale bar indicates 300 μ m. (B) Effectiveness of therapies were compared by monitoring D4M tumor growth every 2 days, on day 25 after inoculation, tumor burden was compared and quantified. n = 3-5, **: p < 0.01, ***: p < 0.001.

6.2.4 Enhancement of long-term immune surveillance, host survival, and anti-metastasis efficacy of therapy

Clinically, a strong cancer immunoediting implies that the “elimination phase” can be hardly completed, thus resulted in a balance between surviving tumor cells and the modified immune system. Such balance may last for years for patients. In our animal model, as the tumor inhibition study continued, we also noticed a long-term sustained tumor inhibition effect in the M+C NP group (**Figure 37A**). Tumor volume was restrained around 200 mm³ for over two weeks after the last dose of treatment, with a significant prolongation of progression-free host

survival (**Figure 37B**). A typical “tumor dormancy” phenomenon suggested the existence of endogenous immune surveillance.

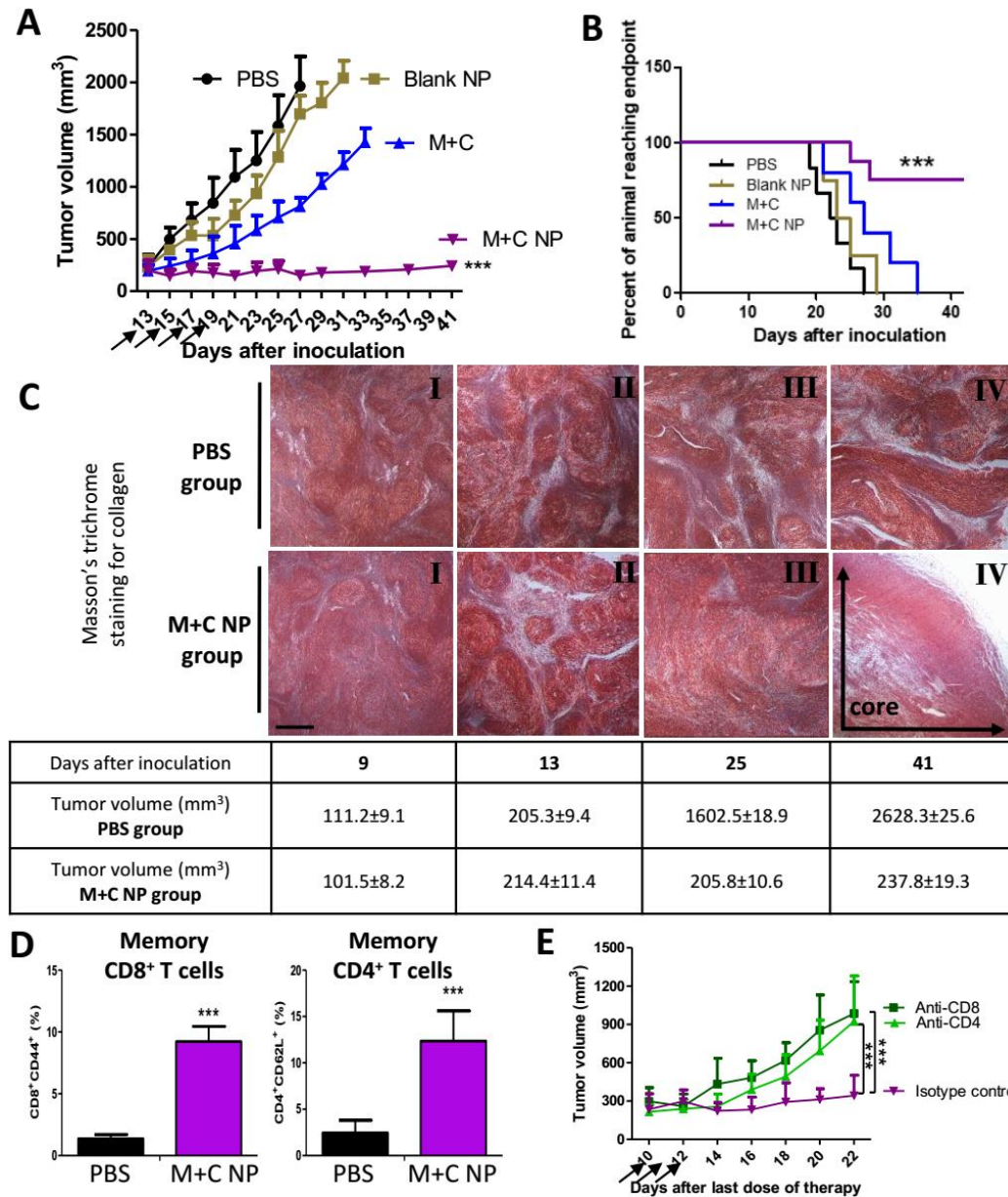


Figure 37. Enhancement of long-term immune surveillance, host survival, and memory immunity. (A) Long term tumor inhibition study. Dosing schedule was consistent for all in vivo studies. Arrows indicate days of drug injection. M+C group: 2 mg/kg of CEL per dose. M+C NP group: 160 µg/kg of CEL per dose. n = 10-12; (B) Long term survival between different treatments. n = 6-8; (C) In M+C NP group, figures depict tumor tissue's collagen staining at different days after tumor cell inoculation. Scale bar indicates 300 µm. n = 3; (D) Tumor tissue immunostaining analysis of memory immune cells within TME at endpoint day of survival study. n = 3; (E) In M+N NP group, tumor-bearing mice were treated with 3 daily injections of anti-CD8 or anti-CD4 antibody or Isotype control (300 µg/mice *i.p.* started from 10 days after the last dose of therapy, arrows) to deplete either CD8⁺ or CD4⁺ T cells *in vivo*. n = 3-4. ***: p < 0.001.

Tumor dormancy can be categorized into two types: cell cycle arrested at G0-1 phase at the cell level, or mostly on a population level represents a balance between tumor cell proliferation and death. Herein, the tumors were restrained as a result of several possible key factors:

1) A turnover of TME morphology. As depicted in **Figure 37C**, the density of fibrosis increased correlatively along with tumor growth (from I to II). The TME was heavily desmoplastic at the start of therapy (depicted in II, ~200 mm³ in tumor volume at day 13 after tumor cell inoculation), and then subjected to de-fibrosis treatment by targeted co-delivery of MIT and CEL aiming at the depletion or deactivation of TAFs (depicted in III, M+C NP group). During over two weeks of host survival observation, the morphological structure of the tumor was largely reframed. At the endpoint of study, an inner necrosis-rich pattern was found in the core area of the residual tumors, along with only a minor level of fibrosis (depicted in IV).

2) Increased levels of immune-surveilling cells. Local CTLs and NK cells are crucial components, but more importantly tumor-specific memory T cells were significantly recruited (**Figure 37D**). The increased memory CD4⁺ and CD8⁺ T cells inside the tumor suggested the effectiveness of ICD in vivo. Reasonably, residual tumor cells may express low but persistent levels of tumor antigens to be recognized and cleared by the immune system. To address such action mechanism, we further depleted CD4⁺ or CD8⁺ T cells in mice bearing the dormant tumor. As shown in Figure 4E, the sustained tumor restrain effect was abolished by the treatment with either anti-CD8 or anti-CD4 antibody, whereas it was not affected when an isotype-matched IgG control was used. The result suggested that a strong immune-surveillance might be the main reason for such dormancy.

3) High expression of CD69 (**Figure 38A**). CD69 is a T cell activation marker. Recent studies in metastatic melanoma patients have reported that the expression of CD69 positively correlates with survival and negatively correlates with metastasis.¹⁹⁷ We found CD69 highly expressed in the remaining cells within the TME, which would help contributing in metastasis inhibition (in both lung and liver) compared to the untreated hosts (**Figure 38B**).

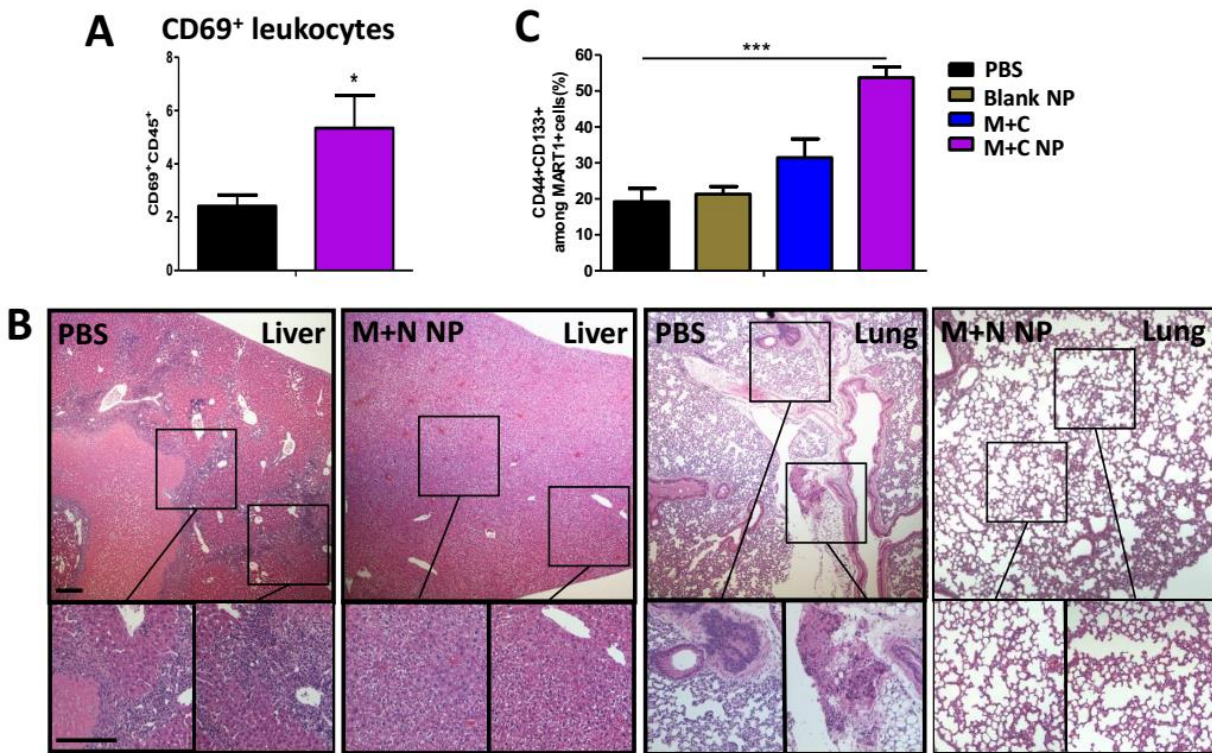


Figure 38. Long-term tumor dormancy and anti-metastasis efficacy of therapy. (A) Tumor flow cytometry analysis of CD69⁺ leukocytes within TME at endpoint day of survival study. n = 3; (B) Tumor metastasis in liver and lung, observed at endpoint day of survival study between PBS and M+C NP group, measured by H&E staining. Scale bar indicates 300 μm; (C) Flow cytometry analysis of CD44⁺CD133⁺ tumor cells within TME at endpoint day of survival study. n = 3. *: p < 0.05, ***: p < 0.001.

4) A high percentage of remaining dormant tumor cells showing the characteristics of cancer stem cells (CSCs) (**Figure 38C**). CSCs are poorly immunogenic and thus avoiding immune-surveillance and clearance.¹⁹⁸ Moreover, CSCs demonstrate a slow growth rate and are

unable to grow into overt tumor mass.¹⁹⁹ Any immunogenic daughter cells from CSCs would be eliminated by immune-surveilling cells, which further stabilized tumor dormancy.

Interestingly, we found that two out of ten mice with remaining dormant tumors eventually had their tumors grown back at a late stage (**Figure 37B**), indicating equilibrium was disturbed in favor of tumor-escape. This suggested the possibilities underlying genetic or epigenetic changes which further allow tumor progression. Main factors to be investigated in such probabilities can be summarized as follows: a) Due to genomic instability, dormant tumor cells express new tumor antigens with specific mutations. Such probability may serve as novel target for the design of neoantigen vaccines; b) The remaining dormant cells may overexpress immune checkpoint ligands, such as PD-L1, gained by gradual increase in resistance. Thus, the checkpoint inhibitors and kinase inhibitor might be applied in combination with new targeted therapy; c) At a late stage, dormant tumors would induce MDSC or Treg proliferation as well as their active suppression of immunity; d) A depletion of T cells or decrease in IFN- γ or IL12 would also trigger immune-escape mechanisms; e) An over-activation of angiogenesis would facilitate tumor progression and even metastasis.

6.2.5 Safety evaluation for chemo-immuno therapy

Safety is an essential aspect for the development of both effective and translational therapy. Thus, biosafety-related toxicological pathology analyses were performed. As shown in **Figure 39A** and **B**, the serum biochemical parameter analysis and the whole blood cell counts were remained within normal range, this suggested that the treatment strategy led to none detectable systemic anemia nor inflammation. Liver and kidney function markers were remained normal. No severe weight loss in hosts were found (**Figure 39C**). Moreover, the H&E staining results also indicated no significant morphological damage among major organs, including

kidney, lung, spleen, liver, and lung (**Figure 39D**). Lack of toxicity of the combination chemo-immuno therapy was certainly the direct result of low drug doses required.

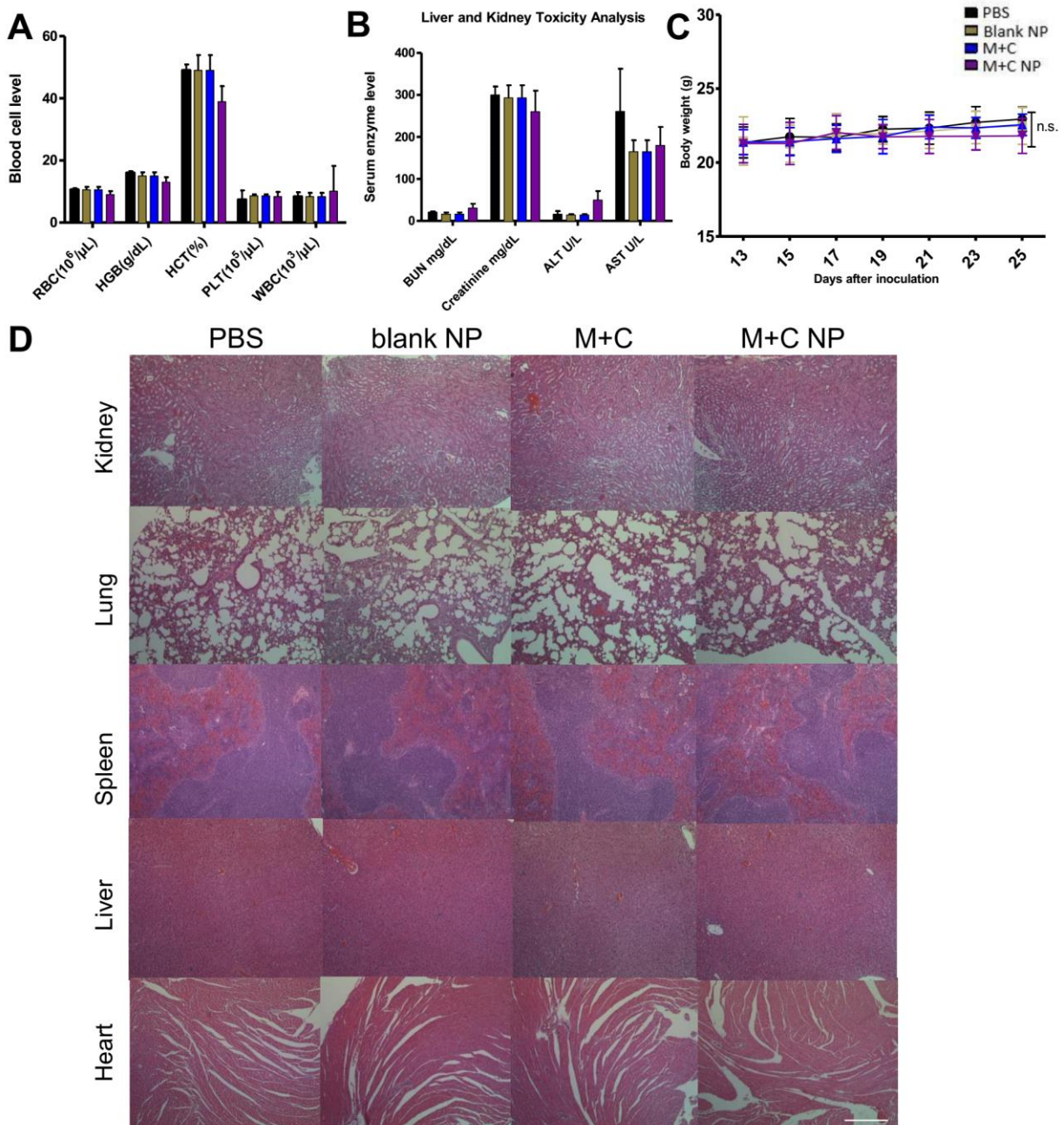


Figure 39. Toxicity evaluation of therapies. (A) and (B) are whole cell counts and serum biochemical marker analysis of tumor bearing mice. Fresh whole blood and serum were collected at endpoint of study. All indicators were among normal biological range. (C) Mice body weight changes under tumor inhibition study. (D) H&E morphology under different therapies. Major organs were collected at endpoint of study and sectioned, stained for H&E analysis. Scale bar indicates 300 μm . n = 5. n.s.: $p > 0.05$.

6.3 Conclusions

In summary, the success described here stems from the strong synergy between MIT and CEL in inducing ICD. The combination also targets TAFs to reduce the desmoplasia of the tumor. The chemo-immuno therapy significantly remodeled immune-suppressive TME, as well as triggered a robust immune memory response. Since only low doses of both drugs were used, the treatment was without any toxicity to the host. Low dose drug-synergy is also clinically beneficial, especially for patients suffering from chemo-toxicities, but the optimization of such synergy needs further investigation. In comparison to personalized vaccines, no matter preventive or therapeutic, our strategy offers a broader application to patients subjects in a way of priming immune system against cancer.

6.4 Materials and methods

6.4.1 Materials

MIT, DOX, Oxaliplatin, and Bortezomib were obtained from Sigma-Aldrich (MO, USA). Active compounds with over 99 % purity, including Dihydroartemisinin, Glycyrrhizin, Curcumin, Tetramethylpyrazine, Resveratrol, Epigallocatechin, CEL, Salvianolic acid B, Salvianolic acid A, Scutellarin, Oleanolic acid, Dihydromyricetin, Osthole, Berberine, Cryptotanshinone, Baicalein, Sinomenine, Lupeol, Wogonin, Cepharanthine, and Adiponectin were obtained from Chengdu Mansite Biotech Co. Ltd (Sichuan, China). NH₂-PEG-OH (MW 2k, CAS No. 32130-27-1) was obtained from Biochempeg Scientific Inc. (MA, USA). Synthetic materials as previous reported were obtained from Sigma-Aldrich MO, USA).

6.4.2 Cell lines and animals

Desmoplastic melanoma models were built according to previously published protocol.²⁰⁰ In detail, murine melanoma cell lines BPD6 and D4M (BRAF^{V600E}, syngeneic with C57BL/6) was kindly provided by Brent Hanks (Duke Cancer Institute) and cultivated in RPMI-1640 Medium added with 10 % FBS and 1 % Penicillin/Streptomycin (PS) (Invitrogen, Carlsbad, CA) at 37 °C and 5 % CO₂. NIH-3T3 cell line (which were activated with 10 ng/mL TGF- β mimicking TAFs in vitro) were cultivated in DMEM Medium also with FBS and PS. Six-week-old female C57BL/6 mice were purchased from Charles River Laboratories (Wilmington, MA). All animal regulations and procedures were accepted by Institutional Animal Care and Use Committee of University of North Carolina at Chapel Hill.

6.4.3 Antibodies

InVivoMAb anti-mouse CD8 α (clone 53-6.7) and anti-mouse CD4 (clone GK1.5) were purchased from BioXcell (West Lebanon, NH).

6.4.4 ICD determination

ICD dosing was determined by in vitro CRT exposure and HMGB1 release. Briefly, BPD6 cells treated with MIT alone or MIT+CEL (5:1 molar ratio), then harvested, PBS washed and fixed in 0.25 % PFA. Primary and secondary antibodies were diluted in blocking buffer and were added to collected samples for 30 min each. Cells were then mounted, and nuclei were stained with Hoechst 33432 (ThermoFisher Scientific), followed by Confocal imaging. For intracellular staining of HMGB1, permeabilization buffer (0.1 % Triton X-100) were applied for 10 min before blocking.

6.4.5 Synergistic effects of MIT and CEL at various combination ratios

Synergy of MIT in combination with CEL were tested using MTT assays. BPD6 and 3T3-T cells were seeded onto 96-well plates (5×10^3 cells per well). After overnight incubation, cells in each well were incubated with various concentrations of MIT, CEL, or combinations of MIT and CEL at a molar ratio of 1:10, 1:5, 1:2, 1:1, 2:1, 5:1, or 10:1 (MIT+CEL). After 24 h incubation, cell cytotoxicity was assessed by MTT assay. The synergy of MIT and CEL combination treatment was evaluated by calculating the combination index (CI) based on the level of synergism (median-effect analysis). The classificatory of synergy are: additive (CI = 1), synergistic (CI < 1), or antagonistic (CI > 1). IC₅₀ value was calculated using GraphPad Prism software.

6.4.6 Synthesis and characterization of the drug-loaded AEAA-modified NP (APS NP)

The APS copolymers were obtained by previous reported method.¹⁸⁷ Briefly, AEAA ligand (71.3 % yield) and AEAA-PEG-2,2-bis(acryloyloxymethyl)propionate (AEAA-PEG-BAP) (91.1 % yield) were first synthesized. Then, all the synthetic materials were dissolved in anhydrous DMSO for Michael-type step-polymerization. The reaction was gently stirred in oil bath (60 °C) for 60 h under nitrogen protection. To obtain the final products of APS NP, the mixture was dropped into excessively cold ethyl ether and dialyzed in a dialysis tube in PBS (pH 7.4) with a molecular weight of MW 5000, followed by freeze-drying (78.4 % yield).

The APS copolymer was confirmed by ¹H NMR (at 500 MHz, Bruker, USA) with deuterated chloroform (CDCl₃) as the solvent. As shown in Figure, the signals at 3.66 ppm are the characteristic peaks for –OCH₂CH₂– in PEG-AEAA; the four peaks at 5.31, 3.15, 3.10, and 2.77 ppm correspond to the –NH-CH₂-CH₂-NH– moieties; the peak at 3.58 ppm is characteristic

for the -O-CH₃ end group in PEG-AEAA. The signals at 2.69, 1.32, and 1.51 ppm indicate a C–C single bond in 1,6-hexanediol. The signals at 4.01 and 2.48 ppm were generated by -O-CH₂- and O-CO-CH₂- moieties in the 1,6-hexanediol diacrylate, respectively. The signal at 2.57 ppm was generated by the C–C single bond and the tertiary amine in the piperazine ring.

APS NP were prepared using the solvent evaporation method. In brief, 10 mg of the APS copolymer and MIT+CEL combination (5:1) were dissolved in 1 mL acetonitrile/methanol (1: 1) and gently added to 10 mL PBS (pH 7.4). The residual methanol and acetonitrile were water-bathed (45 °C) for 15 min. The solution was centrifuged at 4,000 rpm (10 min) and filtered by 0.18 µm filter membranes to remove the unloaded MIT and CEL. The Non-drug loaded blank APS NP were prepared by the same process but without loading any cargo. To evaluate the redox-sensitivity and pH-triggered charge reversal, the zeta potential and nanoparticle size were measured DLS (Malvern, United Kingdom) under different conditions: the normal physiological conditions (pH 7.4), the acidic extracellular TME (pH 6.5), and the intracellular reductive environment (10 mM GSH). The stability of drug-loaded NPs was recorded for 72 h. DLE and DEE of MIT and CEL in NP were quantified using HPLC (Shimadzu LC-20AT, Japan). The morphological examination was detected under JEOL 100CX II TEM (JEOL, Japan). The particle size changes of the APS NP (1 mg/mL) under reductive (10 mM GSH) and/or acidic environments (pH 6.5 or 5.0) were investigated using DLS measurements.

6.4.7 Controlled MIT and CEL release from APS NP in vitro

The release kinetics of MIT and CEL from the NP was investigated in four different mediums using the dialysis tube method. The medium consisted of either 1) pH 7.4, 0.01 M PBS buffer, 2) pH 7.4, 0.01 M PBS buffer with 10 mM GSH, 3) pH 6.5, 0.01 M PBS buffer, or 4) pH 6.5, 0.01 M PBS buffer with 10 mM GSH. Tween 80 (0.5 % w/w) were added to all medium,

then 1.0 mL of the MIT+CEL-loaded NPs solutions (0.1 mg/mL) were transferred into dialysis bags (MW 3500) with 30 mL of such medium. The release of drugs in different mediums were measured using HPLC.

6.4.8 Biocompatibility assay

The hemolytic activity was measured at pH 7.4, pH 6.5, and pH 5.0 with red blood cells (RBCs). Mice RBCs were extracted from plasma by 2,000 rpm centrifugation for 15 min and two washes. Triton X-100 was used as a positive control. The suspensions of RBCs were added to copolymer samples (0.1 to 2 mg/mL) or Triton X-100, and then compared between groups.

6.4.9 Drug distribution assays

To investigate the distribution of drug-loaded NP in vivo, Cy5-loaded NP (3 μ g/kg) was prepared by the same method as previously mentioned.¹⁸⁷ Mice were injected with Cy5-loaded APS NP and sacrificed after 24 h. Tumors and major organs were collected accordingly and subject to IVIS[®] Kinetics Optical System (Perkin Elmer, CA) for imaging and quantifications.

The intra-tumoral cellular uptake of NPs was evaluated using flow cytometer. Briefly, tumor tissues were dissociated with 1 mg/mL collagenase and 200 μ g/mL DNAase (Invitrogen) in DMED/2 % FBS for 40 min to generate a single-cell suspension. Major cell populations within TME, such as tumor cells, TAFs, macrophages, MDSCs, Tregs, and DCs were stained for quantification. The ratios of Cy5-loaded NP distributed in these different cell populations were calculated accordingly.

LC/MS instrument (Shimadzu LCMS-2020, Japan) was also utilized to quantitatively analyze the accumulation of drugs (delivered by APS NP or delivered *i.v.* as free drug) in the tumor site at predetermined times (4, 8, 12, 24 h) and to study the pharmacokinetics profile. The

separation of analyses was by using Thermo Scientific C18 column (100 mm × 4.6 mm, 2.6 μm) with flow rate of 0.2 mL/min and 35 °C column temperature.

6.4.10 Assays on tumor growth, metastasis and host survival

On day 0, mice were inoculated subcutaneously on lower flank with 1×10^6 BPD6 cells. Tumor growth were measured by digital caliper where $\text{volume} = 0.5 \times \text{length} \times \text{width} \times \text{height}$. Mice were randomized into treatment groups ($n = 15\text{-}20$) when tumor volume reach $\sim 200\text{-}300 \text{ mm}^3$. Groups were named as follows: PBS treated control (the PBS group), APS NP with no drug loaded (the blank NP group), MIT+CEL (5:1) administrated *i.v.* (2 mg/kg of CEL per dose) (the M+C group), MIT+CEL (5:1) formulated into APS NP and administrated *i.v.* (160 μg/kg of CEL per dose) (the M+C NP group), and as single controls, MIT loaded APS NP (the M NP group), as well as CEL loaded APS NP (the C NP group). Treatment groups were administrated on day 13, 15, 17, 19 after tumor inoculation. Mice weight and health conditions were monitored every 2 days. Once tumors reached $\sim 20 \text{ mm}$ in one dimension, mice were humanely sacrificed. Long-term host survival was monitored and calculated by Kaplan-Meier curves in GraphPad Prism software. At the endpoint of survival monitor, metastasis study was performed as major organs were collected, fixed in 4 % PFA, and H&E stained for pathology observation.

6.4.11 Cell cycle assay

Briefly, BPD6 and 3T3-T cells were seeded in 6-well plate (1.5×10^5 cells per well) and incubated for 48 h. Then, cells were treated with either blank APS NPs (100 mg/mL), MIT, CEL, MIT and CEL in combination (the MIT+CEL group), or MIT+CEL-loaded NPs (the MIT+CEL NP group) for 48 h. Cells were then collected, fixed, stained with PI staining solution, and then

measured by flow cytometer (BD Biosciences, USA). For each sample, 10,000 events were recorded and compared between groups.

6.4.12 Apoptosis assay

Cell apoptosis assay was performed by Annexin V-FITC/PI double staining. Briefly, cells were seeded in 6-well plate (1.5×10^5 cells per well) and incubated for 24 h. Then, cells were treated with either blank APS NPs (100 mg/mL), MIT, CEL, MIT+CEL, or MIT+CEL NPs for 48 h. Cells were stained with Annexin V-FITC assay kit (Biovision, USA) and then measured by flow cytometer (BD Biosciences, USA). For each sample, 10,000 events were collected.

6.4.13 Flow cytometry assay

The flow cytometry assay mainly characterized the change of immune cells within TME, as previously reported. In brief, mice were humanely sacrificed and the whole tumors were collected and incubated at 37 °C for 40-50 min, with the addition of collagenase A and DNAase. After three rounds of PBS washes, single cell suspensions were harvested in MACs buffer, then subjected to fluorescein-conjugated staining. For intracellular staining, penetration buffer (BD, Franklin Lakes, NJ) must be applied before adding antibodies. All stained cells were subject to flow cytometer.

6.4.14 Immunofluorescence staining and Masson trichrome staining

Staining was performed on paraffin-embedded sections from tumor tissues. Briefly, all tissues for paraffin-embedding were resected, rinsed in PBS, and placed in 4 % PFA for over 48 h at 4 °C. Immunofluorescence staining was performed by deparaffinization, antigen retrieval, permeabilization, and blocking in 1 % bovine serum albumin. All antibodies conjugated with fluorophores were added to tissue slides for at least 12 h at 4 °C. Then, nuclei were

counterstained with Prolong® Diamond Antifade Mountant with DAPI (ThermoFisher Scientific). Stained slides were imaged with Zeiss 880 Confocal microscopy (Germany). Five randomly microscopic fields were selected and quantified by Image J software. The Masson Trichrome assay was performed to detect collagen among tumor tissue. Tumor slides were stained using a Masson Trichrome Kit by the UNC Tissue Procurement Core.

6.4.15 Quantitative real-time PCR (RT-PCR) assay

Total RNA was extracted from the whole tumor using RNeasy® Microarray Tissue Mini Kit (Qiagen, Hilden, Germany). We then reverse-transcribed cDNA with iScript™ cDNA Synthesis Kit and amplify cDNA with iScript™ Reverse Transcription Supermix for RT-PCR (Bio-Rad, Hercules, CA). RT-PCR reactions were run in 7500 Real-Time PCR System and subject to analysis with 7500 Software, compared to and normalized by GAPDH endogenous control.

6.4.16 TUNEL assay

According to DeadEnd Fluorometric TUNEL System (Promega, Madison, WI) instructions, tumor tissue slides were stained and subject to fluorescence microscopy imaging. Fragmented DNA of apoptotic cells (FITC-positive) indicate TUNEL-positive nuclei. Slides were mounted, and nuclei were stained with Prolong® Diamond Antifade Mountant with DAPI (ThermoFisher Scientific), followed by imaging under Confocal microscopy.

6.4.17 Safety of treatments

All mice under different treatments were humanely sacrificed at endpoint of tumor inhibition study, where whole blood and serum of hosts were harvested and subject to test by UNC histology facility. Creatinine, BUN, AST and ALT indicate renal and liver functions. RBC,

WBC, PLT, HGB and HCT indicate myelosuppression level. Major organs were collected, H&E stained and compared. Throughout the tumor inhibition study, mice body weights were monitored and recorded every other day starting from the treatment.

6.4.18 Statistical analysis

One-way ANOVA and a two tailed Student's t-test were performed in Prism 5.0 Software. Data were compare with PBS control group and between groups. Data averages from each group were present as mean \pm SD. *: $p < 0.05$, **: $p < 0.01$, ***: $p < 0.001$.

CHAPTER 7

SUMMARY AND FUTURE PERSPECTIVES

Management of advanced melanoma is still a major challenge and gaining a better understanding of melanoma biology is essential to address the challenges associated with existing therapies. In clinical practice, the immune system in cancer patients has always been weakened by tumor invasion and chemotherapy, and the understanding of immunotherapy in recent years has become a promising strategy for cancer treatment and immune system reconstruction.⁴⁵ To effectively diagnose and treat melanoma, and also provide preventive insights, we learn from successful animal models that present relative clinical symptoms. Adoptive T-cell therapy, therapeutic vaccines, and chimeric antigen receptor (CAR) T-cell therapy are some of the novel strategies currently being explored in clinical trials.

NPs can be potentially exploited as efficient drug delivery vehicles and may reduce side effects associated with some of the present therapeutics. Theoretically, the NP platforms can be exploited for combinatorial therapy by designing multi-modal particles. However, clinical translation of NP technologies needs further improvement. Although most investigations have focused on delivering therapy directly to melanocytes, a few of them have achieved better effects in an advanced melanoma models. Thus, more and more studies have explored the therapeutic potential of other target sites associated with melanoma.²⁰¹

Among those immunotherapies, cancer vaccines, which can be characterized by the use of subunit antigens, has been studied widely in cancer treatment over the years, and many clinical trials have been conducted based on these vaccination strategies. Although the identification and production of antigens has been accomplished, most cancer vaccine studies have failed to illustrate clinical benefit. Traditional vaccines are administered by intramuscular injection, where the local immune response is triggered in muscle cells and muscle-resident immune cells before the antigen-presenting cells like DCs infiltrate from circulation to capture antigens.²⁰² However, the same strategy cannot be simply employed in the treatment of cancer due to the complex microenvironment of the tumor, especially in advanced tumor models, where DCs in the TME are largely tolerogenic with compromised antigen capturing and presenting abilities.

For those failed vaccine clinical studies, most of the therapy employed a naked administration of the vaccine, and the rest were compromised by vectors like DCs, viral vectors, and even naked nucleic acids, which can hardly induce immune response because the immune cell evolved as more likely to recognize a dense, highly repetitive epitope arrangement of the antigen. However, the nanoparticle-based vaccine with targeted delivery-loading antigen brought promise to cancer vaccine development.²⁰³ With further understanding of TME, immunotherapy has reshaped the landscape of traditional chemotherapy and made novel delivery target strategies possible.²⁰⁴ Our group has revealed that a key mechanism of drug resistance in advanced melanoma models is due to the barrier created by stroma cells, which are a main component of the tumor immunosuppressive microenvironment, and further proved that the suppressive TME could be reversed by silencing the inhibitory cytokines secreted by tumor and stroma cells.⁸⁵ By co-formulating the immune-modulating agents with traditional chemotherapy drugs, a synergistic tumor inhibition effect was observed.^{87, 103} The work in this dissertation further indicated that co-

delivering vaccines with microenvironment modulation would greatly enhance treatment of melanoma.

For better vaccine design, systemic DC-targeted RNA vaccines formulated with lipid carriers in Phase 1 trials have indicated the possibility of a universally applicable strategy that could formulate polypeptide-antigen-based vaccines in the form of RNA.²⁰⁵ Aluminum salts, which act in part by generating antigen depots (and in part by stimulating chemokines) at the injection site, have been used in human vaccines for almost 80 years. In recent years, novel adjuvants, especially PRR ligands, have raised much attention. Because PRR activation can stimulate the production of different cytokines/chemokines that could further increase the host's ability to eliminate the pathogen. The encapsulation of pathogen-associated molecular patterns (PAMPs) to activate PRRs in vaccine formulations can often enhance and accelerate the induction of vaccine-specific immune response. PAMPs adjuvants can trigger the innate responses generating adaptive responses toward vaccine components.^{206, 207}

Several studies have shown that co-delivery of immunomodulatory agents, such as PAMP ligands, can enhance the immune response by cancer vaccines. This strategy can be accomplished by nanoparticle-based cancer vaccines, which incorporate the ligands into nanoparticles by encapsulation and covalent conjugation. Several formulation strategies have been developed for ligand conjugation. Adjuvants were co-encapsulated and further modifications were made to enhance the deposition of LNs to initiate stimulation. Superior tumor inhibition was observed in subcutaneous models and metastasis models. Because a considerable number of DCs reside in LNs, LNs can be a good target for cancer vaccines. Direct LN-targeting protein NPs show rapid targeting and prolonged retention, providing a new solution for melanoma treatment.²⁰⁸ In light of the recent publication from Ribas group,²⁰⁹ vaccine strategy

developed in this dissertation would help CTL infiltrate into TME, thus potentially work synergistically with the reported high response rates (70% OR/32% CR) of DM to anti-PD-1 therapy in clinics.

The study and clinical application of checkpoint inhibitors in cancer immunotherapy has shown excellent potential. In clinical settings, the antibody is given systemically and significantly increases the survival rate in advanced melanoma patients. Recent reports indicate that the side effects of autoimmune disease were observed due to the blockade of the normal function of T cells residing in normal tissue.²¹⁰ Thus, our development of a local macromolecule delivery vesicle has been proposed as a solution. Moreover, co-stimulatory molecules such as PD-L2 are still being studied, as well as the glycosylation of PD-L1, may serve as new target in immune checkpoint therapy.

The desmoplasia of our established tumor model resulted from not only oncogenic BRAF mutation and PTEN silencing, but also tumor-specific signaling pathway network (e.g., Wnt/beta-catenin signaling could be upregulating collagen production independent of other aspects of the DM phenotype). On murine model of DM, the most effective treatment we employed so far is the combination of chemo-immuno therapy that synergistically induce immunogenic tumor cell death thus boosting immune-recognition and long-term memory immune-surveillance. To identify neoantigens released from ICD is a possible direction of pursuing in the design of second-wave targeted therapy, thus eradicating residual tumor cells. Compared to personalized designed vaccination, this approach offers general and broader application. Melanoma, especially DM are highly metastatic, thus the identification of circulating tumor cells is also crucial for early detection and prevention of tumor metastasis, as well as facilitating a deeper understanding of tumor dormancy. In addition, tumor stroma within

immunosuppressive TME supported tumor cell growth as well as serving as the major source of collagen production. Our unpublished work indicates that FAP⁺ stroma cells neighboring tumor cells also harbor BRAF mutations in DM model, and that BRAF vaccination partially depletes these FAP⁺ cells, which improves CD8⁺ T cells' functions within the TME. Thus, the function of these oncogenic hybrid cells in the role of tumorigenesis, metastasis and EMT transition is of great interested in our follow-up studies.

REFERENCES

1. Siegel, R. L.; Miller, K. D.; Jemal, A., Cancer Statistics, 2016. *CA Cancer J Clin* **2016**, *66*, 7-30.
2. Houghton, A. N.; Polsky, D., Focus on Melanoma. *Cancer Cell* **2002**, *2*, 275-278.
3. Balch, C. M.; Soong, S. J.; Gershenwald, J. E.; Thompson, J. F.; Reintgen, D. S.; Cascinelli, N.; Urist, M.; McMasters, K. M.; Ross, M. I.; Kirkwood, J. M.; Atkins, M. B.; Thompson, J. A.; Coit, D. G.; Byrd, D.; Desmond, R.; Zhang, Y.; Liu, P. Y.; Lyman, G. H.; Morabito, A., Prognostic Factors Analysis of 17,600 Melanoma Patients: Validation of the American Joint Committee on Cancer Melanoma Staging System. *J Clin Oncol* **2001**, *19*, 3622-3634.
4. Azijli, K.; Stelloo, E.; Peters, G. J.; AJ, V. D. E., New Developments in the Treatment of Metastatic Melanoma: Immune Checkpoint Inhibitors and Targeted Therapies. *Anticancer Res* **2014**, *34*, 1493-1505.
5. Dudley, D. J., The Immune System in Health and Disease. *Baillieres Clin. Obstet. Gynaecol.* **1992**, *6*, 393-416.
6. Liu, Q.; Das, M.; Liu, Y.; Huang, L., Targeted Drug Delivery to Melanoma. *Adv Drug Deliv Rev* **2017**.
7. DeSantis, C. E.; Lin, C. C.; Mariotto, A. B.; Siegel, R. L.; Stein, K. D.; Kramer, J. L.; Alteri, R.; Robbins, A. S.; Jemal, A., Cancer Treatment and Survivorship Statistics, 2014. *CA Cancer J Clin* **2014**, *64*, 252-271.
8. Clark, W. H., Jr.; Elder, D. E.; Guerry, D. t.; Epstein, M. N.; Greene, M. H.; Van Horn, M., A Study of Tumor Progression: The Precursor Lesions of Superficial Spreading and Nodular Melanoma. *Hum Pathol* **1984**, *15*, 1147-1165.
9. Platz, A.; Egyhazi, S.; Ringborg, U.; Hansson, J., Human Cutaneous Melanoma; a Review of Nras and Braf Mutation Frequencies in Relation to Histogenetic Subclass and Body Site. *Mol Oncol* **2008**, *1*, 395-405.
10. Gloster, H. M., Jr.; Brodland, D. G., The Epidemiology of Skin Cancer. *Dermatol Surg* **1996**, *22*, 217-226.

11. Eskandarpour, M.; Huang, F.; Reeves, K. A.; Clark, E.; Hansson, J., Oncogenic Nras Has Multiple Effects on the Malignant Phenotype of Human Melanoma Cells Cultured in Vitro. *Int J Cancer* **2009**, *124*, 16-26.
12. Hall, B. E.; Bar-Sagi, D.; Nassar, N., The Structural Basis for the Transition from Ras-Gtp to Ras-Gdp. *Proc Natl Acad Sci U S A* **2002**, *99*, 12138-12142.
13. Marampon, F.; Ciccarelli, C.; Zani, B. M., Down-Regulation of C-Myc Following Mek/Erk Inhibition Halts the Expression of Malignant Phenotype in Rhabdomyosarcoma and in Non Muscle-Derived Human Tumors. *Mol Cancer* **2006**, *5*, 31.
14. Sharma, S. G.; Gulley, M. L., Braf Mutation Testing in Colorectal Cancer. *Arch Pathol Lab Med* **2010**, *134*, 1225-1228.
15. Xing, M.; Westra, W. H.; Tufano, R. P.; Cohen, Y.; Rosenbaum, E.; Rhoden, K. J.; Carson, K. A.; Vasko, V.; Larin, A.; Tallini, G.; Tolaney, S.; Holt, E. H.; Hui, P.; Umbricht, C. B.; Basaria, S.; Ewertz, M.; Tufaro, A. P.; Califano, J. A.; Ringel, M. D.; Zeiger, M. A., *et al.*, Braf Mutation Predicts a Poorer Clinical Prognosis for Papillary Thyroid Cancer. *J Clin Endocrinol Metab* **2005**, *90*, 6373-6379.
16. Chong, H.; Vikis, H. G.; Guan, K. L., Mechanisms of Regulating the Raf Kinase Family. *Cell Signal* **2003**, *15*, 463-469.
17. Davies, H.; Bignell, G. R.; Cox, C.; Stephens, P.; Edkins, S.; Clegg, S.; Teague, J.; Woffendin, H.; Garnett, M. J.; Bottomley, W.; Davis, N.; Dicks, E.; Ewing, R.; Floyd, Y.; Gray, K.; Hall, S.; Hawes, R.; Hughes, J.; Kosmidou, V.; Menzies, A., *et al.*, Mutations of the Braf Gene in Human Cancer. *Nature* **2002**, *417*, 949-954.
18. Michaloglou, C.; Vredeveld, L. C.; Mooi, W. J.; Peeper, D. S., Braf(E600) in Benign and Malignant Human Tumours. *Oncogene* **2008**, *27*, 877-895.
19. Wangari-Talbot, J.; Chen, S., Genetics of Melanoma. *Front Genet* **2012**, *3*, 330.
20. Inamdar, G. S.; Madhunapantula, S. V.; Robertson, G. P., Targeting the Mapk Pathway in Melanoma: Why Some Approaches Succeed and Other Fail. *Biochem Pharmacol* **2010**, *80*, 624-637.

21. Saldanha, G.; Purnell, D.; Fletcher, A.; Potter, L.; Gillies, A.; Pringle, J. H., High Braf Mutation Frequency Does Not Characterize All Melanocytic Tumor Types. *Int J Cancer* **2004**, *111*, 705-710.
22. Shao, Y.; Aplin, A. E., Akt3-Mediated Resistance to Apoptosis in B-Raf-Targeted Melanoma Cells. *Cancer Res* **2010**, *70*, 6670-6681.
23. Gao, N.; Zhang, Z.; Jiang, B. H.; Shi, X., Role of Pi3k/Akt/Mtor Signaling in the Cell Cycle Progression of Human Prostate Cancer. *Biochem Biophys Res Commun* **2003**, *310*, 1124-1132.
24. Hocker, T. L.; Singh, M. K.; Tsao, H., Melanoma Genetics and Therapeutic Approaches in the 21st Century: Moving from the Benchside to the Bedside. *J Invest Dermatol* **2008**, *128*, 2575-2595.
25. Stahl, J. M.; Sharma, A.; Cheung, M.; Zimmerman, M.; Cheng, J. Q.; Bosenberg, M. W.; Kester, M.; Sandirasegarane, L.; Robertson, G. P., Deregulated Akt3 Activity Promotes Development of Malignant Melanoma. *Cancer Res* **2004**, *64*, 7002-7010.
26. Khanna, C.; Hunter, K., Modeling Metastasis in Vivo. *Carcinogenesis* **2005**, *26*, 513-523.
27. Zaidi, M. R.; Day, C. P.; Merlino, G., From Uvs to Metastases: Modeling Melanoma Initiation and Progression in the Mouse. *J Invest Dermatol* **2008**, *128*, 2381-2391.
28. Merlino, G.; Flaherty, K.; Acquavella, N.; Day, C. P.; Aplin, A.; Holmen, S.; Topalian, S.; Van Dyke, T.; Herlyn, M., Meeting Report: The Future of Preclinical Mouse Models in Melanoma Treatment Is Now. *Pigment Cell Melanoma Res* **2013**, *26*, E8-E14.
29. Talmadge, J. E.; Singh, R. K.; Fidler, I. J.; Raz, A., Murine Models to Evaluate Novel and Conventional Therapeutic Strategies for Cancer. *Am J Pathol* **2007**, *170*, 793-804.
30. Gajewski, T. F.; Schreiber, H.; Fu, Y. X., Innate and Adaptive Immune Cells in the Tumor Microenvironment. *Nat Immunol* **2013**, *14*, 1014-1022.
31. McKinney, A. J.; Holmen, S. L., Animal Models of Melanoma: A Somatic Cell Gene Delivery Mouse Model Allows Rapid Evaluation of Genes Implicated in Human Melanoma. *Chin J Cancer* **2011**, *30*, 153-162.

32. Herlyn, M.; Fukunaga-Kalabis, M., What Is a Good Model for Melanoma? *J Invest Dermatol* **2010**, *130*, 911-912.
33. Beaumont, K. A.; Mohana-Kumaran, N.; Haass, N. K., Modeling Melanoma in Vitro and in Vivo. *Healthcare (Basel)* **2013**, *2*, 27-46.
34. Combest, A. J.; Roberts, P. J.; Dillon, P. M.; Sandison, K.; Hanna, S. K.; Ross, C.; Habibi, S.; Zamboni, B.; Muller, M.; Brunner, M.; Sharpless, N. E.; Zamboni, W. C., Genetically Engineered Cancer Models, but Not Xenografts, Faithfully Predict Anticancer Drug Exposure in Melanoma Tumors. *Oncologist* **2012**, *17*, 1303-1316.
35. Albino, A. P.; Le Strange, R.; Oliff, A. I.; Furth, M. E.; Old, L. J., Transforming Ras Genes from Human Melanoma: A Manifestation of Tumour Heterogeneity? *Nature* **1984**, *308*, 69-72.
36. Goel, V. K.; Lazar, A. J.; Warneke, C. L.; Redston, M. S.; Haluska, F. G., Examination of Mutations in Braf, Nras, and Pten in Primary Cutaneous Melanoma. *J Invest Dermatol* **2006**, *126*, 154-160.
37. Kato, M.; Takahashi, M.; Akhand, A. A.; Liu, W.; Dai, Y.; Shimizu, S.; Iwamoto, T.; Suzuki, H.; Nakashima, I., Transgenic Mouse Model for Skin Malignant Melanoma. *Oncogene* **1998**, *17*, 1885-1888.
38. Robins, A. H., *Biological Perspectives on Human Pigmentation*. Cambridge University Press: Cambridge, UK ; New York, 2005; p xiii, 253 p.
39. Sauter, E. R.; Herlyn, M., Molecular Biology of Human Melanoma Development and Progression. *Mol Carcinog* **1998**, *23*, 132-143.
40. Gray-Schopfer, V.; Wellbrock, C.; Marais, R., Melanoma Biology and New Targeted Therapy. *Nature* **2007**, *445*, 851-857.
41. Aubin, F.; Humbey, O.; Humbert, P.; Laurent, R.; Mougin, C., [Melanoma: Role of Ultraviolet Radiation: From Physiology to Pathology]. *Presse Med* **2001**, *30*, 546-551.
42. Soengas, M. S.; Lowe, S. W., Apoptosis and Melanoma Chemoresistance. *Oncogene* **2003**, *22*, 3138-3151.

43. Avril, M. F.; Aamdal, S.; Grob, J. J.; Hauschild, A.; Mohr, P.; Bonerandi, J. J.; Weichenthal, M.; Neuber, K.; Bieber, T.; Gilde, K.; Guillem Porta, V.; Fra, J.; Bonnetterre, J.; Saiag, P.; Kamanabrou, D.; Pehamberger, H.; Suflarsky, J.; Gonzalez Larriba, J. L.; Scherrer, A.; Menu, Y., Fotemustine Compared with Dacarbazine in Patients with Disseminated Malignant Melanoma: A Phase Iii Study. *J Clin Oncol* **2004**, *22*, 1118-1125.
44. Schwartzenuber, D. J.; Lawson, D. H.; Richards, J. M.; Conry, R. M.; Miller, D. M.; Treisman, J.; Gailani, F.; Riley, L.; Conlon, K.; Pockaj, B.; Kendra, K. L.; White, R. L.; Gonzalez, R.; Kuzel, T. M.; Curti, B.; Leming, P. D.; Whitman, E. D.; Balkissoon, J.; Reintgen, D. S.; Kaufman, H., *et al.*, Gp100 Peptide Vaccine and Interleukin-2 in Patients with Advanced Melanoma. *N Engl J Med* **2011**, *364*, 2119-2127.
45. Zhu, Z.; Liu, W.; Gotlieb, V., The Rapidly Evolving Therapies for Advanced Melanoma--Towards Immunotherapy, Molecular Targeted Therapy, and Beyond. *Crit Rev Oncol Hematol* **2016**, *99*, 91-99.
46. Chapman, P. B.; Hauschild, A.; Robert, C.; Haanen, J. B.; Ascierto, P.; Larkin, J.; Dummer, R.; Garbe, C.; Testori, A.; Maio, M.; Hogg, D.; Lorigan, P.; Lebbe, C.; Jouary, T.; Schadendorf, D.; Ribas, A.; O'Day, S. J.; Sosman, J. A.; Kirkwood, J. M.; Eggermont, A. M., *et al.*, Improved Survival with Vemurafenib in Melanoma with Braf V600e Mutation. *N Engl J Med* **2011**, *364*, 2507-2516.
47. Long, G. V.; Stroyakovskiy, D.; Gogas, H.; Levchenko, E.; de Braud, F.; Larkin, J.; Garbe, C.; Jouary, T.; Hauschild, A.; Grob, J. J.; Chiarion Sileni, V.; Lebbe, C.; Mandala, M.; Millward, M.; Arance, A.; Bondarenko, I.; Haanen, J. B.; Hansson, J.; Utikal, J.; Ferraresi, V., *et al.*, Combined Braf and Mek Inhibition Versus Braf Inhibition Alone in Melanoma. *N Engl J Med* **2014**, *371*, 1877-1888.
48. Wilden, S. M.; Lang, B. M.; Mohr, P.; Grabbe, S., Immune Checkpoint Inhibitors: A Milestone in the Treatment of Melanoma. *J Dtsch Dermatol Ges* **2016**, *14*, 685-695.
49. Topalian, S. L.; Taube, J. M.; Anders, R. A.; Pardoll, D. M., Mechanism-Driven Biomarkers to Guide Immune Checkpoint Blockade in Cancer Therapy. *Nat Rev Cancer* **2016**, *16*, 275-287.
50. Middleton, M. R.; Grob, J. J.; Aaronson, N.; Fierlbeck, G.; Tilgen, W.; Seiter, S.; Gore, M.; Aamdal, S.; Cebon, J.; Coates, A.; Dreno, B.; Henz, M.; Schadendorf, D.; Kapp, A.; Weiss, J.; Fraass, U.; Statkevich, P.; Muller, M.; Thatcher, N., Randomized Phase Iii Study of Temozolomide Versus Dacarbazine in the Treatment of Patients with Advanced Metastatic Malignant Melanoma. *J Clin Oncol* **2000**, *18*, 158-166.

51. Sasse, A. D.; Sasse, E. C.; Clark, L. G.; Ulloa, L.; Clark, O. A., Chemoimmunotherapy Versus Chemotherapy for Metastatic Malignant Melanoma. *Cochrane Database Syst Rev* **2007**, CD005413.
52. Srivastava, A.; Ralhan, R.; Kaur, J., Angiogenesis in Cutaneous Melanoma: Pathogenesis and Clinical Implications. *Microscopy Research and Technique* **2003**, *60*, 208-224.
53. Perez, D. G.; Suman, V. J.; Fitch, T. R.; Amatruda, T.; Morton, R. F.; Jilani, S. Z.; Constantinou, C. L.; Egner, J. R.; Kottschade, L. A.; Markovic, S. N., Phase 2 Trial of Carboplatin, Weekly Paclitaxel, and Biweekly Bevacizumab in Patients with Unresectable Stage Iv Melanoma. *Cancer* **2009**, *115*, 119-127.
54. Eberle, J.; Hossini, A. M., Expression and Function of Bcl-2 Proteins in Melanoma. *Curr Genomics* **2008**, *9*, 409-419.
55. Bedikian, A. Y.; Garbe, C.; Conry, R.; Lebbe, C.; Grob, J. J.; Genasense Melanoma Study, G., Dacarbazine with or without Oblimersen (a Bcl-2 Antisense Oligonucleotide) in Chemotherapy-Naive Patients with Advanced Melanoma and Low-Normal Serum Lactate Dehydrogenase: 'The Agenda Trial'. *Melanoma Res* **2014**, *24*, 237-243.
56. McConnell, J. L.; Wadzinski, B. E., Targeting Protein Serine/Threonine Phosphatases for Drug Development. *Mol Pharmacol* **2009**, *75*, 1249-1261.
57. Van Cutsem, E.; van de Velde, H.; Karasek, P.; Oettle, H.; Vervenne, W. L.; Szawlowski, A.; Schoffski, P.; Post, S.; Verslype, C.; Neumann, H.; Safran, H.; Humblet, Y.; Perez Ruixo, J.; Ma, Y.; Von Hoff, D., Phase Iii Trial of Gemcitabine Plus Tipifarnib Compared with Gemcitabine Plus Placebo in Advanced Pancreatic Cancer. *J Clin Oncol* **2004**, *22*, 1430-1438.
58. Villanueva, J.; Vultur, A.; Lee, J. T.; Somasundaram, R.; Fukunaga-Kalabis, M.; Cipolla, A. K.; Wubbenhorst, B.; Xu, X.; Gimotty, P. A.; Kee, D.; Santiago-Walker, A. E.; Letrero, R.; D'Andrea, K.; Pushparajan, A.; Hayden, J. E.; Brown, K. D.; Laquerre, S.; McArthur, G. A.; Sosman, J. A.; Nathanson, K. L., *et al.*, Acquired Resistance to Braf Inhibitors Mediated by a Raf Kinase Switch in Melanoma Can Be Overcome by Cotargeting Mek and Igf-1r/Pi3k. *Cancer Cell* **2010**, *18*, 683-695.
59. Bucheit, A. D.; Davies, M. A., Emerging Insights into Resistance to Braf Inhibitors in Melanoma. *Biochem Pharmacol* **2014**, *87*, 381-389.

60. Hirata, E.; Girotti, M. R.; Viros, A.; Hooper, S.; Spencer-Dene, B.; Matsuda, M.; Larkin, J.; Marais, R.; Sahai, E., Intravital Imaging Reveals How Braf Inhibition Generates Drug-Tolerant Microenvironments with High Integrin Beta1/Fak Signaling. *Cancer Cell* **2015**, *27*, 574-588.
61. Deng, W.; Gopal, Y. N.; Scott, A.; Chen, G.; Woodman, S. E.; Davies, M. A., Role and Therapeutic Potential of Pi3k-Mtor Signaling in De Novo Resistance to Braf Inhibition. *Pigment Cell Melanoma Res* **2012**, *25*, 248-258.
62. Rodrik-Outmezguine, V. S.; Chandarlapaty, S.; Pagano, N. C.; Poulikakos, P. I.; Scaltriti, M.; Moskatel, E.; Baselga, J.; Guichard, S.; Rosen, N., Mtor Kinase Inhibition Causes Feedback-Dependent Biphasic Regulation of Akt Signaling. *Cancer Discov* **2011**, *1*, 248-259.
63. Poulikakos, P. I.; Zhang, C.; Bollag, G.; Shokat, K. M.; Rosen, N., Raf Inhibitors Transactivate Raf Dimers and Erk Signalling in Cells with Wild-Type Braf. *Nature* **2010**, *464*, 427-430.
64. Freeman, G. J.; Long, A. J.; Iwai, Y.; Bourque, K.; Chernova, T.; Nishimura, H.; Fitz, L. J.; Malenkovich, N.; Okazaki, T.; Byrne, M. C.; Horton, H. F.; Fouser, L.; Carter, L.; Ling, V.; Bowman, M. R.; Carreno, B. M.; Collins, M.; Wood, C. R.; Honjo, T., Engagement of the Pd-1 Immunoinhibitory Receptor by a Novel B7 Family Member Leads to Negative Regulation of Lymphocyte Activation. *J Exp Med* **2000**, *192*, 1027-1034.
65. Lu, B.; Finn, O. J., T-Cell Death and Cancer Immune Tolerance. *Cell Death Differ* **2007**, *15*, 70-79.
66. Das, R.; Verma, R.; Sznol, M.; Boddupalli, C. S.; Gettinger, S. N.; Kluger, H.; Callahan, M.; Wolchok, J. D.; Halaban, R.; Dhodapkar, M. V.; Dhodapkar, K. M., Combination Therapy with Anti-Ctla-4 and Anti-Pd-1 Leads to Distinct Immunologic Changes in Vivo. *J Immunol* **2015**, *194*, 950-959.
67. Anderson, A. C.; Joller, N.; Kuchroo, V. K., Lag-3, Tim-3, and Tigit: Co-Inhibitory Receptors with Specialized Functions in Immune Regulation. *Immunity* **2016**, *44*, 989-1004.
68. Ogi, C.; Aruga, A., Immunological Monitoring of Anticancer Vaccines in Clinical Trials. *Oncoimmunology* **2013**, *2*, e26012.
69. Rosenberg, S. A.; Dudley, M. E., Adoptive Cell Therapy for the Treatment of Patients with Metastatic Melanoma. *Curr Opin Immunol* **2009**, *21*, 233-240.

70. Rosenberg, S. A.; Yang, J. C.; Sherry, R. M.; Kammula, U. S.; Hughes, M. S.; Phan, G. Q.; Citrin, D. E.; Restifo, N. P.; Robbins, P. F.; Wunderlich, J. R.; Morton, K. E.; Laurencot, C. M.; Steinberg, S. M.; White, D. E.; Dudley, M. E., Durable Complete Responses in Heavily Pretreated Patients with Metastatic Melanoma Using T-Cell Transfer Immunotherapy. *Clinical Cancer Research* **2011**, *17*, 4550-4557.

71. Garfall, A. L.; Maus, M. V.; Hwang, W.-T.; Lacey, S. F.; Mahnke, Y. D.; Melenhorst, J. J.; Zheng, Z.; Vogl, D. T.; Cohen, A. D.; Weiss, B. M.; Dengel, K.; Kerr, N. D. S.; Bagg, A.; Levine, B. L.; June, C. H.; Stadtmauer, E. A., Chimeric Antigen Receptor T Cells against Cd19 for Multiple Myeloma. *New England Journal of Medicine* **2015**, *373*, 1040-1047.

72. Kaufman, H. L.; Kohlhapp, F. J.; Zloza, A., Oncolytic Viruses: A New Class of Immunotherapy Drugs. *Nat Rev Drug Discov* **2015**, *14*, 642-662.

73. Kakavand, H.; Wilmott, J. S.; Menzies, A. M.; Vilain, R.; Haydu, L. E.; Yearley, J. H.; Thompson, J. F.; Kefford, R. F.; Hersey, P.; Long, G. V.; Scolyer, R. A., Pd-L1 Expression and Tumor-Infiltrating Lymphocytes Define Different Subsets of Mapk Inhibitor–Treated Melanoma Patients. *Clinical Cancer Research* **2015**, *21*, 3140-3148.

74. Hu-Lieskovan, S.; Robert, L.; Homet Moreno, B.; Ribas, A., Combining Targeted Therapy with Immunotherapy in Braf-Mutant Melanoma: Promise and Challenges. *J Clin Oncol* **2014**, *32*, 2248-2254.

75. Ribas, A.; Hodi, F. S.; Callahan, M.; Konto, C.; Wolchok, J., Hepatotoxicity with Combination of Vemurafenib and Ipilimumab. *New England Journal of Medicine* **2013**, *368*, 1365-1366.

76. Bazak, R.; Houri, M.; El Achy, S.; Kamel, S.; Refaat, T., Cancer Active Targeting by Nanoparticles: A Comprehensive Review of Literature. *J Cancer Res Clin Oncol* **2015**, *141*, 769-784.

77. Guo, S.; Lin, C. M.; Xu, Z.; Miao, L.; Wang, Y.; Huang, L., Co-Delivery of Cisplatin and Rapamycin for Enhanced Anticancer Therapy through Synergistic Effects and Microenvironment Modulation. *ACS Nano* **2014**, *8*, 4996-5009.

78. Xu, Z.; Ramishetti, S.; Tseng, Y. C.; Guo, S.; Wang, Y.; Huang, L., Multifunctional Nanoparticles Co-Delivering Trp2 Peptide and CpG Adjuvant Induce Potent Cytotoxic T-Lymphocyte Response against Melanoma and Its Lung Metastasis. *J Control Release* **2013**, *172*, 259-265.

79. Anselmo, A. C.; Mitragotri, S., Nanoparticles in the Clinic. *Bioengineering & Translational Medicine* **2016**, *1*, 10-29.
80. Klemm, F.; Joyce, J. A., Microenvironmental Regulation of Therapeutic Response in Cancer. *Trends Cell Biol* **2015**, *25*, 198-213.
81. Junttila, M. R.; de Sauvage, F. J., Influence of Tumour Micro-Environment Heterogeneity on Therapeutic Response. *Nature* **2013**, *501*, 346-354.
82. Rammensee, H.; Bachmann, J.; Emmerich, N. P.; Bachor, O. A.; Stevanovic, S., Syfpeithi: Database for Mhc Ligands and Peptide Motifs. *Immunogenetics* **1999**, *50*, 213-219.
83. Cintolo, J. A.; Datta, J.; Xu, S.; Gupta, M.; Somasundaram, R.; Czerniecki, B. J., Type I-Polarized Braf-Pulsed Dendritic Cells Induce Antigen-Specific Cd8⁺ T Cells That Impact Braf-Mutant Murine Melanoma. *Melanoma Res* **2016**, *26*, 1-11.
84. Guo, X.; Huang, L., Recent Advances in Nonviral Vectors for Gene Delivery. *Acc Chem Res* **2012**, *45*, 971-979.
85. Xu, Z.; Wang, Y.; Zhang, L.; Huang, L., Nanoparticle-Delivered Transforming Growth Factor-Beta Sirna Enhances Vaccination against Advanced Melanoma by Modifying Tumor Microenvironment. *ACS Nano* **2014**, *8*, 3636-3645.
86. Czerkinsky, C. C.; Nilsson, L. A.; Nygren, H.; Ouchterlony, O.; Tarkowski, A., A Solid-Phase Enzyme-Linked Immunospot (Elispot) Assay for Enumeration of Specific Antibody-Secreting Cells. *J Immunol Methods* **1983**, *65*, 109-121.
87. Lu, Y.; Miao, L.; Wang, Y.; Xu, Z.; Zhao, Y.; Shen, Y.; Xiang, G.; Huang, L., Curcumin Micelles Remodel Tumor Microenvironment and Enhance Vaccine Activity in an Advanced Melanoma Model. *Mol Ther* **2016**, *24*, 364-374.
88. Andreatta, M.; Nielsen, M., Gapped Sequence Alignment Using Artificial Neural Networks: Application to the Mhc Class I System. *Bioinformatics* **2016**, *32*, 511-517.
89. Nielsen, M.; Lundegaard, C.; Worning, P.; Lauemoller, S. L.; Lamberth, K.; Buus, S.; Brunak, S.; Lund, O., Reliable Prediction of T-Cell Epitopes Using Neural Networks with Novel Sequence Representations. *Protein Sci* **2003**, *12*, 1007-1017.

90. Tseng, Y. C.; Xu, Z.; Guley, K.; Yuan, H.; Huang, L., Lipid-Calcium Phosphate Nanoparticles for Delivery to the Lymphatic System and Spect/Ct Imaging of Lymph Node Metastases. *Biomaterials* **2014**, *35*, 4688-4698.
91. Medzhitov, R.; Janeway, C. A., Jr., Decoding the Patterns of Self and Nonself by the Innate Immune System. *Science* **2002**, *296*, 298-300.
92. Umansky, V.; Sevko, A., Tumor Microenvironment and Myeloid-Derived Suppressor Cells. *Cancer Microenviron* **2013**, *6*, 169-177.
93. Rigel, D. S.; Carucci, J. A., Malignant Melanoma: Prevention, Early Detection, and Treatment in the 21st Century. *CA Cancer J Clin* **2000**, *50*, 215-236; quiz 237-240.
94. Restifo, N. P.; Dudley, M. E.; Rosenberg, S. A., Adoptive Immunotherapy for Cancer: Harnessing the T Cell Response. *Nat Rev Immunol* **2012**, *12*, 269-281.
95. Allen, T. M.; Cullis, P. R., Drug Delivery Systems: Entering the Mainstream. *Science* **2004**, *303*, 1818-1822.
96. Li, J.; Chen, Y. C.; Tseng, Y. C.; Mozumdar, S.; Huang, L., Biodegradable Calcium Phosphate Nanoparticle with Lipid Coating for Systemic Sirna Delivery. *J Control Release* **2010**, *142*, 416-421.
97. Reddy, R.; Zhou, F.; Nair, S.; Huang, L.; Rouse, B. T., In Vivo Cytotoxic T Lymphocyte Induction with Soluble Proteins Administered in Liposomes. *J Immunol* **1992**, *148*, 1585-1589.
98. Chen, W. S.; Xu, P. Z.; Gottlob, K.; Chen, M. L.; Sokol, K.; Shiyanova, T.; Roninson, I.; Weng, W.; Suzuki, R.; Tobe, K.; Kadowaki, T.; Hay, N., Growth Retardation and Increased Apoptosis in Mice with Homozygous Disruption of the Akt1 Gene. *Genes Dev* **2001**, *15*, 2203-2208.
99. Liu, Q.; Zhu, H.; Liu, Y.; Musetti, S.; Huang, L., Braf Peptide Vaccine Facilitates Therapy of Murine Braf-Mutant Melanoma. *Cancer Immunol Immunother* **2017**.
100. Motzer, R. J.; Hutson, T. E.; Tomczak, P.; Michaelson, M. D.; Bukowski, R. M.; Rixe, O.; Oudard, S.; Negrier, S.; Szczyluk, C.; Kim, S. T.; Chen, I.; Bycott, P. W.; Baum, C. M.; Figlin, R. A., Sunitinib Versus Interferon Alfa in Metastatic Renal-Cell Carcinoma. *N Engl J Med* **2007**, *356*, 115-124.

101. Yang, F.; Jove, V.; Xin, H.; Hedvat, M.; Van Meter, T. E.; Yu, H., Sunitinib Induces Apoptosis and Growth Arrest of Medulloblastoma Tumor Cells by Inhibiting Stat3 and Akt Signaling Pathways. *Mol. Cancer Res.* **2010**, *8*, 35-45.
102. Santini, D.; Vincenzi, B.; Venditti, O.; Dell'Aquila, E.; Frezza, A. M.; Silletta, M.; Guida, F. M.; Grasso, R. F.; Silvestris, N.; Lanzetta, G.; Tonini, G., Sunitinib in Malignant Melanoma: A Treatment Option Only for Kit-Mutated Patients? *Future Oncol.* **2013**, *9*, 1809-1811.
103. Huo, M.; Zhao, Y.; Satterlee, A. B.; Wang, Y.; Xu, Y.; Huang, L., Tumor-Targeted Delivery of Sunitinib Base Enhances Vaccine Therapy for Advanced Melanoma by Remodeling the Tumor Microenvironment. *J Control Release* **2017**, *245*, 81-94.
104. Meng, F.; Zhong, Z.; Feijen, J., Stimuli-Responsive Polymersomes for Programmed Drug Delivery. *Biomacromolecules* **2009**, *10*, 197-209.
105. Saha, R. N.; Vasanthakumar, S.; Bende, G.; Snehalatha, M., Nanoparticulate Drug Delivery Systems for Cancer Chemotherapy. *Mol. Membr. Biol.* **2010**, *27*, 215-231.
106. Miao, L.; Li, J.; Liu, Q.; Feng, R.; Das, M.; Lin, C. M.; Goodwin, T. J.; Dorosheva, O.; Liu, R.; Huang, L., Transient and Local Expression of Chemokine and Immune Checkpoint Traps to Treat Pancreatic Cancer. *ACS Nano* **2017**, *11*, 8690-8706.
107. Luo, C.; Miao, L.; Zhao, Y.; Musetti, S.; Wang, Y.; Shi, K.; Huang, L., A Novel Cationic Lipid with Intrinsic Antitumor Activity to Facilitate Gene Therapy of Trail DNA. *Biomaterials* **2016**, *102*, 239-248.
108. Miao, L.; Liu, Q.; Lin, C. M.; Luo, C.; Wang, Y.; Liu, L.; Yin, W.; Hu, S.; Kim, W. Y.; Huang, L., Targeting Tumor-Associated Fibroblasts for Therapeutic Delivery in Desmoplastic Tumors. *Cancer Res* **2017**, *77*, 719-731.
109. Zhou, L.; Yang, K.; Andl, T.; Wickett, R. R.; Zhang, Y., Perspective of Targeting Cancer-Associated Fibroblasts in Melanoma. *J. Cancer* **2015**, *6*, 717-726.
110. Rygiel, T. P.; Stolte, E. H.; de Ruiter, T.; van de Weijer, M. L.; Meyaard, L., Tumor-Expressed Collagens Can Modulate Immune Cell Function through the Inhibitory Collagen Receptor Lair-1. *Mol. Immunol.* **2011**, *49*, 402-406.
111. Liu, D.; Li, G.; Avella, D. M.; Kimchi, E. T.; Kaifi, J. T.; Rubinstein, M. P.; Camp, E. R.; Rockey, D. C.; Schell, T. D.; Staveley-O'Carroll, K. F., Sunitinib Represses Regulatory T Cells to

Overcome Immunotolerance in a Murine Model of Hepatocellular Cancer. *Oncoimmunology* **2017**, *7*, e1372079.

112. Jones, E. A.; Pringle, J. H.; Angel, C. A.; Rees, R. C., Th1/Th2 Cytokine Expression and Its Relationship with Tumor Growth in B Cell Non-Hodgkin's Lymphoma (Nhl). *Leuk. Lymphoma* **2002**, *43*, 1313-1321.

113. Bracci, L.; Schiavoni, G.; Sistigu, A.; Belardelli, F., Immune-Based Mechanisms of Cytotoxic Chemotherapy: Implications for the Design of Novel and Rationale-Based Combined Treatments against Cancer. *Cell Death Differ.* **2014**, *21*, 15-25.

114. Zhao, Y.; Wang, W.; Guo, S.; Wang, Y.; Miao, L.; Xiong, Y.; Huang, L., Polymetformin Combines Carrier and Anticancer Activities for in Vivo Sirna Delivery. *Nat Commun* **2016**, *7*, 11822.

115. Tao, L.; Huang, G.; Song, H.; Chen, Y.; Chen, L., Cancer Associated Fibroblasts: An Essential Role in the Tumor Microenvironment. *Oncol. Lett.* **2017**, *14*, 2611-2620.

116. Cohen, N.; Shani, O.; Raz, Y.; Sharon, Y.; Hoffman, D.; Abramovitz, L.; Erez, N., Fibroblasts Drive an Immunosuppressive and Growth-Promoting Microenvironment in Breast Cancer Via Secretion of Chitinase 3-Like 1. *Oncogene* **2017**, *36*, 4457-4468.

117. Somasundaram, R.; Zhang, G.; Fukunaga-Kalabis, M.; Perego, M.; Krepler, C.; Xu, X.; Wagner, C.; Hristova, D.; Zhang, J.; Tian, T.; Wei, Z.; Liu, Q.; Garg, K.; Griss, J.; Hards, R.; Maurer, M.; Hafner, C.; Mayerhofer, M.; Karanikas, G.; Jalili, A., *et al.*, Tumor-Associated B-Cells Induce Tumor Heterogeneity and Therapy Resistance. *Nat Commun* **2017**, *8*, 607.

118. Miao, L.; Guo, S.; Lin, C. M.; Liu, Q.; Huang, L., Nanoformulations for Combination or Cascade Anticancer Therapy. *Adv Drug Deliv Rev* **2017**, *115*, 3-22.

119. Kalluri, R.; Zeisberg, M., Fibroblasts in Cancer. *Nat Rev Cancer* **2006**, *6*, 392-401.

120. Wu, X.; Wu, X.; Ma, Y.; Shao, F.; Tan, Y.; Tan, T.; Gu, L.; Zhou, Y.; Sun, B.; Sun, Y.; Wu, X.; Xu, Q., Cug-Binding Protein 1 Regulates Hsc Activation and Liver Fibrogenesis. *Nat Commun* **2016**, *7*, 13498.

121. Kim, J. H.; Park, Y. M.; Shin, J. S.; Park, S. J.; Choi, J. H.; Jung, H. J.; Park, H. J.; Lee, K. T., Fraxinellone Inhibits Lipopolysaccharide-Induced Inducible Nitric Oxide Synthase and

Cyclooxygenase-2 Expression by Negatively Regulating Nuclear Factor-Kappa B in Raw 264.7 Macrophages Cells. *Biol. Pharm. Bull.* **2009**, 32, 1062-1068.

122. Sun, Y.; Qin, Y.; Gong, F. Y.; Wu, X. F.; Hua, Z. C.; Chen, T.; Xu, Q., Selective Triggering of Apoptosis of Concanavalin a-Activated T Cells by Fraxinellone for the Treatment of T-Cell-Dependent Hepatitis in Mice. *Biochem. Pharmacol.* **2009**, 77, 1717-1724.

123. Wu, X. F.; Ouyang, Z. J.; Feng, L. L.; Chen, G.; Guo, W. J.; Shen, Y.; Wu, X. D.; Sun, Y.; Xu, Q., Suppression of Nf-Kappab Signaling and Nlrp3 Inflammasome Activation in Macrophages Is Responsible for the Amelioration of Experimental Murine Colitis by the Natural Compound Fraxinellone. *Toxicol. Appl. Pharmacol.* **2014**, 281, 146-156.

124. Dasargyri, A.; Hervella, P.; Christiansen, A.; Proulx, S. T.; Detmar, M.; Leroux, J. C., Findings Questioning the Involvement of Sigma-1 Receptor in the Uptake of Anisamide-Decorated Particles. *J Control Release* **2016**, 224, 229-238.

125. Giavina-Bianchi, M. H.; Giavina-Bianchi, P. F. J.; Festa, C. N., Melanoma: Tumor Microenvironment and New Treatments. *An. Bras. Dermatol.* **2017**, 92, 156-166.

126. Olbryt, M., [Role of Tumor Microenvironment in the Formation and Progression of Skin Melanoma]. *Postepy Hig Med Dosw (Online)* **2013**, 67, 413-432.

127. Gupta, A.; Eral, H. B.; Hatton, T. A.; Doyle, P. S., Nanoemulsions: Formation, Properties and Applications. *Soft Matter* **2016**, 12, 2826-2841.

128. Jaiswal, M.; Dudhe, R.; Sharma, P. K., Nanoemulsion: An Advanced Mode of Drug Delivery System. *3 Biotech* **2015**, 5, 123-127.

129. Hu, K.; Miao, L.; Goodwin, T. J.; Li, J.; Liu, Q.; Huang, L., Quercetin Remodels the Tumor Microenvironment to Improve the Permeation, Retention, and Antitumor Effects of Nanoparticles. *ACS Nano* **2017**, 11, 4916-4925.

130. Lu, H.; Yu, Z.; Liu, S.; Cui, L.; Chen, X.; Yao, R., Cugbp1 Promotes Cell Proliferation and Suppresses Apoptosis Via Down-Regulating C/Ebalpha in Human Non-Small Cell Lung Cancers. *Med. Oncol.* **2015**, 32, 82.

131. Lindau, D.; Gielen, P.; Kroesen, M.; Wesseling, P.; Adema, G. J., The Immunosuppressive Tumour Network: Myeloid-Derived Suppressor Cells, Regulatory T Cells and Natural Killer T Cells. *Immunology* **2013**, 138, 105-115.

132. Hawinkels, L. J.; Paauwe, M.; Verspaget, H. W.; Wiercinska, E.; van der Zon, J. M.; van der Ploeg, K.; Koelink, P. J.; Lindeman, J. H.; Mesker, W.; ten Dijke, P.; Sier, C. F., Interaction with Colon Cancer Cells Hyperactivates Tgf-Beta Signaling in Cancer-Associated Fibroblasts. *Oncogene* **2014**, *33*, 97-107.
133. Liu, C.; Zhang, Y.; Lim, S.; Hosaka, K.; Yang, Y.; Pavlova, T.; Alkasalias, T.; Hartman, J.; Jensen, L.; Xing, X.; Wang, X.; Lu, Y.; Nie, G.; Cao, Y., A Zebrafish Model Discovers a Novel Mechanism of Stromal Fibroblast-Mediated Cancer Metastasis. *Clin. Cancer Res.* **2017**, *23*, 4769-4779.
134. Zhang, Q.; Liu, X. Y.; Zhang, T.; Zhang, X. F.; Zhao, L.; Long, F.; Liu, Z. K.; Wang, E. H., The Dual-Functional Capability of Cytokine-Induced Killer Cells and Application in Tumor Immunology. *Hum. Immunol.* **2015**, *76*, 385-391.
135. Zhou, Q.; Zhang, Y.; Du, J.; Li, Y.; Zhou, Y.; Fu, Q.; Zhang, J.; Wang, X.; Zhan, L., Different-Sized Gold Nanoparticle Activator/Antigen Increases Dendritic Cells Accumulation in Liver-Draining Lymph Nodes and Cd8+ T Cell Responses. *ACS Nano* **2016**, *10*, 2678-2692.
136. Palucka, K.; Banchereau, J., Dendritic-Cell-Based Therapeutic Cancer Vaccines. *Immunity* **2013**, *39*, 38-48.
137. Walzer, T.; Dalod, M.; Robbins, S. H.; Zitvogel, L.; Vivier, E., Natural-Killer Cells and Dendritic Cells: "L'union Fait La Force". *Blood* **2005**, *106*, 2252-2258.
138. Yang, X.; Lin, Y.; Shi, Y.; Li, B.; Liu, W.; Yin, W.; Dang, Y.; Chu, Y.; Fan, J.; He, R., Fap Promotes Immunosuppression by Cancer-Associated Fibroblasts in the Tumor Microenvironment Via Stat3-Ccl2 Signaling. *Cancer Res* **2016**, *76*, 4124-4135.
139. Mace, T. A.; Ameen, Z.; Collins, A.; Wojcik, S.; Mair, M.; Young, G. S.; Fuchs, J. R.; Eubank, T. D.; Frankel, W. L.; Bekaii-Saab, T.; Bloomston, M.; Lesinski, G. B., Pancreatic Cancer-Associated Stellate Cells Promote Differentiation of Myeloid-Derived Suppressor Cells in a Stat3-Dependent Manner. *Cancer Res* **2013**, *73*, 3007-3018.
140. Bodogai, M.; Moritoh, K.; Lee-Chang, C.; Hollander, C. M.; Sherman-Baust, C. A.; Wersto, R. P.; Araki, Y.; Miyoshi, I.; Yang, L.; Trinchieri, G.; Biragyn, A., Immunosuppressive and Prometastatic Functions of Myeloid-Derived Suppressive Cells Rely Upon Education from Tumor-Associated B Cells. *Cancer Res* **2015**, *75*, 3456-3465.

141. Guy, T. V.; Terry, A. M.; Bolton, H. A.; Hancock, D. G.; Shklovskaya, E.; Fazekas de St. Groth, B., Pro- and Anti-Tumour Effects of B Cells and Antibodies in Cancer: A Comparison of Clinical Studies and Preclinical Models. *Cancer Immunol Immunother* **2016**, *65*, 885-896.
142. Liepelt, A.; Tacke, F., Stromal Cell-Derived Factor-1 (Sdf-1) as a Target in Liver Diseases. *Am. J. Physiol. Gastrointest. Liver Physiol.* **2016**, *311*, G203-209.
143. Xing, F.; Saidou, J.; Watabe, K., Cancer Associated Fibroblasts (Cafs) in Tumor Microenvironment. *Front Biosci (Landmark Ed)* **2010**, *15*, 166-179.
144. Tiwari, R.; Bargmann, W.; Bose, H. R., Jr., Activation of the Tgf-Beta/Smad Signaling Pathway in Oncogenic Transformation by V-Rel. *Virology* **2011**, *413*, 60-71.
145. Eyler, C. E.; Rich, J. N., Looking in the Mir-Ror: Tgf-Beta-Mediated Activation of Nf-Kappab in Glioma. *J. Clin. Invest.* **2012**, *122*, 3473-3475.
146. Roy, A.; Saraf, S., Limonoids: Overview of Significant Bioactive Triterpenes Distributed in Plants Kingdom. *Biol. Pharm. Bull.* **2006**, *29*, 191-201.
147. Xu, F.; Liu, C.; Zhou, D.; Zhang, L., Tgf-Beta/Smad Pathway and Its Regulation in Hepatic Fibrosis. *J. Histochem. Cytochem.* **2016**, *64*, 157-167.
148. Lasfar, A.; Cohen-Solal, K. A., Resistance to Transforming Growth Factor Beta-Mediated Tumor Suppression in Melanoma: Are Multiple Mechanisms in Place? *Carcinogenesis* **2010**, *31*, 1710-1717.
149. Lu, Y.; Yang, W.; Qin, C.; Zhang, L.; Deng, J.; Liu, S.; Qin, Z., Responsiveness of Stromal Fibroblasts to Ifn-Gamma Blocks Tumor Growth Via Angiostasis. *J Immunol* **2009**, *183*, 6413-6421.
150. Landskron, G.; De la Fuente, M.; Thuwajit, P.; Thuwajit, C.; Hermoso, M. A., Chronic Inflammation and Cytokines in the Tumor Microenvironment. *J Immunol Res* **2014**, *2014*, 149185.
151. Lahn, M.; Kloeker, S.; Berry, B. S., Tgf-Beta Inhibitors for the Treatment of Cancer. *Expert Opin Investig Drugs* **2005**, *14*, 629-643.
152. Saunier, E. F.; Akhurst, R. J., Tgf Beta Inhibition for Cancer Therapy. *Curr. Cancer Drug Targets* **2006**, *6*, 565-578.

153. Banerjee, R.; Tyagi, P.; Li, S.; Huang, L., Anisamide-Targeted Stealth Liposomes: A Potent Carrier for Targeting Doxorubicin to Human Prostate Cancer Cells. *Int. J. Cancer* **2004**, *112*, 693-700.
154. Crosby, T.; Fish, R.; Coles, B.; Mason, M. D., Systemic Treatments for Metastatic Cutaneous Melanoma. *Cochrane Database Syst Rev* **2000**, CD001215.
155. Krysko, D. V.; Garg, A. D.; Kaczmarek, A.; Krysko, O.; Agostinis, P.; Vandenabeele, P., Immunogenic Cell Death and Damps in Cancer Therapy. *Nat Rev Cancer* **2012**, *12*, 860-875.
156. Zhou, Y.; Kipps, T. J.; Zhang, S., Wnt5a Signaling in Normal and Cancer Stem Cells. *Stem Cells Int* **2017**, *2017*, 5295286.
157. Inoue, S.; Setoyama, Y.; Odaka, A., Doxorubicin Treatment Induces Tumor Cell Death Followed by Immunomodulation in a Murine Neuroblastoma Model. *Exp Ther Med* **2014**, *7*, 703-708.
158. Kumawat, K.; Gosens, R., Wnt-5a: Signaling and Functions in Health and Disease. *Cell Mol Life Sci* **2016**, *73*, 567-587.
159. Buttlar, K.; Becker, J.; Pukrop, T.; Wilting, J., Maldevelopment of Dermal Lymphatics in Wnt5a-Knockout-Mice. *Dev Biol* **2013**, *381*, 365-376.
160. Okamoto, M.; Udagawa, N.; Uehara, S.; Maeda, K.; Yamashita, T.; Nakamichi, Y.; Kato, H.; Saito, N.; Minami, Y.; Takahashi, N.; Kobayashi, Y., Noncanonical Wnt5a Enhances Wnt/Beta-Catenin Signaling During Osteoblastogenesis. *Sci Rep-Uk* **2014**, *4*.
161. Spranger, S.; Bao, R.; Gajewski, T. F., Melanoma-Intrinsic Beta-Catenin Signalling Prevents Anti-Tumour Immunity. *Nature* **2015**, *523*, 231-235.
162. Madhunapantula, S. V.; Robertson, G. P., The Pten-Akt3 Signaling Cascade as a Therapeutic Target in Melanoma. *Pigment Cell Melanoma Res* **2009**, *22*, 400-419.
163. Zhang, Y. N.; Poon, W.; Tavares, A. J.; McGilvray, I. D.; Chan, W. C. W., Nanoparticle-Liver Interactions: Cellular Uptake and Hepatobiliary Elimination. *J Control Release* **2016**, *240*, 332-348.

164. Jarnagin, W. R.; Debs, R. J.; Wang, S. S.; Bissell, D. M., Cationic Lipid-Mediated Transfection of Liver Cells in Primary Culture. *Nucleic Acids Res* **1992**, *20*, 4205-4211.

165. Joyce, J. A.; Fearon, D. T., T Cell Exclusion, Immune Privilege, and the Tumor Microenvironment. *Science* **2015**, *348*, 74-80.

166. Salmon, H.; Idoyaga, J.; Rahman, A.; Leboeuf, M.; Remark, R.; Jordan, S.; Casanova-Acebes, M.; Khudoynazarova, M.; Agudo, J.; Tung, N.; Chakarov, S.; Rivera, C.; Hogstad, B.; Bosenberg, M.; Hashimoto, D.; Gnjjatic, S.; Bhardwaj, N.; Palucka, A. K.; Brown, B. D.; Brody, J., *et al.*, Expansion and Activation of Cd103(+) Dendritic Cell Progenitors at the Tumor Site Enhances Tumor Responses to Therapeutic Pd-L1 and Braf Inhibition. *Immunity* **2016**, *44*, 924-938.

167. Tas, F., Metastatic Behavior in Melanoma: Timing, Pattern, Survival, and Influencing Factors. *J Oncol* **2012**, *2012*, 647684.

168. Lee, Y. S.; Kim, S. Y.; Song, S. J.; Hong, H. K.; Lee, Y.; Oh, B. Y.; Lee, W. Y.; Cho, Y. B., Crosstalk between Ccl7 and Ccr3 Promotes Metastasis of Colon Cancer Cells Via Erk-Jnk Signaling Pathways. *Oncotarget* **2016**, *7*, 36842-36853.

169. Tutunea-Fatan, E.; Majumder, M.; Xin, X.; Lala, P. K., The Role of Ccl21/Ccr7 Chemokine Axis in Breast Cancer-Induced Lymphangiogenesis. *Mol Cancer* **2015**, *14*, 35.

170. Xiong, W. J.; Hu, L. J.; Jian, Y. C.; Wang, L. J.; Jiang, M.; Li, W.; He, Y., Wnt5a Participates in Hepatic Stellate Cell Activation Observed by Gene Expression Profile and Functional Assays. *World J Gastroentero* **2012**, *18*, 1745-1752.

171. Pashirzad, M.; Shafiee, M.; Rahmani, F.; Behnam-Rassouli, R.; Hoseinkhani, F.; Ryzhikov, M.; Moradi Binabaj, M.; Parizadeh, M. R.; Avan, A.; Hassanian, S. M., Role of Wnt5a in the Pathogenesis of Inflammatory Diseases. *J Cell Physiol* **2017**, *232*, 1611-1616.

172. Nagasaka, M.; Alhasan, R. S.; Crosby, M.; Thummala, N.; Kim, S.; Abrams, J.; Sukari, A., Toxicities Associated with Checkpoint Inhibitor Immunotherapy: The Karmanos Cancer Center Experience. *J. Clin. Oncol.* **2017**, *35*.

173. Wei, W.; Chua, M. S.; Grepper, S.; So, S. K., Soluble Frizzled-7 Receptor Inhibits Wnt Signaling and Sensitizes Hepatocellular Carcinoma Cells Towards Doxorubicin. *Mol Cancer* **2011**, *10*, 16.

174. Patients with Desmoplastic Melanoma May Respond to Pd-1 Blockade. *Cancer Discov.* **2018**.
175. Burkholder, B.; Huang, R. Y.; Burgess, R.; Luo, S.; Jones, V. S.; Zhang, W.; Lv, Z. Q.; Gao, C. Y.; Wang, B. L.; Zhang, Y. M.; Huang, R. P., Tumor-Induced Perturbations of Cytokines and Immune Cell Networks. *Biochim Biophys Acta* **2014**, *1845*, 182-201.
176. Kuai, R.; Sun, X.; Yuan, W.; Xu, Y.; Schwendeman, A.; Moon, J. J., Subcutaneous Nanodisc Vaccination with Neoantigens for Combination Cancer Immunotherapy. *Bioconjug. Chem.* **2018**.
177. Zhu, G.; Lynn, G. M.; Jacobson, O.; Chen, K.; Liu, Y.; Zhang, H.; Ma, Y.; Zhang, F.; Tian, R.; Ni, Q.; Cheng, S.; Wang, Z.; Lu, N.; Yung, B. C.; Wang, Z.; Lang, L.; Fu, X.; Jin, A.; Weiss, I. D.; Vishwasrao, H., *et al.*, Albumin/Vaccine Nanocomplexes That Assemble in Vivo for Combination Cancer Immunotherapy. *Nat Commun* **2017**, *8*, 1954.
178. Gebremeskel, S.; Johnston, B., Concepts and Mechanisms Underlying Chemotherapy Induced Immunogenic Cell Death: Impact on Clinical Studies and Considerations for Combined Therapies. *Oncotarget* **2015**, *6*, 41600-41619.
179. Kepp, O.; Menger, L.; Vacchelli, E.; Locher, C.; Adjemian, S.; Yamazaki, T.; Martins, I.; Sukkurwala, A. Q.; Michaud, M.; Senovilla, L.; Galluzzi, L.; Kroemer, G.; Zitvogel, L., Crosstalk between Er Stress and Immunogenic Cell Death. *Cytokine Growth Factor Rev.* **2013**, *24*, 311-318.
180. Presant, C. A.; Gams, R.; Bartolucci, A., Mitoxantrone in Malignant Melanoma. *Cancer Treat Rep* **1984**, *68*, 903-905.
181. Arseneau, J. C.; Schoenfeld, D. A.; Borden, E. C., A Phase Ii Study of Dihydroxyanthracenedione (Dhad, Mitoxantrone, Nsc 301739) in Advanced Malignant Melanoma. *Invest New Drugs* **1986**, *4*, 53-56.
182. Kannaiyan, R.; Shanmugam, M. K.; Sethi, G., Molecular Targets of Celastrol Derived from Thunder of God Vine: Potential Role in the Treatment of Inflammatory Disorders and Cancer. *Cancer Lett* **2011**, *303*, 9-20.
183. Zou, L.; Chen, F.; Bao, J.; Wang, S.; Wang, L.; Chen, M.; He, C.; Wang, Y., Preparation, Characterization, and Anticancer Efficacy of Evodiamine-Loaded Plga Nanoparticles. *Drug Deliv* **2016**, *23*, 908-916.

184. Zhou, X.; Seto, S. W.; Chang, D.; Kiat, H.; Razmovski-Naumovski, V.; Chan, K.; Bensoussan, A., Synergistic Effects of Chinese Herbal Medicine: A Comprehensive Review of Methodology and Current Research. *Front Pharmacol* **2016**, *7*, 201.
185. Feng, L.; Zhang, D.; Fan, C.; Ma, C.; Yang, W.; Meng, Y.; Wu, W.; Guan, S.; Jiang, B.; Yang, M.; Liu, X.; Guo, D., Er Stress-Mediated Apoptosis Induced by Celastrol in Cancer Cells and Important Role of Glycogen Synthase Kinase-3beta in the Signal Network. *Cell Death Dis* **2013**, *4*, e715.
186. Kepp, O.; Senovilla, L.; Vitale, I.; Vacchelli, E.; Adjemian, S.; Agostinis, P.; Apetoh, L.; Aranda, F.; Barnaba, V.; Bloy, N.; Bracci, L.; Breckpot, K.; Brough, D.; Buque, A.; Castro, M. G.; Cirone, M.; Colombo, M. I.; Cremer, I.; Demaria, S.; Dini, L., *et al.*, Consensus Guidelines for the Detection of Immunogenic Cell Death. *Oncoimmunology* **2014**, *3*, e955691.
187. Chen, F.; Zhang, J.; Wang, L.; Wang, Y.; Chen, M., Tumor Ph(E)-Triggered Charge-Reversal and Redox-Responsive Nanoparticles for Docetaxel Delivery in Hepatocellular Carcinoma Treatment. *Nanoscale* **2015**, *7*, 15763-15779.
188. Zhang, J.; Chen, R.; Chen, F.; Chen, M.; Wang, Y., Nucleolin Targeting As1411 Aptamer Modified Ph-Sensitive Micelles: A Dual-Functional Strategy for Paclitaxel Delivery. *J Control Release* **2015**, *213*, e137-138.
189. Hu, Y.; Gong, X.; Zhang, J.; Chen, F.; Fu, C.; Li, P.; Zou, L.; Zhao, G., Activated Charge-Reversal Polymeric Nano-System: The Promising Strategy in Drug Delivery for Cancer Therapy. *Polymers* **2016**, *8*, 99.
190. Wu, G.; Fang, Y. Z.; Yang, S.; Lupton, J. R.; Turner, N. D., Glutathione Metabolism and Its Implications for Health. *J. Nutr.* **2004**, *134*, 489-492.
191. Kuppusamy, P.; Li, H.; Ilangoan, G.; Cardounel, A. J.; Zweier, J. L.; Yamada, K.; Krishna, M. C.; Mitchell, J. B., Noninvasive Imaging of Tumor Redox Status and Its Modification by Tissue Glutathione Levels. *Cancer Res* **2002**, *62*, 307-312.
192. Chen, F. Q.; Zhang, J. M.; Fang, X. F.; Yu, H.; Liu, Y. L.; Li, H.; Wang, Y. T.; Chen, M. W., Reversal of Paclitaxel Resistance in Human Ovarian Cancer Cells with Redox-Responsive Micelles Consisting of Alpha-Tocopheryl Succinate-Based Polyphosphoester Copolymers. *Acta Pharmacol. Sin.* **2017**, *38*, 859-873.
193. Meng, F.; Cheng, R.; Deng, C.; Zhong, Z., Intracellular Drug Release Nanosystems. *Mater. Today* **2012**, *15*, 436-442.

194. Tran Janco, J. M.; Lamichhane, P.; Karyampudi, L.; Knutson, K. L., Tumor-Infiltrating Dendritic Cells in Cancer Pathogenesis. *J Immunol* **2015**, *194*, 2985-2991.
195. Ricci, M. S.; Zong, W. X., Chemotherapeutic Approaches for Targeting Cell Death Pathways. *Oncologist* **2006**, *11*, 342-357.
196. Martinez-Lostao, L.; Anel, A.; Pardo, J., How Do Cytotoxic Lymphocytes Kill Cancer Cells? *Clin. Cancer Res.* **2015**, *21*, 5047-5056.
197. Hillen, F.; Baeten, C. I. M.; van de Winkel, A.; Creytens, D.; van der Schaft, D. W. J.; Winnepenninckx, V.; Griffioen, A. W., Leukocyte Infiltration and Tumor Cell Plasticity Are Parameters of Aggressiveness in Primary Cutaneous Melanoma. *Cancer Immunol Immun* **2008**, *57*, 97-106.
198. Fridman, W. H.; Pages, F.; Sautes-Fridman, C.; Galon, J., The Immune Contexture in Human Tumours: Impact on Clinical Outcome. *Nat Rev Cancer* **2012**, *12*, 298-306.
199. Bruttel, V. S.; Wischhusen, J., Cancer Stem Cell Immunology: Key to Understanding Tumorigenesis and Tumor Immune Escape? *Front. Immunol.* **2014**, *5*, 360.
200. Liu, Q.; Zhu, H.; Tiruthani, K.; Shen, L.; Chen, F.; Gao, K.; Zhang, X.; Hou, L.; Wang, D.; Liu, R.; Huang, L., Nanoparticle-Mediated Trapping of Wnt Family Member 5a in Tumor Microenvironments Enhances Immunotherapy for B-Raf Proto-Oncogene Mutant Melanoma. *ACS Nano* **2018**.
201. DePeralta, D. K.; Boland, G. M., Melanoma: Advances in Targeted Therapy and Molecular Markers. *Ann Surg Oncol* **2015**, *22*, 3451-3458.
202. Faries, M. B.; Morton, D. L., Therapeutic Vaccines for Melanoma: Current Status. *BioDrugs* **2005**, *19*, 247-260.
203. Gause, K. T.; Wheatley, A. K.; Cui, J.; Yan, Y.; Kent, S. J.; Caruso, F., Immunological Principles Guiding the Rational Design of Particles for Vaccine Delivery. *ACS Nano* **2017**, *11*, 54-68.
204. Olszanski, A. J., Current and Future Roles of Targeted Therapy and Immunotherapy in Advanced Melanoma. *J Manag Care Spec Pharm* **2014**, *20*, 346-356.

205. Kranz, L. M.; Diken, M.; Haas, H.; Kreiter, S.; Loquai, C.; Reuter, K. C.; Meng, M.; Fritz, D.; Vascotto, F.; Hefesha, H.; Grunwitz, C.; Vormehr, M.; Husemann, Y.; Selmi, A.; Kuhn, A. N.; Buck, J.; Derhovanessian, E.; Rae, R.; Attig, S.; Diekmann, J., *et al.*, Systemic Rna Delivery to Dendritic Cells Exploits Antiviral Defence for Cancer Immunotherapy. *Nature* **2016**, 534, 396-401.

206. Miyaji, E. N.; Carvalho, E.; Oliveira, M. L.; Raw, I.; Ho, P. L., Trends in Adjuvant Development for Vaccines: Damps and Pamps as Potential New Adjuvants. *Braz J Med Biol Res* **2011**, 44, 500-513.

207. Melero, I.; Gaudernack, G.; Gerritsen, W.; Huber, C.; Parmiani, G.; Scholl, S.; Thatcher, N.; Wagstaff, J.; Zielinski, C.; Faulkner, I.; Mellstedt, H., Therapeutic Vaccines for Cancer: An Overview of Clinical Trials. *Nat Rev Clin Oncol* **2014**, 11, 509-524.

208. Lee, B. R.; Ko, H. K.; Ryu, J. H.; Ahn, K. Y.; Lee, Y. H.; Oh, S. J.; Na, J. H.; Kim, T. W.; Byun, Y.; Kwon, I. C.; Kim, K.; Lee, J., Engineered Human Ferritin Nanoparticles for Direct Delivery of Tumor Antigens to Lymph Node and Cancer Immunotherapy. *Sci Rep* **2016**, 6, 35182.

209. Eroglu, Z.; Zaretsky, J. M.; Hu-Lieskovan, S.; Kim, D. W.; Algazi, A.; Johnson, D. B.; Liniker, E.; Ben, K.; Munhoz, R.; Rapisuwon, S.; Gherardini, P. F.; Chmielowski, B.; Wang, X.; Shintaku, I. P.; Wei, C.; Sosman, J. A.; Joseph, R. W.; Postow, M. A.; Carlino, M. S.; Hwu, W. J., *et al.*, High Response Rate to Pd-1 Blockade in Desmoplastic Melanomas. *Nature* **2018**, 553, 347-350.

210. Suarez-Almazor, M. E.; Kim, S. T.; Abdel-Wahab, N.; Diab, A., Review: Immune-Related Adverse Events with Use of Checkpoint Inhibitors for Immunotherapy of Cancer. *Arthritis Rheumatol* **2017**, 69, 687-699.